

# Exploring and Enhancing Conductivity in Semiconductor Nanoparticle Films

by

**Venda Jane Porter**

B.A. Chemistry and B.A. Physics  
Hamline University, St. Paul, MN, 2002

Submitted to the Department of Chemistry in Partial Fulfillment of the Requirements for the  
Degree of

**DOCTOR OF PHILOSOPHY**

at the

MASSACHUSETTS INSTITUTE OF TECHNOLOGY

June 2007

© 2007 MASSACHUSETTS INSTITUTE OF TECHNOLOGY  
All Rights Reserved

Signature of Author \_\_\_\_\_

Department of Chemistry  
May 16, 2007

Certified by \_\_\_\_\_

Moungi G. Bawendi  
Professor of Chemistry  
Thesis Supervisor

Accepted by \_\_\_\_\_

Robert W. Field  
Chairman, Department Committee of Graduate Students



This doctoral thesis has been examined by a committee of the Department of Chemistry as follows:

Professor Keith Nelson

---

Chairman

Professor Mounji G. Bawendi

---

Thesis Supervisor

Professor Sylvia Ceyer

Professor Marc Kastner



# Exploring and Enhancing Conductivity in Semiconductor Nanoparticle Films

by

Venda Jane Porter

Submitted to the Department of Chemistry on May 16, 2007 in Partial Fulfillment of the Requirements for the Degree of Doctor of Philosophy in Chemistry

## ABSTRACT

Semiconductor nanocrystals (NCs) are a promising material for use in opto-electronic devices as their optical properties tune with particle size. NCs formed via colloidal synthesis are suspended in solution by the organic ligands which passivate the NC surface after synthesis, and NCs can be deposited from solution to form NC solids. In theory, 'designer solids' having different electrical properties can be formed by changing, and even mixing, the types of NCs in the NC solids. However, the organic ligands capping each NC hinder charge transport between NCs in the solid. This thesis presents a study of how methods developed to enhance conductivity alter the physics of charge transport through the NC solid.

Chapter 2 describes a post-deposition ligand exchange that decreases interparticle spacing and increases photogenerated current by over three orders of magnitude. In addition, the larger currents allow for the investigation of the nature of the CdSe NC/gold electrode interface which is found to impede electron and hole injection into the NC film. In Chapter 3 the electronic height of the tunnel barrier between CdSe NCs is changed by separating NCs with a thin ZnS inorganic shell rather than organic ligands. The inorganic shell is found to passivate the NC surface better than the ligands. This reduces non-radiative exciton recombination and allows for large room temperature photocurrents. The semiconductor material is switched from CdSe to CdTe in Chapter 4 and, though CdTe NC films are composed of NCs having the same capping ligand and a similar size as those in the CdSe NC films, the conduction mechanism in the CdTe NC film is different. Specifically, holes rather than electrons are found to be the majority carrier and photocurrent amplification is observed. Finally, in Chapter 5 and Appendix A, the potential of CdTe and CdSe NC films in photovoltaic devices is investigated. In the study of CdSe/CdTe NC mixed films (Chapter 5) it is found that NC surface states reduce device efficiency. In multi-size CdSe NC gradients (Appendix A) the characteristics of the NC/polymer interface are found to dominate charge transport.

Thesis Supervisor: Mounji G. Bawendi, Ph.D.

Title: Professor of Chemistry



*For My Family and Friends*





# Table of Contents

Title Page .....	1
Signature Page .....	3
Abstract .....	5
Dedication .....	7
Table of Contents .....	9
List of Figures .....	13

## Chapter 1:

<b>Introduction.....</b>	<b>16</b>
1.1 Semiconductor Nanocrystals .....	16
1.1.1 Semiconductor Fundamentals .....	16
1.1.2 History of Semiconductor Research .....	18
1.1.3 Future Directions for Semiconductor Devices.....	19
1.2 Semiconductor NC Fundamentals .....	20
1.2.1 Quantum Confinement.....	20
1.2.2 Solution Synthesis.....	23
1.2.3 Preparation of NC Solids .....	26
1.3 Charge Transport in NC Films.....	29
1.3.1 Dark current in NC Films .....	29
1.3.2 Photocurrent in NC Films .....	36
1.4 NC Solids for Device Applications.....	39
1.4.1 NC based Solar Cells .....	39
1.4.2 NC Photodetectors .....	42
1.4.3 Miscellaneous NC Devices .....	43
1.5 Thesis Overview .....	44
1.6 References.....	45

## Chapter 2:

<b>Photoconductivity Studies of Chemically Treated CdSe Nanocrystal Films .....</b>	<b>49</b>
2.1 Introduction.....	49
2.2 Experimental .....	50
2.2.1 Sample Preparation .....	50
2.2.2 Conductivity Measurements .....	51
2.2.3 Treatment .....	52
2.2.4 Transmission Electron Microscopy .....	52
2.2.5 Atomic Force Microscopy .....	53
2.2.6 Glancing Incidence Small Angle X-ray Scattering (GISAXS).....	53
2.2.7 Fluorescence Microscopy .....	54
2.3 Results.....	55
2.3.1 Interparticle Spacing as a function of Chemical Treatment.....	55
2.3.2 Current in Chemically Treated CdSe NC Films .....	57
2.3.3 Fluorescence Quenching.....	64
2.3.4 Temperature Dependence of the Photocurrent .....	66
2.4 Discussion .....	67
2.4.1 Effect of Different Ligands on the Photoconductivity.....	67

2.4.2	Voltage Dependence of the Photocurrent .....	68
	<i>Saturation due to Blocking Contacts</i> .....	68
	<i>Linear Region due to 100 % Exciton Ionization Efficiency</i> .....	70
2.4.3.	Modified Goodman and Rose Model.....	72
2.4.4.	Using the Model to Understand the Effects of Different Chemical Treatments.....	77
2.4.5	Using the Model to Understand the Temperature Dependence .....	79
2.5	Conclusion .....	80
2.6	References.....	82
<b>Chapter 3:</b>		
<b>Room Temperature Photocurrent Displaying 100% Internal Quantum Efficiency in CdSe/ZnS Inorganic Nanocrystal Films .....</b>		<b>84</b>
3.1	Introduction.....	84
3.2	Experimental.....	87
3.2.1	Synthesis .....	87
3.2.2	Sample Preparation .....	88
3.2.3	Conductivity Measurements .....	89
3.2.4	Transmission Electron Microscopy .....	90
3.2.5	Thermal Gravimetric Analysis (TGA).....	90
3.2.6	FTIR and UV-Vis .....	91
3.2.7	Glancing Incidence Small Angle X-ray Scattering (GISAXS).....	91
3.2.8	Quantum Yield (QY) .....	91
3.3	Results.....	92
3.4	Discussion.....	103
3.5	Conclusion .....	111
3.6	References.....	112
<b>Chapter 4:</b>		
<b>Temperature-, Gate-, and Photo-induced Conductance of Close-packed CdTe Nanocrystal Films .....</b>		<b>114</b>
4.1	Introduction.....	114
4.2	Experimental.....	115
4.2.1	CdTe NC Synthesis.....	115
4.2.2	Sample preparation .....	117
4.2.3	Electrical Measurements.....	118
4.3	Results.....	120
4.3.1	Dark Current in CdTe NC Films.....	120
4.3.2	Temperature Dependence of the Dark Current.....	128
4.3.3	Photocurrent in CdTe NC Films .....	130
4.4	Discussion.....	137
4.4.1	Origin of the Dark Current in CdTe NC Films.....	137
4.4.2	Secondary Photocurrent due to a “Non-Blocking” Contact between CdTe NCs and Gold Electrodes.....	140
4.4.3	Carrier Recombination.....	143
4.4.4	Physical Mechanism Behind the Photoconductive Gain and Decay .....	145
4.4.5	Phenomenological Model for Conductance.....	146
4.5	Conclusions.....	150

4.6	References.....	151
<b>Chapter 5:</b>		
<b>Designer CdSe/CdTe NC Solids for Photovoltaic Devices .....</b>		<b>152</b>
5.1	Introduction.....	152
5.2	Experimental.....	154
5.2.1	CdSe and CdTe NC Synthesis .....	154
5.2.2	CdSe/CdTe Nanobarbell (NB) Synthesis.....	155
5.2.3	Film Preparation.....	156
5.2.4	R-Cadmium Cap Exchange.....	159
5.2.5	Overcoating of CdTe NCs with ZnS.....	161
5.2.6	Electrical Measurements.....	162
5.2.7	Optical Measurements .....	163
5.2.8	X-ray Photoelectron Spectroscopy (XPS) .....	164
5.3	Results and Discussion .....	164
5.3.1	Study of CdSe/CdTe NB films and mixed films of CdTe and CdSe NCs Between Parallel Electrodes – Photoconductive Mode .....	164
	<i>CdTe and CdSe NC mixed films</i> .....	164
	<i>CdSe/CdTe NB films</i> .....	167
5.3.2	Layered CdTe and CdSe Nanocrystal Thin Films Sandwiched between Electrodes – Photovoltaic Mode .....	170
5.3.3	Modifying the Surface of CdTe Nanoparticles.....	176
	<i>Ligand Exchange with Cadmium Oleate</i> .....	176
	<i>Growing an Inorganic Shell via Overcoating</i> .....	179
	<i>Sintering of the NC film</i> .....	180
5.4	Conclusions.....	182
5.5	References.....	183
<b>Chapter 6:</b>		
<b>Concluding Remarks .....</b>		<b>186</b>
<b>Appendix A:</b>		
<b>Size Dependent Charge Transport and Collection in Junctions Containing Multi- Size Arrays of CdSe Nanocrystals .....</b>		<b>188</b>
A.1	Introduction.....	188
A.2	Experimental .....	189
A.2.1	Synthesis .....	189
A.2.2	NC Film Preparation .....	190
A.2.3	Optical Characterization .....	191
A.2.4	Atomic Force Microscopy .....	191
A.2.5	Transmission Electron Microscopy and Preparation of NC Cross- sections.....	191
A.2.6	Device Fabrication.....	192
	<i>Nomenclature</i> .....	193
	<i>ITO and PEDOT:PSS</i> .....	194
	<i>Layered Films of CdSe NCs</i> .....	195
	<i>Eutectic Gallium Indium Electrode (EGaIn)</i> .....	196
A.2.7	Electrical Measurements.....	200
	<i>Forward Bias Measurement Setup</i> .....	200

	<i>Photocurrent Measurement Setup</i> .....	202
A.3	Results and Discussion.....	204
A.3.1	CdSe NC Film Characterization .....	204
A.3.2	Forward Bias Measurements – Potential of NC Gradient as a n-type Charge Transport Layer .....	207
	<i>Origin of Rectification</i> .....	210
	<i>Electron Injection and Extraction</i> .....	214
	<i>Field Dependence of the Current</i> .....	221
	<i>Summary</i> .....	228
A.3.3	Photoexcitation – Origin of Exciton Separation and Photovoltaic Effect in the NC Gradient.....	230
	<i>Photocurrent Mechanism</i> .....	230
	<i>Energy Transfer</i> .....	240
	<i>Open Circuit Voltage</i> .....	241
	<i>Summary</i> .....	242
A.4	Conclusions.....	244
A.5	References.....	245
	<b>Curriculum Vitae</b> .....	<b>249</b>
	<b>Acknowledgements</b> .....	<b>252</b>

## List of Figures

Figure 1.1: Energy band diagrams for an insulator and a semiconductor. ....	17
Figure 1.2: The effect of quantum confinement on the electronic band structure and absorbance of CdSe nanocrystals.....	21
Figure 1.3: The absorbance spectra and band structure for CdSe and PbSe NCs .....	23
Figure 1.4: NC synthesis setup .....	26
Figure 1.5: Optical microscope images of CdSe NC films.....	27
Figure 1.6: Schematic of an electrochemical cell used to dope NC films .....	34
Figure 1.7: Cartoon to represent the energy cost and relevant rates involved in the field assisted ionization of an exciton .....	39
Figure 2.1: GISAXS data to determine interparticle spacing in treated CdSe NC films. ....	56
Figure 2.2: Dark current at 77 K before and after butylamine treatment. ....	57
Figure 2.3: Photocurrent at 77 K before and after chemical treatment.....	59
Figure 2.4: Photocurrent at 77 K before and after treatment with sodium hydroxide.....	62
Figure 2.5: Intensity dependence of the photocurrent after chemical treatment.....	62
Figure 2.6: Low voltage photocurrent data for a treated vs. reference CdSe NC film. ...	63
Figure 2.7: Fluorescence quenching data.....	65
Figure 2.8: Temperature dependence of the photocurrent before and after treatment....	66
Figure 2.9: Schematic of the Goodman and Rose Model .....	74
Figure 2.10: Fit of data to the modified Goodman and Rose Model.....	76
Figure 3.1: Energy levels relative to vacuum for a CdSe/ZnS NC film. ....	86
Figure 3.2: Temperature dependence of CdSe photocurrent. ....	93
Figure 3.3: Hysteresis in the photocurrent for CdSe NC films.....	94
Figure 3.4: Photocurrent verses electric field for a CdSe/ZnS NC film .....	95
Figure 3.5: Photocurrent verses electric field for an annealed CdSe/ZnS NC film.....	96
Figure 3.6: Dark current for an annealed CdSe/ZnS NC film .....	97
Figure 3.7: Bandwidth and sensitivity of the photocurrent in an annealed CdSe/ZnS NC film .....	97
Figure 3.8: TGA and FTIR for an annealed CdSe/ZnS NC film.....	99
Figure 3.9: Absorbance spectra and GISAXS of annealed CdSe/ZnS NC films.....	99
Figure 3.10: Photocurrent verses electric field for samples B, C, and D.....	102
Figure 3.11: Temperature dependence of the photocurrent of the CdSe/ZnS (Samples A, B, C, and D) and CdSe core NC films measured in this study .....	102
Figure 3.12: Photocurrent verses electric field for annealed CdSe/ZnS NRs.....	103
Figure 3.13: Extracting the tunnel barrier height in NC films.....	109
Figure 4.1: Absorbance spectra of CdTe NCs .....	117
Figure 4.2: Schematic of the differential conductance measurement system. ....	119
Figure 4.3: Dark current, $I$ , at 87 K as a function of $V_{ds}$ at various gate voltages.....	122
Figure 4.4: Dark current, $I$ , at 87 K as a function of gate voltage with various $V_{ds}$ .....	123
Figure 4.5: Dark current, $I$ , before and after treatment with butylamine.....	124
Figure 4.6: Differential conductance, $di/dV$ , as a function of $V_g$ .....	126
Figure 4.7: Field dependence of the dark and photocurrent in CdTe NC films.....	127

Figure 4.8: Temperature dependence of the dark current, I, (butylamine treated) .....	129
Figure 4.9: Temperature dependence of CdTe photocurrent before and after treatment.	131
Figure 4.10: The photoexcitation intensity dependence of CdTe NC photocurrent .....	133
Figure 4.11: Temperature dependence of the photocurrent decay in CdTe NC films. ..	134
Figure 4.12: Dark and photocurrent as a function of exposure to air .....	135
Figure 4.13: XPS spectra for a CdTe NC film before and after exposure to air.....	136
Figure 4.14: Energy level diagram for a CdTe NC with an electron accepting state. ...	140
Figure 4.15: Schematic displaying the mechanism for secondary photocurrent. ....	143
Figure 4.16: Fit of the phenomenological model to the CdTe NC film photocurrent ...	147
Figure 4.17: Fit of the phenomenological model to the CdTe NC film dark current ....	149
Figure 5.1: TEM and STEM characterization of CdSe/CdTe NBs.....	156
Figure 5.2: Schematic of planar and sandwich device geometries. ....	158
Figure 5.3: Band alignment of CdTe and CdSe.....	165
Figure 5.4: Photocurrent versus electric field for mixed films of CdSe and CdTe NCs	167
Figure 5.5: Photocurrent versus electric field for a CdSe/CdTe NB film.....	168
Figure 5.6: Differential conductance, $di/dV$ , for a CdSe/CdTe NB film.....	169
Figure 5.7: Temperature dependence of the dark current for a CdSe/CdTe NB film....	169
Figure 5.8: The structure, PCA spectra, and i-V curve of Device #1 .....	173
Figure 5.9: The structure, PCA spectra, and i-V curve of Device #2 .....	174
Figure 5.10: The structure, PCA spectra, and i-V curve of Device #3 .....	175
Figure 5.11: Photo of a CdTe NC solution of CdTe NCs with and without the addition of cadmium oleate. Dark and photocurrent for a CdTe NC + cadmium oleate film. ....	177
Figure 5.12: XPS spectra of CdTe and CdTe + cadmium oleate NC films. ....	178
Figure 5.13: Dark and photocurrent versus electric field for a sintered CdTe NC film	181
Figure A.1: Diagram of the process used to make cross-sectional TEM samples.....	192
Figure A.2: Schematic diagrams of selected films of NCs on ITO/PEDOT:PSS. ....	193
Figure A.3: AFM images of bare ITO and ITO covered with PEDOT:PSS .....	194
Figure A.4: AFM images of S, M, and L NC films and spin-cast calibration curves ...	196
Figure A.5: Formation of an EGaIn electrode. ....	198
Figure A.6: Photographs of a PDMS “donut” filled with EGaIn. ....	200
Figure A.7: Schematic illustration of the dark current measurement setup.....	201
Figure A.8: Schematic diagram of the setup used for photocurrent experiments.....	203
Figure A.9: TEM micrograph of a cross-section of the multi-size NC film.....	205
Figure A.10: Absorbance spectra of S, M, and L NCs in solution and films .....	206
Figure A.11: Energy diagram for the ITO/P/NC/EGaIn junctions .....	207
Figure A.12: $\langle J \rangle \log$ vs. V for the junctions ITO/P/X/EGaIn, X = LLL and SSS.....	209
Figure A.13: $\langle J \rangle \log$ vs. V for the junction ITO/P/EGaIn .....	211
Figure A.14: Ranges for the turn-on voltage for all of the junctions studied. ....	213
Figure A.15: Hypothetical parabolic potential energy surfaces for the reactant (NC-/PEDOT:PSS+) and product (NC/PEDOT:PSS).....	218
Figure A.16: Energy Gap and Tunneling Barrier representations of the effect of the accumulation of charge at the NC/PEDOT:PSS interface.....	221
Figure A.17: Plots of $\ln(\langle J \rangle \log / V)$ vs. $ V $ at $V > V_{ON}$ for the junctions ITO/P/X/EGaIn. X = LLL, LMS, LLS, MMM, SL, SML, SSS.....	224

Figure A.18: I-V plots and EQE for ITO/P/SSS/EGaIn in the dark, with 565 nm, and 660 nm (LED) excitation. ....	232
Figure A.19: Ground state absorbance spectra of the films LMS and SML.....	235
Figure A.20: Ratio of $I_{\text{light}}$ to $I_{\text{dark}}$ as a function of voltage for SML and LMS. ....	236
Figure A.21: Ground state absorbance spectra for films of the S, M, and L NCs and PCA spectra for ITO/PEDOT:PSS/X/EGaIn, X = LLL, LMS and SML. ....	237
Figure A.22: The proposed “electron conduction” mechanism for the generation of photocurrent in the ITO/P /NC/EGaIn junctions. ....	238

# Chapter 1

## Introduction

### 1.1 Semiconductor Nanocrystals

The work in this thesis focuses on the study of electrical conduction through solids composed of semiconductor nanocrystals. To provide motivation for this study, Chapter 1 begins with a brief introduction to semiconductors and semiconductor technology. A rundown of the fundamentals of nanocrystals follows including the basic synthesis and photo-physics of colloidal semiconductor NCs. Finally, a review of the research to date in the field of charge transport through NC solids, and a summary of recent attempts to use NC solids in optoelectronic devices, is provided in order to give the reader a frame of reference for the significance of the experiments and results presented in this thesis.

#### 1.1.1 Semiconductor Fundamentals

When atoms assemble to form a solid, the atomic states of each atom mix forming extended bands across the solid. The spacing between bands, and the extent to which the electrons fill the bands, determines whether a material will be a metal, insulator, or semiconductor (Figure 1.1). If an energy band is full of electrons, then current cannot flow and the material is an insulator. In a metal the bands are partially filled and the material can conduct. A semiconductor resembles an insulator in that its highest occupied energy band (valence band)



is completely full; however, the spacing between the valence band and the next empty state (conduction band) is small enough for some percentage of electrons to be thermally excited to the conduction band. Therefore, the conductivity through a semiconductor can be tuned by adjusting the temperature, and thus the density of electrons in the conduction band. When electrons are thermally excited to the conduction band, space is left behind in the valence band and so now conduction of electrons in the valence band is possible. Rather than discussing the collective movement of electrons in the valence band, it is simpler to describe the movement of the empty space. It is referred to as a ‘hole’ and considered a positively charged particle as it moves in the opposite direction of the electrons in the valence band.

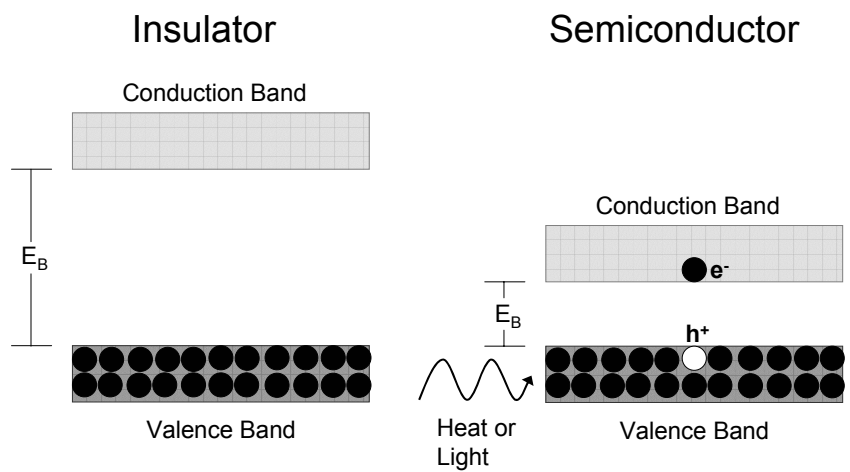


**Figure 1.1:** Energy band diagrams for an insulator and a semiconductor.

The density of electrons in the conduction and valence bands can also be tuned through doping the semiconductor with impurity atoms. For instance, electrons can be added to silicon by incorporating phosphorus atoms into the lattice. Phosphorus has five valence electrons as opposed to the four of silicon. Silicon can also be doped with holes with the substitution of boron atoms which have 3 valence electrons. In addition to heat, light having energy greater than the band gap can be used to excite electrons from the valence band into the conduction

band. The ability to tune the conductance of a material with experimentally controllable parameters allows for a multitude of applications for semiconductor materials.

### **1.1.2 History of Semiconductor Research**

The earliest observation of a characteristic semiconductor property is dated back to 1833 when Michael Faraday observed that the resistance of  $\text{Ag}_2\text{S}$  increased as the temperature decreased.<sup>1</sup> Other 19<sup>th</sup> century investigators are credited with the discovery of other semiconductor properties. In 1839 Becquerel observed a photovoltage when light shone on selenium (the photovoltaic effect) and in 1879 E. H. Hall found that when a magnetic field is applied across a conducting solid a potential difference is generated (the Hall Effect).<sup>1</sup> Carl Ferdinand Braun commercialized the first semiconductor device. The device was known as the cat's whiskers and it detected radio waves through the rectification of current flow in  $\text{PbS}$ .<sup>1</sup> Other semiconductor devices followed over the next 30 years such as selenium and copper-copper oxide rectifiers used to convert alternating to direct current. Copper oxide photocells were also used by the film industry to turn markings on film into sound.<sup>1</sup>

The research and design of semiconductor devices really escalated after the introduction of quantum mechanics and its application to the behavior of solids in the 1930's. The invention of the germanium transistor in 1947 at Bell Labs by Shockley, Brattain, and Bardeen<sup>1</sup> soon followed, marking the start of the semiconductor revolution and the incorporation of semiconductor technology into nearly every aspect of daily life. The transistor comprises the framework of the integrated circuits which run our computers, cell phones, cars, and many other devices today. The lasers in our CD and DVD players are based on semiconductors, as are solar cells, LEDs (light emitting diodes), and my personal favorite, the remote control of my television. With semiconductors being an integral part of modern society, it is no surprise that a

tremendous amount of research is focused on the invention of new semiconductor materials and the improvement of existing semiconductor devices.

### **1.1.3 Future Directions for Semiconductor Devices**

The ability to easily fine tune the absorption and emission wavelengths of a semiconductor material would aid in the design and optimization of semiconductor devices such as solid state lasers, LEDs, photodetectors, night vision, and especially solar cells. A major energy loss in solar cells is the transformation of some of the energy of absorbed light into thermal energy. An exciton created by the absorption of a photon having energy greater than the band gap of a semiconductor will immediately relax to the band edge, losing the excess energy to phonons. Therefore, the maximum efficiency a silicon solar cell can ever achieve is 31%.<sup>2</sup> In order to harvest all of the energy of the solar spectrum, a tandem cell of semiconductors having different band gap energies must be constructed.

Small semiconductors, termed quantum dots (QDs) or nanocrystals (NCs), exhibit optical properties which vary when the dimensions of the semiconductor become small in three dimensions.<sup>3</sup> QDs can be produced through lithography,<sup>4</sup> crystallographic strain,<sup>5</sup> or colloidal synthesis.<sup>6</sup> With the ability to fine tune the optical properties of semiconductors, many new applications can be realized, and improvements made to existing semiconductor technology.

This thesis focuses on the study of electrical conduction through films of colloidal NCs. Colloidal NCs are produced via the pyrolysis of organometallic precursors in a solvent solution. This reaction results in small semiconductor crystals whose surface is passivated with organic ligands. These ligands keep the NCs suspended in solution and they can be deposited from solution onto a variety of substrates to form films of NCs. The study of electrical conduction through NC films is key to the realization of NC optoelectronic devices. In order to engineer

efficient devices, it is necessary to develop an understanding of the conduction mechanisms by which electrical current travels through NC films. This is a substantial challenge as the organic ligands which passivate the NC surface act as a physical and electronic barrier to conduction through the NC solid. Besides use in device applications, a solid in which the band gap, site energies, and electronic coupling are all tunable is an incredible medium in which to explore the fundamental physics of charge transport.

## **1.2 Semiconductor NC Fundamentals**

### **1.2.1 Quantum Confinement**

When a semiconductor absorbs light, the energy of the photon is used to promote an electron to the conduction band and a hole is left behind in the valence band. This electron-hole pair is termed an exciton, and it is bound through coulomb attraction of the negatively charged electron to the positively charged hole. The distance between the electron and hole of the exciton in the semiconductor lattice is termed the exciton Bohr radius [Figure 1.2(a)], similar in concept to the Bohr radius of an electron orbiting the nucleus in an atom. When the dimensions of a semiconductor become smaller than the exciton Bohr radius, the exciton is physically confined. The physical confinement of the exciton results in changes in the energetic spectrum of the semiconductor.<sup>3,7,8</sup> As the size of the semiconductor becomes smaller, the energy gap between the conduction and valence bands increases [Figure 1.2(b)]. In general, the relationship between band gap energy and particle size goes roughly like that of a particle in a spherical box,  $E_g \sim 1/a^2$ , where  $a$  is the radius of the particle. The physical confinement also results in quantization of the continuous energy levels of the conduction and valence bands. The quantization of the energy bands is one reason NCs are often called ‘artificial atoms’. The

absorption spectrum of a NC exhibits the effects of the quantization as it contains features resulting from the transitions between the quantized states [Figure 1.2(c)].

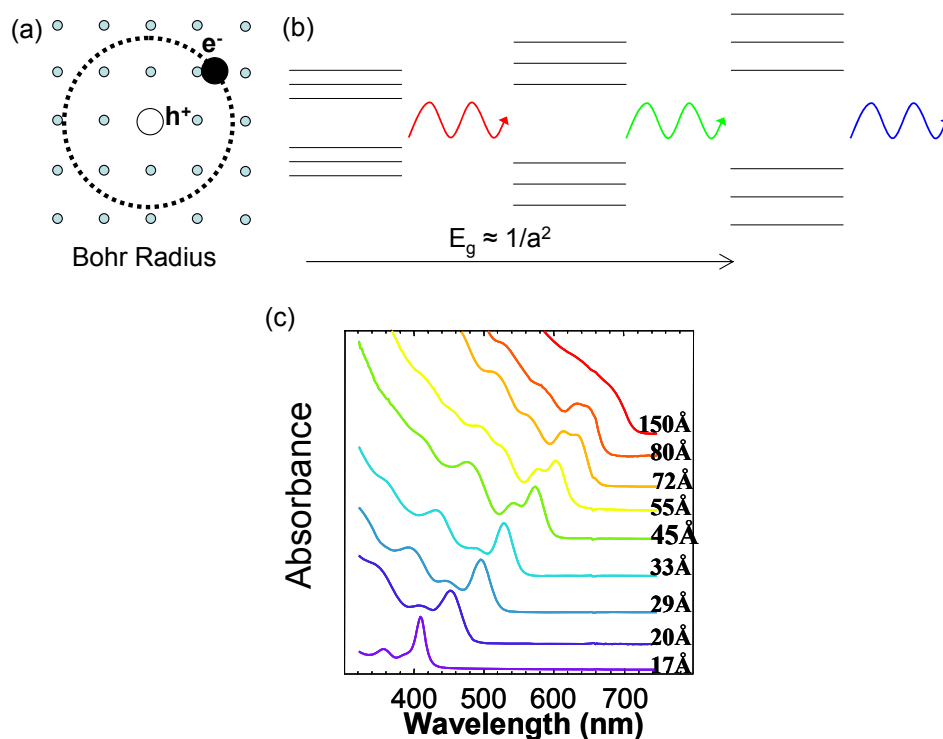


**Figure 1.2:** (a) Bohr radius of an exciton and (b) the effect of quantum confinement on the electronic band structure and emission of a nanocrystal. (c) The absorbance spectrum of CdSe as a function of particle diameter is given below. The image of the absorbance spectra is from the Ph.D. thesis of Christopher Murray.<sup>9</sup>

While the blue shift of the band gap energy and quantization of energy levels are a general effect of confinement, the exact energy level spacing and optical effects are specific to a semiconductor material. The emission and absorption properties depend on other factors such as the Bohr radius of the given semiconductor, the effective masses of the electron and hole, and the shape of the nanoparticle. The absorbance and emission spectra for CdSe and PbSe NCs are shown in Figure 1.3. In CdSe, the effective mass of the hole is six times that of the electron<sup>10</sup> which results in closer spacing between the quantized states of the valence band than the conduction band. In PbSe, the electron and hole effective masses are approximately equal<sup>10</sup> and

the quantized energy levels in the conduction and valence bands are spaced equally. In addition, the sensitivity of the band gap energy blue shift to NC size is material dependent. The Bohr radius in CdSe is  $\sim 6 \text{ nm}^{10}$  and so by tuning the NC diameter from 1.2-11.5 nm the emission can be experimentally varied from 410 nm – 670nm.<sup>6</sup> In PbSe the Bohr radius is  $23 \text{ nm}^{10}$  and the emission can be experimentally tuned from  $1.1 \mu\text{m}$  (2.6 nm) to  $2.2 \mu\text{m}$  (9.5 nm).<sup>11</sup> Finally, NC shape can also affect the optical properties. When CdSe nanorods (NRs) grow longer than 12 nm they are no longer confined in that dimension. Absorption is dominated by radial confinement along the diameter of the NR and so the absorbance spectrum remains the same, despite change to the rod length.<sup>12</sup> 1D confinement does effect exciton fine structure and results in linearly polarized emission from the NRs.<sup>13</sup> For CdSe tetrapods, the features in the absorption spectrum also depend only on the diameter of the NC core and not the length of the arms.<sup>14</sup>

In conclusion, quantum confinement can be employed to tune the absorption and emission characteristics of a semiconductor. However, the results of confinements are extremely material dependent allowing for the creation of particles with new and interesting optical and electrical properties.

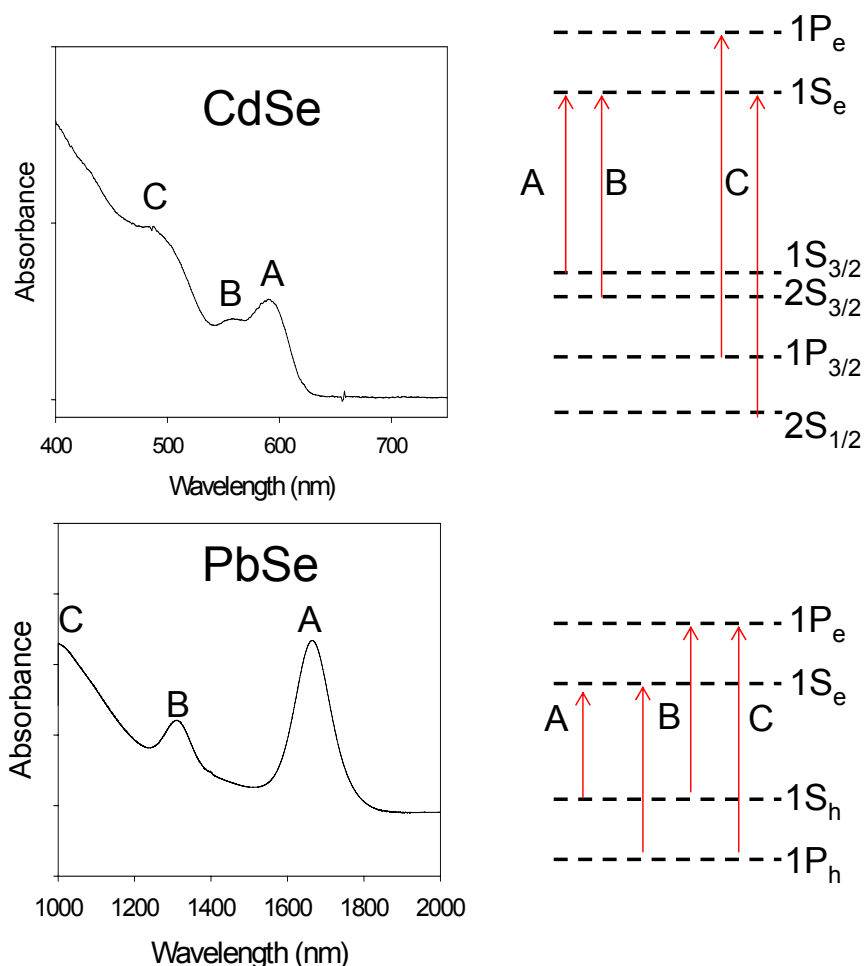


**Figure 1.3:** The absorbance spectra (left) and electronic band structure (right) for CdSe and PbSe NCs. The features in the absorbance spectra are labeled with their corresponding transitions between energy levels. As a note, the transition labeled ‘B’ in PbSe has undergone debate as though the energy spacing between A and B corresponds to a 1S to 1P transition, it is spin forbidden. Some argue it is actually a 1P to 1P transition<sup>15</sup> while others argue that the S and P states are significantly mixed in PbSe NCs.<sup>16</sup>

### 1.2.2 Solution Synthesis

Since the first application of the pyrolysis method to the synthesis of CdSe NCs in the early nineties by Murray et. al.,<sup>6</sup> there has been a significant amount of work improving and modifying the NC synthesis. NCs of CdSe, CdTe, CdS, PbS, PbSe, PbTe, ZnS, ZnSe, InAs, and InP are all routinely made as are core/shell combinations such as CdSe/ZnS<sup>17,18</sup> and

CdTe/CdSe.<sup>19</sup> In addition, nanoparticles of different of shapes and compositions have been created such as CdTe and CdSe tetrapods,<sup>14</sup> CdSe/CdTe nanobarbells,<sup>20</sup> PbTe cubes,<sup>21</sup> and even CdSe dendrimer hyperbranched structures.<sup>22</sup> In this section a typical synthesis of CdSe NCs is described and the function of each chemical in the reaction is explained. A schematic of the reaction setup is given in Figure 1.4. The synthesis of other semiconductor materials vary depending on the availability and reactivity of specific organometallic precursors, but the general elements and procedure remains the same.

A cadmium salt precursor ( $\text{Cd}(\text{OH})_2$ ,  $\text{Cd}(\text{acac})_2$ , or  $\text{CdO}$ ) is degassed in the presence of a reducing agent (dodecanol, hexadecanediol, or oleic acid) and a high boiling point solvent (tri-n-octyl phosphine (TOP), tri-n-octylphosphine oxide (TOPO), octadecene, or oleylamine). This transforms the cadmium into an active form of the cation. There are two types of solvents employed in the literature, coordinating and non-coordinating.<sup>23</sup> TOP, TOPO, and various amines are termed coordinating solvents as their phosphine, oxygen, or nitrogen head groups can bind to both Cd and Se during the reaction and even cap the NCs after the reaction is finished. Long oily alkane molecules, such as octadecene, are not believed to interact with the organometallic elements during the reaction and so are termed non-coordinating solvents. When non-coordinating solvents are used the reducing agent, such as oleic acid, commonly becomes the capping ligand. After the cadmium precursor is prepared, the solution is heated to a high temperature (360 °C for CdSe NCs) and the anion precursor, TOP selenide (TOPSe), is injected. The temperature of the reaction solution rapidly drops after injection of the room temperature TOPSe. Nucleation of CdSe particles occurs until the temperature reaches a temperature regime in which growth onto existing NCs dominates. The reaction is held at this temperature until the desired size is achieved and then the reaction is cooled. To summarize, the general procedure for



the synthesis of NCs involves removing all excess oxygen and water from the cation and anion precursors. The active form of the cation precursor is often prepared by the reduction of a metallic salt. The cation and anion precursors are then injected into a solvent solution at a temperature high enough for NC nucleation and are then grown to a desired size.

Many conditions can be varied to adjust the size, and size distribution, of the NCs. As mentioned previously, the longer the solution is kept at a growth temperature, the larger the NC will grow. However, as the NC grows the size distribution often becomes broader. Other techniques can be employed to form NCs with specific band gap energy upon injection in order to obtain the best possible size distribution. The temperature of injection can be changed: The higher the temperature the more nuclei and thus the smaller the NCs because precursors are used up before the reaction cools to growth temperature. The reactivity of the precursors can be modified as well. TBPSe is more reactive than TOPSe and so produces more nuclei and thus smaller NCs. The amount of impurities in the coordinating solvent also affects the size of the NC. For instance 99% TOPO produces large particles and 90% TOPO smaller NCs. The ratio of 99% to 90% TOPO can be varied to make intermediate sized particles. The exact chemical composition of the active impurities is unknown, but it is speculated that they are short chain phosphonic or phosphinic acids which act as growth inhibitors as the greater the percentage of impurities, the smaller the NCs. The impurities may also be dialkyl phosphines which are good reducing agents and would speed up nucleation.<sup>24</sup> The molar ratio of Cd to Se can also be adjusted, with more Cd resulting in larger NCs. If the Cd is added in significant excess, rods will be grown as Cd adds preferentially along the c-axis in a wurtzite crystal.<sup>12</sup> Other NCs of unusual geometries are formed by adjusting the cation and anion concentrations during the reaction.<sup>14,25</sup>

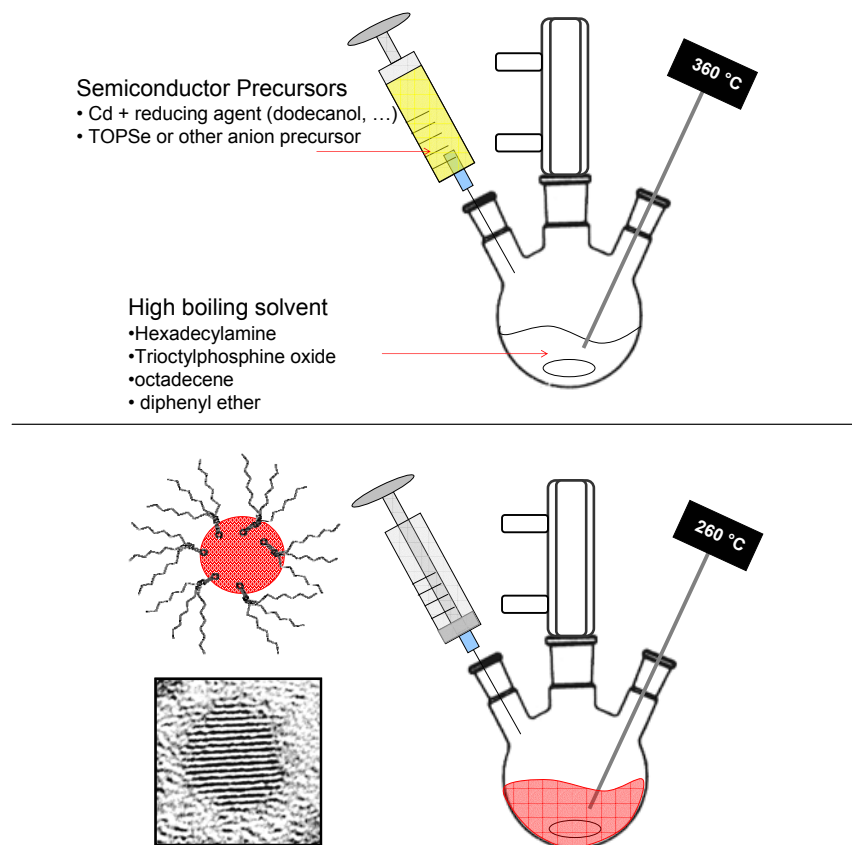


**Figure 1.4:** Schematic of the reaction flask and reagents used in the synthesis of CdSe NCs. The precursors are loaded in the syringe and injected into the high temperature solvent solution (top). After injection (bottom) crystalline NCs capped with organic ligands are formed. The high resolution TEM image of a CdSe NC was taken by F. Mikulec.<sup>26</sup>

### 1.2.3 Preparation of NC Solids

The NCs remain suspended in the oily solvent solution after the synthesis is completed. To use the NCs for any application, be it biological imaging or in an LED, the excess oily solvent must be removed. For the formation of NC solids, the removal of the excess solvent is a key step in making optically clear and close-packed films (Figure 1.5).<sup>27-29</sup> To extract the NCs from solution, a non-solvent such as methanol or acetone is added until the NCs precipitate. The addition of the non-solvent is stopped when the solution transforms from clear to cloudy. The cloudy solution is next centrifuged to separate the NCs from the solvent. The precipitate containing the NCs is saved while the supernatant containing the oily solvent is discarded. The

NCs are then dissolved in a solvent with a low boiling point such as hexane or chloroform and passed through a syringe filter to remove any aggregated NCs or salts from the solution. This precipitation process is repeated until the NC film is optically clear upon deposition. If the precipitation process is repeated too many times all of the organic capping ligands will be stripped from the surface of the NC and the NCs will aggregate. Each new NC recipe produces NCs with different capping ligands, sizes, shapes, and compositions, and so requires a different precipitation procedure. However, the general procedure above serves as a template to begin the processing of each new NC system.

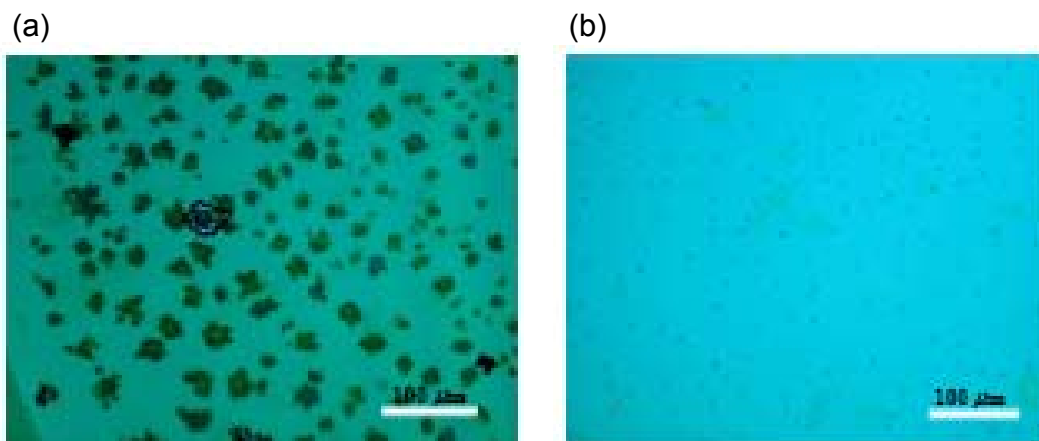


**Figure 1.5:** Optical microscope images of CdSe NC films. (a) A NC film that has not undergone rigorous precipitation and filtering procedure to remove excess organics. The dark spots are crystallized organic molecules. (b) An image of a film which has been precipitated three times and filtered. The tiny spots are pinholes formed as the solvent evaporates. Image from the Ph.D. thesis of Mirna Jarosz.<sup>27</sup>

Once the NCs are processed, they can be deposited onto substrates from the low boiling solvent solution to form NC solids. Two methods are employed to deposit NCs; drop-casting and spin-coating. In spin-coating, a substrate is covered with NC solution and then spun at high speed (~1000-5000 rpm) to wick away excess material and leave a thin film of NCs behind. Films made from spin coating tend to be uniform in thickness, but a considerable amount of NC

material is lost during deposition. It has been determined that films spun out of chloroform are of the highest quality.<sup>30</sup>

To drop-cast a NC film, a small aliquot of NC solution is placed on a substrate and allowed to dry. NC films displaying either local or long range order can be formed by varying the surface chemistry of the substrate, and the drying rate and polarity of the solvent mixture.<sup>29,31</sup> A ratio of 9:1 hexane:octane was found to form glassy, close-packed films displaying local but no long range order when deposited on hydrophobic surfaces. For most charge transport measurements, minimizing interparticle spacing is of primary importance and the close-packed films have the greatest packing density. However, there is also interest in studying charge transport and other physical phenomena in ordered NC superlattices, especially binary superlattices composed of NCs with different optical, physical, electrical, and magnetic properties. The first CdSe NC superlattices were face-centered cubic and formed by deposition from a 9:1 solution of octane:octanol.<sup>31</sup> It was proposed that as the alcohol concentration rose, during the evaporation of octane, the NCs dispersed from solution slowly enough to find equilibrium sites on the lattice, rather than just sticking to the nearest NC.<sup>29</sup> Today it is known that many other variables besides the solvent evaporation rate and NC size distribution can be adjusted to tune the structure of NC superlattices. AB, AB<sub>2</sub>, AB<sub>3</sub>, AB<sub>4</sub>, AB<sub>6</sub>, and AB<sub>13</sub> composites with a variety of symmetries, and composed of different semiconductors, have been built through tuning the Coulomb interactions of charges on the NC surface (charge comes from the capping ligands), van der Waals forces, steric repulsion, substrate interactions, and entropic space filling forces.<sup>32,33</sup> Some of the new nanocomposites even demonstrate an enhancement of electrical properties over NC films of a single semiconductor. For example PbTe-Ag<sub>2</sub>Te NC

films show an enhancement of p-type conductivity when the PbTe- Ag<sub>2</sub>Te ratio is 1:1, as opposed to all PbSe or Ag<sub>2</sub>Te.<sup>34</sup>

### **1.3 Charge Transport in NC Films**

In section 1.3 a literature review of conductivity studies of semiconductor NC solids is presented. The two different subject headings in this section refer to the method by which charges are created in the NC film. ‘Photocurrent’ describes the conduction of electrons and holes generated through the field assisted ionization of photo-excited excitons, while ‘dark current’ refers to electrons and/or holes created through thermal generation, injection from electrodes, or doping. All means of charge generation allow for the study of charge transport in NC films, yet different information can be learned from each method. Photo-excitation results in uniform charge generation throughout the film but exciton binding energy must be accounted for in any conduction model. In the study of dark current, it can be difficult to inject carriers into the NC film and space charge effects may dominate NC to NC transport. However, when doping is employed, the transport of electrons, holes, or both can be studied. Information learned about charge transport in NC solids using all of the previously mentioned charge generation mechanisms will be discussed in the following sections.

#### **1.3.1 Dark current in NC Films**

Early conductivity studies focused on charge transport through CdSe NC films as CdSe was the most characterized semiconductor NC. Unfortunately, TOPO capped CdSe NC films are insulators (resistivity  $\sim 10^{14} \Omega \text{ cm}$ ),<sup>35</sup> hindering efforts to understand charge transport through semiconductor NC arrays. There is little to no thermally generated carrier density in the film, so electrons and holes must be injected from the electrodes in order to study charge transport.

Ginger and Greenham used a variety of metal electrodes with different work functions to inject charge into CdSe NC films.<sup>36</sup> The device they studied consisted of an indium tin oxide transparent electrode (ITO), a 200 nm thick spin-cast film of CdSe NCs, and an evaporated metal electrode. They found that electrodes such as ITO and gold, which have work functions more negative than the -4.5 eV conduction band of the CdSe NCs, had difficulty injecting electrons into the film. Calcium and aluminum electrodes, with less negative work functions, allowed for larger currents and rectification with the ITO electrode. The magnitude of the current injected from calcium and aluminum electrodes was approximately the same, despite the difference in work function between the two metals, so it was concluded that the measured current was dominated by transport through the bulk NC film. The dark current was observed to decay in time and this decay was fit with a stretched exponential. Stretched exponentials are observed in systems in which the relaxation or decay process has a high degree of disorder. A model was proposed in which injected charges are caught in trap sites in the film, and so remain clustered around the injecting electrode. As the trapped charge density increases, the field dropped at the injecting electrode decreases, and the current decays in time. The disorder in trapping states and trapping rates, gives rise to the stretched exponential decay.

Morgan, et. al. also observed a decay of the current injected into a CdSe NC film, yet they found a power law to be a better fit to the decay.<sup>35</sup> The magnitude of the current also scaled with field, conflicting with the space charge limited current model of Ginger and Greenham in which current should scale as  $V^2/L^3$  where V is the applied voltage and L is the distance between the electrodes. The device used to inject charge in Morgan's study was a field effect transistor consisting of planar gold electrodes lithographically patterned onto silicon oxide with a silicon back gate. The CdSe NCs were deposited on top of the gold electrodes, negating the possibility

of damage to the CdSe NC surface as a result of metal evaporation. The proposed model to describe the power law decay is again the build up of a space charge region near the injecting electrode, however the space charge is not a result of trapped charges but rather a Coulomb glass in which charges in a disordered insulator experience long range Coulomb interactions. These interactions result in a minimum separation of charges in the film and lead to a gap (Coulomb gap) in the density of states. Relaxation of the Coulomb glass limits the conduction. The power law exponent of the decay was found to increase with both an increase of temperature and decrease of interparticle spacing (TBPO capping ligand, 7 Å, opposed to TOPO, 11 Å), consistent with the model in which charge transport should proceed faster as NCs get closer together. Ginger and Greenham also observed an increase current when the cap is changed to pyridine (7 Å spacing) from TOPO and it is difficult to understand how a model contingent on an extrinsic trap density should be sensitive to interparticle spacing.<sup>36</sup>

Both the Morgan and Ginger and Greenham models suggest a build up of charge near the injecting electrode which slowly moves into the film over time. The injection of charge from gold electrodes into a CdSe NC film has been imaged by Drndic et. al. using electric-force microscopy (EMF).<sup>37</sup> The charge moves into, and out of, the film very slowly, taking approximately four hours to discharge. As injected charge remains in the film for a long time, the NC film is a different system every time the voltage is turned on and off on time scales less than four hours. This explains many of the memory effects observed in the current through NC films.<sup>35</sup>

Drndic, et. al. also studied charge transport through CdSe NC films (using the same device as Morgan) after thermal annealing to decrease interparticle spacing.<sup>38</sup> The magnitude of the dark current was found to increase by over three orders of magnitude after annealing;

however, it still displayed a slow, power law decay in time. The voltage dependence of the dark current before decay was fit with a simple exponential expression.

$$I = \frac{V}{R_o} \exp\left(-\frac{|V|}{V_o}\right) \quad (1.1)$$

This expression is logical as the high energetic barrier between NCs, resulting from the organic ligands, necessitates tunneling transport and Equation 1.1 is commonly used in simple tunneling models. In Equation 1.1,  $I$  is current,  $V$  is applied voltage,  $R_o$  is a characteristic resistivity, and  $V_o$  is a characteristic voltage. However, the value of  $V_o$  extracted from fits to the data is on the order of  $\sim 30$  eV, two orders of magnitude smaller than the value calculated using Equation 1.2 from a tunneling expression.

$$V_o = \sqrt{\left(\frac{2m^*}{\hbar^2}\right)} (\Phi_B) \frac{ed^2}{2\varepsilon_m L} \quad (1.2)$$

In Equation 1.2,  $d = 1.1$  nm (interparticle spacing),  $L = 2$   $\mu$ m (electrode width),  $\varepsilon_m = 3.7$  (NC film dielectric constant), and  $\Phi_B$  is the height of the tunnel barrier resulting from the organic capping ligands,  $\sim 1$  eV. In order to fit the data to Equation 1.1 and 1.2, the tunnel barrier must be  $\sim 20$   $\mu$ eV, an improbably small number considering at room temperature charges could thermally hop over this barrier and transport would not proceed via tunneling.  $V_o$  on the order of tens of volts corresponds to a voltage drop across each NC in the array of  $\sim 100$  meV. This is on the order of the Coulomb interaction energy between charges on neighboring NCs, suggesting the importance of Coulomb interactions in charge transport through a NC film. As a note, Equation 1.1 can also be used to fit dark current through films of CdSe NCs capped with butylamine (Appendix A) and CdTe NCs (Chapter 4). The observation of this field dependence in different NC systems suggests it may be characteristic of charge transport through NC films.



Novikov et. al. recently proposed another model for the power law decay of the dark current.<sup>39</sup> In this model the current flows in a NC array through a series of conducting channels which run in parallel between the electrodes. Each channel opens randomly to conduct a unit of charge. The conduction events are uncorrelated and so only depend on the waiting time distribution (WTD) between events. The longer a system is observed, the greater the probability is for a channel to be closed, and this is why the current decays in time. Using a Levy WTD, the power law decays for annealed CdSe NC arrays could be fit. In conclusion, while this anomalous transport model is not as intuitive as the Coulomb glass or trapping models, it is a new way to view charge transport in NC films. It is not necessarily any less probable than the other two models as to produce a power law decay with the non-stationary models (Coulomb glass, trapping) the system must relax in an identical, coherent manner over many hours which is unlikely.

The previous studies and models all found that charge injected into a CdSe NC film resulted in a slow decay of current in time. Recently Yu, et. al. measured steady state conduction in a CdSe NC film after doping it with electrons in an electrochemical cell.<sup>40</sup> The electrochemical set up consists of two interdigitated working electrodes made up of 50 Pt electrodes. The Pt interdigitated electrodes are covered with the CdSe NC film and everything is immersed in an electrolyte solution along with a silver reference electrode (Figure 1.6). A small, constant potential is dropped across the two interdigitated electrodes while the potential between these two working electrodes and the reference is varied. In essence, this is the same as measuring the conductance across source drain electrodes in an field effect transistor (FET) as the gate electrode is used to change the charge density. The advantage of the electrochemical cell is that as the 'gate' electrode consists of ions in the electrolyte which can migrate extremely

close to the surface of the NC film. It is analogous to having a 1 nm oxide layer in a solid state FET with an extraordinarily high dielectric constant, and thus breakdown voltage. Yu et. al. found that as the charge density is increased, the current followed the behavior expected for the filling of  $1S_e$  and  $1P_e$  NC orbitals; the magnitude of the current peaks at  $1S_e$  half filling and even decreases slightly before the filling of the  $1P_e$ . The current is correlated with the optical bleach of the  $1S_e$  and  $1P_e$  states. A film of CdSe NCs capped with 1,4-phenylenediamine measured in the electrochemical cell displayed a mobility ( $\mu$ ) of  $\sim 0.8 \times 10^{-2} \text{ cm}^2/\text{Vs}$ , the highest ever in CdSe NC films. However, it is unclear how well this value will transfer to a solid state device as in the electrochemical cell all trapping states are passivated by charges in the electrolyte solution.

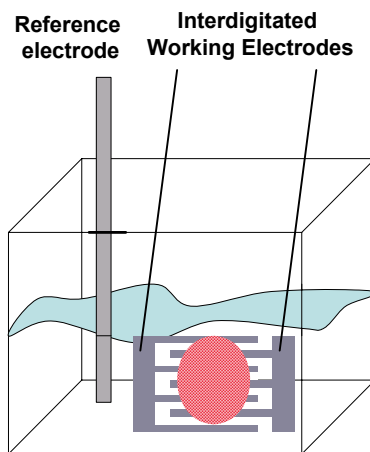


**Figure 1.6:** Schematic an electrochemical cell used to dope NC films. In the cell interdigitated platinum electrodes covered with a NC film are immersed in the electrolyte solution. A silver reference electrode is also immersed in the solution.

In another study, Yu, et. al. used the electrochemical cell to probe the fundamental nature of the charge transport in a CdSe NC film.<sup>41</sup> The CdSe NC film was doped with electrons and then the entire system, including the electrolyte, was cooled to 4 K. The conductance at low bias was measured as a function of temperature and found to follow Equation 1.3, consistent with

variable range hopping conduction including a coulomb gap, also known as Efros-Shklovskii variable range hopping (ES-VRH).

$$G \propto \exp\left(\frac{-B}{T^{\frac{1}{2}}}\right) \quad (1.3)$$

In a system in which charge transport takes place between localized states at low temperature, charges may not hop to the nearest neighbor site. (The term ‘hopping’ can stand for tunneling conduction or thermally activated conduction over a barrier as it is a general term for charge transport between localized sites.) Instead, the charge will maximize the probability of a hopping transition by finding the lowest activation energy and shortest hopping distance, hence the term variable range hopping. Including Coulomb interactions between all of the charges gives the final expression for the temperature dependence of the conductance. Yu, et. al. found  $T^{1/2}$  from 11 to 120 K, which is remarkable as in amorphous semiconductors ES-VRH is not expected at such high temperatures. For instance, in amorphous germanium ES-VRH is not observed above 0.15 K. This difference is attributed to the discrete energy states of the NCs which result in larger densities of states,  $g_0$ , than in an amorphous system. The temperature below which one expects ES-VRH,  $T_c$ , is proportional to  $g_0$ . Above 120 K the conductance has an Arrhenius temperature dependence attributed to nearest neighbor hopping.

ES-VRH was also observed by Wehrenberg, et. al. in PbSe NC films doped with electrons in an electrochemical cell<sup>42</sup> and by Romero, et. al. in PbSe NC films in a solid state FET.<sup>43</sup> PbSe NC film on a silicon inverted FET was found to be insulating as deposited and it was annealed to reduce interparticle spacing and increase conductivity. After annealing at 473 K, the conductivity increased by two orders of magnitude and exhibited ES-VRH temperature dependence below 200 K. Another study measuring PbSe NC films in a FET chemically doped

with hydrazine,<sup>44</sup> found VRH but the temperature dependence was  $T^{1/4}$  not  $T^{1/2}$ .  $T^{1/4}$  is consistent with Mott VRH in which there is no Coulomb gap in the density of states resulting from electron interactions. There is debate over which model should be observed in the PbSe NC film. If the dielectric constant of PbSe is taken to be  $\sim 100$  (close to bulk), rather than 8,<sup>44</sup>  $T^{1/2}$  should not be observed above 10 K. In addition, if the conductance is measured away from zero bias the electric field dependence will reduce the temperature dependence which could result in  $T^{1/2}$  rather than  $T^{1/4}$  dependence.

### 1.3.2 Photocurrent in NC Films

Another mechanism used to uniformly ‘dope’ a NC film is to create excitons with light and apply an electric field to separate the exciton into free electrons and holes. Leatherdale, et. al. measured photoconductivity in CdSe NC films and developed a model in which the temperature and electric field dependence of the conductivity is dominated by the ionization of excitons (i.e. the generation of free electrons and holes) rather than conduction through the NC film.<sup>45</sup>

$$i = e \cdot I \cdot A \cdot \eta(E) \cdot G \quad (1.4)$$

Equation 1.4 is used to describe photoconductivity in bulk semiconductors,<sup>46</sup> and it is modified slightly to describe conduction in NCs in that the exciton separation efficiency has a field dependence.  $e$  is the charge on an electron,  $I$  is the intensity of the excitation light,  $A$  is the absorption of the film in excitons per photon,  $\eta(E)$  is the field dependent exciton separation efficiency and  $G$  is the photoconductive gain, i.e. how many charges are extracted from the film per absorbed photon,  $G = \frac{(\mu_n \tau_n + \mu_p \tau_p) \cdot V}{L^2}$ .  $G$  is a function of the mobility,  $\mu$ , and the lifetime,

$\tau$ , of the electrons and holes as well as the applied voltage,  $V$ , and distance between the electrodes,  $L$ .

When an exciton is excited in a NC film, it can do one of three things; relax radiatively ( $k_r$ ), relax nonradiatively ( $k_{nr}$ ), or be ionized into a free electron and hole by the applied electric field ( $k_E$ ). Therefore the probability to separate an exciton is a function of these three rates.

$$\eta(E) = \frac{k_E(E)}{k_E(E) + k_{nr} + k_r} \quad (1.5)$$

The temperature and field dependence of the CdSe NC films is consistent with Equation 1.5. Leatherdale, et. al. found that the magnitude of the photocurrent decreased as the temperature increased. The non-radiative decay rate increases as the temperature increases and is believe to be responsible for the observed temperature dependence of the photocurrent. This is logical as there should be more thermally accessible trapping or recombination states at higher temperatures which would cause exciton recombination before ionization. Higher electric fields must be applied to separate the same number of excitons at room temperature when compared to low temperature.

The field dependence of the photocurrent was found to be exponential. As the photoconductive gain,  $G$ , is linear with field, it was determined that the exponential behavior must be coming from the carrier generation term,  $\eta(E)$ , as the absorption and intensity have no field dependence (Equation 1.4). A model was developed based on the energy cost of separating an exciton and assisting one of the charges in tunneling to a neighboring NC to fit these results. A cartoon depicting this model is given in Figure 1.7. The parameters which affect the tunneling probability are the tunnel barrier height and width. The height is considered to be the difference between the conduction band of the NC and LUMO of the organic capping ligand (1 eV in this study) and the width is the interparticle spacing. As the interparticle spacing decreased from 11

Å (TOPO capping ligand) to 7 Å (TBPO capping ligand), the photocurrent increased in magnitude, consistent with the tunneling model.

The intensity dependence of the photocurrent was found to be monomolecular which indicates that photogenerated electrons or holes recombine with trapped carriers already present in the film. Given the high trap density, it is possible that the actual tunneling mechanism may not be from NC core to NC core but between trap sites on the surface of the NC. As the trap site supplies some of the energy to separate the exciton, the energy cost for trap to trap tunneling should be less than for core to core. A complex equation describing the photocurrent is derived from Fermi's golden rule and found to fit the photoconductivity data.

$$I(\nu) = \frac{\exp\left(\frac{-4\sqrt{2}\hbar^2 d}{3m(e\nu - \gamma)} \left[ \left(\frac{m\phi}{\hbar^2}\right)^{3/2} - \left(\frac{m(\phi + \gamma - e\nu)}{\hbar^2}\right)^{3/2} \right]\right)}{1 + \exp\left(-\frac{\gamma - e\nu}{a}\right)} \quad (1.6)$$

In Equation 1.6,  $I$  is the photocurrent,  $\nu$  is the site-to-site potential,  $d$  is the QD spacing,  $m$  is the electron mass,  $\phi$  is the tunnel barrier height,  $\gamma$  is the energy difference between the initial and final states (energy cost),  $e$  is the electron charge, and  $a$  describes to degree of wavefunction “tailing” outside of the QD. From the fit, the energy cost to separate an exciton was calculated to be ~150 meV. This is intermediate between the value for core to core and trap to trap tunneling, indicating both mechanisms may be active in the CdSe NC film.

Jarosz, et. al. found the CdSe NC films composed of CdSe NCs synthesized from a cadmium salt, rather than a Cd(CH<sub>3</sub>)<sub>2</sub> recipe, did not display monomolecular recombination, indicating the trap density in the new NC films is lower.<sup>47</sup> In addition, the trap density was further reduced by implementing a rigorous NC processing procedure before film deposition and depositing, measuring, and storing the films in a nitrogen or vacuum environment. All of these

methods appear to have reduced the density of traps in the NC film, demonstrating that film processing can have a significant impact on photoconductivity.

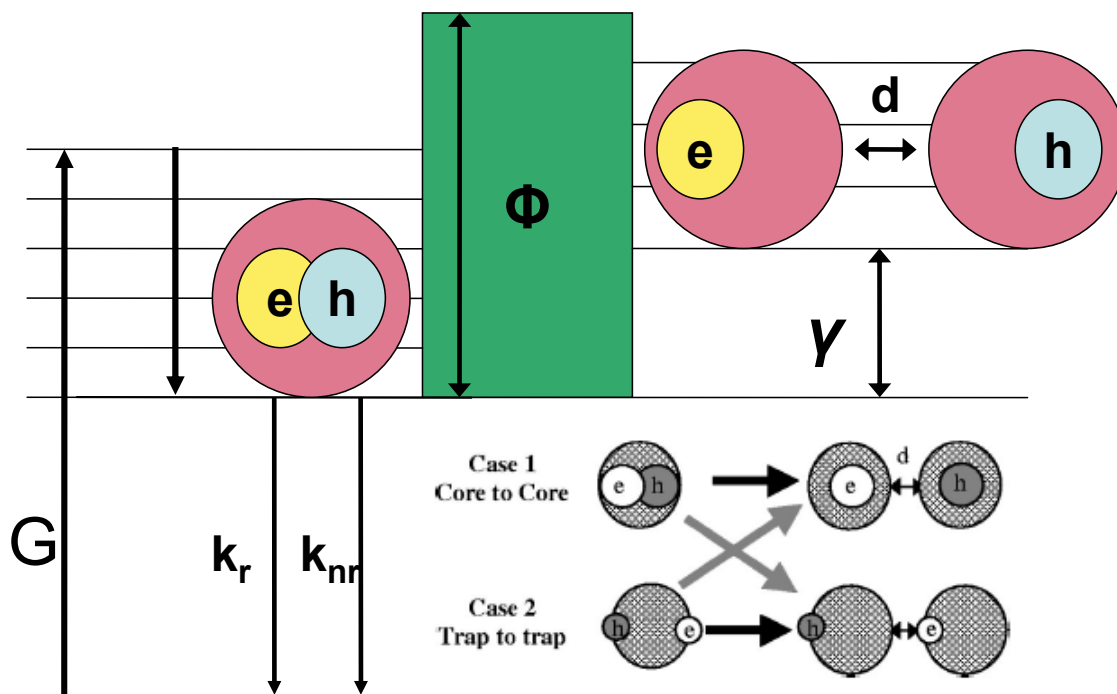


**Figure 1.7:** Cartoon to represent the energy cost and relevant rates involved in the field assisted ionization of an exciton.  $G$  is the exciton generation rate,  $k_r$  is the radiative relaxation rate,  $k_{nr}$  is the nonradiative relaxation rate,  $\Phi$  is the height of the tunnel barrier,  $d$  is the width of the tunnel barrier, and  $\gamma$  is the energy cost to separating an exciton. The energy cost can be due to core to core, trap to trap, or some combination of the two processes as illustrated in the lower right corner of the figure. Both drawings are from the Ph.D. thesis of Catherine Leatherdale.<sup>48</sup>

## 1.4 NC Solids for Device Applications

### 1.4.1 NC based Solar Cells

Owing to the low conductivity of NC films, much of the work in field of NC solar cells has studied NCs dispersed in a hole conducting polymer. The polymer should aid in exciton separation and the transportation of holes to the electrode. Over 10 years ago, Greenham, et. al.

reported that by dispersing CdSe NCs in poly(2-methoxy,5-(2'-ethyl-hexyloxy)-p-phenylenevinylene), MEH-PPV, the photoluminescence of the polymer was quenched.<sup>49</sup> The work function offset between the HOMO and LUMO of MEH-PPV and the conduction and valence bands of the CdSe NCs cause exciton separation at the interface of these two materials; electrons go into the CdSe and holes go into the MEH-PPV. When this polymer/NC blend was placed between ITO and aluminum electrodes the device displayed a photovoltaic effect. The mechanism consisted of exciton separation at the interface of the polymer and NC and then the conduction of electrons through the CdSe and holes through the MEH-PPV as predicted. The external quantum efficiency (EQE) at 514 nm increased with the increase of CdSe NCs density in the polymer and reached a maximum EQE of 12% with 90% loading by weight of NCs. This number is for CdSe NCs capped with pyridine, when capped with TOPO ligands the EQE is only  $5 \times 10^{-3}\%$ . This is consistent with a slower rate of exciton separation when the NC and polymer are farther apart due to longer capping ligands on the NC surface. In addition, this result is consistent with a charge transfer, rather than an energy transfer mechanism, as the probability of charge transfer goes with increased wavefunction overlap. The open-circuit voltage for the device varied as a function of light intensity, but maxed out at  $\sim 0.5$  eV, which is the work function offset between the ITO and aluminum electrodes. It is the field generated by the difference in the potential energy of the electrodes which provides the directionality for the flow of current in polymer/NC blends.

The 12% efficiency of the MEH-PPV/CdSe device was specific for 514 nm excitation and for solar excitation the efficiency was extrapolated to be 0.1%. The efficiency of polymer/NC blend photovoltaic devices has increased since the publication of this paper in 1996. CdSe nanorods mixed with poly(3-hexylthiophene), P3HT, have achieved efficiencies under AM



1.5 solar excitation of 1.7 %.<sup>50</sup> It is proposed that this enhancement is a result of the rod length which, in theory, allows an electron to travel longer distances before it must tunnel to the next NR, thus enhancing electron mobility. Data shows that the efficiency does in fact scale with rod length. Other devices composed of branched CdSe nanoparticles dispersed in a poly(*p*-phenylenvinylene) derivative, OC1C10-PPV, also achieved similar efficiency values.<sup>51</sup> A device consisting of hyperbranched CdSe NCs in P3HT has achieved an efficiency of 2.2%.<sup>52</sup> These nanostructures resemble dendrimers with many inorganic arms branching off of the NC core. In this device, a thin layer of hyperbranched nanostructures in P3HT is placed between the electrodes. The arms of each hyperbranched nanoparticle span the distance between the electrodes offering a single pathway for electron transport to the electrode. Each individual nanoparticle acts as its own solar cell and this is evidenced by the lack of variation in the open circuit voltage ( $V_{oc}$ ) as the CdSe loading fraction increases. In polymer/NR devices,  $V_{oc}$  increases with loading as more rods increases the mobility and charge extraction from the device. The highest polymer/NC device to date demonstrated an efficiency of 2.8%.<sup>53</sup> This device consists of CdSe tetrapods and OC1C10-PPV once again, only this time the polymer/NC blend is spun from a high boiling solvent, 1,2,4-trichlorobenzene, and the tetrapod and polymer layers phase separate into an electron and hole transport layer. While there are fewer interfaces in this geometry for exciton separation, the improvement in charge transport to the electrodes appears to raise the device efficiency. IR absorbing NCs have also been incorporated into polymer/NC photovoltaic devices but reported solar efficiencies are still well below 1 %.<sup>54,55</sup>

There is also a report of an all-NC heterojunction solar cell composed of ITO, a layer of CdTe NRs, a layer of CdSe NRs, and an aluminum electrode.<sup>56</sup> The NRs in this device are capped with pyridine. The heterojunction device performs better than all CdSe NR, all CdTe

NR, or CdSe/CdTe NR blends; however, the efficiency is still low. After sintering of the NRs at 400 °C, the device efficiency rises to 2.1% and to 2.9% when the aluminum electrodes are replaced by calcium electrodes. However, after sintering, the NRs no longer experience quantum confinement and the absorbance shifts to that of amorphous bulk CdSe and CdTe. While progress has been made towards NC solar cells, the efficiency of these devices is still very low when compared to bulk semiconductor cells such as CdTe/CdS thin film heterojunction solar cells which have reported 16.5% efficiency.<sup>57</sup> It is likely that transport through the NC layers, as well as exciton separation at polymer interfaces, is hindered by traps on the NC surface. Surface trapping need to addressed before the advantages NCs have to offer solar power generation can be realized.

#### **1.4.2 NC Photodetectors**

NC films are a promising material for photodetectors as NC absorption and emission are tunable across the visible and NIR wavelengths. A photodetector can be run in photovoltaic or photoconductive mode. In a photoconductive mode the energy to separate excitons comes from an applied external electric field, rather than a limited internal field like in a photovoltaic device. A photodetector consisting of a CdSe NC film capped with butylamine sandwiched between ITO/PEDOT:PSS and silver electrodes has been constructed in the Bawendi lab.<sup>58</sup> This detector displayed 15% EQE and 70% IQE with -6 V applied bias (photoconductive mode). The response of the detector is also fast displaying a 50 kHz 3-dB roll off and it can detect current with  $10 \mu\text{W}/\text{cm}^2$  514 nm photoexcitation.

The development of NC IR photodetectors is an extremely active area of research as 1.5  $\mu\text{m}$  is the optimal wavelength for fiber optic communication. Photodetectors consisting of PbS

NCs (1300 nm, 1<sup>st</sup> abs. feature) between gold electrodes have demonstrated photoconductive gains on the order of 10,000, meaning each absorbed photon produces 10,000 charges.<sup>59</sup> (The mechanism for photoconductive gain will be discussed in detail in Chapter 4.) However, the response of this device is quite slow, ~18 Hz 3-dB bandwidth. This is possibly a result of the amplification process as the charge is cycling through the circuit 10,000 times before recombining. Creating a NC IR photodetector with the right balance between sensitivity and speed remains a challenge.

### 1.4.3 Miscellaneous NC Devices

The memory effects observed in CdSe NC films have been utilized to build a NC memory device.<sup>60</sup> As charges leave a CdSe NC film slowly, earlier measurements affect future measurements. In the memory device reported by Fischbein, et. al. the first application of voltage is considered the write step and the second application of voltage is the read step. The charges can be removed with photoexcitation, or application of voltage having an opposite bias, which would clear the memory device.

NC films have also been used as a material for nanoscale transistors.<sup>44</sup> PbSe NCs can be made n-type (electron rich) through cap exchange with hydrazine, a small basic molecule which passivates the NC surface, decreases interparticle spacing, and reduces the NC core with extra electrons. Heating the hydrazine capped PbSe NCs removes the hydrazine and makes the PbSe NCs p-type (hole rich). This process is reversible. The n- or p-type PbSe films are deposited on a silicon inverted FET and are sensitive to the gate voltage. The devices display channel mobilities of  $\mu_{\text{sat(n-type)}} = 0.95 \text{ cm}^2/\text{Vs}$  and  $\mu_{\text{sat(p-type)}} = 0.18 \text{ cm}^2/\text{Vs}$ . The ability to produce n- and p-type NC materials opens the door for many applications including p/n junction diodes and solar cells.

## 1.5 Thesis Overview

During the past five years a considerable amount of research has focused on the enhancement of conductivity in NC films in order to create electronic devices which make use of the intrinsic optical properties of NCs. The work in this thesis focuses on understanding the fundamental physics involved in charge transport through NC films, as it is necessary to identify the parameters which influence conduction before optimal devices can be engineered. While quantum confinement is responsible for some of the differences between electrical conduction in bulk semiconductors and semiconductor NC solids, physical factors such as the organic ligands passivating the NC surface and unpassivated surface states have an effect as well. One of the recurring themes in this thesis is the influence of the NC surface on conduction in NC solids, not a surprising result as the number of surface atoms in the NC film is much higher than in a bulk solid.

Each chapter in this thesis discusses methods to modify the NC surface and how these modifications alter the physics of charge transport through the NC solid. The effect of interparticle spacing on photoconductivity in a CdSe NC films is studied in Chapter 2. The interparticle spacing is adjusted by varying the length and functionality of the organic capping ligands. In Chapter 3 the height of the energetic tunnel barrier between CdSe NCs is modified. Conduction through CdTe NC films is investigated in Chapter 4 and surface states are found to have an integral role in the observed charge transport mechanisms. Finally, in Chapter 5, CdTe and CdSe NCs are mixed in various combinations to form an ideal solar material, but it is found that surface states dominate charge transport in this system and reduce the efficiency of devices composed of this ‘designer’ NC material.

## 1.6 References

1. J. Orton, *The Story of Semiconductors*. 2004, New York: Oxford University Press.
2. A. J. Nozik. *Physica E* **14**, 115 (2002).
3. L. E. Brus. *The Journal of Chemical Physics* **79**, 5566 (1983).
4. M. A. Kastner. *Physics Today* **46**, 24 (1993).
5. R. Notzel. *Semiconductor Science and Technology* **11**, 1365 (1996).
6. C. B. Murray, D. J. Norris and M. G. Bawendi. *Journal of the American Chemical Society* **115**, 8706 (1993).
7. A. L. Efros, Efros, A. L. *Soviet Physics Semiconductors* **16**, 772 (1982).
8. A. L. Efros and M. Rosen. *Physical Review B* **58**, 7120 LP (1998).
9. C. B. Murray, Ph.D. thesis, Massachusetts Institute of Technology, Cambridge, 1995.
10. H. Landolt and R. Bornestein, *Numerical Data and Functional Relationships in Science and Technology*. 1961, Berlin: Springer-Verlag.
11. J. S. Steckel, S. Coe-Sullivan, V. Bulovic and M. G. Bawendi. *Advanced Materials* **15**, 1862 (2003).
12. X. Peng, L. Manna, W. Yang, J. Wickham, E. Scher, A. Kadavanich and A. P. Alivisatos. **404**, 59 (2000).
13. J. Hu, L.-s. Li, W. Yang, L. Manna, L.-w. Wang and A. P. Alivisatos. *Science* **292**, 2060 (2001).
14. L. Manna, D. J. Milliron, A. Meisel, E. C. Scher and A. P. Alivisatos. **2**, 382 (2003).
15. P. Liljeroth, P. A. Z. van Emmichoven, S. G. Hickey, H. Weller, B. Grandidier, G. Allan and D. Vanmaekelbergh. *Phys. Rev. Lett.* J1 - PRL **95**, (2005).
16. B. L. Wehrenberg, C. Wang and P. Guyot-Sionnest. *J. Phys. Chem. B* **106**, 10634 (2002).
17. B. O. Dabbousi, J. RodriguezViejo, F. V. Mikulec, J. R. Heine, H. Mattoussi, R. Ober, K. F. Jensen and M. G. Bawendi. *Journal of Physical Chemistry B* **101**, 9463 (1997).
18. M. A. Hines and P. Guyot-Sionnest. *J. Phys. Chem.* **100**, 468 (1996).

19. S. Kim, Y. T. Lim, E. G. Soltesz, A. M. De Grand, J. Lee, A. Nakayama, J. A. Parker, T. Mihaljevic, R. G. Laurence, D. M. Dor, L. H. Cohn, M. G. Bawendi and J. V. Frangioni. *Nature Biotechnology* **22**, 93 (2004).
20. J. E. Halpert, V. J. Porter, J. P. Zimmer and M. G. Bawendi. *Journal of the American Chemical Society* **128**, 12590 (2006).
21. J. J. Urban, D. V. Talapin, E. V. Shevchenko and C. B. Murray. *Journal of the American Chemical Society* **128**, 3248 (2006).
22. A. G. Kanaras, C. Sonnichsen, H. Liu and A. P. Alivisatos. *Nano Lett.* **5**, 2164 (2005).
23. A. Peng, X. G. Peng. *J. Am. Chem. Soc.* **124**, 3343 (2001).
24. J. S. Steckel, Ph.D. thesis, Massachusetts Institute of Technology, Cambridge, 2006.
25. L. Manna, E. C. Scher and A. P. Alivisatos. *Journal of the American Chemical Society* **122**, 12700 (2000).
26. F. V. Mikulec, Ph.D. thesis, Massachusetts Institute of Technology, Cambridge, 1999.
27. M. V. Jarosz, Ph.D. thesis, Massachusetts Institute of Technology, Cambridge, 2004.
28. C. Kagan, Ph.D. thesis, Massachusetts Institute of Technology, Cambridge, 1996.
29. C. B. Murray, C. R. Kagan and M. G. Bawendi. *Annual Review of Materials Science* **30**, 545 (2000).
30. D. C. Oertel, Ph.D. thesis, Massachusetts Institute of Technology, Cambridge, 2007.
31. C. B. Murray, C. R. Kagan and M. G. Bawendi. *Science* **270**, 1335 (1995).
32. E. V. Shevchenko, D. V. Talapin, C. B. Murray and S. O'Brien. *Journal of the American Chemical Society* **128**, 3620 (2006).
33. E. V. Shevchenko, D. V. Talapin, N. A. Kotov, S. O'Brien and C. B. Murray. **439**, 55 (2006).
34. J. J. Urban, D. V. Talapin, E. V. Shevchenko, C. R. Kagan and C. B. Murray. *Nature Materials* **6**, 115 (2007).
35. N. Y. Morgan, C. A. Leatherdale, M. Drndic, M. V. Jarosz, M. A. Kastner and M. Bawendi. *Physical Review B* **66**, (2002).
36. D. S. Ginger and N. C. Greenham. *Journal of Applied Physics* **87**, 1361 (2000).
37. M. Drndic, R. Markov, M. V. Jarosz, M. G. Bawendi, M. A. Kastner, N. Markovic and M. Tinkham. *Applied Physics Letters* **83**, 4008 (2003).

38. M. Drndic, M. V. Jarosz, N. Y. Morgan, M. A. Kastner and M. G. Bawendi. *Journal of Applied Physics* **92**, 7498 (2002).
39. D. S. Novikov, M. Drndic, L. S. Levitov, M. A. Kastner, M. V. Jarosz and M. G. Bawendi. *Physical Review B* **72**, (2005).
40. D. Yu, C. J. Wang and P. Guyot-Sionnest. *Science* **300**, 1277 (2003).
41. D. Yu, C. Wang, B. L. Wehrenberg and P. Guyot-Sionnest. *Phys. Rev. Lett.* **92**, 216802 (2004).
42. B. L. Wehrenberg, D. Yu, J. Ma and P. Guyot-Sionnest. *J. Phys. Chem. B* **109**, 20192 (2005).
43. H. E. Romero and M. Drndic. *Phys. Rev. Lett.* **95**, 156801 (2005).
44. D. V. Talapin and C. B. Murray. *Science* **310**, 86 (2005).
45. C. A. Leatherdale, C. R. Kagan, N. Y. Morgan, S. A. Empedocles, M. A. Kastner and M. G. Bawendi. *Physical Review B* **62**, 2669 (2000).
46. R. H. Bube, *Photoconductivity of Solids*. 1960, New York: Wiley.
47. M. V. Jarosz, N. E. Stott, M. Drndic, N. Y. Morgan, M. A. Kastner and M. G. Bawendi. *Journal of Physical Chemistry B* **107**, 12585 (2003).
48. C. A. Leatherdale, Ph.D. thesis, Massachusetts Institute of Technology, Cambridge, 2000.
49. N. C. Greenham, X. Peng and A. P. Alivisatos. *Physical Review B* **54**, 17628 LP (1996).
50. W. U. Huynh, J. J. Dittmer and A. P. Alivisatos. *Science* **295**, 2425 (2002).
51. B. Sun, E. Marx and N. C. Greenham. *Nano Lett.* **3**, 961 (2003).
52. I. Gur, N. A. Fromer, C. P. Chen, A. G. Kanaras and A. P. Alivisatos. *Nano Letters* **7**, 409 (2007).
53. B. Sun, H. J. Snaith, A. S. Dhoot, S. Westenhoff and N. C. Greenham. *Journal of Applied Physics* **97**, 014914 (2005).
54. A. Maria, P. W. Cyr, E. J. D. Klem, L. Levina and E. H. Sargent. *Applied Physics Letters* **87**, 213112 (2005).
55. S. Zhang, P. W. Cyr, S. A. McDonald, G. Konstantatos and E. H. Sargent. *Applied Physics Letters* **87**, 233101 (2005).
56. I. Gur, N. A. Fromer, M. L. Geier and A. P. Alivisatos. *Science* **310**, 462 (2005).

57. A. Morales-Acevedo. *Solar Energy Materials and Solar Cells* **90**, 2213 (2006).
58. D. C. Oertel, M. G. Bawendi, A.C. Arango, V. Bulovic. *Applied Physics Letters* **87**, 213505 (2005).
59. G. Konstantatos, I. Howard, A. Fischer, S. Hoogland, J. Clifford, E. Klem, L. Levina and E. H. Sargent. *Nature* **442**, 180 (2006).
60. M. D. Fischbein and M. Drndic. *Applied Physics Letters* **86**, 193106 (2005).



## Chapter 2

# Photoconductivity Studies of Chemically Treated CdSe Nanocrystal Films\*

### 2.1 Introduction

Enhancing the photoconductivity in NC films would advance the understanding of the physics of charges in NCs and enable the realization of efficient NC applications. Until the study presented here, an increase in photoconductivity had only been achieved by annealing NC films at temperatures high enough to decompose the organic capping ligand between NCs.<sup>1</sup> This reduces interparticle spacing and modifies the height of the tunnel barrier. However, the high temperature annealing step cannot be used with NC films deposited on flexible polymer substrates or with NCs that melt or alloy at lower temperatures than those required for removal of the ligands. In Chapter 2, we present a method to increase the photoconductivity in CdSe NC films by over three orders of magnitude with a room temperature post-deposition cap exchange that replaces the bulky trioctylphosphine ligands with shorter ligands which decrease the interparticle spacing. This is an extension of a technique presented by Yu, et. al.<sup>2</sup> However, while they claim that conjugated or cross-linking types of ligands are required to enhance the current, we show that the main factors leading to the increase in conductivity are the degree of surface passivation and the spacing between NCs after ligand exchange.

---

\* Much of this chapter appears in print: M. V. Jarosz, V. J. Porter, B. R. Fisher, M. A. Kastner and M. G. Bawendi, *Physical Review B* **70**, (2004) and M. V. Jarosz, Ph.D. thesis, Massachusetts Institute of Technology, Cambridge, 2004.

With the significant increase in photocurrent, it is possible to observe 100% exciton ionization efficiency and to understand the relationship between CdSe NCs and the gold electrodes. While the untreated samples show a photocurrent that is highly voltage dependent at all voltages, such behavior is observed only at low voltages for the samples treated with small basic ligands such as amines or sodium hydroxide. At higher voltages, the photocurrent becomes linear with voltage, and at the highest applied voltages, the photocurrent exhibits saturation. A model is introduced to explain the three regimes of voltage dependence in the treated samples by assuming non-injecting contacts and a highly voltage dependent ionization efficiency which saturates at unity at the voltage for which the current-voltage ( $i$ - $V$ ) curve becomes linear. As well as predicting the trends observed in the voltage dependence of the photocurrent, the model also predicts that the product of the mobility and lifetime for electrons is probably not more than  $\sim 10$  times greater than the product for holes. This is surprising as a study of conductivity in CdSe NC films claimed that the hole mobility is five orders of magnitude less than the electron mobility.<sup>3</sup>

## 2.2 Experimental

### 2.2.1 Sample Preparation

CdSe NCs with a diameter of 40 Å are synthesized using a method based on a cadmium salt precursor.<sup>4</sup> A cadmium precursor solution consisting of cadmium hydroxide (98%), tri-*n*-octylphosphine (TOP, 90%), and cis-9-octadecenoic acid (99%) is degassed under vacuum for one hour. After cooling to room temperature, the selenium precursor, tri-*n*-octylphosphine selenide (TOPSe, 1.5 M solution), is added and the precursors are injected into a 335 °C

coordinating solvent solution containing TOP, oleylamine, and dioctyl ether. Upon cooling, butanol is added to the growth solution.

An aliquot of the growth solution is removed and processed following previously established procedures for making close-packed films.<sup>5-11</sup> After an initial precipitation with methanol, the precipitate is dissolved in hexane and placed in the freezer for 10 minutes to encourage precipitation of salts. The sample is then centrifuged and butanol is added to the supernatant. This solution is passed through a 0.2  $\mu\text{m}$  filter and a second precipitation is carried out with methanol. The resulting precipitate is dissolved in hexane and butanol, passed through a 0.1  $\mu\text{m}$  filter, and again precipitated with methanol. The final precipitate is dissolved in hexane and dried under vacuum. The powder of NCs is dissolved in a 9:1 mixture of hexane:octane, filtered through a 0.02  $\mu\text{m}$  filter, and dried under vacuum once again. The NC powder is then brought into the inert atmosphere of the glovebox, where it is redissolved in 9:1 hexane:octane. Films are deposited by drop-casting this solution onto lithographically patterned silicon substrates.

The silicon devices are fabricated by thermally growing 330 nm of oxide on degenerately doped silicon substrates and patterning 200 x 800 x 0.1  $\mu\text{m}^3$  gold bar electrodes using a standard lift off procedure.<sup>12</sup> The spacing between electrodes is 1 $\mu\text{m}$ . The devices are mounted on chip carriers, and electrical contacts from the electrodes to the chip carrier are made prior to film deposition.

### **2.2.2 Conductivity Measurements**

All photoconductivity measurements are carried out under vacuum in a Janis VPF-100 cryostat. The 514 nm line of an Ar<sup>+</sup> laser is used to excite the samples. The laser beam with an intensity of  $\sim 14 \text{ mW/cm}^2$  (unless otherwise stated) is focused onto a pair of gold electrodes. It

has been shown in a previous study that photocurrent is not due to photoinjection from the gold electrodes.<sup>5</sup> Current measurements are made with a Keithley 6517 electrometer, which also supplies the source-drain voltage. For the photocurrent versus voltage curves, the voltage is stepped in 2 V increments from 0 V to 20 V, and in 10 V increments from 20 V to 100 V. The data points are recorded after a delay of 10 seconds. Unless otherwise stated, the data are taken with the sample at 77 K.

### **2.2.3 Treatment**

After measuring the photoconductivity of a NC film, the sample is returned to the glovebox where it is immersed in a 0.1 M solution of the selected reagent: butylamine, aniline, 1,6-diaminohexane, 1,4-phenylenediamine, tri-*n*-butylphosphine, or sodium hydroxide. The solvent for each solution is anhydrous acetonitrile, except for sodium hydroxide which is dissolved in anhydrous methanol due to its limited solubility in acetonitrile. The sample is soaked for 10 minutes, rinsed with 1 mL of solvent, and dried in an oven at 70 °C for 1 hr to remove excess solvent.<sup>2</sup> Two types of butylamine-treated samples are presented: one dried in the oven and the other dried in the glovebox overnight. For all samples not dried overnight, the reference and treated devices were measured on the same day.

### **2.2.4 Transmission Electron Microscopy**

The spacing between close-packed NCs in the reference samples is found using transmission electron microscopy (TEM). Samples are prepared by drop casting a solution of NCs onto a carbon TEM grid. The solution is ~ 200 times more dilute than the solution used to make films in order to form a monolayer of NCs on the TEM grid. The sample is imaged on a JEOL 200CX electron microscope under 100,000 times magnification. After averaging the NC

spacing for over ninety NCs, the interdot spacing in the pre-treated films was determined to be  $1.1 \text{ nm} \pm 0.3 \text{ nm}$ , which is consistent with previous studies.<sup>11</sup>

### **2.2.5 Atomic Force Microscopy**

Sample thicknesses are measured using atomic force microscopy (AFM), with a Digital Instruments Nanoscope IIIa in D3000 tapping mode. AFM samples are prepared in the same manner as the samples used for electrical measurements, except that they are deposited in air onto clean glass slides. The sample is scratched down to the glass to remove the NC film from a small region of the sample. A  $30\text{-}50 \text{ }\mu\text{m} \times 30\text{-}50 \text{ }\mu\text{m}$  region, half over the glass slide and half over the film, is scanned by the AFM, allowing a calculation of the average height of the film relative to the glass slide. Heights are measured in three separate regions on each sample. After chemical treatment, the average height of the film is measured in the same regions. As the size of the CdSe core does not change (there is no shift in the position of the band-edge feature in the absorbance spectrum), the decrease in the thickness of the films is due to a decrease in NC spacing after treatment with 1,4-phenylenediamine, 1,6-diaminohexane, aniline, or tri-n-butylphosphine. The analysis is less straightforward after treatment with butylamine and sodium hydroxide, because some of the film is redissolved so interparticle spacing is only given by glancing incidence x-ray scattering measurements.

### **2.2.6 Glancing Incidence Small Angle X-ray Scattering (GISAXS)**

GISAXS is also used to obtain changes in relative interparticle spacing after chemical treatments. Measurements are performed on a Rigaku 300 Rotaflex diffractometer with a 185 mm focusing circle in Glancing Incidence mode. In Glancing Incidence mode only the x-ray detector is rotated while the sample is held at a small incident angle. GISAXS assists in the

analysis of thin films as the small incident angle limits diffraction to points on the surface of the film, keeping the peak to background ratio high.

Samples are prepared in the same manner as for electrical and AFM measurements, differing only in that samples are deposited in air on clean pieces of silicon. The samples are then chemically treated. For the GISAXS measurements, the accelerating voltage on the copper anode is 60 kV and the flux is 300 mA. The incident angle is set to an angle between 1 ° and 2 ° depending on the exact position of the sample in its holder. The detector continuously scans  $2\theta$  from 1.7 ° to 7 ° at a rate of 0.8 ° per minute and collects data every 0.02 °.

### **2.2.7 Fluorescence Microscopy**

Fluorescence microscopy is used to study fluorescence quenching as a function of applied voltage in the electrically active portion of the NC film. The device structure is the same as that used for the photoconductivity measurements. A home-built epifluorescence, wide field microscope is used to image inside a cold finger cryostat with a 0.7 mm thick window. The objective is a 60x 0.7 NA DIC Nikon objective with a working distance of  $\sim 2$  mm, with the correction collar set to 0.75 mm. The excitation source is an Ar<sup>+</sup> laser operating at 514 nm and  $\sim 300$  W/cm<sup>2</sup>. Collection of the fluorescence is passed through a 514 nm notch filter and a dielectric band pass filter to eliminate excitation light from the collected path. This collected light is then imaged on a 1024 x 1024 pixel CCD detector (Princeton Instruments Micromax, Roper Scientific).

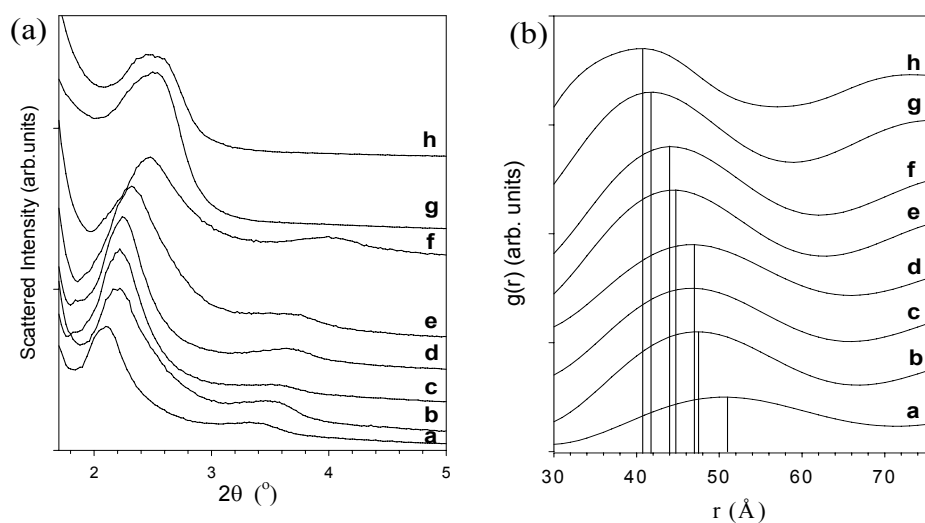
## 2.3 Results

### 2.3.1 Interparticle Spacing as a function of Chemical Treatment

Interparticle spacing found using AFM and GISAXS is summarized in Table 1. The raw data from GISAXS is displayed in Figure 2.1(a). Previous studies have shown that the first peak in the GISAXS scan results from interference between NCs and gives information about interparticle spacing.<sup>8</sup> Subsequent peaks are a result of atomic scattering. To obtain the structure factor,  $S(q)$ , the background is subtracted from the total intensity. The structure factor can be Fourier transformed using Equation (2.1) to find the pair distribution function,  $g(r)$ .

$$g(r) = 1 + \frac{1}{2\pi^2 r \rho_o} \int_0^\infty [S(q) - 1] q \sin(qr) W(i) e^{-\alpha^2 q^2} dq \quad (2.1)$$

In Equation (2.1)  $r$  is distance in angstroms,  $\rho_o$  is the average electron density, and  $q = \frac{4\pi \sin \theta}{\lambda}$  where  $\lambda$  is the wavelength of the x-rays (1.54 Å) and  $\theta$  is half the angle measured by GISAXS. As  $S(q)$  is a finite data set, a convergence factor,  $e^{-\alpha^2 q^2}$ , is added to minimize false features resulting from early termination.<sup>13</sup> A step function,  $W(i)$ , has also been included to isolate the first peak from those resulting from atomic scattering. The pair distribution functions,  $g(r)$ , for the reference and treated samples are presented in Figure 2.1(b). The peak of  $g(r)$  is the core to core spacing in the NC film. Interparticle spacing is extracted by subtracting the diameter of the NC from the peak value of  $g(r)$ . The diameter of the CdSe NC core, as determined from the position of the first peak in the absorbance spectrum, is 40 Å.<sup>6</sup>



Chemical Treatment	Chemical Structure	Interparticle Spacing (Å) AFM	Interparticle Spacing (Å $\pm$ 0.3 Å) GISAXS
Reference		---	11.0
1,4-phenylenediamine	<chem>Nc1ccc(N)cc1</chem>	5-7	7.5
Aniline	<chem>Nc1ccccc1</chem>	5-7	6.8
Tri-n-butylphosphine		7	6.8
Butylamine (dried overnight)	No oven, <chem>NCCCC</chem>	5-7	4.6
1,6-diaminohexane	<chem>NCCCCCCN</chem>	3-5	4.1
Butylamine (oven-dried)	Oven, <chem>NCCCC</chem>	---	1.9
Sodium Hydroxide	$\text{Na}^+ \text{OH}^-$	---	0.6

**Figure 2.1:** (a) GISAXS raw data for ‘a’ reference, ‘b’ 1,4-phenylenediamine, ‘c’ aniline, ‘d’ tri-n-butylphosphine, ‘e’ butylamine (dried at room temperature overnight), ‘f’ 1,6-diaminohexane, ‘g’ butylamine (dried at 70°C for one hour), ‘h’ sodium hydroxide. Data is offset for clarity. (b) The pair distribution function  $g(r)$  for the reference and treated samples. The solid line marks the center of the peak and the labels are the same as in (a). Table 2.1 lists the interparticle spacing from AFM and GISAXS for the reference and treated samples.



### 2.3.2 Current in Chemically Treated CdSe NC Films

The dark current from 0 to 100 V is below the noise ( $< 0.1$  pA) for all reference and treated samples. An example of the dark current before and after treatment with butylamine is displayed in Figure 2.2. These results agree well with those found in previous studies of photoconductivity in CdSe NC films.<sup>1,5,9,14</sup>

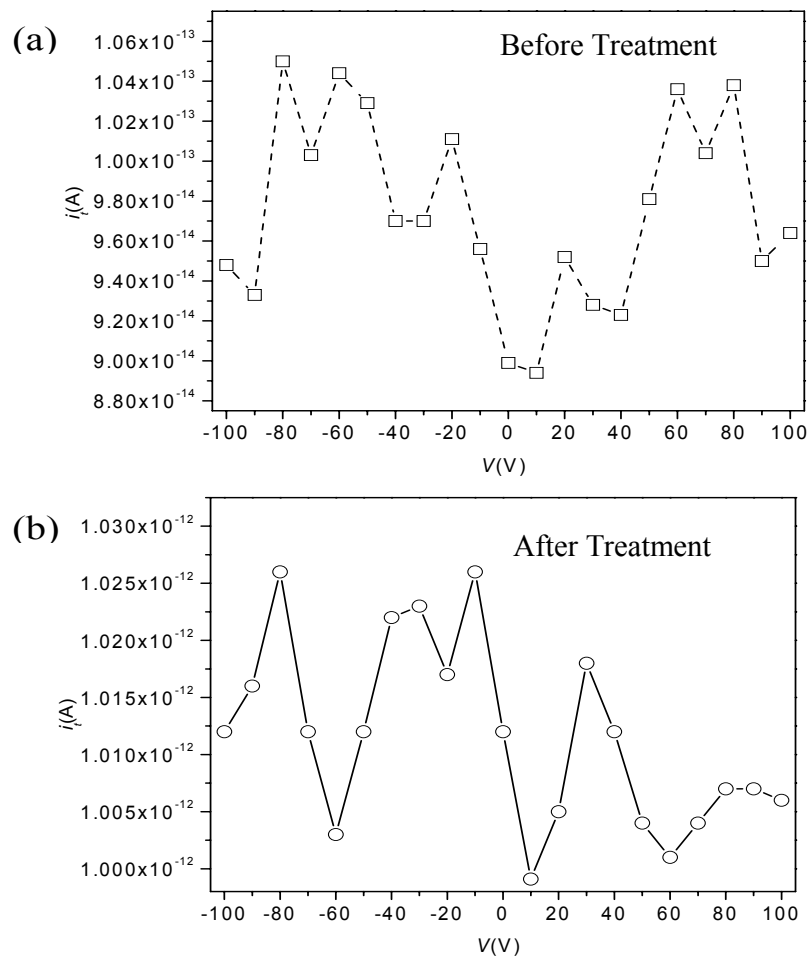


**Figure 2.2:** Dark current at 77K (a) before (open squares, dashed line) and (b) after treatment with butylamine and drying at 70°C for one hour (open circles, solid line).

Figures 2.3 and 2.4 are photo-induced current versus voltage ( $i$ - $V$ ) curves for films of CdSe NCs measured at 77 K. Each  $i$ - $V$  curve is scaled to display the untreated (reference) and treated films on the same plot. The photocurrent of the reference sample is given on the right y-axis, and the photocurrent after treatment is shown on the left y-axis. The lines connecting the data points serve only as a visual aid. In each figure, the current for the reference is highly nonlinear in voltage over the entire range. The currents at 50 and 100 V are typically on the order of 0.1-1 pA and 5-50 pA, respectively.

The  $i$ - $V$  curve shown in Figure 2.3(a) is for a sample treated with butylamine, an unconjugated molecule with a single amine group; this sample was dried overnight at room temperature. Upon treatment, the photoconductivity increases 82 fold at 100 V and 310 fold at 50 V. In addition, the shape of the  $i$ - $V$  curve after treatment becomes linear above  $\sim 60$  V. When a sample is treated with butylamine and dried in the oven at 70 °C, as opposed to drying at room temperature overnight, there is a much larger increase in the photoconductivity. Figure 2.3(b) shows a 145 fold increase in photocurrent at 100 V and a 1280 fold increase at 50 V. As in Figure 1(a), the  $i$ - $V$  curve in Figure 2.3(b) also shows a transition to a linear regime; however, this transition occurs at  $\sim 14$  V. Furthermore, saturation of the photocurrent is evident in Figure 2.3(b), above  $\sim 70$  V. Analysis of GISAXS data shows that NCs in butylamine treated films are brought 2.7 Å closer together when dried at an elevated temperature rather than dried at room temperature overnight.

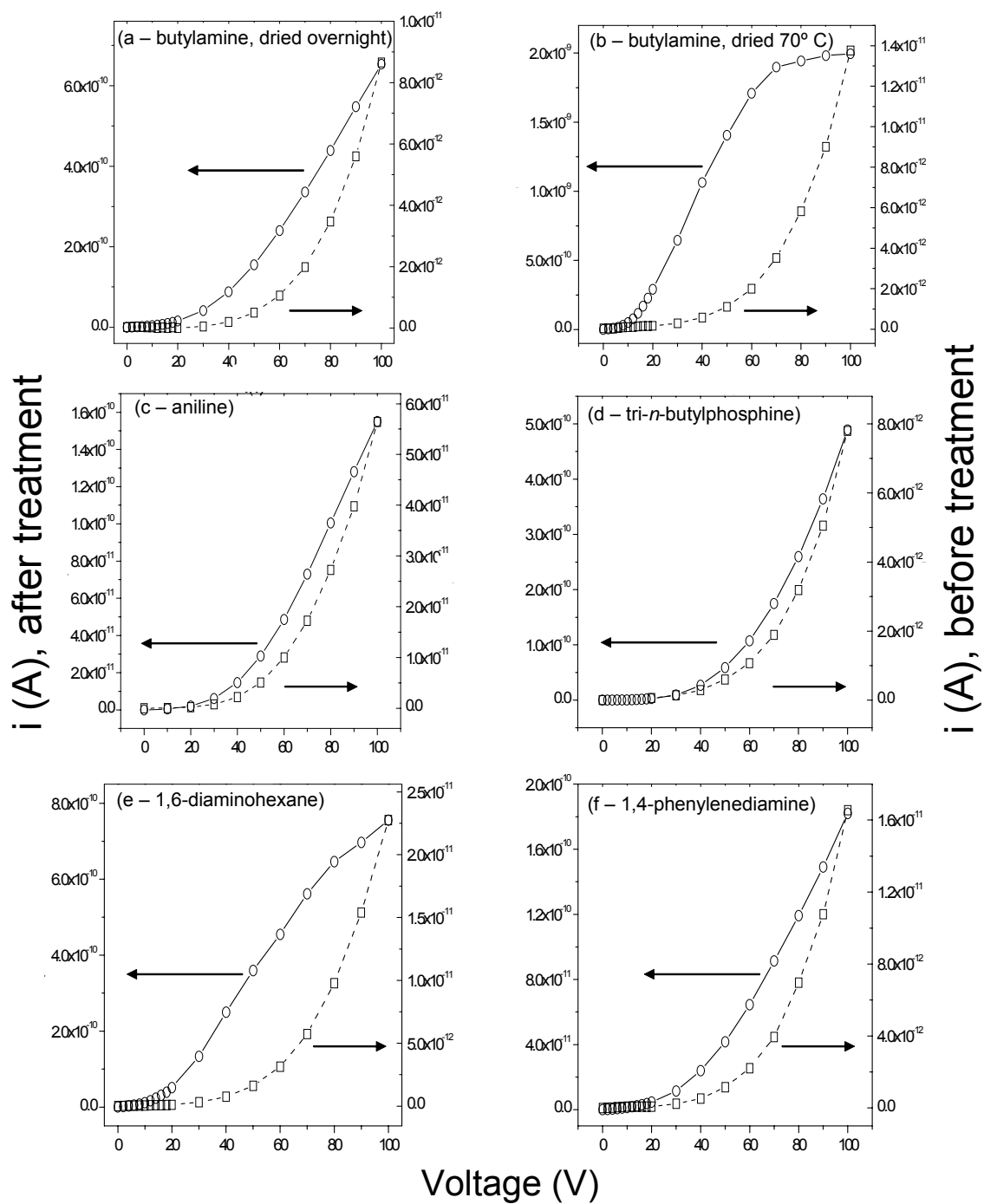


**Figure 2.3:** Photocurrent at 77K before (open squares, dashed line) and after (open circles, solid line) treatment with (a) butylamine (dried at room temperature overnight), (b) butylamine (dried at  $70^\circ\text{C}$  for one hour), (c) aniline, (d) tri-*n*-butylphosphine, (e) 1,6-diaminohexane, and (f) 1,4-phenylenediamine. The x-axis and left and right y-axes are the same for all (a)-(f).

Figure 2.3(c) displays the results for treatment with aniline, a conjugated molecule with one amine group. The photocurrent increases 3 fold at 100 V upon treatment and 6 fold at 50 V. The shape of the reference curve is nonlinear over the entire voltage range, whereas the treatment induces a linear regime above  $\sim 60$  V. The magnitude of the photocurrent at 100 V is hundreds of picoamps, similar to Figures 2.3(a), 2.3(d), and 2.3(f). GISAXS data shows that the spacing between NCs after treatment with aniline is  $\sim 6.8$  Å.

Figure 2.3(d) shows the result of treatment with a shorter analog of TOP, tri-*n*-butylphosphine (TBP). GISAXS data suggests that the NC spacing after treatment with TBP is 6.8 Å, which is identical to the spacing of the aniline-treated sample in Figure 2.3(c). Both samples have photocurrents on the order of hundreds of picoamps at 100 V. However, the shape of the *i-V* curve for the TBP-treated sample does not show a linear region like that of the sample treated with aniline.

Figure 2.3(e) is data for a sample treated with 1,6-diaminohexane, an unconjugated diamine. At 100 V, the conductivity of the treated sample has increased 33 fold over that of the reference and at 50 V it has increased 225 fold. The shape of the 1,6-diaminohexane treated *i-V* curve is similar to those of the butylamine-amine treated samples in that there is a clear linear region. For the former, the linear region begins at  $\sim 30$  V. There is also evidence of photocurrent saturation beginning above  $\sim 80$  V. The magnitude of the photocurrent at 100 V is on the order of hundreds of picoamps, similar to that of the sample treated with butylamine and dried overnight. GISAXS data shows that after treatment with 1,6-diaminohexane the NC spacing is  $\sim 4.1$  Å.

Treatment with 1,4-phenylenediamine, a conjugated diamine, also shows an increase in photoconductivity. However, the magnitude of the photocurrent at 100 V is less than for

treatment with aniline, 1,6-diaminohexane, or butylamine. Figure 2.3(f) shows an 11 fold increase in photocurrent at 100 V, a 36 fold increase at 50 V, and the onset of a linear response at 60V. Interdot spacing after this treatment is  $\sim 7.5\text{\AA}$ , slightly larger than the aniline-treated sample.

The reason amines increase the photocurrent may be attributed to their basic and passivating nature, as discussed below. Therefore, treatment with a very small and strong base, also known to increase photoluminescence quantum yield,<sup>15</sup> should increase photoconductivity as well. Figure 2.4 shows the result of treatment with sodium hydroxide. The photocurrent increases by a factor of 440 at 100 V and by a factor of 5100 at 50 V. The shape of the  $i$ - $V$  curve resembles that of the sample treated with butylamine (oven-dried) in that it has a linear region followed by saturation. In addition, GISAXS shows that NCs are  $0.6\text{\AA}$  apart, even closer than the butylamine (oven-dried) sample. The linear region starts at  $\sim 18\text{ V}$ , and the current is on the order of nanoamps.

Figure 2.5 shows the photocurrent intensity dependence for a sample treated with sodium hydroxide at a voltage corresponding to photocurrent saturation. The current is linear in intensity to within the error and the reason for the linear dependence is discussed in section 2.4.2.

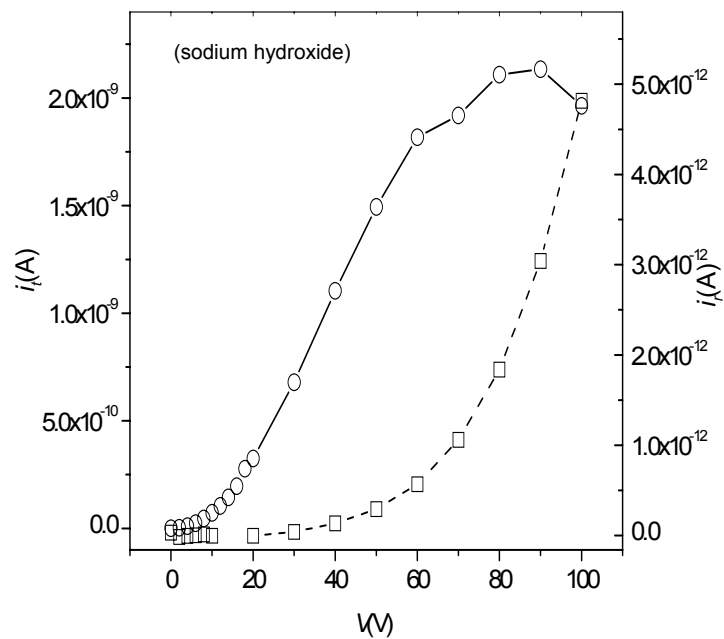


**Figure 2.4:** Photocurrent at 77 K before (open squares, dashed line) and after (open circles, solid line) treatment with sodium hydroxide.

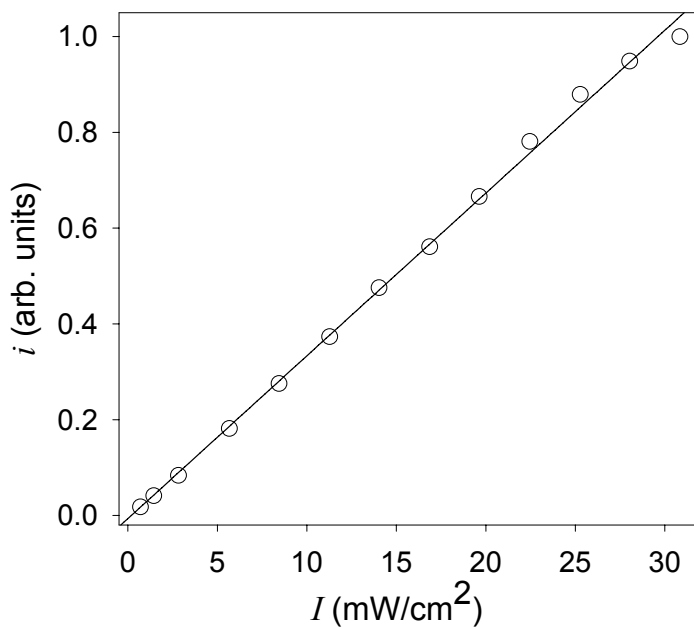


**Figure 2.5:** Intensity dependence of the photocurrent for a sample treated with sodium hydroxide at 100 V, after the photocurrent has saturated with voltage. Open circles represent data and the solid line represents a linear fit.

The open circles in Figure 2.6 represent the low voltage portion of the  $i$ - $V$  curve for the butylamine-treated sample dried at 70 °C; the full  $i$ - $V$  curve for the same sample is shown in Figure 2.3(b). The solid line in Figure 2.6 represents the photocurrent of the untreated sample, scaled in voltage and current to demonstrate that the shape of the  $i$ - $V$  curve for the treated sample in the low voltage regime is the same as the shape of the reference  $i$ - $V$  curve at all voltages. The nonlinear portion of the  $i$ - $V$  curve at low voltages is not significantly altered by any of the treatments.

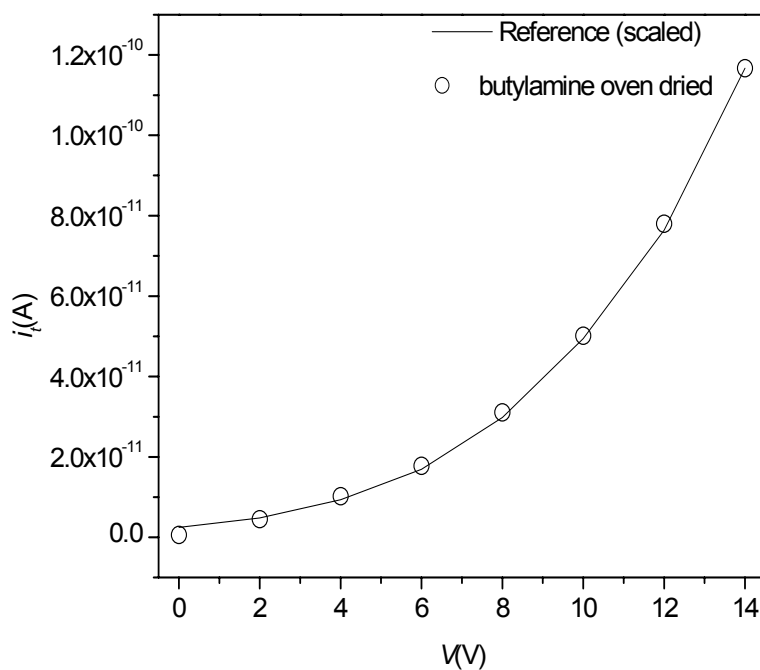


**Figure 2.6:** Photocurrent data (open circles) for a sample treated with butylamine and dried at 70°C for one hour, plotted with reference data (solid line). The current and voltage values for the reference data are scaled to illustrate that the shape of the butylamine treated  $i$ - $V$  curve, at low voltages, is the same as the shape of the reference at all voltages.

### 2.3.3 Fluorescence Quenching

Figure 2.7(a) shows the correlation between the photoconductivity and photoluminescence of a sample treated with 1,6-diaminohexane. The  $i$ - $V$  curve for the sample (solid line, open circles) is plotted in conjunction with fluorescence quenching data (solid squares).  $\Delta I_F$  represents the change in fluorescence intensity when the electric field is applied. It is not possible to determine a quantitative value for the percent fluorescence quenching because of a high level of background fluorescence. The white region of Figure 2.7(a) represents the voltage range over which the  $i$ - $V$  curve exhibits highly voltage dependent behavior, and the white-gray boundary is approximately where the  $i$ - $V$  curve becomes linear. The degree of fluorescence quenching increases quickly when the voltage is high enough for the  $i$ - $V$  curve to become linear and then saturate. Figure 2.7(b) demonstrates that while no significant fluorescence quenching is observed when +20 V is applied, a distinctive and reversible fluorescence quenching is observed when +100 V is applied. The voltage is cycled on and off for +20 V and +100 V to demonstrate the fluorescence quenching is indeed a result of the voltage.



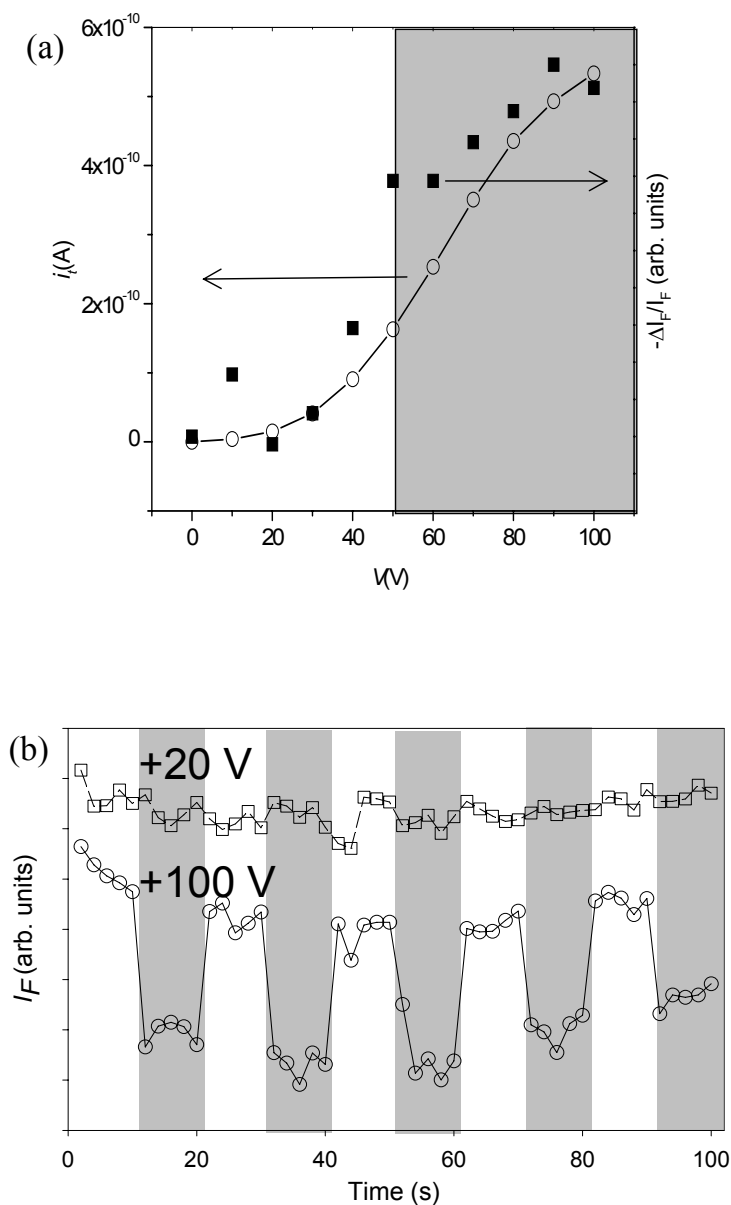


**Figure 2.7:** (a) Fluorescence quenching data (filled squares) for a sample treated with 1,6-diaminohexane compared to the  $i$ - $V$  curve (open circles, solid line) for the same sample. The shaded region contains voltages at which the  $i$ - $V$  curve is linear and unity exciton ionization efficiency is predicted. (b) Time trace of the fluorescence intensity for the same sample as in (a) where the white region corresponds to 0 V and the shaded region corresponds to +20 V (open squares, dashed line) or +100 V (open circles, solid line). The curves corresponding to +20 V and +100 V are offset for clarity. A quantitative number for the percent fluorescence quenching in (a) and (b) was not obtainable due to high background fluorescence.

### 2.3.4 Temperature Dependence of the Photocurrent

Figure 2.8(a) shows the  $i$ - $V$  curves for a reference sample at 77 K and 300 K; the photocurrent at 100 V is more than 30 times smaller at 300 K than at 77 K, consistent with previous observations.<sup>5</sup> Figure 2.8(b) shows the  $i$ - $V$  curves for a sample treated with butylamine and oven-dried, taken at 77 K and 300 K; the photocurrent at 100 V is only about 5 times smaller at 300 K than at 77 K. The photocurrent at 300 K still reaches a linear regime, although not until a higher voltage. Furthermore, while the treated  $i$ - $V$  curve at 77K saturates at 90 V, at 300 K saturated photocurrent is not observed in the range of voltages that are measured.

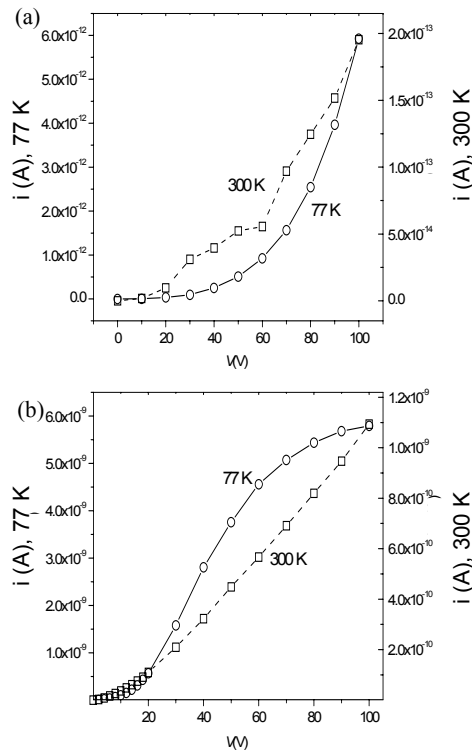


**Figure 2.8:** (a) Photocurrent before treatment at 77 K (open circles, solid line) and 300 K (open squares, dashed line). (b) Photocurrent after treatment with butylamine (oven-dried) at 77 K (open circles, solid line) and 300 K (open squares, dashed line).

## 2.4 Discussion

### 2.4.1 Effect of Different Ligands on the Photoconductivity

A comparison of the  $i$ - $V$  curves in Figures 2.3(a) – 2.3(f) and Figure 2.4 suggests that two phenomena increase photoconductivity and affect  $i$ - $V$  curve shapes: NC spacing, and the functionality of the reagent used for treatment. Amine functionality is expected to passivate recombination centers at the NC surface, as indicated by the increase the photoluminescence quantum yield of amine coated NCs.<sup>4,16-19</sup> The increase in photoconductivity for the TBP treated sample is predominantly caused by the decrease in NC spacing, whereas the increase for the aniline treated sample can result from both a decrease in NC spacing and an increase in surface passivation.

It has been suggested that the use of cross-linking molecules can improve the conductivity of NC films.<sup>2,20</sup> While the photoconductivity does improve with 1,6-diaminohexane, shown in Figure 2.3(e), it increases with butylamine as well. Furthermore, the NCs are 0.5 Å closer together after the 1,6-diaminohexane treatment compared to the butylamine dried overnight treatment. This implies that cross-linking has less of an impact than surface passivation and NC spacing.

Conjugation also does not affect the photoconductivity as much as passivation and NC spacing as is evidenced by the shape of the  $i$ - $V$  curve and the magnitude of the photocurrent in Figure 2.3(c) (aniline treatment). In fact, aniline may have less of a passivating effect than 1,6-diaminohexane or butylamine because its bulkier phenyl group may inhibit surface binding. In addition, if conjugation or cross-linking were responsible for the increase in photoconductivity, treatment with 1,4-phenylenediamine should have displayed the greatest improvement. The fact that the photoconductivity does not increase dramatically, as seen in Figure 2.3(f), strengthens

the argument that surface passivation and NC spacing, rather than conjugation or cross-linking, are responsible for the larger photocurrents and the changes in the  $i$ - $V$  curve shapes.

The similarities between the results obtained after treatment with sodium hydroxide, and after treatment with oven-dried butylamine, suggest a similar mechanism by which the photocurrent is improved. The major difference between treatment with sodium hydroxide or oven-dried butylamine and treatment with the other four amines is the degree to which the NC spacing is decreased.

## 2.4.2 Voltage Dependence of the Photocurrent

### *Saturation due to Blocking Contacts*

Previous studies<sup>5</sup> have established that photoconduction in CdSe NC films is limited by field-induced ionization of photo-generated excitons; the majority carrier is assumed to be the electron. The exciton ionization process requires an electron to tunnel to a neighboring NC, and thus is highly dependent on voltage. A model for this voltage dependence has been previously proposed<sup>5</sup> and it is summarized in section 1.3.2. The shapes of the reference  $i$ - $V$  curves seen in Figures 2.3, 2.4, 2.6 and 2.8 correspond well to those previously reported, where the highly voltage dependent  $i$ - $V$  curve is attributed to the voltage dependence of exciton ionization.

The most obvious change in the voltage dependence of the  $i$ - $V$  curves upon treatment with reagents is seen in Figures 2.3(b) and 2.4, the sample treated with butylamine and dried at 70 °C, and the sample treated with sodium hydroxide, respectively. For these, the photocurrent saturates to a constant value at high voltages. In traditional photoconductors, such a saturation of photocurrent with voltage is seen when both the minority and majority carriers are mobile but it is not possible to inject either carrier from the electrodes.<sup>21,22</sup> The contacts in this situation are referred to as blocking,<sup>23</sup> and photocurrent is maintained by carriers being extracted at the

electrodes. The photocurrent under these circumstances is referred to as primary photocurrent<sup>21,24</sup> because it comes only from carriers generated within the sample.

It is not surprising that the contacts are blocking. From previous dark conductivity studies one knows that it is difficult to inject electrons into the conduction band, and nearly impossible to inject holes into the valence band, of a CdSe NC from a gold electrode.<sup>1,3,12</sup> Figure 2.2(a) and 2.2(b) are *i*-*V* curves in the dark from  $\pm 100$  V. Any dark current it is lost in the noise and less than 0.1 pA. The difficulty to inject electrons can be explained by the positions of the conduction and valence states of CdSe NCs with respect to the Fermi level of gold: for 4 nm diameter CdSe NCs, the conduction state is  $\sim 0.5$  eV above and the valence state is  $\sim 1.6$  eV below the Fermi level of gold.<sup>3,25,26</sup>

Complete saturation of the photocurrent occurs at voltages that are high enough to rapidly extract carriers before recombination in the film. Thus, the electron and hole lifetimes are transit-time limited rather than being recombination-time limited. When the photocurrent saturates, the photoconductive gain, *G*, becomes equal to unity. This can be seen from the following equation for photoconductive gain, which is valid for primary photoconductors:<sup>21,24</sup>

$$G = \frac{l_p + l_n}{L}, \quad (2.2)$$

where *L* is the distance between the electrodes, and *l<sub>p</sub>* and *l<sub>n</sub>* are the distances traveled by the hole and electron, respectively, before recombination, trapping, or arrival at an electrode. Since *L* is the maximum value for *l<sub>p</sub>* + *l<sub>n</sub>*, the maximum value for the photoconductive gain, *G*, is 1.<sup>21</sup>

The photocurrent, *i*, is related to *G* as follows:<sup>21</sup>

$$i = e \cdot F \cdot G, \quad (2.3)$$

where  $e$  is the charge of an electron and  $F$  is the number of free carriers (ionized excitons) created per second by photoexcitation anywhere in the sample. Thus we interpret the saturation of the photocurrent as a saturation of  $G$  at  $G = 1$ .

In the saturation regime of the  $i$ - $V$  curve, we can determine the value of  $F$  for  $G = 1$ ,  $F_{sat}$ . Whether or not this value is reasonable, given the photoexcitation intensity and NC film absorption, serves as a check on the applicability of the model. To experimentally determine the photon absorption, a thin film of CdSe NCs is deposited on a glass slide and treated with butylamine. The thickness after treatment is determined by AFM to be 45 nm, and the absorption is 6% at 514 nm. The height of the NC film used in the  $i$ - $V$  measurements is 100 nm. The absorption found above from the 45 nm thick film corresponds to a 100 nm thick film having 13% absorption at 514 nm. Based on the data in Figure 2.3(b),  $F_{sat}$  is calculated to be  $\sim 1.3 \times 10^{10}$  electrons per second. Using Equation 2.4, given the excitation intensity of 1 mW, the active area between the electrodes, and assuming one carrier per absorbed photon (an ionization probability of  $S=1$ ), the above value of  $F_{sat}$  leads to an absorption,  $A$ , of  $\sim 0.13$ . This corresponds to 13 % absorption, consistent with the direct measurement of absorption.

In addition to explaining the saturation of the photocurrent with voltage, Equation 2.3 also predicts that the photocurrent in the saturation regime should be linear with intensity, since  $F_{sat}$  depends linearly on intensity (see also Equation 2.4 below). The expected linear dependence is seen in Figure 2.5.

#### *Linear Region due to 100 % Exciton Ionization Efficiency*

There is a significant difference between the photoconductivity of the amine and base treated CdSe NC films at low voltages and at high voltages. As is seen in the  $i$ - $V$  curve for a sample treated with butylamine and dried at 70 °C (Figure 2.6), at low voltages the photocurrent

has the same strong dependence on voltage present at all voltages for the reference sample. This voltage dependence has been previously ascribed to the highly voltage dependent nature of exciton ionization efficiency.<sup>5</sup> However, to observe saturation of the photoconductivity at high voltages,  $F$  must be voltage independent. The rate of carrier generation in the entire sample is

$$F = I \cdot A \cdot S \quad (2.4)$$

where  $I$  is the intensity in units of photons per second,  $A$  is the absorption in units of excitons per photon, and  $S$  is the ionization efficiency in units of separated electrons per exciton ( $0 \leq S \leq 1$ ). Since  $F$  is constant and  $S$  is monotonically increasing with field, we must have  $S = 1$  in the saturation regime.

In fact, the existence of a linear regime in the  $i$ - $V$  curves of all of the amine- and base treated samples is also consistent with  $S = 1$ . In steady state, the photocurrent can be written as

$$i = e \cdot F \cdot \frac{(\mu_n \tau_n + \mu_p \tau_p) \cdot V}{L^2}, \quad (2.5)$$

where  $\tau_n$  and  $\tau_p$  are the lifetimes of the electron and hole, respectively,  $\mu_n$  and  $\mu_p$  are the electron and hole mobilities, respectively, and  $V$  is the applied voltage. This is a modification of Equation 2.3 to highlight the voltage dependence of  $G$ . This equation predicts a linear voltage dependence if  $F$  (and therefore  $S$ ) is field independent. In the low-voltage regime (and at all voltages for the reference samples), where  $S$  (and therefore  $F$ ) has a strong field dependence, the photocurrent becomes similarly strongly dependent on voltage.

The slope of the linear region in the  $i$ - $V$  plot is  $\frac{(\tau_n \mu_n + \tau_p \mu_p) e \cdot F}{L^2}$ .  $F$  is equal to  $F_{\text{sat}}$  as  $S=1$  in the linear region, and  $e$  and  $L$  are known. Therefore, fitting the slope of the  $i$ - $V$  curve allows  $(\tau_n \mu_n + \tau_p \mu_p)$  to be extracted. For the butylamine sample dried in the oven shown in Figure 2.3(b),  $F_{\text{sat}} \sim 1.3 \times 10^{10}$  electrons per second. Fitting a line to the linear region gives

$(\tau_n\mu_n + \tau_p\mu_p) \sim 1.8 \times 10^{-10} \text{ cm}^2\text{V}^{-1}$ . In the linear region every exciton is separated but the electron and hole recombine before reaching the electrodes. Thus  $\tau_p$  and  $\tau_n$  are both equal to the recombination time. The recombination time must be faster than 10 seconds (data points were taken every ten seconds) or else the linear region would have not been observed. The graph would have transitioned directly from the highly voltage dependent region to saturation. Setting  $\tau_p$  and  $\tau_n$  equal to 10 seconds gives a lower bound for  $(\mu_n + \mu_p)$  of  $1.8 \times 10^{-11} \text{ cm}^2\text{V}^{-1}\text{s}^{-1}$ . When measuring the time dependence of the photocurrent decay after the excitation light is blocked, it was found that  $\tau$  was faster than the  $10 \mu\text{s}$  resolution of the current amplifier so  $(\mu_n + \mu_p)$  is most likely closer to  $1.8 \times 10^{-5} \text{ cm}^2\text{V}^{-1}\text{s}^{-1}$ .

The above model predicts that at voltages where the  $i$ - $V$  curve becomes linear, a drop in fluorescence intensity should be observed from the NCs between the electrodes because excitons ionize rather than recombine in the NCs. Furthermore, the amount of fluorescence quenching should saturate to a constant value at these voltages. This is not inconsistent with the data of Figure 2.7.

### 2.4.3. Modified Goodman and Rose Model

In fact, Equation 2.5 is an oversimplification. While it can predict the general trends of the observed  $i$ - $V$  characteristics (highly voltage dependent, then linear, then saturated), it cannot explain why the linear portions of the  $i$ - $V$  curves do not extrapolate to zero applied field at zero photocurrent. We show that this discrepancy is a direct consequence of having field dependent ionization efficiency at low voltages, and of having blocking contacts. Were  $S$  constant, the  $i$ - $V$  curves would simply be linear at low voltages and would saturate at high voltages when  $G = 1$ .



Blocking contacts lead to the accumulation of charge near each electrode. In the case of CdSe NCs, where it is believed that  $\mu_n \tau_n > \mu_p \tau_p$ , positive charge would build up near the cathode, as the electrons are swept out of the region adjacent to the cathode and the less mobile holes are left behind. In the reverse case, with  $\mu_n \tau_n < \mu_p \tau_p$ , negative charge will build up near the anode. Either case leads to a disproportionate amount of the applied voltage being dropped across the region where significant charge is accumulated. Goodman and Rose<sup>22</sup> use a simplified model to describe this problem for the case  $\mu_n \tau_n < \mu_p \tau_p$ . They assume that a photoconductor in a sandwich geometry is divided into three regions: near the anode (region 1), near the cathode (region 3), and in the center of the photoconductor (region 2) (Figure 2.9). The widths of the regions near the anode and cathode are given by the mean drift length of the minority carrier since it must be able to pass through each of the regions without recombining. Since  $\mu_n \tau_n < \mu_p \tau_p$ , negative charge builds up in region 1 and a disproportionate amount of the applied voltage drops across this region. It is assumed that recombination does not occur in either region 1 or region 3, and that in region 2 recombination and generation are balanced. This model is applicable for voltages below  $V_0$ , at which the current density saturates to the value  $J_0$ . The current density and voltage variables,  $J$  and  $V$ , respectively, are converted to the dimensionless variables  $j = J/J_0$ , and  $v = V/V_0$ . The Goodman and Rose model predicts<sup>22</sup>

$$j = \frac{(1+b) \{-b + [b^2 + 4(1-b)(1+b^2)v / (1+b)^2]^{1/2}\}}{2(1-b)}, \quad (2.6)$$

where  $b \equiv \frac{\mu_n \tau_n}{\mu_p \tau_p}$ .

Equation 2.6 still holds true for the case in which  $\mu_n \tau_n > \mu_p \tau_p$ , except that the  $b$  in Equation 2.6 must be replaced with  $\beta = 1/b$ .

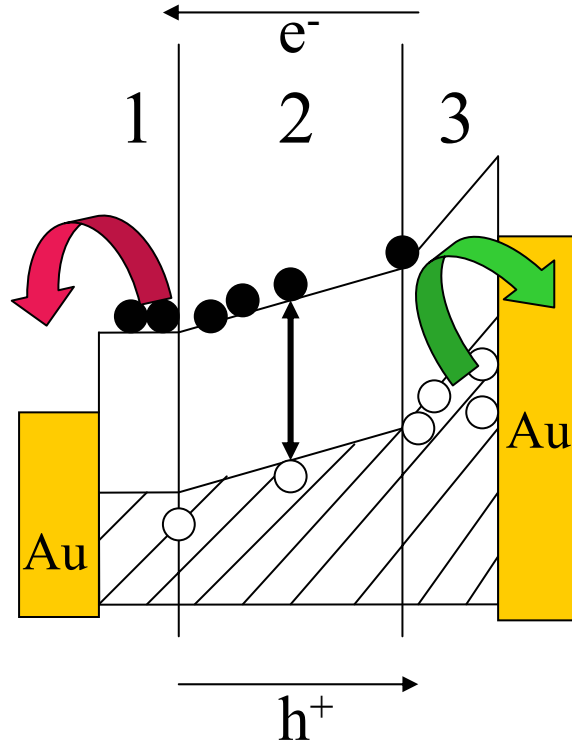


**Figure 2.9:** Schematic of the Goodman and Rose Model

We modify the Goodman and Rose model to allow for field-dependent generation rates (i.e., ionization efficiencies) by allowing each of the three regions to have different generation rates, defined as  $g_1$ ,  $g_2$ , and  $g_3$ . Furthermore, it is assumed that the generation rates in each region saturate to the same value,  $g_{sat}$  at high fields. This allows for a modification of Equation 2.6 as follows:

$$j = \frac{\varepsilon_{1s}(1+b) \left\{ -b\varepsilon_{12} + \left[ b^2\varepsilon_{12}^2 + 4v(1+b^2)(1-b\varepsilon_{12} + b^2\varepsilon_{13}^2 - b^2\varepsilon_{12}\varepsilon_{13}) / (1+b)^2 \right]^{1/2} \right\}}{2(1-b\varepsilon_{12} + b^2\varepsilon_{13}^2 - b^2\varepsilon_{12}\varepsilon_{13})}, \quad (2.7)$$

where  $b$  is still defined as in Equation 2.6, and  $\varepsilon_{1s} = \frac{g_1}{g_{sat}}$ ,  $\varepsilon_{12} = \frac{g_1}{g_2}$ , and  $\varepsilon_{13} = \frac{g_1}{g_3}$ . If  $\varepsilon_{1s} = \varepsilon_{12} =$

$\varepsilon_{13} = 1$ , Equation 2.7 reduces to Equation 2.6.

It is assumed that the generation rate in each region follows the same field-dependence. Since we use our model only as a qualitative tool to understand the effect of field-dependent generation rates, a simple dependence that rises to a maximum is chosen:

$$g(E) = g_{sat}(1 - \exp(-E/E_s)), \quad (2.8)$$

where  $E_s$  defines how strongly the generation rate depends on field. Introducing field-dependent generation rates results in a problem that cannot be solved analytically, since the  $g_i$  depends on the field  $E_i$  in region  $i$ , and  $E_i$  depends on  $g_i$ . Instead, we solve the problem iteratively, using Equation 2.6 to determine starting values for  $E_1$ ,  $E_2$ , and  $E_3$ , which in turn determines the starting values for  $g_1$ ,  $g_2$ , and  $g_3$ . These are then used for the calculation of  $j$  at the subsequent voltage steps.

The solid line in Figure 2.10 is the result of the iterative solution to Equation 2.7, given a value for  $b$  of 0.6 and  $E_s = 0.7 V_0/L$ . Because Equation 2.7 is not valid for  $V > V_0$ , we use a horizontal line to represent the photocurrent after saturation. The open circles in Figure 2.10 represent photocurrent data for a sample treated with butylamine and dried at 70 °C, with the current and voltage scaled for comparison. The  $j$ - $v$  curve represented by the solid line in Figure 2.10 qualitatively reproduces the  $i$ - $V$  curves of the amine- and base-treated samples: at low voltages, the photocurrent is highly voltage dependent, because of the voltage dependence of the generation rate, at voltages corresponding to  $E > E_s$ , the photocurrent becomes linear in voltage, and finally, at very high voltages the photocurrent saturates. In addition, the simulation shows that the non-zero voltage intercept of the linear region of the  $i$ - $V$  curves is the result of having blocking electrodes and of having a field-dependent exciton ionization efficiency.

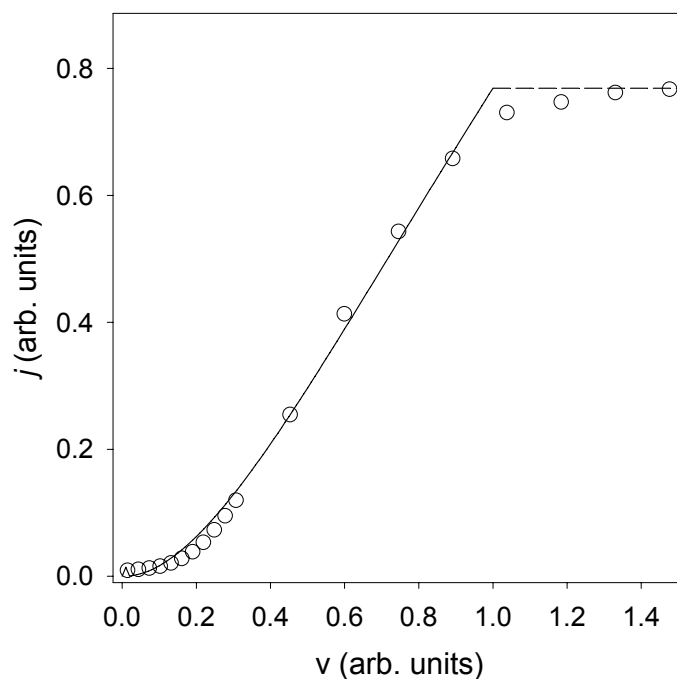


**Figure 2.10:** Simulation of the current-voltage characteristics (solid line) for a photoconductor in a sandwich structure with two mobile carriers, non-injecting electrodes, and a field-dependent generation rate. For this simulation, the field characterizing the generation rate saturation is set to 0.7 times the field characterizing the current saturation. The ratio of  $\mu\tau$  for the two carriers is set to 0.6. The simulation breaks down at saturation, at which point the current is given by the horizontal dashed line. For comparison, photocurrent data (open circles) for a sample treated with butylamine and dried at 70 °C are also presented. The current and voltage are scaled so that both are equal to one when the photocurrent saturates. The data is meant to be qualitatively compared to the simulation, since the simulation is not a result of a fit to the data.

It also seems clear from the simulation that the  $\mu\tau$  products for holes and electrons in films of CdSe NCs may not be as different from each other as has been previously proposed.<sup>3</sup> For values of  $b$  less than  $\sim 0.1$ , the simulated  $j$ - $v$  curve displays  $j \propto v^{1/2}$  behavior at voltages that are far lower than what is observed for Figure 2.3(b) and Figure 2.4. This suggests that  $\mu_n\tau_n$  probably does not exceed 10 times  $\mu_p\tau_p$  in these films. It is not possible to determine whether this is also true for the other treated samples, since they do not exhibit saturation, and thus there is no reference voltage for a comparison to Figure 2.10.

However, even for the samples that do exhibit a clear saturation, one should be cautious when drawing quantitative conclusions from the simulation based on the Goodman and Rose model because there are several limitations. First, the field dependence for the generation rate in Equation (2.8) is chosen for convenience, and is simpler than the actual field dependence. Second, the physics of the Goodman and Rose model is based on a photoconductor in sandwich geometry, whereas the measurements presented here are for a planar geometry with a gate electrode. Third, the Goodman and Rose model simplifies the problem by defining three distinct regions within the photoconductor when in reality the boundaries between the regions are not so abrupt. Nevertheless, the simulation provides important context for understanding the physics in our measurements.

#### **2.4.4. Using the Model to Understand the Effects of Different Chemical Treatments**

The simulation also helps to explain the differences in the shapes of the  $i$ - $V$  curves for the different types of samples measured. As  $E_s$  decreases, the simulated  $j$ - $v$  curve in Figure 9 shows that the transition to a linear regime also occurs at lower voltages. Comparing with experiment, this implies that unity ionization efficiency is achieved at lower voltages, for example for the sample treated with butylamine followed by drying at 70 °C than for the sample treated with butylamine and dried overnight.

The changes in the photocurrent behavior for the amine and base treated samples, compared to the reference samples, can now clearly be attributed to a substantial increase in the exciton ionization efficiency. The ionization efficiency depends on both the exciton lifetime (with no applied voltage) and the distance between neighboring NCs. The amine and base treatments passivate non-radiative decay pathways and bring the NCs closer together.

The effect of distance is seen by comparing Figure 2.3(a), the sample treated with butylamine and dried overnight, and Figure 2.3(b), the sample treated with butylamine and dried at 70 °C. The chemical treatment in each case is the same, so the main difference is that the NCs are 4.6 Å apart for the sample in Figure 2.3(a), and only 1.9 Å apart for the sample in Figure 2.3(b). Bringing the NCs closer together increases the rate of electron tunneling between NCs and increases the ionization efficiency.

The effect of exciton lifetime (with no applied field) can be seen by comparing Figure 2.3(c), the sample treated with aniline, and Figure 2.3(d), the sample treated with tri-*n*-butylphosphine (TBP). In each case, the NC spacing is the same, so the main difference is the functionality of the reagent used for treatment. Amines (and a basic environment in general) are known to increase quantum yield<sup>4,15-19</sup> by decreasing the rate of non-radiative exciton recombination through surface passivation. Since decreasing the rate of non-radiative exciton recombination makes the rate of ionization more competitive, it also increases the ionization efficiency.

Comparing the *i-V* curves in Figures 2.3(a) and 2.3(c,f) confirms the above assertions. AFM and GISAXS analysis suggests that the NC spacing after treatment with butylamine (dried overnight; Figure 2.3(a)), aniline [Figure 2.3(c)], and 1,4-phenylenediamine [Figure 2.3(f)] are all ~ 6-8 Å. The fact that all of these treatments result in similar improvements in photoconductivity and similar changes in the shapes of the *i-V* curves confirm that these effects are predominantly the result of the passivating nature of the amine functionality. Whether or not the amines used for treatment are conjugated or are diamines capable of cross-linking does not appear to have a strong effect. As expected, treatment with 1,6-diaminohexane results in a

similar  $i$ - $V$  curve that reaches a linear regime at slightly lower voltage than the other amine treatments, since the NC spacing is reduced to 4.1 Å.

#### 2.4.5 Using the Model to Understand the Temperature Dependence

Previous studies<sup>5</sup> have shown that the photoconductivity in CdSe NC films decreases with increasing temperature. This has been attributed to the increase in the non-radiative exciton recombination rate at higher temperatures, which leads to a decrease in exciton ionization efficiency for a given voltage. Figure 2.8(a) shows that the photocurrent for a reference sample at 100 V is more than 30 times smaller at 300 K than it is at 77 K, consistent with previous observations. Figure 2.8(b) shows that the photocurrent at 100 V for a sample treated with butylamine and dried at 70 °C is only about 5 times smaller at 300 K than it is at 77 K. The weaker dependence of the photocurrent on temperature as well as the relative shapes of the  $i$ - $V$  curves at 77 K and 300 K for the treated sample are consistent with the above model. Because of the increase in the non-radiative exciton recombination rate at 300 K, the  $i$ - $V$  curve of the treated sample enters the linear regime, indicative of unity ionization efficiency, at a higher voltage at 300 K than at 77 K. Furthermore, while the treated  $i$ - $V$  curve at 77 K saturates at 100 V, saturation is not observed at 300 K at the voltages applied in this study. This is because the photocurrent at 300 K is not as high as at 77 K, and according to Equation (2.3) saturation should occur at a given current rather than a given voltage, independent of temperature.

## 2.5 Conclusion

Photoconductivity of CdSe NC films can be increased by post-deposition treatment with butylamine, aniline, 1,6-diaminohexane, 1,4-phenylenediamine, tri-*n*-butylphosphine, and sodium hydroxide. The  $i$ - $V$  characteristics of the films after treatment confirm that the mechanism for improvement is an increase in the exciton ionization efficiency, which is achieved by increased NC surface passivation (due to the basic nature of amines and sodium hydroxide) and decreased NC spacing. For treatment with all of the amines and with sodium hydroxide, unity exciton ionization efficiency is attained. Furthermore, after treatment with sodium hydroxide or butylamine (when the sample is dried in the oven), the NC spacing is reduced enough for the photoconductivity to saturate at high voltage. This saturation is consistent with a model in which the electron lifetime becomes transit-time limited because there are two mobile carriers which are not replenished at the electrodes. We have presented a model that qualitatively reproduces the  $i$ - $V$  characteristics of the amine and base treated samples by assuming blocking contacts and field-dependent generation rates that saturate at a voltage below the voltage necessary for photocurrent saturation.

These results and conclusions have important consequences for the potential use of CdSe NCs for optoelectronic applications such as photodetectors or solar cells. In addition to providing a method for achieving significant photocurrent at 77 K and room temperature, our results imply that photocurrent cannot be increased further unless injection or electrons and holes from the electrodes is facilitated. Potential methods to aid in carrier injection include using a lower work function metal for the electrodes (for instance calcium or aluminum), converting from a lateral to a vertical structure so that another semiconductor could be introduced between the NCs and the electrodes in order to produce a gradient for electron and hole injection, and



choosing another type of semiconductor NC with conduction and valence levels that align more favorably with the work function of gold.

## 2.6 References

1. M. Drndic, M. V. Jarosz, N. Y. Morgan, M. A. Kastner and M. G. Bawendi, *Journal of Applied Physics* **92**, 7498 (2002).
2. D. Yu, C. J. Wang and P. Guyot-Sionnest. *Science* **300**, 1277 (2003).
3. D. S. Ginger and N. C. Greenham. *Journal of Applied Physics* **87**, 1361 (2000).
4. B. K. H. Yen, N. E. Stott, K. F. Jensen and M. G. Bawendi. *Advanced Materials* **15**, 1858 (2003).
5. C. A. Leatherdale, C. R. Kagan, N. Y. Morgan, S. A. Empedocles, M. A. Kastner and M. G. Bawendi. *Physical Review B* **62**, 2669 (2000).
6. C. B. Murray, D. J. Norris and M. G. Bawendi. *Journal of the American Chemical Society* **115**, 8706 (1993).
7. C. B. Murray, C. R. Kagan and M. G. Bawendi. *Science* **270**, 1335 (1995).
8. C. B. Murray, C. R. Kagan and M. G. Bawendi. *Annual Review of Materials Science* **30**, 545 (2000).
9. M. V. Jarosz, N. E. Stott, M. Drndic, N. Y. Morgan, M. A. Kastner and M. G. Bawendi. *Journal of Physical Chemistry B* **107**, 12585 (2003).
10. C. R. Kagan, C. B. Murray and M. G. Bawendi. *Physical Review B* **54**, 8633 (1996).
11. C. R. Kagan, C. B. Murray, M. Nirmal and M. G. Bawendi. *Physical Review Letters* **76**, 1517 (1996).
12. N. Y. Morgan, C. A. Leatherdale, M. Drndic, M. V. Jarosz, M. A. Kastner and M. Bawendi. *Physical Review B* **66**, 075339 (2002).
13. B. E. Warren, *X-ray Diffraction*. 1969, Addison-Wesley Publishing Company.
14. C. Kagan, Ph.D. thesis, Massachusetts Institute of Technology, Cambridge, 1996.
15. L. Spanhel, M. Haase, H. Weller and A. Henglein. *Journal of the American Chemical Society* **109**, 5649 (1987).
16. D. V. Talapin, A. L. Rogach, I. Mekis, S. Haubold, A. Kornowski, M. Haase and H. Weller. *Colloids and Surfaces a-Physicochemical and Engineering Aspects* **202**, 145 (2002).
17. W.-K. Woo, Ph.D. thesis, Ph. D. Thesis, Massachusetts Institute of Technology, Cambridge, MA, 2002.

18. X. G. Peng, M. C. Schlamp, A. V. Kadavanich and A. P. Alivisatos. *Journal of the American Chemical Society* **119**, 7019 (1997).
19. D. V. Talapin, A. L. Rogach, A. Kornowski, M. Haase and H. Weller. *Nano Letters* **1**, 207 (2001).
20. P. Guyot-Sionnest and C. Wang. *Journal of Physical Chemistry B* **107**, 7355 (2003).
21. R. H. Bube, *Photoconductivity of Solids*. 1960, New York: Wiley.
22. A. M. Goodman and A. Rose. *Journal of Applied Physics* **42**, 2823 (1971).
23. A. Rose, *Concepts in Photoconductivity and Allied Problems*. 1963, London: Interscience Publishers.
24. F. C. Nix. *Reviews of Modern Physics* **4**, 723 (1932).
25. B. O. Dabbousi, M. G. Bawendi, O. Onitsuka and M. F. Rubner. *Applied Physics Letters* **66**, 1316 (1995).
26. H. Mattoussi, L. H. Radzilowski, B. O. Dabbousi, E. L. Thomas, M. G. Bawendi and M. F. Rubner. *Journal of Applied Physics* **83**, 7965 (1998).

## Chapter 3

# Room Temperature Photocurrent Displaying 100% Internal Quantum Efficiency in CdSe/ZnS Inorganic Nanocrystal Films

### 3.1 Introduction

In recent years a number of methods have been developed to increase both the dark and photoconductivity in NC films. Thermal annealing has been employed to reduce interparticle spacing and to modify the chemical nature of the capping ligand.<sup>1,2</sup> Post-deposition cap exchange, as described in Chapter 2, has also been used to decrease NC spacing by replacing the bulky tri-octylphosphine or oleic acid ligands, which cap the NCs after synthesis, with smaller ligands.<sup>3-5</sup> In addition, the conductivity has been enhanced through chemical doping of the NCs, either with an electrochemical cell,<sup>6,7</sup> or by cap exchanging with a reducing agent such as hydrazine<sup>8</sup> or sodium biphenyl.<sup>9,10</sup> With the enhanced dark and photocurrents, a better picture of the physics of charge transport in NC films has been formed. For example, variable range hopping has been observed in doped CdSe and also PbSe films.<sup>2,8,11</sup> Chemical annealing has also allowed for the observation of unity photoconductive gains in CdSe NC films<sup>3</sup> and photoconductive gains greater than unity in CdTe<sup>4</sup> and PbS NC films.<sup>12</sup> The nature of the NC/electrode contact determines if photoconductive gain is possible in the system, and the ratio between the mobility of the electron and hole determines the degree of photoconductive gain. If the electrode cannot inject electrons or holes into a NC film it is “blocking”, the maximum photoconductive gain is 1 electron per absorbed photon, and the photocurrent is classified as primary. If the contact is “non-blocking” there is the potential for gains greater than one and the

photocurrent is classified as secondary.<sup>12</sup> Secondary photocurrent in CdTe NC films is described in detail in Chapter 4.

All of methods to enhance conductivity through NC films involve the exchange, removal, or decomposition of the native capping ligand on the NC surface. The modification of the NC surface can result in unpassivated states that may trap electrons and/or holes during conduction. In fact, it is the surface trap states, induced by chemically stripping off all ligands from PbS NCs, which allow for photoconductive gains up to 10,000 in PbS photodetectors.<sup>12</sup> Due to the trapping of one charge carrier, the other cycles through the circuit until it recombines with the trapped carrier. Trap induced secondary photocurrents can potentially last for days as the recombination lifetime is the release rate of the trap site, resulting in photodetectors with a slow response time.<sup>13</sup> Trap induced secondary photocurrent is also not ideal for solar devices because, although the photocurrent may be high, one of the charge carriers will not be extracted from the device and work cannot be done. Finally, since the electrodes can inject charge carriers, secondary photoconductors may also have significant dark currents.

A primary photoconducting system, such as CdSe NCs with gold electrodes, offers an advantage over secondary photoconducting systems in that there is little to no dark current,<sup>3,14</sup> and that the observation of photocurrent displaying 100% internal quantum efficiency (IQE) indicates that both electrons and holes are extracted from the film.<sup>3</sup> (By definition, IQE is number of charges extracted from a device per absorbed photon. 100% IQE is equivalent to a photoconductive gain of 1 in a primary photoconductor.) Butylamine treated CdSe NC photodetectors also exhibit a 50 kHz 3-dB bandwidth,<sup>15</sup> a significantly faster photoresponse than the 18 Hz 3-dB bandwidth observed in the PbS system.<sup>12</sup> Despite these advantages, the surface of the CdSe NCs has a detrimental effect on the photoconductivity in this system as surface

states result in an increase of the non-radiative decay rate ( $k_{nr}$ ) of the exciton. Non-radiative decay is a competing process with radiative decay ( $k_r$ ) and field assisted ionization of the exciton. Because  $k_{nr}$  slows as the temperature decreases, photocurrents are larger in magnitude at liquid nitrogen temperatures than at room temperature.<sup>14</sup> Achieving optimal device performance when cooled with liquid nitrogen is not ideal, or practical, for many optoelectronic devices applications, especially solar cells.

In this chapter it is shown that by removing a majority of the organic ligands in a film composed of CdSe/ZnS core/shell NCs (Figure 3.1) a NC film can be constructed, in which i) the magnitude of the photocurrent is larger at room temperature than low temperature and ii) the photocurrent displays 100% internal quantum efficiency. The CdSe/ZnS NC films also show low dark current and a 14 kHz 3-dB bandwidth. Finally, the experimental methods used to construct CdSe/ZnS NC films and remove the organic ligands are detailed, and the application of these methods to other core/shell semiconductor combinations is discussed.

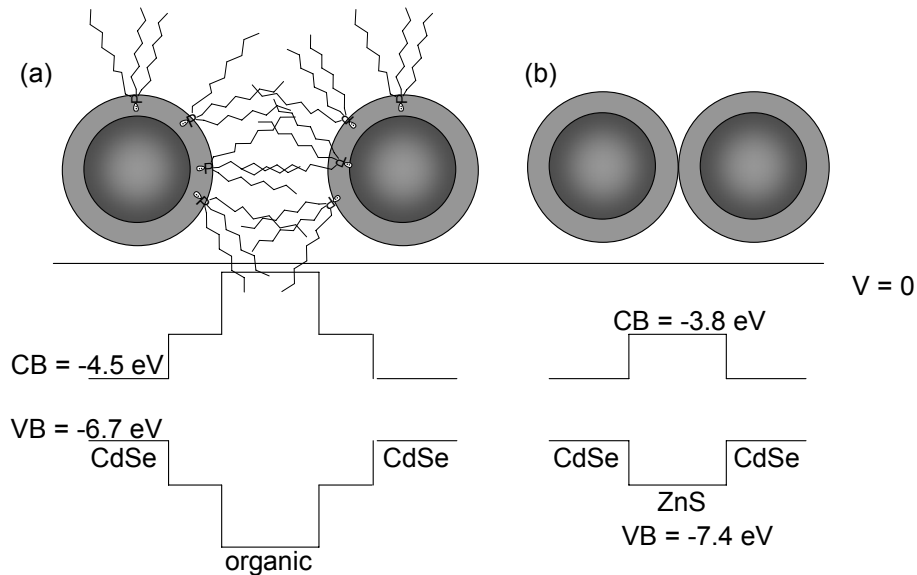


**Figure 3.1:** Schematic of a NC film and energy levels relative to vacuum for a CdSe/ZnS NC film (a) before thermal annealing and (b) after annealing to remove all of the organic ligands. The inner black circles are CdSe cores and the grey circle is the ZnS shell.

## 3.2 Experimental

### 3.2.1 Synthesis

CdSe NCs are synthesized according to a previously published procedure.<sup>16,17</sup> Methods for preparing high QY CdSe/ZnS (core/shell) particles from ZnEt<sub>2</sub> and (TMS)<sub>2</sub>S have been reported previously<sup>16,18,19</sup> and are followed to grow ZnS shells on CdSe cores in this study. In general, the CdSe growth solution is precipitated once with methanol and centrifuged. The supernatant is discarded, and the precipitant re-dissolved in 3 ml of hexane and filtered through a 0.2 μm filter. A flask with trioctylphosphine oxide (TOPO) and hexaphosphonic acid (HPA) is heated to 100 °C and degassed for one hour. The solution is cooled to 60 °C and CdSe cores are added in hexane. Hexane is pulled off under vacuum, and the solution is heated to 160 °C. A small amount of CdMe<sub>2</sub> (5:1 ratio Zn:Cd) is used along with ZnEt<sub>2</sub> as the cationic precursor to aid in lattice matching the ZnS shell. ZnEt<sub>2</sub>, CdMe<sub>2</sub> and (TMS)<sub>2</sub>S in trioctylphosphine (TOP) are added dropwise over the span of an hour, with the cationic and anionic precursors added in separate syringes to prevent nucleation in the syringe. Sample A is prepared in this manner.

Recently, the successive ion layer adhesion and reaction (SILAR) method has been reported as a way to achieve high QYs without the use of pyrophoric reactants.<sup>20-22</sup> In addition, this method theoretically allows layer by layer control of the shell material, providing greater tuning of the tunneling barrier. The reaction flask is prepared as above, with the substitution of octadecene (ODE) and octadecylamine (ODA) for TOPO and HPA. The precursors are Cd oleate, Zn oleate, and elemental sulfur in ODE. Cation and anion precursors are added alternately at 230 °C to form distinct monolayers. Using the SILAR method, a 7.5 monolayer graded shell was grown sequentially with 2 monolayers of CdS, 3.5 monolayers of Zn<sub>0.5</sub>Cd<sub>0.5</sub>S and 2 monolayers of ZnS on the CdSe cores (Sample B). Consistent with previous literature,

these nanocrystals had a QY of 59% after a single precipitation.<sup>20</sup> To decrease this minimum tunneling distance, a procedure for thin shell (2-4 monolayers) SILAR particles is investigated. For these particles, the use of CdS buffer layers to reduce the lattice strain is limited by the desired shell thickness. A CdSe/ZnS particle with a two monolayer shell (Sample C) was grown with one monolayer  $\text{Zn}_{0.5}\text{Cd}_{0.5}\text{S}$  and one monolayer of ZnS. A CdSe/ZnS particle with a shell of four monolayers (Sample D) was grown with 1 monolayer CdS, 1 monolayer ZnCdS and 2 monolayers of ZnS. In general we found the SILAR method produced NCs with high QYs when the shell was grown to 4-7 layers but did not achieve QYs as high as those in NCs overcoated with pyrophoric reagents when the shell was only 2-3 layers.

### 3.2.2 Sample Preparation

Both CdSe and CdSe/ZnS NCs are precipitated from growth solution following previous methods for making optically clear close-packed films.<sup>3,14,23-29</sup> First, butanol is added to an aliquot of growth solution and then methanol is added dropwise until the solution becomes cloudy. The sample is centrifuged and the supernatant discarded. The precipitate is dissolved in a minimal amount of hexane, filtered through a 0.2  $\mu\text{m}$  syringe filter, and precipitated from solution a second time. The CdSe NC precipitate is dissolved in hexane, filtered through a 0.1  $\mu\text{m}$  syringe filter, and precipitated from solution with methanol a third time after which it dissolved in 9:1 hexane:octane and passed through a 0.02  $\mu\text{m}$  syringe filter. The CdSe/ZnS NC crash out is stopped after the second precipitation and the precipitate is dissolved in 9:1 hexane:octane and filtered through 0.1 and 0.02  $\mu\text{m}$  syringe filters. Two precipitations are all the core/shell NCs need to form optically clear films. Further processing removes too many ligands and the particles aggregate.



The processed NC solutions are drop cast onto the measurement device which consists of 200 X 800 X 0.1  $\mu\text{m}^3$  gold electrodes lithographically patterned onto a quartz substrate. The electrodes are spaced by 2  $\mu\text{m}$ . The quartz devices are attached to a 28 pin chip carrier with silver epoxy and contacts are made from the electrodes to the chip carrier with a gold wire bonder. The NC films are between 100 and 200 nm thick. When films are drop cast onto an uneven surface such as the electrodes on the quartz substrate, the film thickness can vary across the device.

Post-deposition cap exchange with butylamine and sodium hydroxide involves soaking the CdSe NC film in a 0.1 M solution of the selected ligand in acetonitrile for 10 min. The film is rinsed with acetonitrile and dried at 70  $^{\circ}\text{C}$  for 1 hr.<sup>3</sup> For the thermal annealing studies, NC films are deposited in air and are heated in a vacuum oven for 30 min at a pressure of 12 mTorr.

To cap exchange CdSe/ZnS NCs into butylamine and then deposit a film, CdSe/ZnS NCs are precipitated from solution two times and, rather than dissolving in the hexane:octane solution, the NC powder is dissolved in 1 mL of butylamine. The sample is stirred in butylamine overnight and then precipitated with methanol, dissolved in 9:1 hexane:octane, and drop cast onto the device. To remove the butylamine ligands, this film is soaked in methanol for 5 min and heated at 100  $^{\circ}\text{C}$  for 1 hr.

### **3.2.3 Conductivity Measurements**

Samples are loaded into a Janis VPF-100 cryostat and measurements are performed under vacuum. A Keithley 6517 electrometer is used to measure current and source voltage and the samples are photoexcited with the 514 nm line of an  $\text{Ar}^+$  laser. Unless stated otherwise, the excitation intensity is 32  $\text{mW}/\text{cm}^2$ . The bandwidth is measured using an ISOMET 1206C

acousto-optic modulator to vary the frequency of laser excitation while the photocurrent is amplified using a Keithley 428 current amplifier and measured with a Stanford Research Systems SR830 DSP lock-in amplifier.

### **3.2.4 Transmission Electron Microscopy**

A JEOL 200 CX electron microscope is used to image the NCs. Samples for TEM are prepared by drop casting a NC solution in 9:1 hexane:octane onto a carbon TEM grid. This solution is  $\sim 200$  times more dilute than the solution used to make films for conductance measurements. The average diameter of the CdSe/ZnS NCs used in this study is found by averaging 200 NCs for each sample. The thickness of the ZnS shell can be found by subtracting the diameter of the CdSe NC core determined from absorbance from the diameter of the CdSe/ZnS particles determined from TEM.

### **3.2.5 Thermal Gravimetric Analysis (TGA)**

TGA measurements are performed on a Seiko Dual TG/DTA 320 Thermogravimetric/Differential Thermal Analyzer. CdSe/ZnS NCs are deposited onto a platinum sample boat from a 9:1 solution of hexane:octane. The sample boat is filled with the NC solution and, when the solvent evaporates,  $\sim 2$  mg of NCs are left behind (the boat is weighed before and after film deposition). The sample is zeroed at the start of the measurement, and the change in mass is monitored as the temperature is ramped from 50 °C to 600 °C at a rate of 10 °C per min. The mass is recorded every 0.5 sec.

### **3.2.6 FTIR and UV-Vis**

For FTIR studies, a film of CdSe/ZnS NCs is deposited onto a BaF<sub>2</sub> IR window. The FTIR spectrum from 4000 to 1000 cm<sup>-1</sup> is taken with a Perkin Elmer System 2000 FTIR before and after heating in the vacuum oven at 300 °C. The absorbance spectrum of the film on the IR window and also spectra of other films deposited on glass slides can be measured from 300 to 1000 nm using a Cary 5000 NIR/UV-Visible Spectrometer.

### **3.2.7 Glancing Incidence Small Angle X-ray Scattering (GISAXS)**

To find the interparticle spacing in CdSe/ZnS NC films, samples are drop cast on a clean piece of silicon. The samples are then mounted on the PANalytical X'PERT PRO multipurpose diffractometer and the diffraction signal is monitored as theta and two theta are swept in unison from 0.5 to 5 ° and data is collected every 0.167 °. The accelerating voltage on the copper anode is 45 kV and the current is 40 mA. The interparticle spacing is found by taking the Fourier transform of the GISAXS signal to find the pair distribution function using the method described in previous publications<sup>3,29</sup> and in Chapter 2.

### **3.2.8 Quantum Yield (QY)**

The QY of each CdSe/ZnS and CdSe NC sample is found by taking the ratio of the sample's fluorescence to that of a Rhodamine 610 reference dye of the same absorbance at 495 nm. The NCs are excited with a 150 W ozone free xenon arc lamp and the fluorescence detected by a photomultiplier tube of a Horiba Jobin-Yvon Fluoromax-3 spectrometer. It should be noted that the QY reported for the samples in this paper is the solution QY after two precipitations.

These QYs appear lower than many of the NC QYs reported in the literature. We believe it is important to give the QY of the NC solution from which the films are deposited, rather than the QY of growth solution, as the QY decreases with precipitations because of the removal of excess ligands from the solution and surface of the NC. Ideally, we would report the QY of the film; however, it is difficult give an accurate reference in solid state due to factors such as scatter and film inhomogeneity.

### 3.3 Results

In the following section electrical measurements of CdSe/ZnS NC films before and after ligand removal are presented. A few electrical measurements on chemically treated CdSe NC films are also provided in order to compare and contrast the two systems. For the CdSe/ZnS NC films, results are given for samples having ZnS shells of differing quality and thickness, as well as for samples in which the organic ligand is removed with different methods. Characterization of the CdSe/ZnS NC films after ligand removal is presented, as well as preliminary measurements evaluating the performance of CdSe/ZnS NC films as a photodetector. Finally, photoconductivity measurements in CdSe/ZnS nanorod films are shown to demonstrate how the methods used to build the CdSe/ZnS NC solids can be applied to a variety of core/shell systems.

Figures 3.2 and 3.3 display photocurrent verses electric field measurements for chemically treated CdSe NC films to illustrate the temperature dependence and influence of charge carrier trapping on the photocurrent in this system. Figure 3.2 is also presented in Chapter 2. It shows photocurrent verses electric field curves for CdSe NC films with trioctylphosphine oxide as the capping ligand [Figure 3.2(a)] and for these films after chemical treatment with 0.1 M butylamine in acetonitrile [Figure 3.2(b)]. The electric field is swept from

0 to  $10 \times 10^5$  V/cm in both graphs. Though the magnitude of the photocurrent is 1000 times greater after chemical treatment, in both plots the photocurrent measured at room temperature (open squares) is lower in magnitude than the photocurrent measured at 77 K (closed circles).

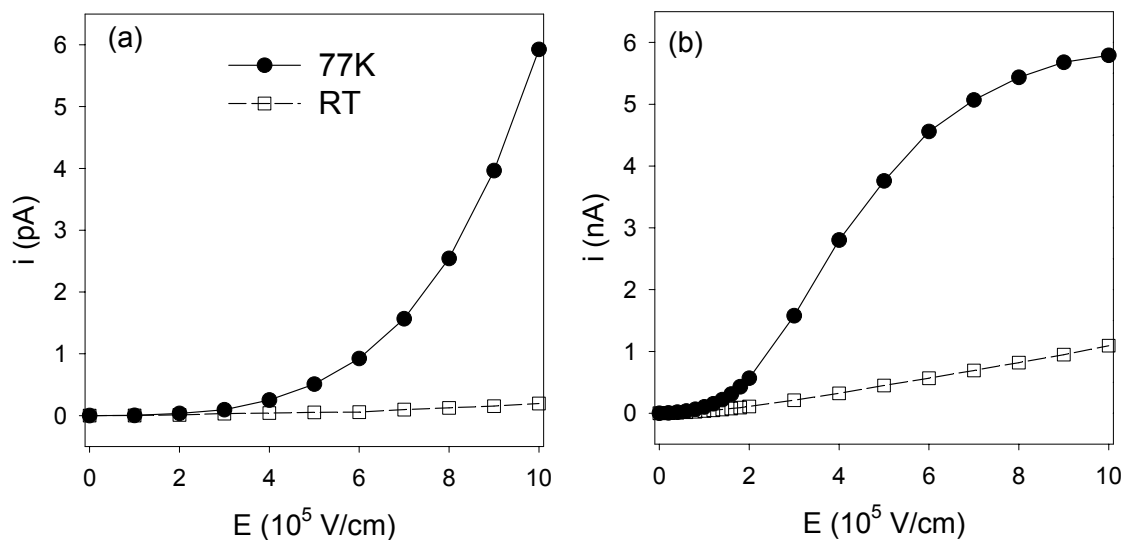


**Figure 3.2:** Photocurrent versus electric field curves for a CdSe NC film (a) before treatment and (b) after chemical treatment with 0.1 M butylamine in acetonitrile. The closed circles designate photocurrent measured at 77 K while the open squares represent photocurrent measured at room temperature. Both the solid and dotted lines serve as guides for the eye.

Photocurrent versus electric field plots of CdSe NC films treated with 0.1 M sodium hydroxide in acetonitrile are displayed in Figure 3.3. In Figures 3.3(a) and 3.3(b), the electric field is swept from 0 to  $10 \times 10^5$  V/cm and from  $10 \times 10^5$  V/cm back to 0 V/cm. Though the films are made from the same size CdSe NCs, and chemically treated in the same manner, there is significant variation in the amount of hysteresis observed in the photocurrent between forward and reverse sweeps of the electric field. It should be noted that the photocurrent is steady state and does not decay in time, only with the sweeping of the electric field.

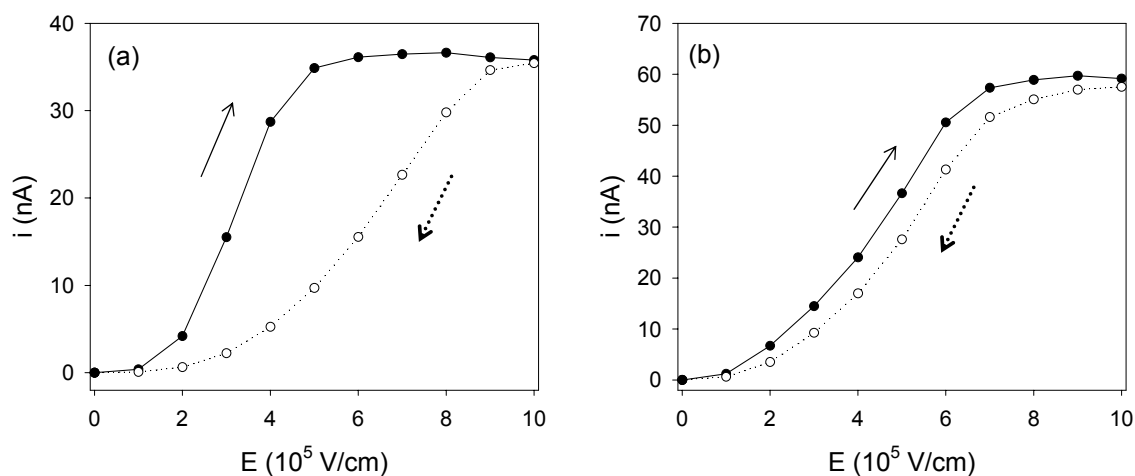


**Figure 3.3:** Photocurrent versus electric field measured at 77 K for CdSe NC films treated with 0.1 M sodium hydroxide in acetonitrile. The photocurrent measured for the sample in (a) displays greater hysteresis than the photocurrent of the sample in (b). The closed circles represent current as the field is swept from 0 V/cm to  $10^6$  V/cm while the open circles represent the current as the field is swept from  $10^6$  V/cm back to 0 V/cm. The solid and dotted lines serve as guides for the eye.

The electrical results for the CdSe/ZnS NC film (Sample A) giving the highest room temperature photocurrent are provided in Figures 3.4-3.7 and the physical characterization of this film is displayed in Figures 3.8 and 3.9. Sample A has a  $0.26 \pm 0.2$  nm shell and 25% QY. The photocurrent versus electric field curves for this sample after film deposition are displayed in Figure 3.4. The magnitude of the photocurrent at room temperature (open squares) is close to that of the photocurrent measured at 77 K (closed circles). The electric field is swept from 0 to  $10 \times 10^5$  V/cm for the data taken at each temperature.

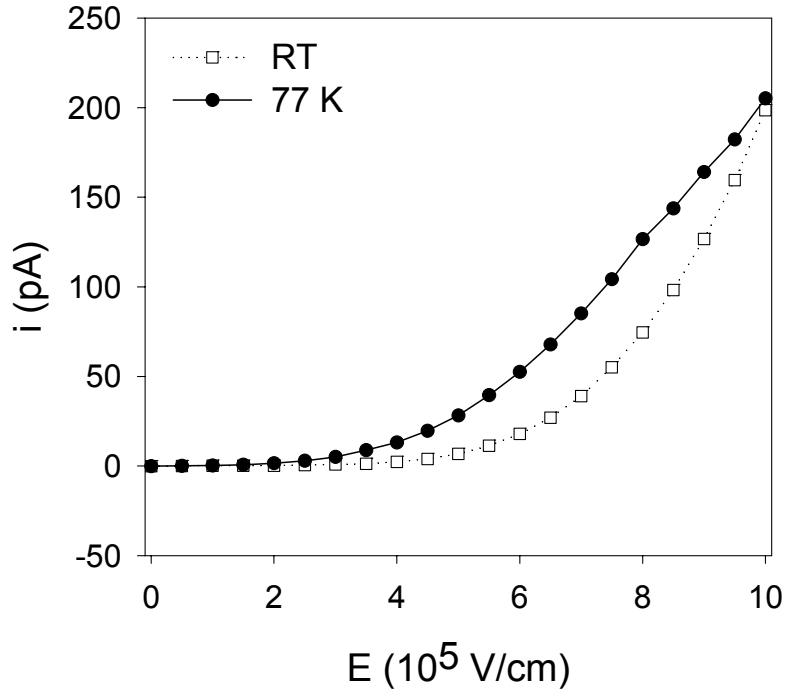


**Figure 3.4:** Photocurrent versus electric field for a CdSe/ZnS NC film. The closed circles represent photocurrent measured at 77 K while the open squares represent photocurrent measured at room temperature. The photocurrent is not scaled and the lines serve as guides for the eyes.

In Figure 3.5 the photocurrent versus electric field results are displayed for Sample A after heating in a vacuum oven at 300 °C. The photocurrent is measured at 77 K (open squares), 150 K (closed triangles), 200 K (open triangles), 250 K (closed circles), and at room temperature (open circles). For the data set at each temperature, the electric field is swept from 0 to 12.5 x 10<sup>5</sup> V/cm. The photocurrent measured at room temperature is the largest in magnitude and displays saturation of photocurrent with applied field at about 7 x 10<sup>5</sup> V/cm and 7.4 nA. The magnitude of the photocurrent decreases as the temperature is lowered and the photocurrent does not saturate.

The inset of Figure 3.5 shows the photocurrent at room temperature as the field is swept from 0 to  $12.5 \times 10^5$  V/cm and back to 0 V/cm. There is little hysteresis between the sweep to positive field and the sweep back to zero. Figure 3.6 shows the dark current measured at room temperature for Sample A. Some of the photodetector characteristics of Sample A are provided in Figure 3.7. Figure 3.7(a) gives the photoresponse of the device as a function of excitation light intensity. The dark current at  $9 \times 10^5$  V/cm is 0.37 pA and photocurrent can be detected above the dark current at  $0.1 \mu\text{W}/\text{cm}^2$  of 514 nm light. The frequency response of the device is displayed in Figure 3.7(b), showing a 3-dB roll off at 14 kHz. This corresponds well to the slowest decay measured in the decay of a photocurrent transient.

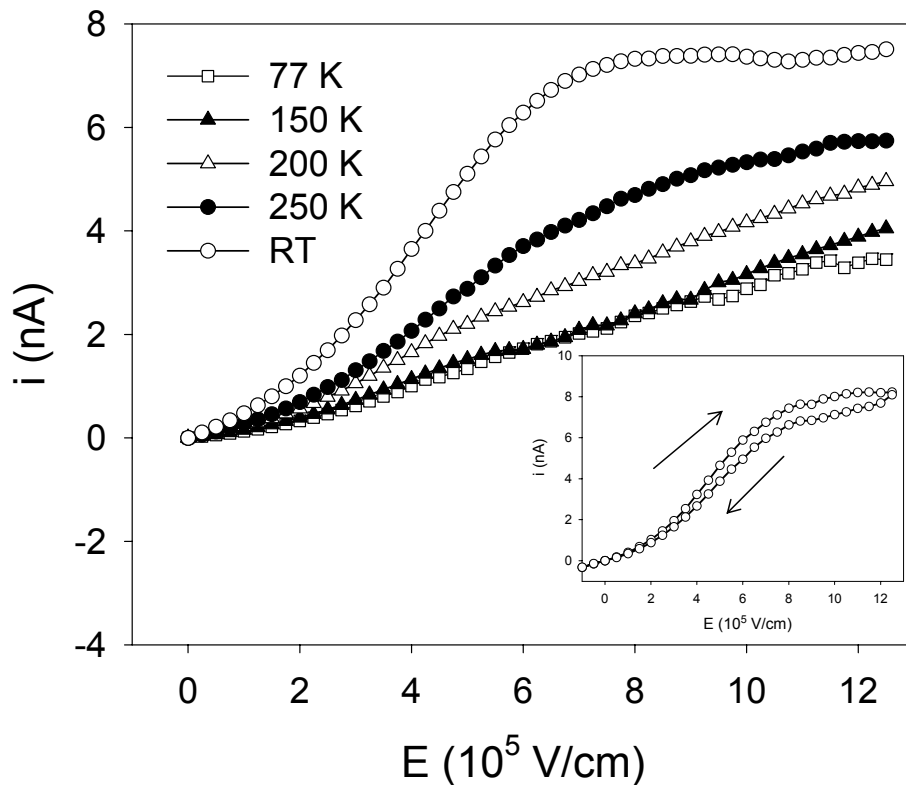


**Figure 3.5:** Photocurrent versus electric field for a CdSe/ZnS NC film annealed at 300 °C and measured at various temperatures: room temperature (open circles), 250 K (closed circles), 200 K (open triangles), 150 K (closed triangles), and 77 K (open squares). The inset is the room temperature as a function of field; the direction of the field sweep is indicated.



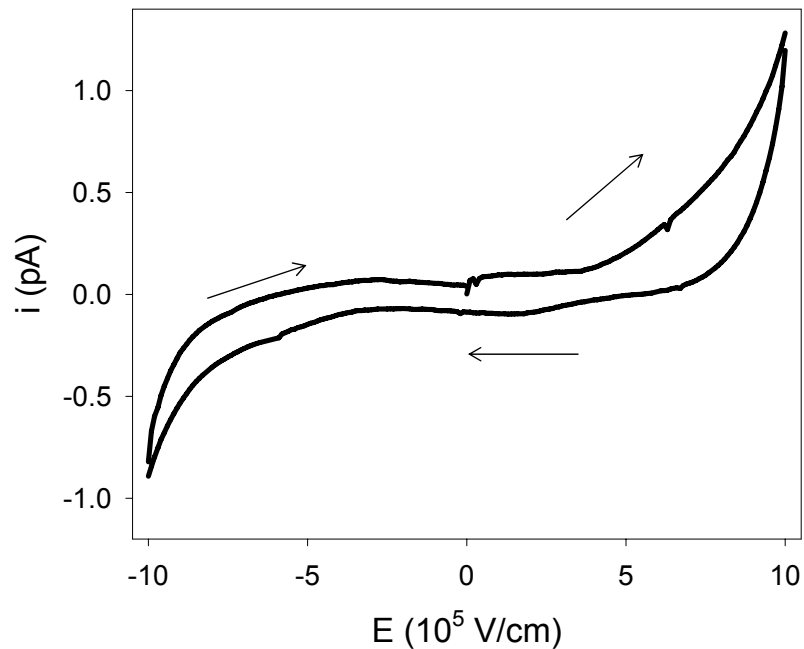


**Figure 3.6:** Dark current for a CdSe/ZnS NC film annealed at 300 °C and measured at room temperature. The electric field is swept from 0 to  $10 \times 10^5$  V/cm, from  $10 \times 10^5$  V/cm to  $-10 \times 10^5$  V/cm, and finally from  $-10 \times 10^5$  V/cm back to 0 V/cm.

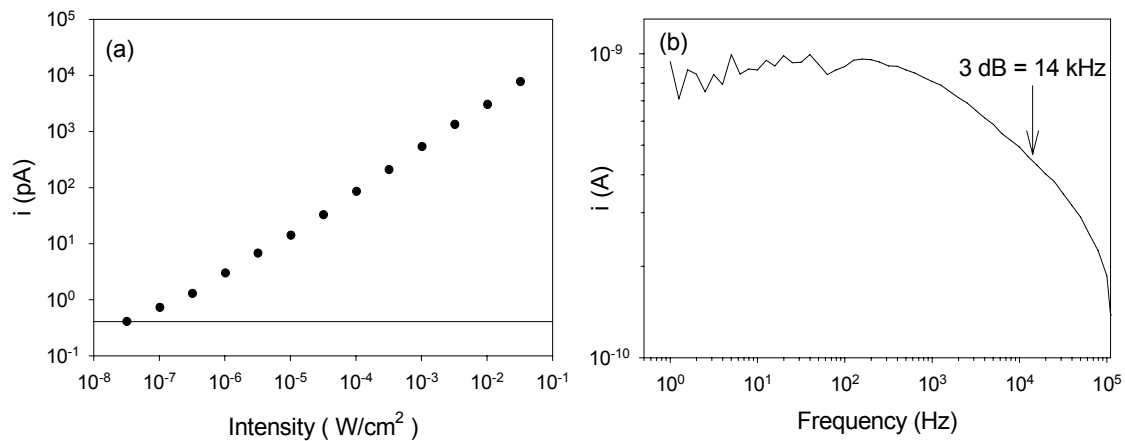
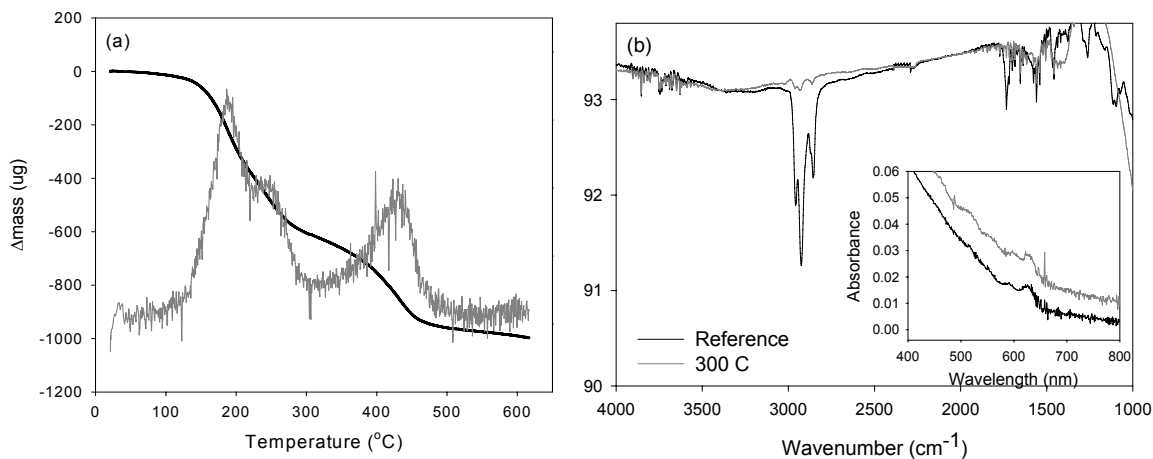


**Figure 3.7:** (a) Photocurrent as a function of intensity of 514 nm excitation light and measured at  $9 \times 10^5$  V/cm (closed circles). The solid line represents the 0.37 pA of dark current in the sample at  $9 \times 10^5$  V/cm. (b) Frequency response of the photocurrent at  $9 \times 10^5$  V/cm and  $2.7$  mW/cm<sup>2</sup>. The 3-dB bandwidth of the device is 14 kHz

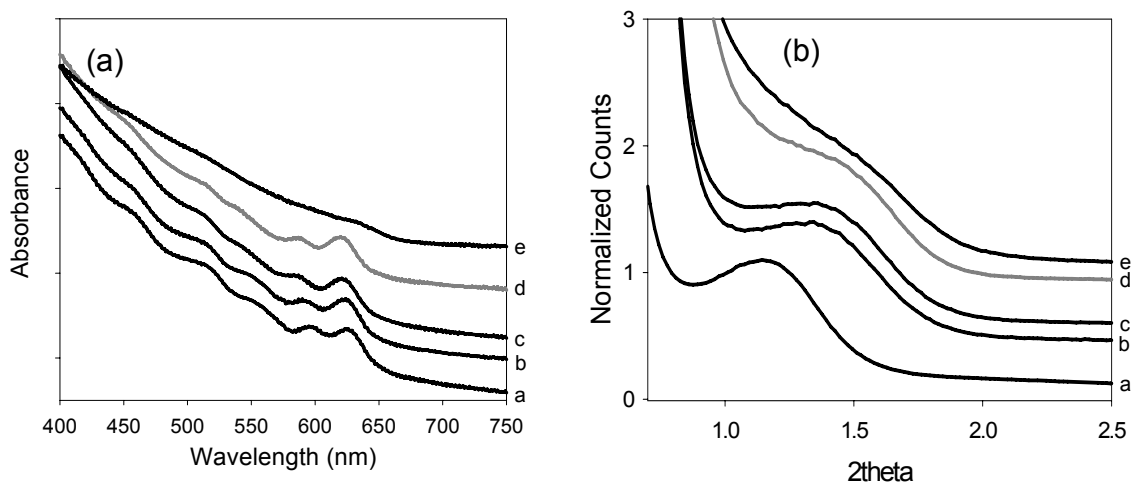
Figures 3.8 and 3.9 show data taken in order to characterize the physical and optical properties of Sample A. Figure 3.8(a) displays thermal gravimetric analysis results. The black line is the change in mass of the sample as a function of temperature. The grey line is the derivative of the black line to emphasize the temperatures at which changes in mass occur. By 300 °C, 0.6 mg of the sample is lost which is ~ 30% of the total sample mass. For CdSe/ZnS NCs capped with octadecylamine, a loss of all of the organic ligand should result in a ~ 30% decrease in sample mass<sup>30</sup> which is consistent with the TGA measurement. The physical identity of the 0.2 mg of material lost around 410 °C is unknown; however, the NC films are not heated above 350 °C in this study.

Figure 3.8(b) is the FTIR spectra for a film of CdSe/ZnS NCs (Sample A) before (black line) and after (grey line) heating to 300 °C. The magnitude of the C-H stretching mode at 3000 cm<sup>-1</sup> is greatly reduced after heating indicating the loss of organics in the film. The inset shows that the absorbance spectrum of this sample before and after heating does not change, indicating there is no loss of inorganic material.

Figure 3.9(a) also displays the absorbance spectra for CdSe/ZnS NC films (Sample A) but this time as a function of different annealing temperatures. Line a is the sample before heating, b is after heating at 200 °C, c is after heating at 250 °C, d is after heating at 300 °C, and e is after heating at 350 °C. There is not much change in the position of the first absorption feature in the samples heated at 200, 250, or 300 °C, but all absorbance features are broadened upon heating to 350 °C in a vacuum oven.



**Figure 3.8:** (a) Thermal Gravimetric Analysis data for a 2 mg sample of ZnS/CdS/CdSe NCs. The solid black line represents the change in mass of the NC sample as a function of temperature. The grey line is the derivative of the solid line to accentuate the change in mass. (b) FTIR of a CdSe/ZnS NC film on a BaF<sub>2</sub> IR window before (black line) and after (grey line) vacuum annealing at 300  $^{\circ}$ C. The inset is the absorbance spectra of the same film before and after heating. The absorbance spectra has been shifted on the y-axis to more clearly see the shape of the curve after heating but neither spectra has been scaled.



**Figure 3.9:** (a) Absorbance spectra of the CdSe/ZnS film as a function of vacuum annealing temperature. The samples are offset for clarity but none of them have been scaled. (b) GISAXS of the CdSe/ZnS film as a function of temperature. The following letters correspond to the same vacuum annealing temperature in 5(a) and 5(b): as deposited (a), 200  $^{\circ}$ C (b), 250  $^{\circ}$ C (c), 300  $^{\circ}$ C (d), 350  $^{\circ}$ C (e).

GISAXS is used to monitor the interparticle spacing as a function of heating temperature in Figure 3.9(b). The letter labels correspond to the same heating conditions given in Figure 3.9(a). The diameter of NCs in Sample A is  $6.15 \pm 0.4$  nm from TEM, and by subtracting the NC diameter from the spacing determined from GISAXS the interparticle spacing is determined. NCs are 1.25 nm apart before heating and  $\sim 0.25$  nm after heating to 200 °C and 250 °C. The peak in the GISAXS data, which represents the interparticle spacing, is significantly broadened after heating to 300 °C and cannot be fit to extract interparticle spacing. After heating at 350 °C, the peak is completely gone. The loss of the GISAXS peak indicates that many of the NCs are touching after heating to 300 °C and that most, if not all, of the NCs touch after heating at 350 °C. When this data is looked at along side the absorbance spectra in Figure 3.9(a), it can be inferred that although most of the NCs are touching after heating at 300 °C, the NCs still experience quantum confinement as the absorbance spectrum remains intact. After heating at 350 °C, the loss of features in the absorbance spectra indicates the ZnS shell and CdSe cores have annealed and formed an amorphous bulk film.

In Figure 3.10, conductivity measurements are presented for CdSe/ZnS NC films with ZnS shells of differing thickness and quality. Figure 3.10(a) shows the photocurrent after annealing for Sample B which has a thick CdS/ZnS graded shell of  $1.75 \pm 0.17$  nm and a QY of 40%. Figure 3.10(b) is for Sample C which has a thin  $0.34 \pm 0.1$  nm shell and a QY of 4%. Sample C has also been annealed. Lastly, Figure 3.10(c) gives the photocurrent verses electric field plots for a CdSe/ZnS NC film, in which the organic ligands are removed with chemical cap exchange followed by mild heating, as opposed to high temperature vacuum annealing. This CdSe/ZnS NC film (Sample D) has a  $0.57 \pm 0.12$  nm shell. In Sample D the TOPO capping ligand has been chemically altered through cap exchanged in solution with butylamine and then

deposited on the device. The device is subsequently soaked in methanol and heated at 100 °C to remove organic ligands. In Figure 3.10 the photocurrent does not display 100% IQE, unlike Sample A (Figure 3.5). Figure 3.11 summarizes the temperature dependence of the samples measured in this study. All of the CdSe/ZnS NC films display room temperature photocurrent that is larger in magnitude than the low temperature photocurrent, while the CdSe NC film chemically treated with butylamine shows a reverse temperature dependence of the photocurrent. We note that the absolute magnitude of the photocurrent cannot be directly compared from sample to sample because the absorption of each device is different. However, the electric field dependence of the photocurrent can be directly compared because the length and width of the electrodes are the same for all samples measured in the study.

Finally, photocurrent results for a CdSe/ZnS nanorod (NR) film heated to 300 °C are shown in Figure 3.12. The photocurrent measured at room temperature (open squares) is larger in magnitude than the photocurrent measured at 77 K (open circles) and it displays near saturation of photocurrent with electric field at a current close to that indicating 100% IQE.

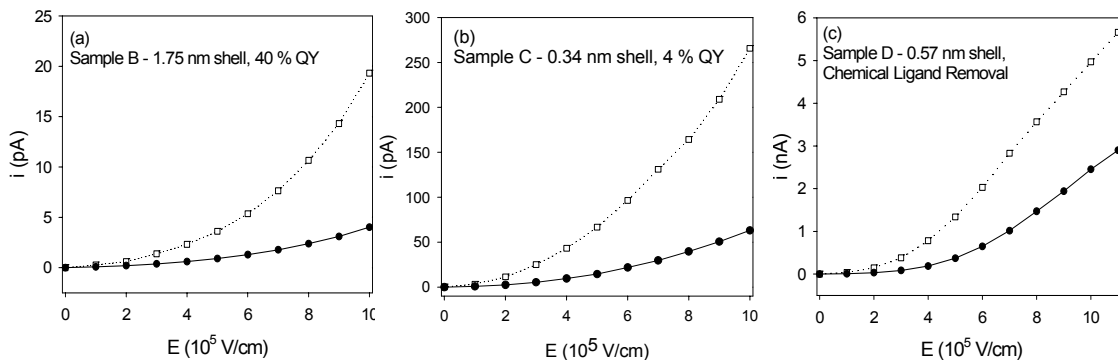


**Figure 3.10:** Photocurrent verses electric field for (a) Sample B, (b) Sample C, and (c) Sample D. The open squares represent photocurrent measured at room temperature while the closed circles stand for photocurrent measured at 77 K. The solid and dotted lines are guides for the eye.

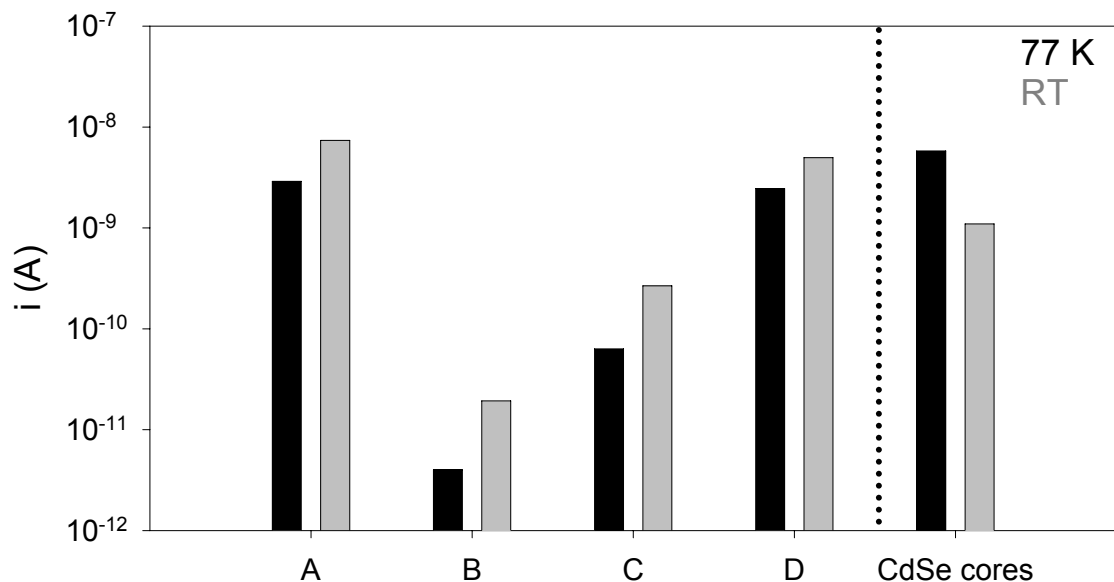


**Figure 3.11:** Bar graph illustrating the variation in the temperature dependence of the photocurrent for the CdSe/ZnS, Samples A, B, C, and D, and CdSe core NC films measured in this study. Each bar represents the magnitude of the photocurrent at  $10^6$  V/cm. The solid black bars represent photocurrent measured at 77 K while the solid grey bars represent photocurrent measured at room temperature.

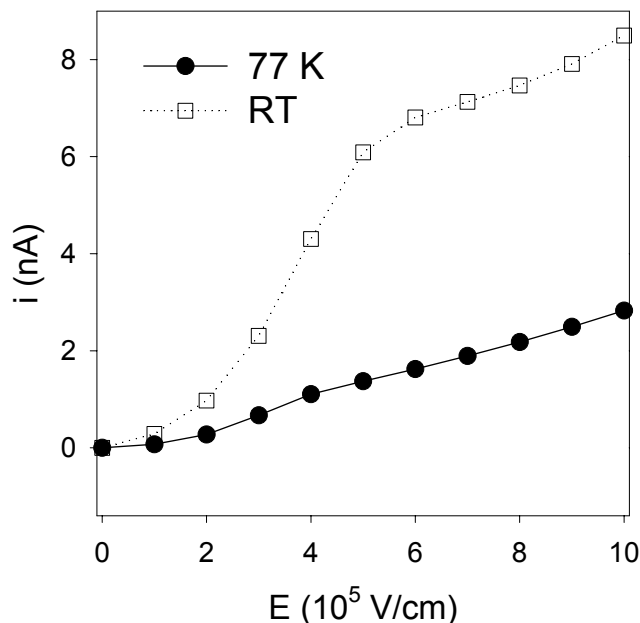


**Figure 3.12:** Photocurrent verses electric field for CdSe/ZnS NRs heated to 300 °C. The open squares represent photocurrent measured at room temperature while the closed circles stand for photocurrent measured at 77 K. The solid and dotted lines are guides for the eye.

### 3.4 Discussion

In this section, a brief review of the theory of primary photoconductivity in NC films is presented in order to elucidate how the surface of the NC can cause room temperature photocurrent to be smaller than low temperature photocurrent in CdSe NC films, and how this temperature dependence is reversed when the CdSe NCs are overcoated with ZnS. For an in depth analyses of primary photoconductivity in CdSe NC films refer to Chapter 2. The advantages of the CdSe/ZnS NC film over chemically treated CdSe NC films are discussed, as well as the benefits of a photodetector made from a primary photoconductor such as CdSe/ZnS NCs between gold electrodes. Finally, some of the key parameters which must be considered when constructing core/shell NC films are presented.

### 3.4.1 Theory of Primary Photoconductivity in NC films

Equation 3.1 is an expression for photoconductivity in a bulk semiconductor<sup>13</sup> modified to include a field dependent exciton separation efficiency,  $\eta(E)$ , characteristic of CdSe semiconductor NCs.<sup>14</sup>

$$i = e \cdot I \cdot A \cdot \eta(E) \cdot G \quad (3.1)$$

In Equation 3.1,  $e$  is the charge of an electron,  $I$  is the intensity in units of photons per second,  $A$  is the absorption of the film in units of excitons per photon,  $\eta(E)$  is the exciton separation efficiency, and  $G$  is the photoconductive gain. Equation 3.2 is an expanded version of Equation 3.1.

$$i = e \cdot I \cdot A \cdot \frac{k_E(E)}{k_E(E) + k_r + k_{nr}} \cdot \frac{(\mu_n \tau_n + \mu_p \tau_p) \cdot E}{L} \quad (3.2)$$

The exciton separation probability is written in terms of the rates which determine its value.<sup>15</sup>  $k_E(E)$  is the electric field dependent rate of exciton ionization,  $k_r$  is the radiative relaxation rate, and  $k_{nr}$  is the non-radiative relaxation rate. The faster the radiative or non-radiative rates, the smaller the exciton separation probability will be for a given field. The final term is  $G$ , the photoconductive gain, shown in a form to represent its electric field dependence.  $\mu_{n,p}$  represents the mobility of the electron or hole,  $\tau_{n,p}$  is the recombination lifetime of each charge carrier,  $E$  is the applied electric field, and  $L$  is the distance between the two electrodes. This term can be further reduced to  $G = \frac{l_n + l_p}{L}$  where  $l_n$  and  $l_p$  are the distances traveled by each charge carrier.<sup>13</sup>

When both the electron and hole reach the electrodes the distances traveled by each carrier will add up to  $L$ ,  $G$  will become equal to 1, and the photocurrent will saturate with applied electric field.



### 3.4.2 Effect of $k_{nr}$ on the Photoconductivity in CdSe NC films

From Equation 3.2, the observed dependence of the photocurrent on field and temperature in CdSe NC films can be understood. The field and temperature dependence both come from the  $\eta(E)$  term. In Figure 3.2(a) photocurrent is exponential because  $k_E(E)$  depends on the tunneling of a charge carrier to a neighboring NC, and the photocurrent is larger at low temperature because  $k_{nr}$  is slower at low temperature.<sup>14</sup> After treatment with butylamine to decrease interparticle spacing, the field dependence displays saturation of photocurrent with electric field indicating every charge carrier is extracted at the electrodes.<sup>3,23</sup> However, saturation is only observed at 77 K, suggesting that at room temperature a larger electric field must be applied to separate the exciton before it recombines non-radiatively. Figure 3.2(b) demonstrates that even after increasing the photocurrent by a factor of 1000, the magnitude of the photocurrent is still a function of  $k_{nr}$ .

Having photocurrent that increases in magnitude as the temperature decreases is unusual for semiconductors. Usually, the current decreases with decreasing temperature because charge carriers do not have enough thermal energy to hop from trap states or the valence band to the conduction band. Trap states are active in the CdSe NC film; however, the temperature dependence of  $k_{nr}$  dominates the magnitude of the photocurrent. The effect of trap states can be observed in the hysteresis of the photocurrent upon sweeping the electric field. Figure 3.3(a) shows that significant hysteresis can be observed in photocurrent measured at 77 K after chemical treatment with sodium hydroxide. The amount of hysteresis varies from sample to sample [Figures 3.3(a) and 3.3(b)] even if samples undergo the same chemical treatment. This most likely occurs because each NC is capped with a different number of ligands which are

stripped and replaced during a cap exchange. If more ligands are removed than are replaced, unpassivated Cd or Se atoms remain exposed on the surface and become trap sites.

### 3.4.3 Enhancing Room Temperature Photoconductivity with CdSe/ZnS NC films

#### *CdSe/ZnS NC films with organic ligands*

While the chemical treatments do an excellent job of enhancing the magnitude of the photocurrent, it would be better if 100% IQE of the photocurrent occurred at lower fields at room temperature, rather than 77 K. To extract all of the charge carriers, either the device must be run at much higher fields to overcome  $k_{nr}$ , or the device must be cooled and operated in a temperature range where there are many active trapping states. CdSe NCs are passivated with a shell of ZnS to slow  $k_{nr}$ . ZnS has a larger band gap than CdSe (Figure 3.1) and has been shown to significantly increase the quantum yield (QY) of NCs as it passivates dangling bonds on the surface of the NC and electrically confines the electron and hole wavefunctions, keeping them away from the new surface of the NC.<sup>18,19</sup> In Figure 3.4, the photocurrents measured at room temperature and 77 K in a film of CdSe/ZnS NCs are of the same order of magnitude. This implies that the dependence of the photocurrent on  $k_{nr}$  is reduced. However, the photocurrent in this film does not display saturation of photocurrent with voltage. While adding the inorganic shell slows  $k_{nr}$ , it also increases the interparticle spacing which reduces  $k_E(E)$  and makes it harder for a charge to tunnel to a neighboring NC. This result confirms previous measurements from Leatherdale, et. al. in which CdSe/ZnS NCs did not display large photocurrents.<sup>14</sup>

#### *CdSe/ZnS NC films after removal of the organic ligands*

By removing all of the organic ligands, the interparticle spacing can be significantly reduced. In fact, the new spacing is just the thickness of the ZnS shell capping the CdSe NCs.

As demonstrated in Figures 3.8 and 3.9, heating the CdSe/ZnS NC film to 300 °C results in a film, in which the majority of the ZnS shells are touching, yet the electronic wavefunctions of each NC remain confined. The room temperature photocurrent in Figure 3.5 displays saturation with applied field at a magnitude of photocurrent which indicates extraction of an electron for every absorbed photon. The current at which saturation should occur can be calculated using Equation 3.2.<sup>3,23</sup> The absorption,  $A$ , is set equal to 5.4%. This value is taken from line 'd' of Figure 3.9(a), the absorbance of a CdSe/ZnS NC film drop cast on a glass slide from the same solution used to make Sample A.  $\eta(E)$  is set equal to 1,  $G$  is set equal to one, and  $I$  is set equal to the number of photons hitting the active area of the sample (determined from fitting the profile of the excitation beam). Using the aforementioned values, the calculated photocurrent is 11.8 nA, larger than the 7.4 nA found experimentally in Figure 3.5. However, this is a reasonable value as two other devices deposited from this solution exhibited photocurrent saturation at 14 nA and 3.5 nA indicating the absorption varies by as much as a factor of 4 from sample to sample. Films drop cast onto the measurement device are not of a uniform thickness because the gold electrodes and wires cause the film to dry unevenly.

The the photocurrent in Figure 3.5 decreases with decreasing temperature indicating that  $k_{nr}$  is no longer the dominating factor. The photocurrent is lower in magnitude at lower temperatures because more carriers are trapped. When the organic ligands are removed there may be unpassivated surface states where the NCs touch because it is unlikely a perfect ZnS crystal is formed. Despite trapping at low temperatures, CdSe/ZnS NC films show promise as a material for device applications because all electrons and holes are extracted at room temperature.

### 3.4.5 CdSe/ZnS NC Photodetectors

A device consisting of a CdSe/ZnS NC film between gold electrodes shows potential as a photodetector (Figure 3.7). The frequency bandwidth of this device is 14 kHz, nearly three orders of magnitude faster than devices which generate currents using the mechanism of secondary photoconductivity.<sup>12</sup> The dark current is also very small in the CdSe/ZnS NC films. For this particular sample geometry and thickness, the dark current is 0.37 pA at  $9 \times 10^5$  V/cm. The low dark current allows for the detection of photocurrent at low excitation intensities. Photocurrent is detected above the noise of the dark current with only  $0.1 \mu\text{W}/\text{cm}^2$  of 514 nm laser excitation.

### 3.4.6 Comparison of CdSe and CdSe/ZnS NC films

In Figure 3.13, the room temperature photocurrent from a CdSe/ZnS sample is plotted against the photocurrent measured at 77 K in a CdSe NC film chemically treated with butylamine. (The *i*-*E* curves have been scaled in current but not in electric field.) These two samples were chosen because the saturation of photocurrent occurred at approximately the same value of applied field. As this transition occurs at the same field, it suggests that the tunneling transmission probability for these two samples is about the same (assuming charges tunnel from NC to NC).

$$|T(E)|^2 = \exp\left[-2 \int_0^d dx \cdot \left(\frac{2m}{\hbar^2}\right) \cdot (\sqrt{\phi_B - E_0 - eEx})\right] \quad (3.3)$$

Equation 3.3 is the WKB approximation for tunneling through a barrier lowered by an applied field.<sup>1</sup> Here *m* is the mass of the electron,  $\hbar$  is Plank's constant,  $\Phi_B$  is the height of the tunnel barrier,  $E_0$  is the initial energy, *e* is the charge of the electron, *E* is the applied electric field, and *d* is interparticle spacing. As the transmission probability for these two samples is

approximately equal, expressions for the transmission probability for the CdSe and CdSe/ZnS can be set equal to each other. We can then solve for  $\Phi_B$  of the organic ligands in the CdSe NC film system as we know  $\Phi_B$  (0.7 eV) and  $d$  (0.5 nm) for the CdSe/ZnS system and  $d$  (0.2 nm) for the CdSe NC film. The tunnel barrier height in a CdSe NC film treated with butylamine had not been previously reported in the literature.  $\Phi_B$  is found to be 4.3 eV which is (for CdSe NCs with a conduction band at -4.5 eV) -0.23 eV below vacuum and a reasonable value for the LUMO of an alkane molecule.<sup>31</sup>

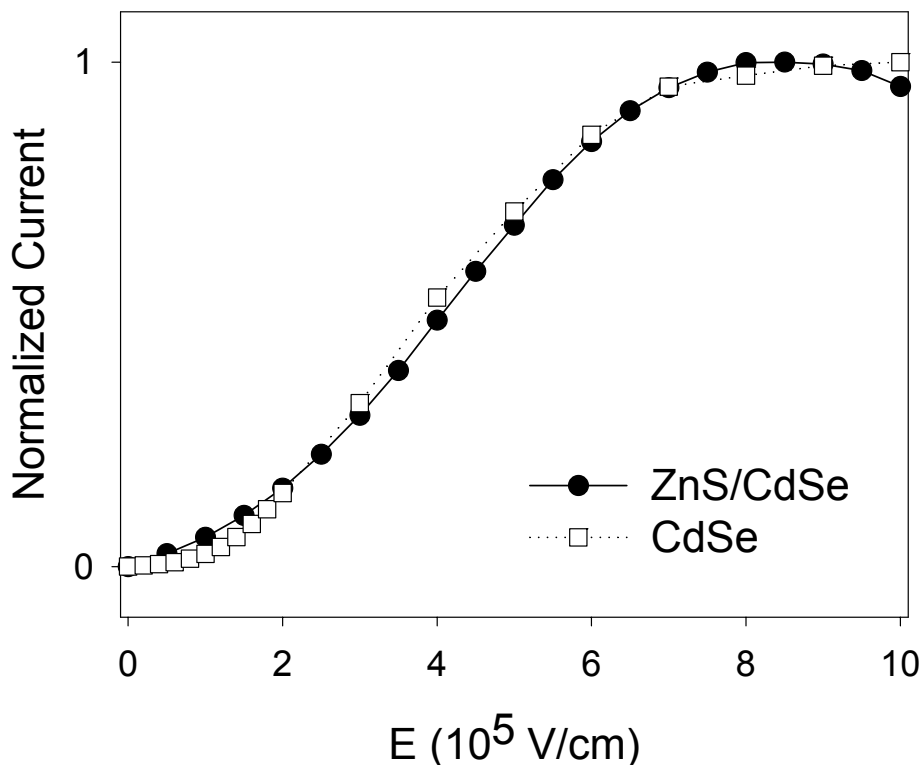


**Figure 3.13:** Photocurrent versus electric field for a CdSe/ZnS NC film (closed circles) and for a CdSe NC film treated with butylamine (open squares). The photocurrent for both samples has been normalized to its maximum value to emphasize the similarity in field dependence between the two samples. The solid and dotted lines serve as guides for the eyes.

The method of forming NC solids in which the organic ligands are removed from core/shell NCs can potentially be applied to a variety of semiconductor materials. Equation 3.3 can be used to estimate the maximum thickness of shell which can be grown and still achieve 100% IQE in systems with different inorganic core and shell materials. By setting the expression for transmission probability of a CdSe/ZnS NC film with  $d$  equal to 0.5 nm and  $\Phi_B$  equal to 0.7 eV equal to the expression for the new system the necessary shell thickness ( $d$ ) can be calculated.

### 3.4.7 Effect of the Shell on Conduction

Figure 3.10(a) demonstrates that despite a significant reduction in  $k_{nr}$  in Sample B (40% QY), the inorganic shell can be too thick to get 100% IQE of the photocurrent. The quality of the inorganic shell matters as well. Figure 3.10(b) shows the photocurrent for Sample C which has 0.68 nm interparticle spacing (close to Sample A) but a QY of only 4% as compared to the 25% QY of Sample A. Though the room temperature photocurrent is larger in magnitude than the photocurrent measured at 77 K, the photocurrent does not show saturation with applied field. This indicates that while  $k_{nr}$  does not hinder exciton separation, the mobility of the carriers in the film is low. This is most likely a result of the many trap sites which may be present in a film with a patchy or uneven ZnS shell, common causes for a low QY.

Finally, heat is not the only mechanism that can be used to remove the organic ligands. Figure 3.10(c) shows the photocurrent results for a film deposited from CdSe/ZnS NCs capped with butylamine (Sample D). After removal of the butylamine ligands, the photocurrent appears linear with electric field indicating that every exciton is separated but one or both carriers are not extracted at the electrodes.<sup>3</sup> The photocurrent does not saturate because Sample D has a thicker shell ( $d = 1.14$  nm) than Sample A. When the butylamine cap exchange is performed on Sample

A, a blue shift is observed in the NC absorbance spectrum. This indicates that the butylamine is removing the atoms on the surface of the NC. For samples with a very thin shell this can have a significant effect on the optical properties. However, for materials in which the melting temperature of the core and/or shell is lower than the temperature at which ligands burn/evaporate, cap exchange into a ligand with a lower boiling point could be used as an alternative method to create a core/shell NC film.

### **3.5 Conclusion**

This study demonstrates that it is possible to reduce the effect of non-radiative recombination on the photocurrent and to achieve 100% IQE of the photocurrent at room temperature by overcoating NC cores with a higher band gap inorganic material and removing a majority of the organic ligands. Reducing the influence of surface states on the photoconductivity in CdSe/ZnS NC films also allows for the use of this material as room temperature photodetector.

A number of core/shell materials can potentially be combined to create conductive NC solids. A first step in creating variations of core/shell solids is given in this paper with the photoconductivity measurements of a CdSe/ZnS nanorod film. To achieve high conductivity in a core/shell NC film, a thin, high quality shell must be grown on the NC core. This can prove to be the most challenging step because the lattice mismatch between different semiconductors can result in core/shell NCs with low QYs. Provided a suitable shell can be grown, and the organic ligands removed, NC solids can be assembled for many different applications.

### 3.6 References

1. M. Drndic, M. V. Jarosz, N. Y. Morgan, M. A. Kastner and M. G. Bawendi, *Journal of Applied Physics* **92**, 7498 (2002).
2. H. E. Romero and M. Drndic, *Phys. Rev. Lett.* J1 - PRL **95**, (2005).
3. M. V. Jarosz, V. J. Porter, B. R. Fisher, M. A. Kastner and M. G. Bawendi, *Physical Review B* **70**, (2004).
4. V. J. Porter, T. Mentzel, S. Charpentier, M. A. Kastner and M. G. Bawendi, *Physical Review B* **73**, (2006).
5. D. Yu, C. J. Wang and P. Guyot-Sionnest, *Science* **300**, 1277 (2003).
6. B. L. Wehrenberg and P. Guyot-Sionnest, *Journal of the American Chemical Society* **125**, 7806 (2003).
7. C. J. Wang, M. Shim and P. Guyot-Sionnest, *Applied Physics Letters* **80**, 4 (2002).
8. D. V. Talapin and C. B. Murray, *Science* **310**, 86 (2005).
9. M. Shim and P. Guyot-Sionnest, *Nature* **407**, 981 (2000).
10. M. Shim, C. J. Wang and P. Guyot-Sionnest, *Journal of Physical Chemistry B* **105**, 2369 (2001).
11. D. Yu, C. Wang, B. L. Wehrenberg and P. Guyot-Sionnest, *Phys. Rev. Lett.* **92**, 216802 (2004).
12. G. Konstantatos, I. Howard, A. Fischer, S. Hoogland, J. Clifford, E. Klem, L. Levina and E. H. Sargent, *Nature* **442**, 180 (2006).
13. R. H. Bube, *Photoconductivity of Solids*. 1960, New York: Wiley.
14. C. A. Leatherdale, C. R. Kagan, N. Y. Morgan, S. A. Empedocles, M. A. Kastner and M. G. Bawendi, *Physical Review B* **62**, 2669 (2000).
15. D. C. Oertel, M. G. Bawendi, A.C. Arango, V. Bulovic, *Applied Physics Letters* **87**, 213505 (2005).
16. P. T. Snee, Y. Chan, D. G. Nocera and M. G. Bawendi, *Advanced Materials* **17**, 1131 (2005).
17. N. E. Stott, Ph.D. thesis, Massachusetts Institute of Technology, 2005.
18. M. A. Hines and P. Guyot-Sionnest, *Journal of Physical Chemistry* **100**, 468 (1996).



19. B. O. Dabbousi, J. RodriguezViejo, F. V. Mikulec, J. R. Heine, H. Mattoussi, R. Ober, K. F. Jensen and M. G. Bawendi, *Journal of Physical Chemistry B* **101**, 9463 (1997).
20. R. G. Xie, U. Kolb, J. X. Li, T. Basche and A. Mews, *Journal of the American Chemical Society* **127**, 7480 (2005).
21. J. J. Li, Y. A. Wang, W. Z. Guo, J. C. Keay, T. D. Mishima, M. B. Johnson and X. G. Peng, *Journal of the American Chemical Society* **125**, 12567 (2003).
22. A. Aharoni, T. Mokari, I. Popov and U. Banin, *Journal of the American Chemical Society* **128**, 257 (2006).
23. M. V. Jarosz, Ph.D. thesis, Massachusetts Institute of Technology, 2004
24. C. R. Kagan, Ph.D. thesis, Massachusetts Institute of Technology, 1996
25. M. V. Jarosz, N. E. Stott, M. Drndic, N. Y. Morgan, M. A. Kastner and M. G. Bawendi, *Journal of Physical Chemistry B* **107**, 12585 (2003).
26. C. R. Kagan, C. B. Murray, M. Nirmal and M. G. Bawendi, *Phys. Rev. Lett.* **76**, 1517 (1996).
27. C. B. Murray, D. J. Norris and M. G. Bawendi, *Journal of the American Chemical Society* **115**, 8706 (1993).
28. C. B. Murray, C. R. Kagan and M. G. Bawendi, *Science* **270**, 1335 (1995).
29. C. B. Murray, C. R. Kagan and M. G. Bawendi, *Annual Review of Materials Science* **30**, 545 (2000).
30. To calculate the total mass of ligands on this NC it is assumed that there is one octadecylamine molecule per surface Zn atom. The mass of the organic ligands is divided by the total mass of the graded core/shell NC, calculated by taking into account the amount of Zn, Cd, S, and Se at each layer in the NC.
31. H. Mizuseki, K. Niimura, C. Majumder and Y. Kawazoe, *Computational Materials Science* **27**, 161 (2003).

## Chapter 4

# Temperature-, Gate-, and Photo-induced Conductance of Close-packed CdTe Nanocrystal Films\*

### 4.1 Introduction

In Chapters 2 and 3, CdSe and CdSe/ZnS NC films were found to form blocking contacts with gold electrodes. As a product of the blocking contacts, these films displayed high photocurrents and little underlying dark current which are both characteristics of a good photodetector. However, another consequence of the blocking contacts is that the electric field does not drop uniformly across the NC film and this prohibits the study of charge transport on a NC to NC level. We decided to study CdTe NC films as CdTe NCs have a different band alignment with gold in hope that this system would have non-blocking contacts and so we could better characterize the mechanism of charge transport in NC solids. In this chapter, we find that CdTe NC films do form non-blocking contacts with gold electrodes. With this system we show that the dominant charge carriers in CdTe NC films are holes, and that the density of holes can be changed by applying a voltage to the gate. Results from photocurrent studies on the CdTe NC films are also presented and the effect of trapping on the dark current and photocurrent is discussed. Secondary photocurrents are observed in the CdTe NC films, and they are examined and contrasted with the photocurrent in CdSe NC films. Finally, as the electric field drop is uniform in this sample, we are able to propose a single phenomenological model of field

---

\* Much of this chapter appears in print: V. J. Porter, T. Mentzel, S. Charpentier, M. A. Kastner and M. G. Bawendi, Phys. Rev. B 73, 155303 (2006).

dependent tunneling between NCs which adequately describes the i-V characteristics for both the dark and photocurrent.

## 4.2 Experimental

### 4.2.1 CdTe NC Synthesis

CdTe NCs with a first absorption feature at 680 nm, emission at 698 nm, and average particle diameter of  $6.2 \pm 0.4$  nm are synthesized by substituting a telluride for a selenide precursor in a previously published procedure for making CdSe NCs.<sup>1</sup> The stoichiometric ratio of precursors in this reaction is 1 mmol Cd: 2.5 mmol 1, 2-hexadecanediol: 3 mmol Te. A solution of cadmium 2, 4-pentanedionate (98%), 1, 2-hexadecanediol, and tri-*n*-octylphosphine (TOP) is degassed for 1 hour at 100 °C, and then the solution is cooled under argon prior to the addition of 1.5 M tri-*n*-octylphosphine telluride (TOPTe). The mixture is then loaded into a syringe and injected into a 360 °C hot solvent solution consisting of 99% tri-*n*-octylphosphine oxide (TOPO), hexadecylamine (HDA), and hexylphosphonic acid (HPA). The NCs are grown for ~ 7 min at 260 °C and then cooled to room temperature. After adding hexane to the growth solution, it is transferred to the nitrogen atmosphere of the glovebox for storage. An absorbance spectrum for this sample is given in Figure 4.1(line a).

The above recipe worked well for the batch of TOP which was in use in our lab from 2004-2005 (TOP batch #1). However, after purchasing a new batch of TOP (TOP batch #2) the same CdTe prep resulted in NCs with very broad absorption features [Figure 4.1(line c)] and very little emission. TEM revealed the CdTe NCs were actually short, stubby nanorods (NRs) which are known to grow when there is a high concentration of cadmium in the reaction

mixture.<sup>2,3</sup> This suggested that the cadmium and tellurium precursors are not reacting quickly and are not consumed during the nucleation portion of the NC reaction. Switching to a more reactive TBP<sub>Te</sub> precursor sped up the reaction and resulted in CdTe NCs with distinct features in the absorption spectrum [Figure 4.1(line d)]. TOP #2 was used up and yet another batch of TOP (TOP batch #3) was used for this reaction. Even with the use of TBP<sub>Te</sub>, the features in the absorbance spectrum were less distinct and the emission of the NCs was quenched [Figure 4.1(line e)]. Filtering the TOP through a column of activated, basic alumina solved this problem and CdTe NCs with good size distribution were synthesized [Figure 4.1(line f)]. The improvement in NC quality using filtered TOP suggests the TOP contains some sort of acidic impurity which binds to the cadmium or tellurium and slows the reaction.

It is not surprising that acids in the reaction mixture have a significant effect on the reaction rate, especially given the important role of phosphonic acids in the formation of nanocrystals with nonspherical geometries.<sup>2,3</sup> In fact, it is difficult to synthesize CdTe NCs having a narrow size distribution without the proper amount of acid in the reaction mixture. This is demonstrated by showing the absorbance spectra for CdTe NCs synthesized with 0.4 g and 0.28 g of hexyl-phosphonic acid [Figure 4.1(line a) and Figure 4.1(line b) respectively]. Without enough acid present to control the reaction rate, the NCs have a poor size distribution. In conclusion, while there are many reaction conditions which can be used to synthesize CdTe NCs, the key ingredients which affect the CdTe NCs size distribution regardless of TOP lot number are seen to be the use of TBP<sub>Te</sub>, rather than TOP<sub>Te</sub>, as the tellurium precursor, the correct molar ratio of hexyl-phosphonic acid to cadmium, and the filtering of the TOP to remove acidic impurities.

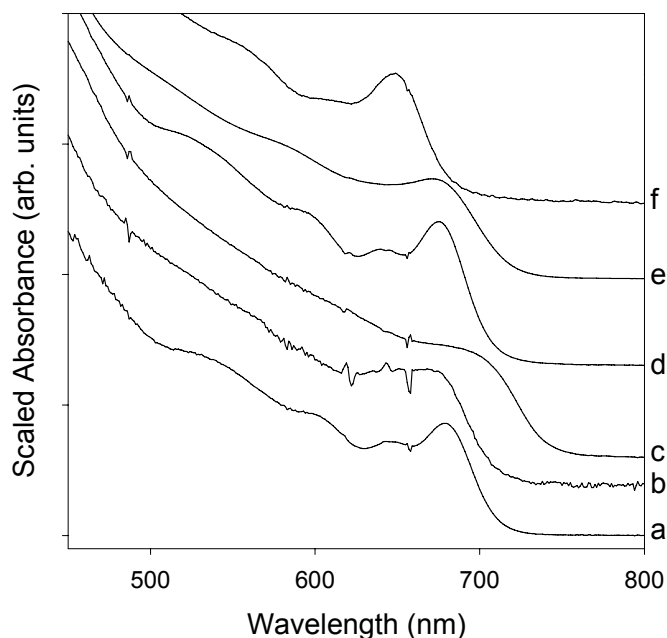


**Figure 4.1:** Absorbance spectra of CdTe NCs for different reaction conditions: (a) using TOPTe and TOP batch #1, (b) TOPTe, TOP batch #1,  $\frac{1}{2}$  amount of HPA, (c) TOPTe and TOP batch #2, (d) TBPTe and TOP batch #2, (e) TBPTe and TOP batch #3, (f) TBPTe and filtered TOP batch #3.

#### 4.2.2 Sample preparation

5 mL of growth solution is processed via previously reported methods to make close-packed films of NCs.<sup>4-11</sup> The main difference between other procedures and the CdTe procedure is that all processing of the CdTe NCs is done in the glovebox to minimize exposure to oxygen and water. The first step is to centrifuge the sample and save the supernatant. (The precipitate consisting of TOPO and other salts is discarded.) The NCs are next precipitated by adding methanol and spinning the solution in the centrifuge. The supernatant is discarded, and the CdTe NCs are redissolved in hexane and butanol. This solution is then filtered through a 0.2  $\mu\text{m}$  filter and the precipitation process is repeated again using 0.1  $\mu\text{m}$  filter. The CdTe NCs are precipitated a third time but now they are dissolved in a 9:1 hexane:octane mixture, rather than

hexane and butanol, and passed through a 0.02  $\mu\text{m}$  filter. This solution is drop cast onto the measurement device, a silicon inverted field effect transistor (FET).

The FETs are fabricated by lithographically patterning gold bar electrodes 200 X 800 X 0.1  $\mu\text{m}^3$  on 330 nm of silicon oxide.<sup>12</sup> The electrodes are spaced by 1 or 2  $\mu\text{m}$ . The FETs are attached onto a 28-pin chip carrier with silver paint and electrical contacts are made from the electrodes to the chip carrier by gold wire bonds. Devices are tested by applying high voltage (100 V) to the source, drain, and gate electrodes prior to nanocrystal deposition to screen for leakage pathways between the electrodes and through the oxide. Devices with leakage greater than 0.5 pA are discarded.

The chemical treatment with butylamine is the same as discussed in Chapter 2. It involves soaking the CdTe NC film in a 0.1 M solution of butylamine in acetonitrile for 10 min, rinsing the film with acetonitrile, and drying in the oven for 1 hr at 70 °C.

### **4.2.3 Electrical Measurements**

All conductivity measurements are performed in a Janis VPF-100 cryostat under vacuum. Samples are loaded into the cryostat in the glovebox and are not directly exposed to air. Current,  $I$ , is measured and the drain-source voltage,  $V_{\text{ds}}$ , is sourced with a Keithley 6517 electrometer. Gate voltage,  $V_{\text{g}}$ , is supplied with an Agilent 6614C DC power supply. An Ar<sup>+</sup> laser at 514 nm is used to photo-excite the samples. It has been shown previously that photocurrent is not a result of photoinjection from the electrodes.<sup>4</sup> The temperature is monitored with a Lakeshore 330 temperature controller. Photocurrent decay measurements are performed by modulating the excitation light with an acousto-optic modulator and monitoring the current with a Keithley 428 current amplifier and Tektronix TDS 7154 oscilloscope.

Differential conductance measurements were carried out by applying a constant  $V_{ds}$  with the Agilent 6614C DC power supply. A small AC voltage (5V, 13 Hz) is added to the drain electrode by a function generator. The resulting AC current is sent to a current amplifier (Ithaco 1211), then to a lock-in amplifier (Princeton Applied Research 5301A), and finally read from a digital multimeter (Hewlett Packard 34401A).  $V_g$  is stepped with a Keithley 2400 sourcemeter. A schematic of the differential conductance measurement setup is given in Figure 4.2.

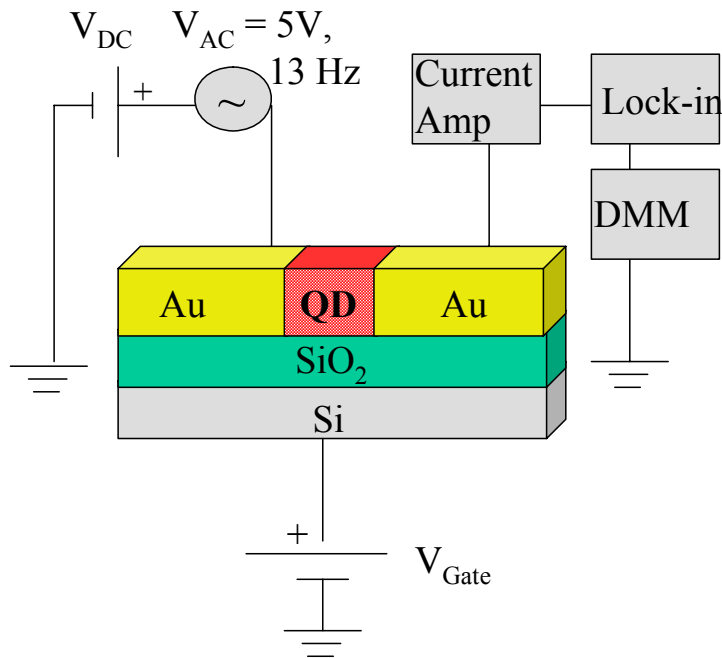


**Figure 4.2:** Schematic of the differential conductance measurement system.

## XPS (X-ray Photoelectron Spectroscopy)

A Kratos AXIS Ultra Imaging X-ray Photoelectron Spectrometer with Delay Line Detector is employed for the XPS measurements. The excitation energy for all spectra is 1487 eV and data is taken in 100 meV steps. CdTe NCs are deposited in the glovebox on a clean piece of polished, n-doped silicon. Samples are removed and quickly taken to the XPS for the measurement to minimize air exposure. The samples are measured again after storage in air for three weeks to observe the effects of oxidation on the composition of the CdTe NC films.

## 4.3 Results

### 4.3.1 Dark Current in CdTe NC Films

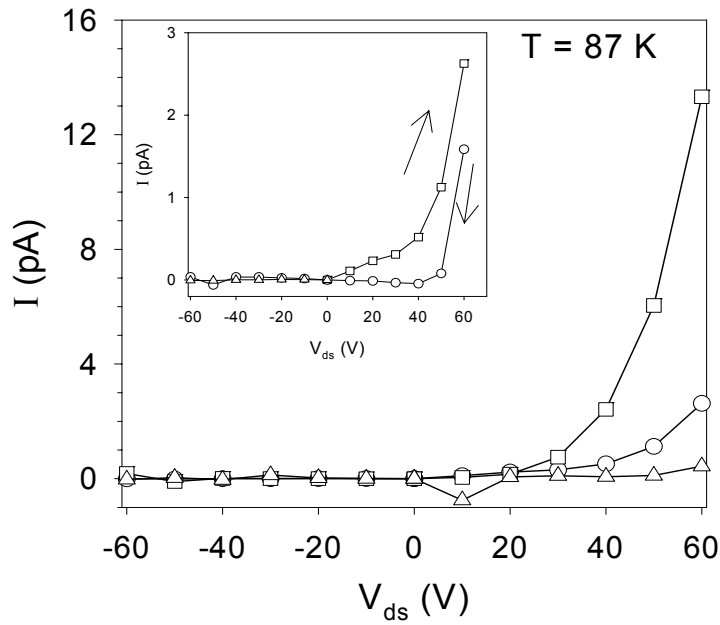
Figure 4.3 shows the dark current through a CdTe NC film versus  $V_{ds}$  at 87 K with gate voltage,  $V_g = 0$  V (open circles), +40 V (open triangles), and -40 V (open squares). The inset displays the complete I-V curve for the sample with the gate grounded. For the latter,  $V_{ds}$  is swept from 0 V to +60 V (open squares), from +60 V to -60 V (open circles), and finally from -60 V back to 0 V (open triangles). The current is hysteretic with more current on the sweep from 0 V to +60 V than on the way down from +60 V to -60 V suggesting it decays with time at these low temperatures (data points are taken every 10 seconds). For the I-V curves in the main part of Figure 4.3, the data shown are for the voltage sweep from 0 V to +60 V and the sweep from 0 V to -60V in order to display the current before it decays.

Figure 4.4 shows the dark current as a function of  $V_g$ , with  $V_{ds} = +60$  V. Consistent with the data in Figure 4.3, the current is largest at negative  $V_g$  and suppressed at positive  $V_g$ . The



current is roughly linear with  $V_g$  when it is varied from 0 V to -40 V, but is smaller in magnitude on the way back from -40 V to 0 V.

Figure 4.5 shows the I-V curves for the dark current before (top panels) and after (lower panels) chemical treatment with butylamine at 295 K [Figure 4.5(a)] and at 87 K [Figure 4.5(b)]. In all four plots of Figure 4.5,  $V_{ds}$  is swept from 0 V to +100 V (open squares), +100 V to -100 V (open circles), and finally from -100 V back to 0 V (open triangles). Note the different scales in the two panels of Fig. 4(a): The dark current at 295 K is approximately three orders of magnitude higher after treatment with butylamine. By contrast, at 87 K [Figure 4.5(b)], the dark current decreases rather than increases with butylamine treatment. Whereas the current is hysteretic and measurable only for positive  $V_g$  at 87 K, it shows little hysteresis and is nearly symmetric with  $V_{ds}$  at 295 K.



**Figure 4.3:** Dark current,  $I$ , at 87 K as a function of drain bias with  $V_g = 0$  V (open circles),  $V_g = -40$  V (open squares), and  $V_g = +40$  V (open triangles). The inset is the full I-V curve with  $V_g = 0$  V and it displays the hysteresis present at low temperature. The current is swept from 0 V to +60 V (open squares), from +60 V to -60 V (open circles), and finally from -60 V to 0 V (open triangles) and it is higher on the sweep from 0 to +60 V than when the sweep is reversed. The solid lines serve as guides to the eye.

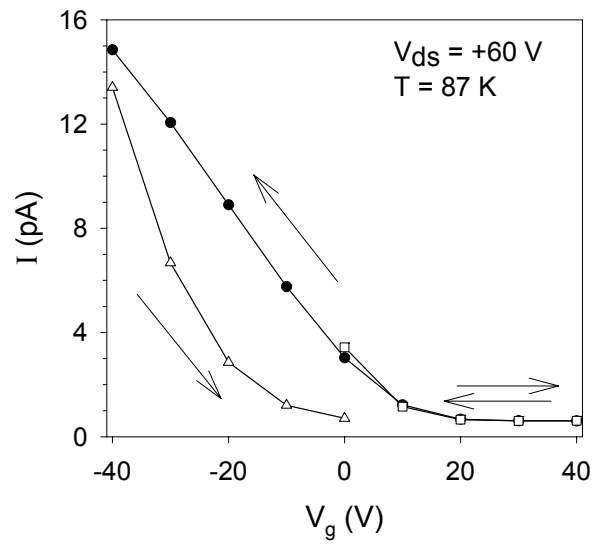


**Figure 4.4:** Dark current,  $I$ , at 87 K as a function of applied gate voltage with  $V_{ds} = +60$  V.  $V_g$  is swept from 0 V to +40 V (open squares), from +40 V to -40 V (filled circles), and finally from -40 V to 0 V (open triangles). The solid lines are guides to the eye.

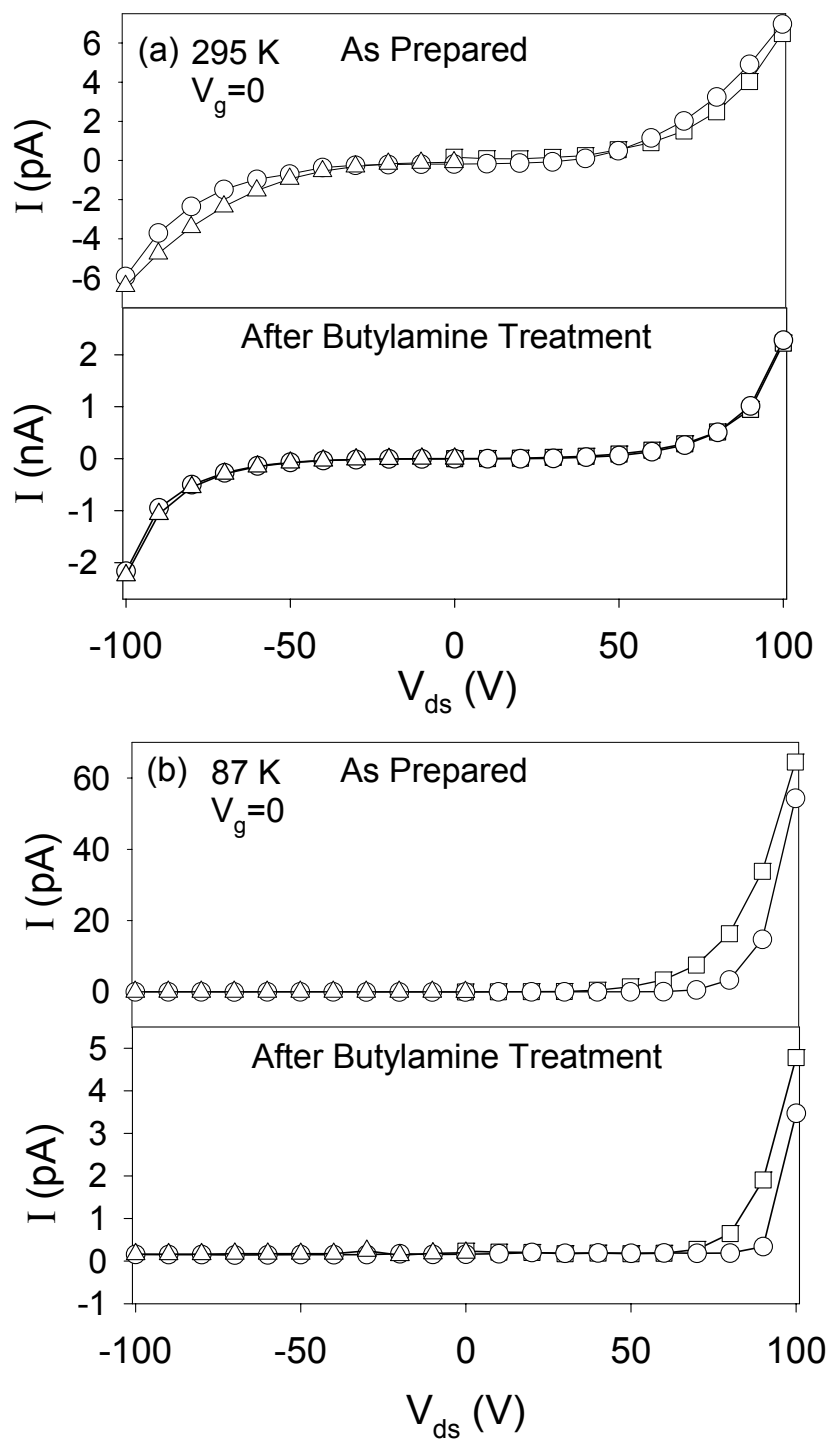


**Figure 4.5:** Dark current,  $I$ , before (top panels) and after (bottom panels) treatment with butylamine at (a) 295 K and (b) 87 K with  $V_g=0$ .  $V_{ds}$  is swept from 0 V to +100 V (open squares), from +100 V to -100 V (open circles), and finally from -100 V to 0 V (open triangles). Solid lines serve as guides to the eye. Note that the current at 295 K increases by almost 1000 times after treatment.

Differential conductance measurements at room temperature as a function of gate voltage are displayed in Figure 4.6 for a sample treated with butylamine. These measurements help to reduce the hysteresis and charging effects which muddle the interpretation of the conductivity measurements, especially at room temperature where there is a large thermally activated charge density. To measure the differential conductance, we apply a small AC voltage of  $2 V_{\text{rms}}$  at 13 Hz in series with a DC voltage of  $|V_{\text{ds}}| = 110 \text{ V}$  across the electrodes (the electrodes are spaced by  $2 \mu\text{m}$  for the data in Figure 4.6). The gate voltage is stepped in increments of 5 V. To minimize the hysteresis, we apply  $V_g$  for 5 seconds and return  $V_g$  to zero for 5 sec for each data point. This effectively is a measurement of how the slope of the  $I$ - $V_{\text{ds}}$  curve at  $|V_{\text{ds}}| = 110 \text{ V}$  varies with gate voltage. For both positive and negative  $V_{\text{ds}}$  the differential conductance increases with increasing negative  $V_g$  and decreases with positive  $V_g$ .

Figure 4.7 demonstrates that the room temperature dark current,  $I$ , and the low temperature photocurrent,  $\Delta I$  defined as the difference between the dark and photocurrents, depend only on electric field and not independently on the separation of the electrodes. Note that since the dark current is in general 2-3 orders of magnitude less than the photocurrent,  $\Delta I$  and the absolute photocurrent are essentially identical. The current is measured across electrodes with gaps of 1 and  $2 \mu\text{m}$  and is found to be the same magnitude for a given field, indicating most of the electric field is dropped uniformly across the NC film, and not the electrode interface. The sample used for Figure 4.7 was deposited onto gold electrodes patterned on a quartz substrate and has no back gate. This was done in order to minimize field drop to the gate and better observe the field scaling effect.

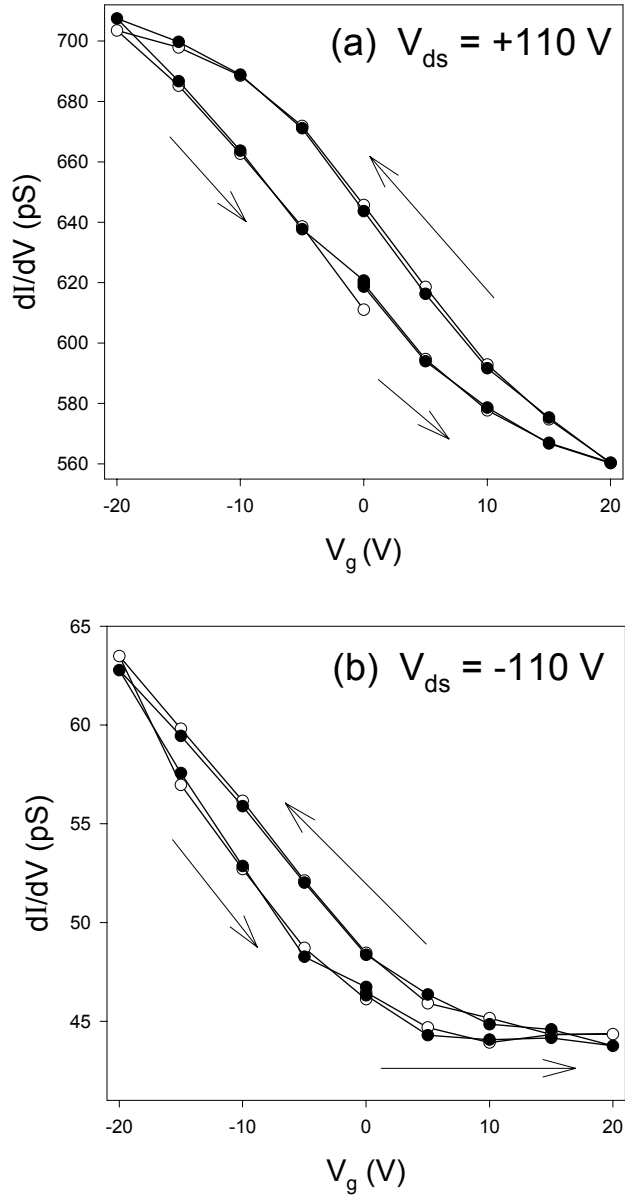


**Figure 4.6:** (a) Differential conductance,  $dI/dV$ , as a function of  $V_g$  with (a)  $V_{ds} = +110$  V and (b)  $V_{ds} = -110$  V.  $V_g$  is applied for 5 s followed by a recovery period of 5 sec at each value of  $V_g$ .  $V_g$  is varied from 0 V to +20 V, from +20 V to -20 V, and finally from -20 V to 0 V.  $V_{ac}$  is  $2 V_{rms}$  at a frequency of 13 Hz. In (a) and (b) the open circles are the first  $V_g$  cycle and the closed circles are the second cycle.

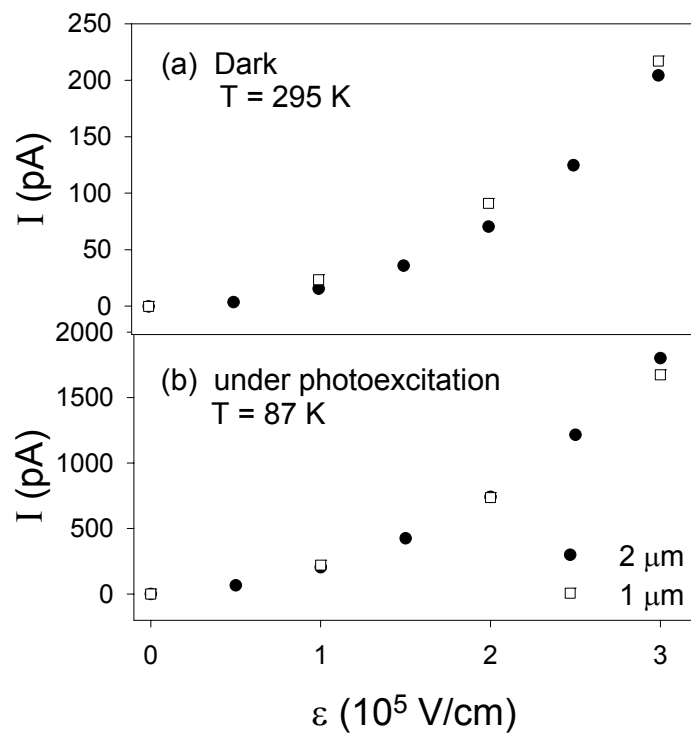


**Figure 4.7:** (a) Dark current,  $I$ , at 295 K (b) and photocurrent,  $\Delta I$ , at 87 K measured on a 1  $\mu\text{m}$  gap (open squares) and on a 2  $\mu\text{m}$  gap (closed circles) and plotted versus electric field,  $\epsilon = V_{\text{ds}}/L$ , where  $L$  is the gap between the electrodes. For (a) and (b)  $V_g = 0$ .

### 4.3.2 Temperature Dependence of the Dark Current

The temperature,  $T$ , dependence of the dark current at  $V_{ds} = -90, -80, -70, -60, -50,$  and  $-40$  V for a butylamine treated sample is plotted in Figure 4.8. The dark current is linear with inverse temperature when plotted on a semi-logarithmic graph, indicating Arrhenius behavior. Solid lines are fits to the Arrhenius equation at each voltage. The noise of our electrometer is  $\sim 0.01$  pA, indicating that except at the most negative voltages, there is no evidence for anything other than a simply activated current. From the fits, the activation energy at each voltage is determined, and the activation energy is plotted versus electric field in the inset of Figure 4.8 and fit to a straight line. The y-intercept of the line gives the zero-field activation energy for the dark current and is found to be  $0.38 \pm 0.02$  eV. From the slope of the line, one can calculate the distance traveled during the rate-limiting step in the activated process:

$$\Delta E = -el\varepsilon, \quad (4.1)$$

where  $\Delta E$  is the activation energy,  $e$  is the charge of the electron,  $l$  is distance, and  $\varepsilon$  is electric field. From the fit of the inset of Figure 4.8 we find  $l = 2.2 \pm 0.2$  nm. We note that before butylamine treatment, the conductance is too small to measure the  $T$  dependence.



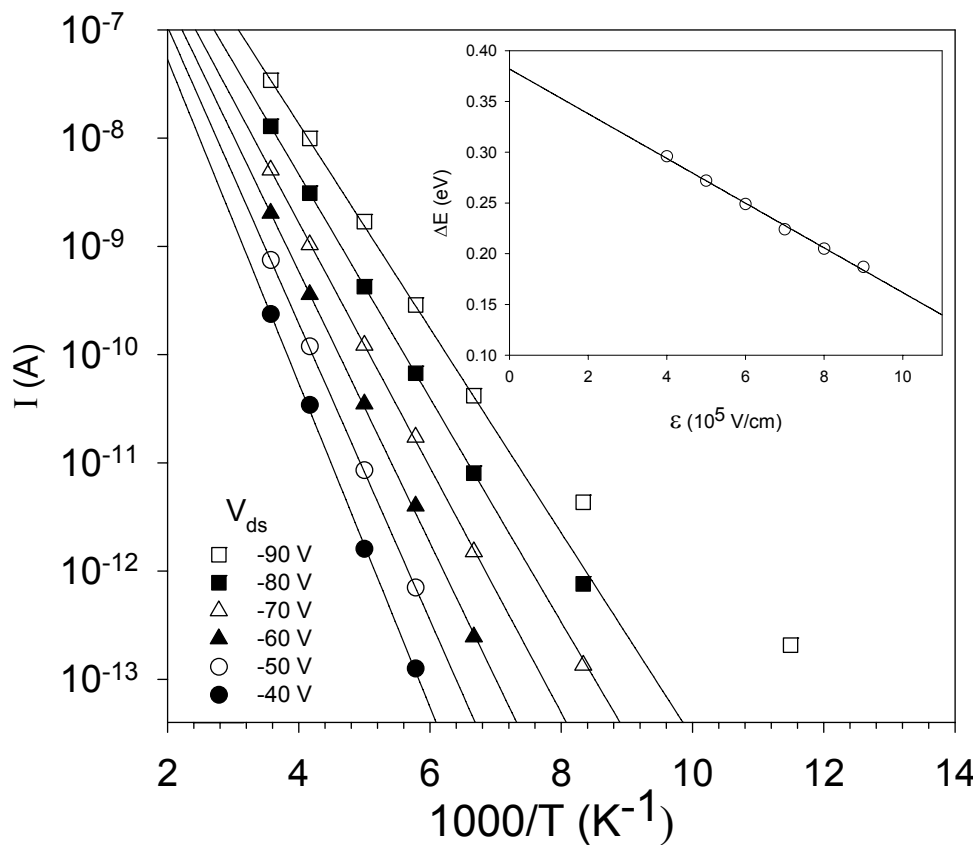


**Figure 4.8:** Temperature dependence of the dark current,  $I$ , (butylamine treated) at various values of  $V_{ds}$  with  $V_g = 0$ . The solid lines are Arrhenius fits to the data at each voltage. The inset is a plot of the activation energy,  $\Delta E$ , as a function of field,  $\epsilon = V_{ds}/L$ , where  $L$  is the electrode separation. The solid line in the inset is a linear fit to the activation energy versus field data.

### 4.3.3 Photocurrent in CdTe NC Films

The photocurrent,  $\Delta I$ , vs.  $V_{ds}$  at 87 K and 295 K are given in Figure 4.9 for both (a) untreated and (b) butylamine-treated films. The axis for the photocurrent at each temperature is scaled to show that the shape of the two I-V curves is the same. The intensity of the 514 nm excitation light is 30 mW/cm<sup>2</sup>. The insets are included to emphasize the variation of the photocurrent magnitude with T. As seen in the insets, the temperature dependence after treatment is opposite to that before treatment: the magnitude of the photocurrent before treatment increases as T decreases, whereas after treatment it decreases with T. For all data in Figure 4.9,  $V_{ds}$  is swept from 0 V to +100 V. Though not shown,  $\Delta I$  in all plots is symmetric in  $V_{ds}$  and displays little hysteresis.

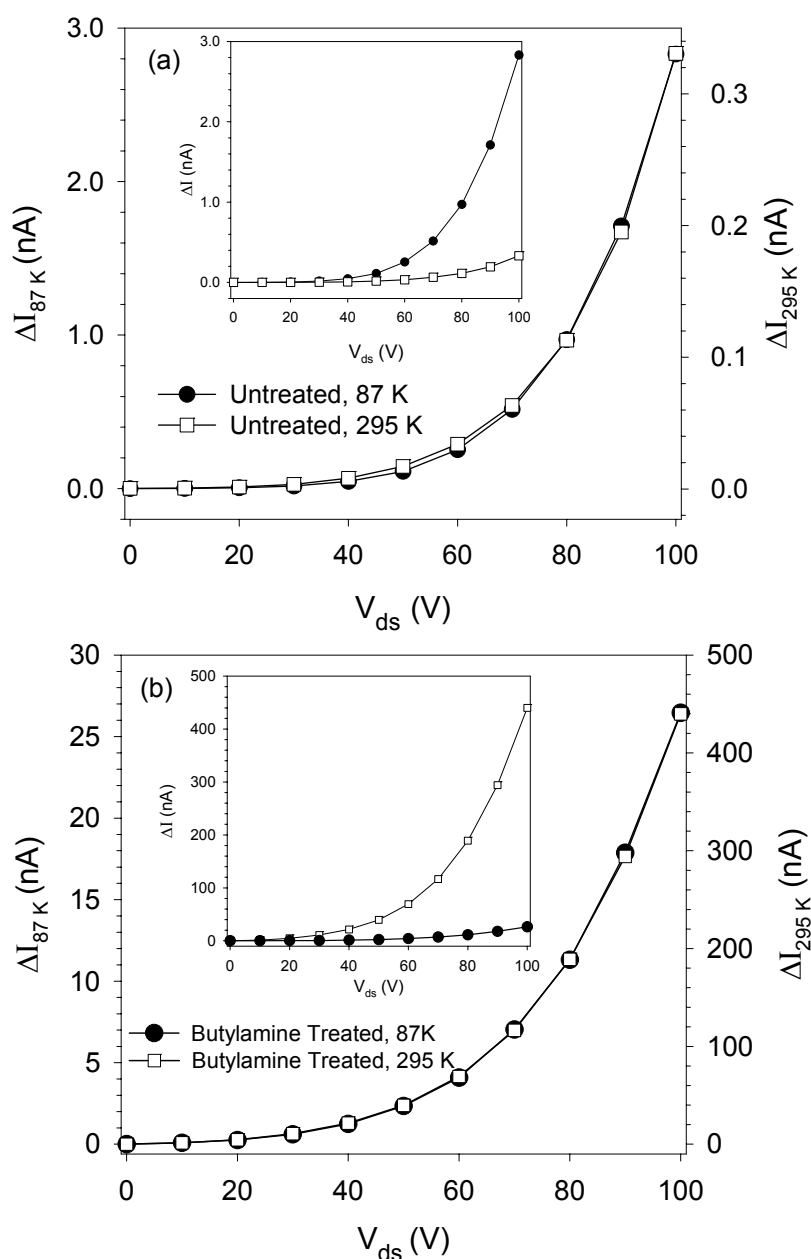


**Figure 4.9:** (a) Photocurrent,  $\Delta I$ , at 87 K (filled circles and left axis) and at 295 K (open squares and right axis) before treatment with butylamine ( $V_g = 0$ ). Each axis is scaled to illustrate the similar shape of the  $\Delta I$ - $V$  curves at the two temperatures. The inset in (a) is the data plotted with a shared y-axis to illustrate the difference in the magnitude of the current at the two temperatures. (b) Photocurrent at 87 K (filled circles and left axis) and at 295 K (open squares and right axis) after treatment with butylamine ( $V_g = 0$ ). The inset in (b) is the data plotted with a shared y-axis. Solid lines are guides to the eye. The photoexcitation intensity is 30 mW/cm<sup>2</sup>.

To study the effect of trapping on the photocurrent, the dependence of  $\Delta I$  on excitation intensity and the decay of  $\Delta I$  when the light is turned off is measured. Figure 4.10 shows the dependence of  $\Delta I$  on photoexcitation intensity.  $V_{ds} = +100$  V is applied to the sample while the photoexcitation intensity is stepped. Measurements are performed on the CdTe NC film after butylamine treatment at 87 K (closed circles) and room temperature (open circles). The photoexcitation intensity dependence of the current is closer to linear at 87 K than at room temperature. Figure 4.11 shows the decay of  $\Delta I$  after the  $30 \text{ mW/cm}^2$  excitation light is turned off at 300 K and 87 K while  $V_{ds}$  is held at -90 V. The photocurrent decay is faster at room temperature than at 87 K.

Figure 4.12 gives the dark and photocurrent measured at room temperature as a function of exposure to oxygen. Each I-V curve is measured twice in succession to check that the increase in current is not a result of sweeping the electric field. The data is taken in a cryostat under vacuum and then the sample is exposed to air for the time indicated in the figure. Both the dark and photocurrents increase by a factor of four after five days of air exposure.

The results presented in Figures 4.3-4.12 depict trends which have been observed on all CdTe NC film samples measured to date. The magnitude of the current varies slightly from sample to sample due to differences in sample thickness, but the I vs.  $V_{ds}$  curves all display the same response to temperature, butylamine treatment, photoexcitation, and gate voltage. Three batches of CdTe NC's were synthesized and 2-3 samples prepared from each batch. Eight samples were measured in total. On each sample 3 separate 1 or 2  $\mu\text{m}$  gaps were tested. In Chapter 4, Figures 4.3 and 4.4, (which demonstrate the gate dependence of the CdTe NC film) are from the same sample. Figs. 4.5, 4.9, 4.10, and 4.11 show the behavior of the dark and

photocurrent after chemical treatment and are from the same sample. Figures. 4.6, 4.7, 4.8, and 4.12 were measured at a later time and each shows data taken from a separate sample.

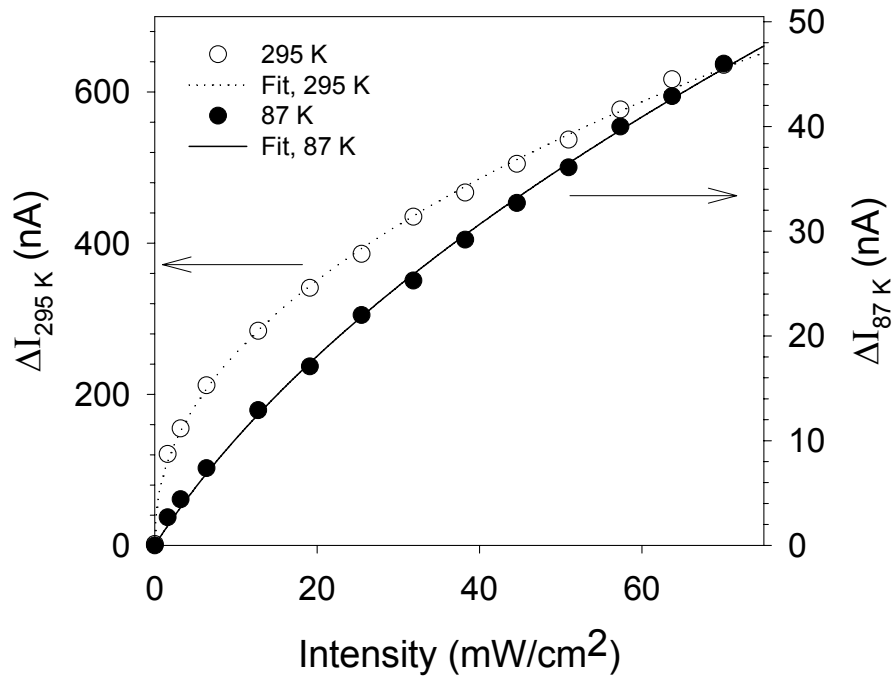


**Figure 4.10:** The photoexcitation intensity dependence of  $\Delta I$ . Data at 87 K and 295 K are represented by filled circles and open circles, respectively. The solid line is a fit to the 87 K data, and the dotted line is a fit to the 295 K data, as discussed in the text. The sample has been treated with butylamine;  $V_{\text{ds}} = +100 \text{ V}$  and  $V_{\text{g}} = 0$ .

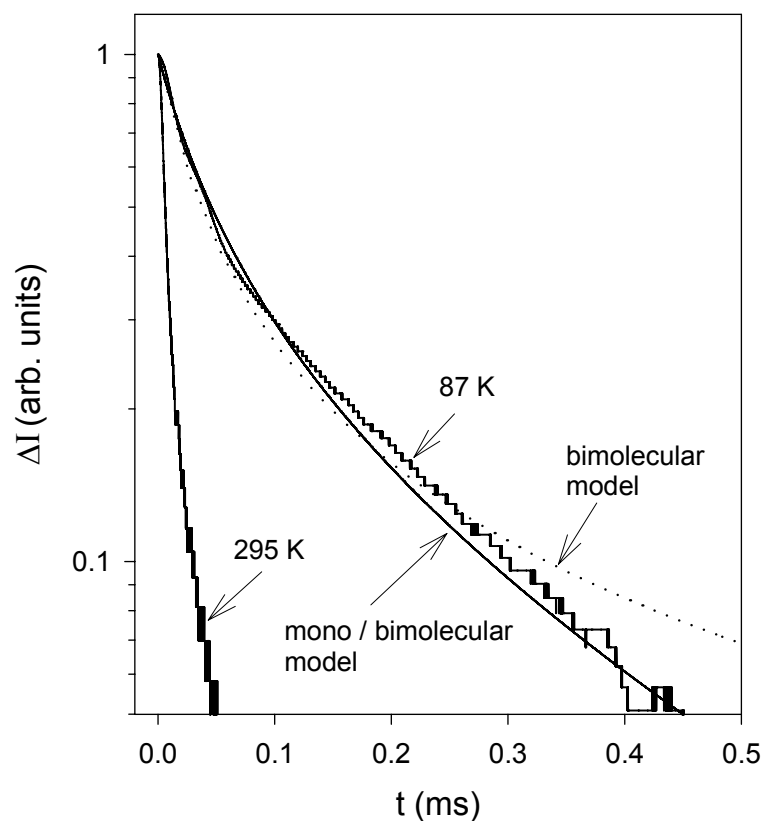


**Figure 4.11:** The photocurrent,  $\Delta I$ , decay at 295 K and 87 K for a sample treated with butylamine.  $V_{ds} = -90$  V,  $V_g = 0$ , and the excitation intensity is  $30$  mW/cm<sup>2</sup> before the photoexcitation is removed. The curve furthest to the right is the photocurrent decay at 87 K while the curve to the left is the photocurrent decay at 295 K. The decay at 87 K is fit with a model for bimolecular recombination (dotted line) and a model for a combination of bimolecular and monomolecular recombination (solid line) as described in the text. The decay at 295 K is, for the most part, faster than the resolution of the current amplifier used for the measurement.

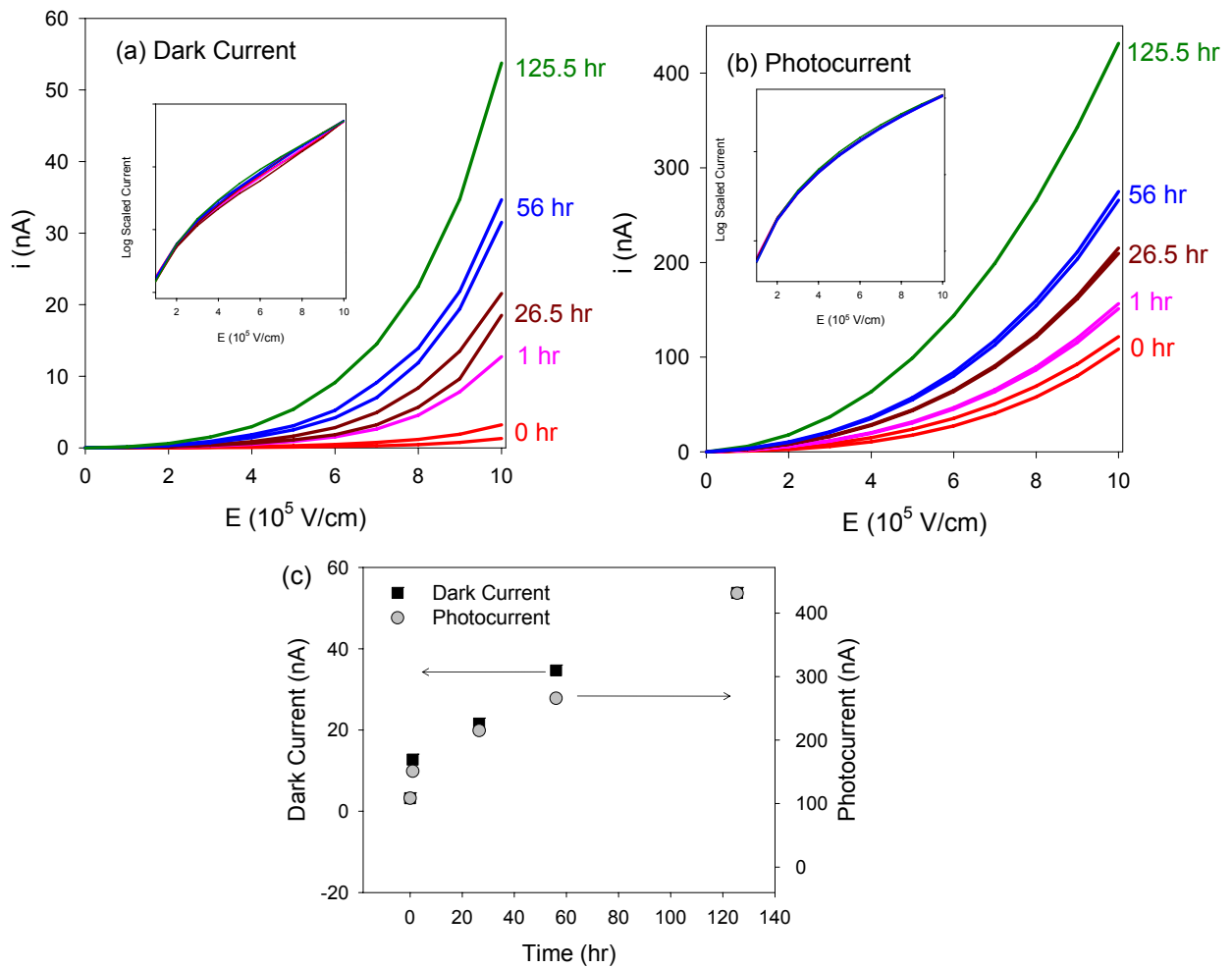


**Figure 4.12:** Room temperature dark (a) and photocurrent (b)  $i$ - $V$  curves as a function of exposure to air. The photocurrent is swept from 0 to  $10 \times 10^5$  V/cm for each curve. Two curves are taken at each air exposure time to demonstrate that it is the air exposure and not sweeping of the electric field which results in the enhancement of the current. The insets of graphs (a) and (b) is the same data scaled in current and plotted on a log plot to highlight the electric field dependence of the current. (c) is the magnitude of the CdTe NC film dark current (black squares) and photocurrent (grey circles) at  $7 \times 10^5$  V/cm as a function of time exposed to air. The current is measured in a cryostat under vacuum and then the sample is opened to air for the designated period of time.

## XPS (X-ray Photoelectron Spectroscopy)

In Figure 4.13 characteristic Te 4d, Te 3d, and Cd 3d peaks are shown before (grey) and after (black) oxidation of the CdTe NC film. In both the Te 4d and Te 3d spectra an additional peak appears to the left of the original peak. The original Te 4d doublet is located at 40.73 and 42.2 eV and was assigned to Te-Cd in a previous study in accordance with bulk CdTe values.<sup>13</sup> A second doublet, shifted  $\sim 3.5$  eV to higher binding energy, appears in the Te 4d spectrum after exposure to air. A second peak also emerges in the Te 3d spectra after air exposure and this peak is also spaced 3.5 eV from the original Te-Cd peak. This shift is attributed to Te-O formation by A. Lobo, et al.<sup>13</sup> In the work by A. Lobo, et al. a  $\sim 3.7$  eV shift was proposed to correspond to Te in the +4 oxidation state and  $\text{TeO}_2$  and  $\text{CdTeO}_3$  are proposed as the surface states. The Cd 3d peak shows a slight shift to higher energies, possibly due to Cd-O formation or oxidation of the ligands which are bonded to the Cd.

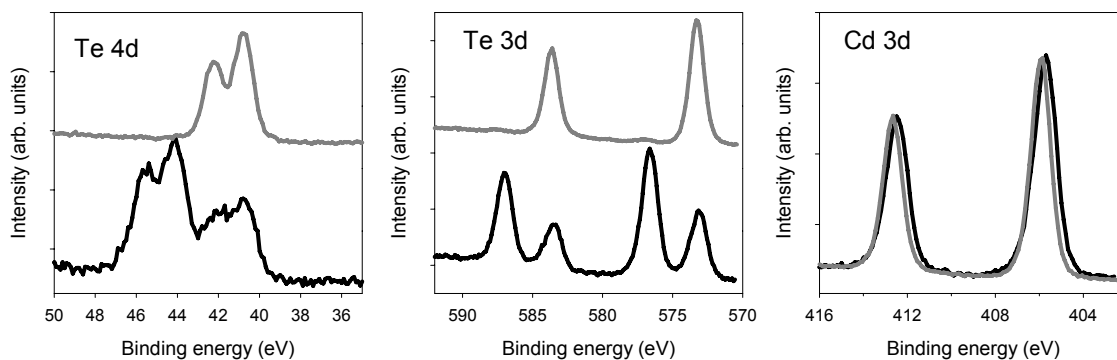


**Figure 4.13:** (a) XPS spectra for a CdTe NC film before (grey line) and after (black line) exposure to air for three weeks. Spectra are provided for the Te 4d, Te 3d, and Cd 3d states.



## 4.4 Discussion

### 4.4.1 Origin of the Dark Current in CdTe NC Films

Previous studies of charge transport in close-packed CdSe NC films, performed on inverted FET structures, found that current resulting from the injection of electrons was on the order of picoamps at  $V_{ds} \sim 100$  V and decayed with time after application of the voltage. The number of electrons injected was affected by the gate, but this current also decayed over time.<sup>12,14</sup> Even after treatment with basic molecules, which were shown to decrease the interparticle spacing, no steady-state dark current was observed in the CdSe NC films.<sup>9</sup> In the present work, we find that at low temperature CdTe NC films, like CdSe NC films, display transient dark current on the order of picoamps. However, unlike CdSe NC films, the room temperature dark current in CdTe NC films is steady-state.

Charge transport in close-packed NC films is expected to be limited by tunneling between NCs and thus to be strongly dependent on the inter-NC spacing.<sup>4,9,10</sup> Treatment with butylamine has been shown to enhance photoconductivity in CdSe NC films by decreasing interparticle spacing from  $\sim 1.1$  to  $\sim 0.2$  nm<sup>9</sup> (See Chapter 2). Similarly, we find that treatment with butylamine increases the room temperature dark conductance in CdTe NC films by more than three orders of magnitude (Figure 4.5), large enough for us to measure the differential conductance as a function of gate voltage. Figure 4.6 shows that the differential conductance at both positive and negative  $V_{ds}$  increases with increasing negative  $V_g$  and decreases with positive  $V_g$ . That we see no increase in differential conductance even at quite large positive  $V_g$  suggests that the electrons' contribution to the current is small. This indicates that holes are the majority carrier.

The low temperature dark current is also most likely carried by holes. Dark current is only present at positive drain bias and increases with the application of a negative gate bias (Figures 4.3 and 4.4), consistent with hole conduction in a FET. The observed hysteresis could be a result of charge build up at the injecting contact,<sup>12</sup> of trapping throughout the film, and/or of the opening and closing of conducting channels between the electrodes.<sup>15</sup> The room temperature dark current I-V curve is nearly symmetric and displays little hysteresis at room temperature [Figure 4.5(a)]. Since we have demonstrated that holes are the dominant carrier, we ascribe this symmetric  $V_{ds}$  dependence to the field dependence of the mobility of the holes, as well as that of their activation energy. This  $V_{ds}$  dependence will be discussed in detail in a section 4.4.5.

The temperature dependence of the dark current, after treatment with butylamine, suggests that the hole density is thermally activated (Figure 4.8). The zero-field activation energy (from the inset of Figure 4.8) is  $0.38 \pm 0.02$  eV. The 0.38 eV thermally activation energy of holes in CdTe NC films is close to the energy of an acceptor state in bulk CdTe located 0.3 eV above the valence band.<sup>16</sup> This acceptor state takes thermally excited electrons from the valence band, leaving holes behind. Thermal activation of electrons to this acceptor state is equivalent to the thermal activation of holes (Figure 4.14). Assuming 1 electron accepting state per NC (6 nm diameter) the density of states would be  $\sim 2 \times 10^{21}$  eV<sup>-1</sup>cm<sup>-1</sup>. It is likely there is more than one electron accepting state per NC, but this approximation will be used to determine if the measured temperature dependence of the dark current is consistent with the existence 0.38 eV thermally activated ‘hole-doping’ state. Using a Boltzmann distribution, at room temperature  $5 \times 10^{14}$  states would be occupied. This population drops to 0.01 at 77 K, consistent with the observed decrease in dark conductance as the temperature is lowered.

The origin of the acceptor state in bulk CdTe is attributed to cadmium vacancies in the lattice. The surface of a CdTe NC contains tellurium atoms, many of which may be unpassivated. It is possible that unpassivated tellurium atoms, i.e. cadmium vacancies on the surface, or additional cadmium vacancies in the lattice are responsible for the state 0.38 eV above the valence band in the CdTe NC film. There is also evidence that an oxidized form of Te may be the acceptor state. The dark current increases with exposure to air [Figure 4.12(a) and (c)], and XPS data [Figure 4.13] shows a  $\text{TeO}_2$  or  $\text{CdTeO}_3$  peak forming with air exposure as well. The inset of Figure 4.12(a) demonstrates, only the magnitude, and not the electric field dependence of the dark current varies significantly with oxygen exposure. In other words, oxidation results in a higher hole carrier density but does not change the conduction mechanism. The CdTe NCs are kept under argon during synthesis, transferred to a nitrogen glove box for processing, and measured under vacuum in a cryostat loaded in the glovebox. However, none of these processes are fully oxygen free, and it is possible that some percentage of the surface tellurium atoms have been oxidized. Prolonged air exposure would create more Te-O sites and thus a larger hole density. Alternately, Te-O could be adding another acceptor state closer to the valence band, resulting in the thermal activation of more electrons. The dependence of the activation energy on oxidation is currently under investigation and will determine which of the two models accurately describes the mechanism for formation of the electron accepting state.

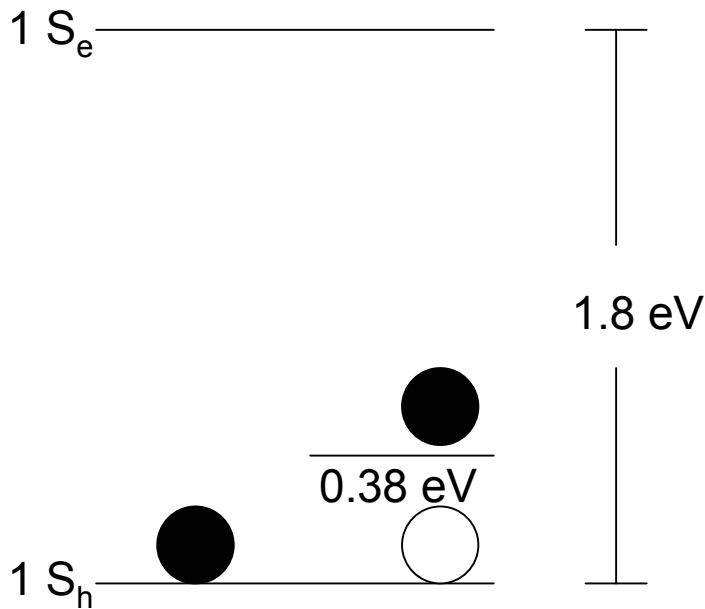


**Figure 4.14:** Energy level diagram for a CdTe NC with an acceptor state 0.38 eV from the valence band. At room temperature this state can be populated with electrons (black circles) thermally excited from the valence band, leaving holes behind (white circles). As the temperature decreases, the number of electrons in the acceptor state (and thus the hole density) decreases as well.

#### 4.4.2 Secondary Photocurrent due to “Non-Blocking” Contact between CdTe NCs and Gold Electrodes

As discussed in Chapters 2 and 3, the photocurrent in CdSe NC films after chemical treatment displays saturation with applied field when every photogenerated carrier reaches an electrode before recombining. The photoconductive gain is found to be equal to unity for this system, indicating that the gold electrodes form blocking contacts with the CdSe NC film. The current for these films is found to saturate at lower applied voltages at 87 K than at room temperature because the exciton lives longer at lower T, and the probability of ionization at a given field is larger. This higher ionization probability also explains why the photocurrent in CdSe NC films is larger at low T than high T.

Before treatment with butylamine, the photocurrent in CdTe NC films [Figure 9(a)] increases with decreasing T, as well. However, after treatment the photocurrent at 295 K is *higher* than the photocurrent at 87 K [Figure 9(b)]. Furthermore, saturation is not observed at either temperature. At the fields used, it is unlikely that the current is limited by field ionization of the exciton. In addition, the magnitude of the current is higher than expected for a photoconductive gain of unity. We infer that the photocurrent in CdTe NC films is a secondary photocurrent, rather than a primary photocurrent as observed in CdSe NC films.

Secondary photocurrents occur when the contacts can inject electrons, holes, or both carriers.<sup>16</sup> The dark current in CdTe NC films is carried by holes, as discussed above, and these holes must be replenished from the gold electrodes to maintain a steady-state current. Assuming that both carriers are mobile, but that only the hole is replenished at the electrodes, the gain does not saturate at unity. Holes contribute to the current until the electron reaches the electrode, or recombines with a hole. A schematic for the mechanism of secondary photocurrent is given in Figure 4.15.

To calculate the photoconductive gain in the scenario where the electron reaches the gold electrode, the lifetime of the hole is set equal to the lifetime of the electron. At high fields the electron reaches the electrode and the lifetimes of both the electron and the hole equal the transit time of the electron.

$$\tau_p = \tau_n = t_n = \frac{L^2}{\mu_n V} \quad , \quad (4.2)$$

where  $\tau_p$  is the hole lifetime,  $\tau_n$  is the electron lifetime,  $t_n$  is the transit time of the electron,  $L$  is the width of the gap,  $\mu_n$  is the electron mobility, and  $V$  is the applied voltage. The photoconductive gain,  $G$ , becomes a linear function of the mobility ratio of the two carriers:<sup>16</sup>

$$G = \left( \frac{\mu_p}{\mu_n} \right) \quad (4.3)$$

(By inserting Equation 4.2 into the expression for G, p.36, and assuming  $\mu_p \gg \mu_n$ , Equation 4.3 can be derived.) Therefore, the gain is expected to be greater than unity if the mobility of the hole is greater than that of the electron. In the second scenario, where the electron and hole recombine before the electron reaches an electrode, the photoconductive gain is again a function of the hole mobility. In this case the hole lifetime equals the electron lifetime (bimolecular recombination time) and the gain is a function of the sum of mobility of the hole and electron and their recombination time.

$$G = \frac{(\mu_n + \mu_p) \cdot \tau \cdot V}{L^2} \quad (4.4)$$

If  $\mu_p > \mu_n$  then

$$G = \frac{\mu_p \cdot \tau \cdot V}{L^2} . \quad (4.5)$$

We do not observe saturation of the photocurrent and so Equation 4.5 best describes the CdTe NC system. Given the excitation intensity, sample area, optical absorption of the film, exciton separation efficiency (assumed to be 1) and a gain of unity, we estimate the maximum primary photocurrent expected in the CdTe NC film to be approximately 40 nA. The current at 100 V and room temperature is 440 nA, resulting in a photoconductive gain of about 10. Were the electron more mobile than the hole, as it is in bulk CdTe,<sup>17</sup> the gain would be less than unity. Thus, the hole has a higher mobility than the electron in the CdTe NC film, and holes effectively cycle through the circuit for a time equal to the recombination time. At 100 V, 10 holes enter and exit the film before recombining with the photogenerated electron and thus travel an effective distance of  $\sim 10^{-3}$  cm. The recombination lifetime is faster than the resolution of our

current amplifier at room temperature, giving an upper bound on  $\tau$  of 10  $\mu\text{s}$ . From this information, we find a lower limit on the hole mobility of  $\sim 10^{-4} \text{ cm}^2/\text{Vs}$  at 100 V.

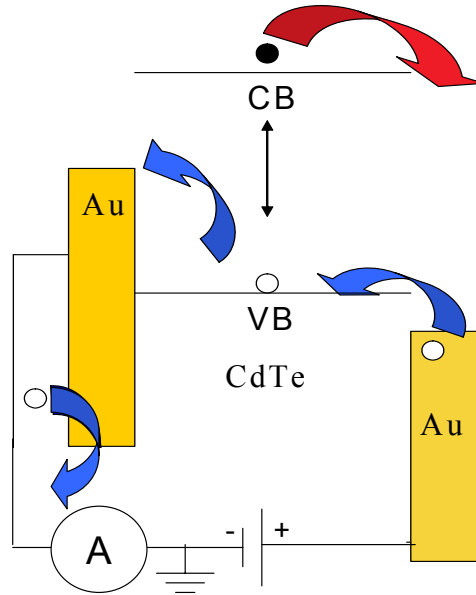


**Figure 4.15:** Schematic displaying the mechanism for secondary photocurrent. Provided the hole can be replenished from gold electrodes and the hole mobility is greater than the mobility of the electron, the hole will cycle through the circuit many times until it recombines with an electron or the electron is extracted at the electrode.

#### 4.4.3 Carrier Recombination

The photoexcitation intensity dependence of the photocurrent (Figure 4.10), fit using the procedure outlined by Jarosz et al., provides information about the recombination mechanism.<sup>8,16</sup> Photogenerated holes, of density  $n$ , can either recombine with the equal density of photogenerated electrons, or with the pre-existing trapped electrons, of density  $N_t$ :

$$F = (N_t + n)nb \quad (4.6)$$

where  $F$  is the carrier photogeneration rate, proportional to photoexcitation intensity, and  $b$  is the bimolecular recombination coefficient. If  $N_t$  is much larger than  $n$  the current is linear in

photoexcitation intensity. However, if  $n$  is larger than  $N_t$ , the current is proportional to the square root of the photoexcitation intensity. Fitting Equation 4.6 to the data at low temperature in Figure 4.10 we find  $\frac{n}{N_t} = 1.34$ , indicating that holes recombine with both free and trapped electrons, approximately equally. At 295 K, the fit is poor because  $\frac{n}{N_t}$  is so large. When the data is instead fit to a power law, as designated by the dotted line in Figure 4.10, the exponent is 0.5, as expected for bimolecular recombination.

When recombination involves both photogenerated and trapped carriers, the current decay from steady state after photoexcitation is removed is predicted to follow

$$\frac{n}{n_o} = \frac{\exp(-N_t b t)}{1 + \frac{n_o b}{N_t b} (1 - \exp(-N_t b t))} \quad (4.7)$$

where  $n_o$  is initial carrier density, and  $t$  is the time after removal of photo-excitation.<sup>16</sup> We fit the low temperature data in Figure 4.11 with Equation 4.7, as well as the bimolecular form, obtained by taking the limit of  $N_t b \rightarrow 0$ . Equation 4.7 is a better fit, confirming that recombination of holes with trapped electrons is significant at low temperatures. From the fit  $\tau = (N_t b)^{-1} = 340 \mu\text{s}$  and  $(n_o b)^{-1} = 55 \mu\text{s}$ . Most of the room temperature photocurrent decay is faster than the 10  $\mu\text{s}$  rise time of the current amplifier. Though the decay could not be fit with the bimolecular form of Equation 4.7, an increase in the decay rate supports the concept that trapping plays a smaller role as the temperature increases. At room temperature, the thermally activated population of holes will eliminate any deeply trapped electron population in the film. As the temperature is lowered, the hole density decreases and there will be a larger number of trapped electrons to recombine with photogenerated holes. This explains the observed



bimolecular recombination, transition to a  $n/N_t$  of 1.34, and why the photogenerated hole density is lower at 77 K.

#### 4.4.4 Physical Mechanism Behind the Photoconductive Gain and Decay

It is inferred from the photoconductivity measurements that the mobility of the hole is larger than the mobility of the electron in CdTe NC films. This is surprising as in bulk CdTe the effective mass of the hole is  $0.63 m_0$ , larger than the  $0.11 m_0$  of the electron.<sup>17</sup> However, as is the case for most of the physical properties of semiconductor nanocrystals, the surface of the NC can explain the deviation of this property from bulk behavior. In Figure 4.14, a schematic is shown for the energy diagram of CdTe containing an electron acceptor state at 0.38 eV. When electrons are thermally excited from the valence band, the state behaves as a doping state, increasing the hole density. However, when the state accepts electrons from the conduction band, it acts as a deep trapping state. This state is 1.4 eV from the conduction band so it is unlikely that electrons can be thermally excited back to the conduction band. The electron remains in this state until it recombines with a hole, and so the state could also be thought of as a recombination center with a minor affinity for holes. Supporting this mechanism is our observation that the fluorescence of CdTe NCs quenches upon air exposure, and that this fluorescence quenching is correlated with the formation of Te-O on the surface of the nanocrystal.<sup>13</sup> In addition, the increase in the photocurrent with extended exposure to air also supports the mechanism [Figure 4.12(b) and (c)]. The photocurrent increases at nearly the same rate as the dark current during air exposure suggesting the same oxidation process is responsible for the increase in both types of current. The more (or deeper) the trap states, the more times the hole can cycle through the circuit before it recombines with the electron, and hence the larger the magnitude of the photocurrent.

#### 4.4.5 Phenomenological Model for Conductance

The transient dark current in films of annealed CdSe has a voltage dependence at fixed time that is well described by the following phenomenological expression:<sup>14</sup>

$$\Delta I \approx \frac{V_{ds}}{R_o} \exp\left(\frac{|V_{ds}|}{V_o}\right) \quad (4.8)$$

Here  $R_o$  is a characteristic resistance and  $V_o$  is a characteristic voltage. We fit (Figure 4.15) the photocurrent data to Equation 4.8 and find good agreement with  $V_o = 29$  V for both 87 K and 295 K. This corresponds to an energy difference from one NC to its neighbor of  $\sim 175$  meV (determined by dividing  $V_o$  by the number of NCs which fit across 1  $\mu\text{m}$ ), similar to the value found in annealed CdSe NC films.<sup>14</sup>  $R_o$  at 87 K is  $1.2 \cdot 10^{11} \Omega$  and  $R_o$  at 295 K is  $7.2 \cdot 10^9 \Omega$ . The temperature dependence of  $R_o$  is consistent with the increased importance of monomolecular recombination at low T. The observation that this simple phenomenological model describes the voltage dependence of the photocurrent, with the same value of  $V_o$  at low, and high T, is very important. As discussed above, the fields are high enough that all excitons are ionized. Therefore, the voltage dependence of Equation 4.8 comes from that of the mobility. The field dependence of the mobility of the holes is well described by

$$\mu \propto \exp\left(\frac{|\mathcal{E}|}{\mathcal{E}_o}\right) \quad (4.9)$$

where  $\mathcal{E}_o$  is a characteristic electric field. However, as in the case of CdSe NC films, the field scale  $\mathcal{E}_o$  is too small to be explained by a simple tunneling model and its definition remains undefined.<sup>14</sup>

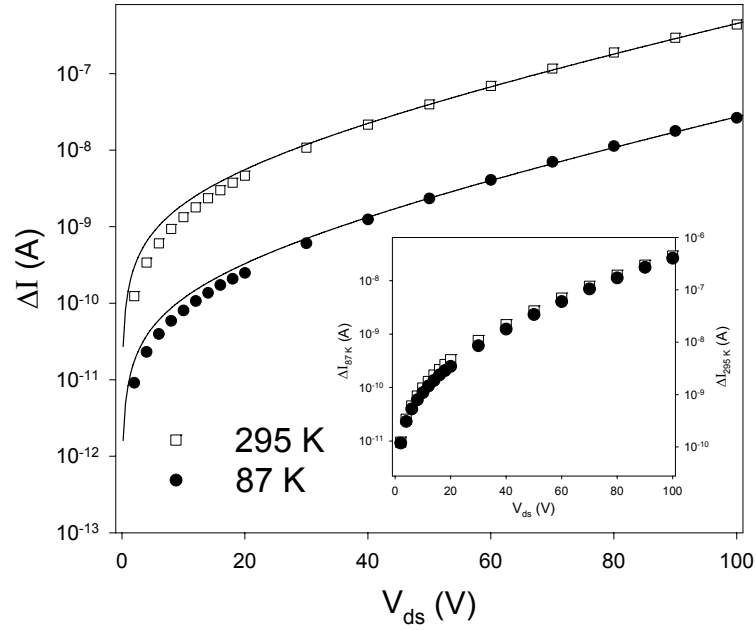


**Figure 4.16:** A semi-logarithmic plot of the photocurrent,  $\Delta I$ , versus  $V_{ds}$  with  $V_g=0$  at 295 K (open circles) and 87 K (closed circles). The solid lines are fits to Equation 4.8. The data are scaled in the inset to show that the field dependence is independent of temperature.

This inspires us to describe the steady-state dark current in the same way: As discussed above, the holes are thermally generated with an activation energy that decreases linearly with voltage (see Figure 4.8). Assuming that the holes, once released from traps, have the field-dependent mobility described by Equation 4.9, we predict that the dark current will be

$$I = \frac{V_{ds}}{R_o} \exp\left(\frac{|V_{ds}|}{V_o} + \frac{a|V_{ds}| - \Delta E_0}{kT}\right) \quad (4.10)$$

where  $\Delta E_0$  is the zero-field activation energy,  $k$  is Boltzmann's constant, and  $a=l/L$  (see Equation 4.1). In Figure 4.17 we use this form to fit the  $I$ - $V_{ds}$  curves at each temperature. We set  $V_o = 29$  V from the photocurrent data and then fit the data at 150 K and 280 K to Equation 4.10 by adjusting  $R_o$  and  $\Delta E_0$ , until both data sets are fit by varying only the temperature. For the best fit  $R_o = 5 \cdot 10^6 \Omega$ ,  $a = 1.5 \cdot 10^{-3}$ , and  $\Delta E_0 = 0.34 \pm 0.02$  eV.  $\Delta E_0$  is close to the value  $0.38 \pm 0.02$  eV value determined from the inset of Figure 4.8.  $R_o$ ,  $a$ ,  $\Delta E_0$ , and  $V_o$  are all held constant in the fits at 240, 200, and 170 K. The agreement of this phenomenological expression with the data is remarkable.

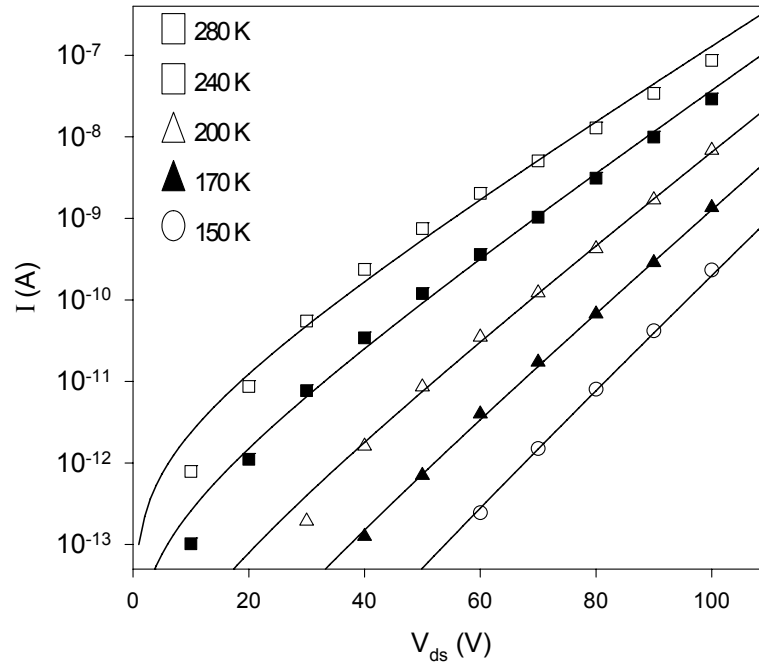


**Figure 4.17:** Dark current,  $I$ , versus  $V_{ds}$  at various temperatures with  $V_g = 0$ . The solid lines are fits as described in the text.

## 4.5 Conclusions

Our studies of the transport properties of CdTe NC films in FET structures lead to the following conclusions which are generally true for CdTe NC films contacting gold electrodes:

- The current is carried by holes, both in the dark and under photoexcitation.
- The secondary photocurrent measured in the CdTe NC films, made possible by the non-blocking gold electrodes, gives a gain greater than unity, showing that holes have a higher mobility than electrons.
- An electron accepting state on the surface of CdTe NCs is responsible for p-type dark current as it accepts thermally excited electrons from the valence band, leaving holes behind. This same state may also be responsible for exciton separation by accepting electrons from the conduction band. These electrons remain trapped in this state until they recombine with a hole, offering an explanation for why the hole mobility is larger than the electron mobility in CdTe NC films.
- The voltage dependence of the photocurrent is temperature independent and leads to a simple phenomenological description of the voltage dependence of the hole mobility.
- The dark current is thermally activated with an energy that decreases linearly with voltage. The voltage dependence of the mobility, extracted from the photocurrent, is the same as that of the dark current.

## 4.6 References

1. P. T. Snee, Y. Chan, D. G. Nocera and M. G. Bawendi, *Advanced Materials* **17**, 1131 (2005).
2. L. Manna, E. C. Scher and A. P. Alivisatos, *Journal of Cluster Science* **13**, 521 (2002).
3. W. W. Yu, Y. A. Wang and X. G. Peng, *Chemistry of Materials* **15**, 4300 (2003).
4. C. A. Leatherdale, C. R. Kagan, N. Y. Morgan, S. A. Empedocles, M. A. Kastner and M. G. Bawendi, *Physical Review B* **62**, 2669 (2000).
5. C. B. Murray, D. J. Norris and M. G. Bawendi, *Journal of the American Chemical Society* **115**, 8706 (1993).
6. C. B. Murray, C. R. Kagan and M. G. Bawendi, *Science* **270**, 1335 (1995).
7. C. B. Murray, C. R. Kagan and M. G. Bawendi, *Annual Review of Materials Science* **30**, 545 (2000).
8. M. V. Jarosz, N. E. Stott, M. Drndic, N. Y. Morgan, M. A. Kastner and M. G. Bawendi, *Journal of Physical Chemistry B* **107**, 12585 (2003).
9. M. V. Jarosz, V. J. Porter, B. R. Fisher, M. A. Kastner and M. G. Bawendi, *Physical Review B* **70**, 195327 (2004).
10. C. Kagan, Ph.D. Thesis, Massachusetts Institute of Technology, 1996
11. C. R. Kagan, C. B. Murray, M. Nirmal and M. G. Bawendi, *Physical Review Letters* **76**, 1517 (1996).
12. N. Y. Morgan, C. A. Leatherdale, M. Drndic, M. V. Jarosz, M. A. Kastner and M. Bawendi, *Physical Review B* **66**, 075339 (2002).
13. A. Lobo, H. Borchert, D. V. Talapin, H. Weller and T. Moller, *Colloids and Surfaces a-Physicochemical and Engineering Aspects* **286**, 1 (2006).
14. M. Drndic, M. V. Jarosz, N. Y. Morgan, M. A. Kastner and M. G. Bawendi, *Journal of Applied Physics* **92**, 7498 (2002).
15. D. S. Novikov, M. Drndic, L. S. Levitov, M. A. Kastner, M. V. Jarosz and M. G. Bawendi, *Phys. Rev. B* **72**, 075309 (2005).
16. R. H. Bube, *Photoconductivity of Solids*. 1960, New York: Wiley.
17. H. Landolt and R. Bornestein, *Numerical Data and Functional Relationships in Science and Technology*. 1961, Berlin: Springer-Verlag.

## Chapter 5

### Designer CdSe/CdTe NC Solids for Photovoltaic Devices

#### 5.1 Introduction

There is considerable interest in colloidal semiconductor nanocrystals (NCs) as an active material for the next generation of solar cells. Clear potential advantages of colloidal NCs are that they can be deposited on any surface and the band gap of a NC can be tuned by changing the size of the NC.<sup>1,2</sup> Because of these advantages, NCs are an ideal material for tandem solar cells. Incorporating NCs of different sizes into a tandem solar cell may boost solar cell efficiency by decreasing energy loss due to thermal relaxation to the band edge. In addition, recent experiments suggest that it may be possible to generate multiple excitons per photon in a single NC which could also increase efficiency.<sup>3-13</sup> However, with the advantages of NCs come some serious challenges because the organic ligands, which allow for the solution processing of the NCs, inhibit exciton separation and decrease the mobility in close-packed NC films.<sup>14-19</sup> The large surface to volume ratio of the NC also results in more unpassivated surface atoms, which may serve as trap states, than would be present in a bulk semiconductor film. The more trap states, the lower the charge carrier mobility, and the greater the probability for bimolecular recombination in the bulk of the film, rather than extraction at the electrodes.<sup>20</sup> Reported efficiencies of NC/polymer hybrid solar cells have not exceeded 2.8%.<sup>21</sup> CdSe/CdTe heterojunction solar cells with 2.9% efficiency processed from NCs have been reported, but this efficiency is not achieved until the NCs are sintered together, burning away all of the organic



ligands in the process.<sup>22</sup> Furthermore, 2.9% is still a very low efficiency when compared to the reported 16.5% efficiency of CdTe/CdS bulk heterojunction solar cells<sup>23</sup> and 13.6% for bulk CdTe solar cells on flexible substrates.<sup>24</sup>

While spinning NCs from solution and then sintering may constitute an alternative route to bulk semiconductor films, many of the particular potential advantages offered by NCs are lost in the process. The absorbance threshold shifts to the semiconductor band edge after sintering, and so the advantage of having a tunable band gap is gone. In addition, the observation of enhanced multi-carrier generation in NCs, as opposed to in bulk semiconductors, is believed to be due to the discrete states of the NC.<sup>12</sup> In order to increase the efficiency of NC solar cells, the physics of charge transport through NC films needs to be well characterized so that methods can be developed to improve the extraction of charge from NC films without destroying the quantum effects.

In this chapter, the photoconductivity in films composed of both CdSe and CdTe NCs, and CdSe/CdTe nanobarbells (NBs) is investigated. These two semiconductor materials form a Type II heterojunction, in which the band offset of the two materials separate excitons at the materials' interface resulting in electrons in the CdSe and holes in the CdTe. Infrared emission from Type II core/shell CdTe/CdSe NCs indicates that recombination occurs between electrons in CdSe and holes in CdTe and this demonstrates that the type II effect is present in NC materials.<sup>25</sup> In this study, CdTe and CdSe NCs are mixed together to create numerous charge separation interfaces throughout the film. If charge transport proceeds via electrons through CdSe and holes through CdTe, carrier recombination in the film may also be reduced. Also, the band gap of CdTe NCs can be tuned from 1.5 to 2.1 eV,<sup>2</sup> covering most of the range of the peak emission power of the solar spectrum.<sup>26</sup> However, we find that trap states on the surface of the

nanoparticles significantly reduce photovoltaic device efficiency; therefore, the Type-II effect cannot be utilized. Specifically the electron acceptor state on the surface of CdTe NCs (presented in Chapter 4) is found to trap electrons in layered thin film NC photovoltaic devices. In this chapter a detailed characterization of the electrical consequences of this surface state is presented along with synthetic methods, including ligand cap exchange and passivation with an inorganic shell, which are employed in an attempt to eliminate this surface state. Unfortunately, none of these methods improved device efficiency. CdSe/CdTe NC films provide an example of how methods used in the construction of bulk semiconductor devices do not directly transfer to the design of NC based devices.

## 5.2 Experimental

### 5.2.1 CdSe and CdTe NC Synthesis<sup>27,28</sup>

In general, 1 mmol of cadmium 2, 4-pentanedionate (98%), 2 mmol of 1, 2-hexadecanediol, and tri-*n*-octylphosphine (TOP) is degassed for 1 hour at 100 °C. This solution is cooled under argon, and 3 mmol of 1.5 M tri-*n*-octylphosphine selenide (TOPSe) or 1.5 M tri-*n*-butylphosphine telluride (TBPTe) is added. The chalcogenide donating precursor is the only difference between the syntheses of the two materials. The mixture is then loaded into a syringe and injected into a 360 °C solvent solution consisting of 99% tri-*n*-octylphosphine oxide (TOPO), 90% hexadecylamine (HDA), and *n*-hexylphosphonic acid (HPA). The NCs are grown for 5-10 min at 260 °C and then cooled to room temperature. Hexane is added to the room temperature growth solution and then it is transferred to the glovebox for storage. The CdTe NCs used in this study have a 6 nm diameter and the CdSe NCs have a 4.9 nm diameter.

### 5.2.2 CdSe/CdTe Nanobarbell (NB) Synthesis<sup>29</sup>

CdSe nanorods (NRs) are prepared by heating cadmium oxide (CdO), octadecylphosphonic acid (ODPA) and TOPO to 300°C in a 3-neck flask until the solution is clear. A solution of degassed toluene, TOP, and TOPSe is injected at 320 °C, and NRs are grown at 260 °C for 15 min. The rods are then precipitated twice from solution by adding methanol/butanol, centrifuging the solution at 3900 RPM, and redispersing in hexane. After the second precipitation, rods are dispersed in hexane, a few drops of octylamine are added, and the solution is allowed to sit for several days until there is a significant increase in quantum yield. Rods were then precipitated as above, dispersed in hexane, and filtered.

To create CdSe/CdTe NBs, a mixture of TOPO, HDA and HPA is first degassed at 140 °C and cooled to 80 °C. Rods dispersed in hexane are added to the pot and the hexane is pulled off under vacuum. Meanwhile, a solution of cadmium 2,4-pentadionate, 1,2-hexadecanediol, and TOP is degassed at 110°C in a separate flask. After degassing, the solution is cooled and TBPTe is added to cadmium solution. The resulting mixture is added dropwise to the pot at 260 °C. The total reaction time after the start of the addition of the precursor solution did not exceed 15 minutes. The CdSe/CdTe NB solution is cooled and the NBs are then immediately precipitated by the addition of toluene to remove excess CdTe NCs from the NB solution. (The NBs are only soluble in chloroform.) CdSe/CdTe NBs appear to be light sensitive and fall out of solution if stored for several days in light. However, they are stable for months when stored in chloroform, in the dark, and in an inert atmosphere. The CdSe NRs are about 20-25 nm in length and 5 nm in diameter and the CdTe NC at the end of each rod is 5.5-6 nm in diameter. A TEM image of these NBs, their optical spectra, and electron energy loss data providing information about the NB chemical composition are presented in Figure 5.1.

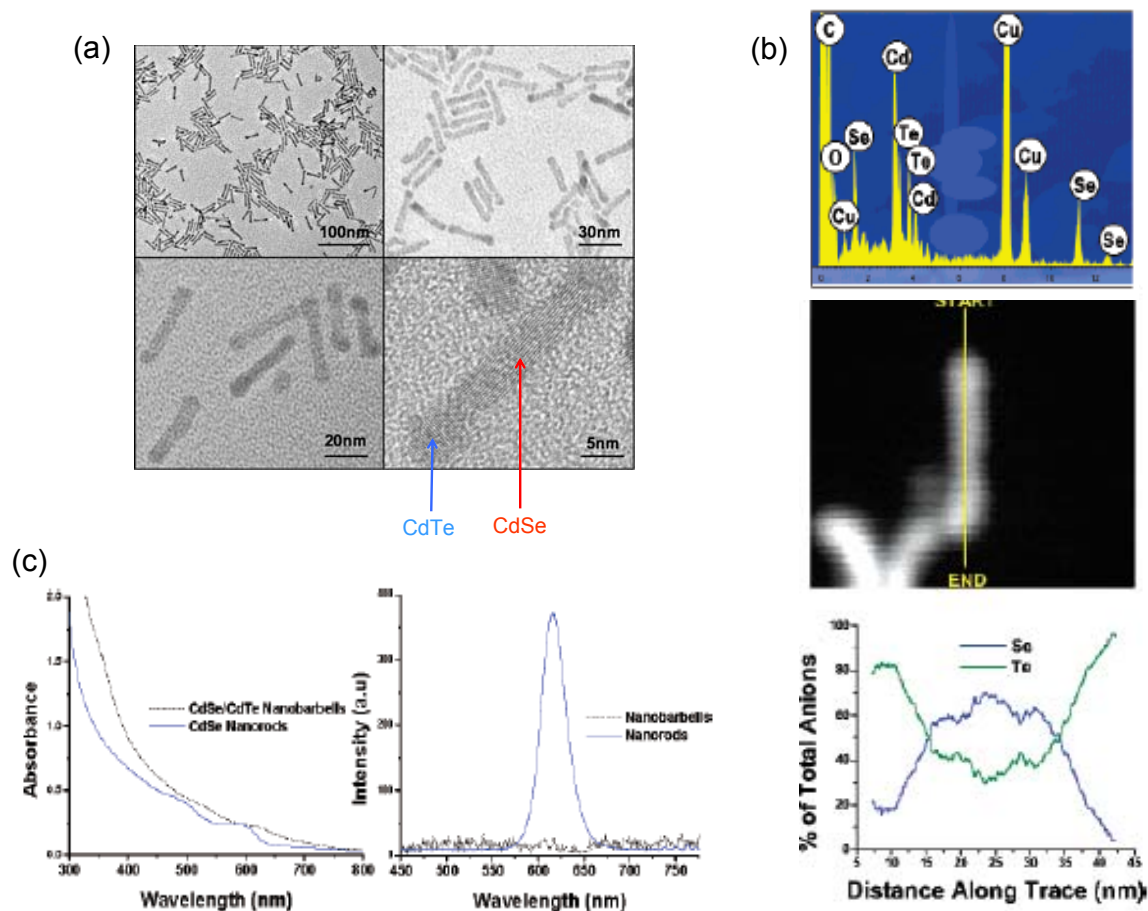


**Figure 5.1:** (a) Transmission electron microscope images taken on a JEOL 200 TEM and expanded (top) and JEOL 2010 HR-TEM (bottom) showing CdSe/CdTe NBs. HR-TEM images show that the CdTe dots are neither wurtzite nor oriented along the  $c$ -axis of the rod. (b) Electron energy loss data from a scanning transmission electron microscope (STEM) trace of a single CdSe/CdTe nanobarbell. The anion ratio at each point along the length of the NB is assessed. These results demonstrate Te is concentrated on the tips of the NB and Se is located along the center of the rod. (c) The absorption (left) and emission (right) spectra of a sample of nanorods before and after the addition of CdTe tips. The images in Figure 5.1 are reproduced with permission from J. Am. Chem. Soc., © 2006, American Chemical Society.<sup>29</sup>

### 5.2.3 Film Preparation

CdTe and CdSe NC growth solutions are processed under nitrogen using previously reported methods to make close-packed films of NCs.<sup>1,16-19,30,31,33</sup> First the sample is centrifuged and the supernatant saved. The precipitate consisting of TOPO and other salts is discarded.

Next the NC solutions are precipitated by adding methanol and spinning at 3900 rpm in the centrifuge. The supernatant is discarded and the NC precipitate is dissolved in hexane and butanol. This solution is then filtered through a 0.2  $\mu\text{m}$  filter. The precipitation process is repeated two more times using 0.1 and 0.02  $\mu\text{m}$  filters.

Two measurement devices are used in this study. The planar device [Figure 5.2(a)] is a silicon inverted field effect transistor (FET) like the ones used in previous chapters. The FETs are fabricated by lithographically patterning gold bar electrodes 200 X 800 X 0.1  $\mu\text{m}^3$  on 330 nm of silicon oxide. The electrodes are spaced by 1 or 2  $\mu\text{m}$ . To deposit NC films on the planar devices the NCs are dissolved in a mixture of 9:1 hexane:octane and the solution is then drop cast onto the measurement device.

For the second device structure (layered NC films) [Figure 5.2(b)], poly(3,4-ethylenedioxythiophene) poly(styrenesulfonate), PEDOT:PSS, is spun from water onto a layer of indium tin oxide (ITO) on glass and then baked at 100  $^{\circ}\text{C}$  for 30 min to cross-link the polymer. PEDOT:PSS is a hole-conducting polymer which has been shown to smooth the surface of ITO (See Appendix A). NC layers, each  $\sim$  25 nm thick, are then spun from chloroform onto the PEDOT:PSS. It has been shown that films spun from chloroform have fewer pinholes and better overall morphology than solutions spun from hexane.<sup>33</sup> Each layer is soaked in a 0.1 M butylamine in acetonitrile solution and baked at 70  $^{\circ}\text{C}$  for 1 hr in order to decrease interparticle spacing and make the films less susceptible to dissolving when the next layer is deposited. The top contact consisting of a eutectic gallium indium solder (EGaIn) wets the surface of the NC film and is contacted with a tungsten wire. The area of the EGaIn electrode is defined by a donut shaped stamp composed of a flexible polymer, cured poly(dimethylsiloxane), PDMS. A detailed investigation of properties of the EGaIn electrode is provided in Appendix A.

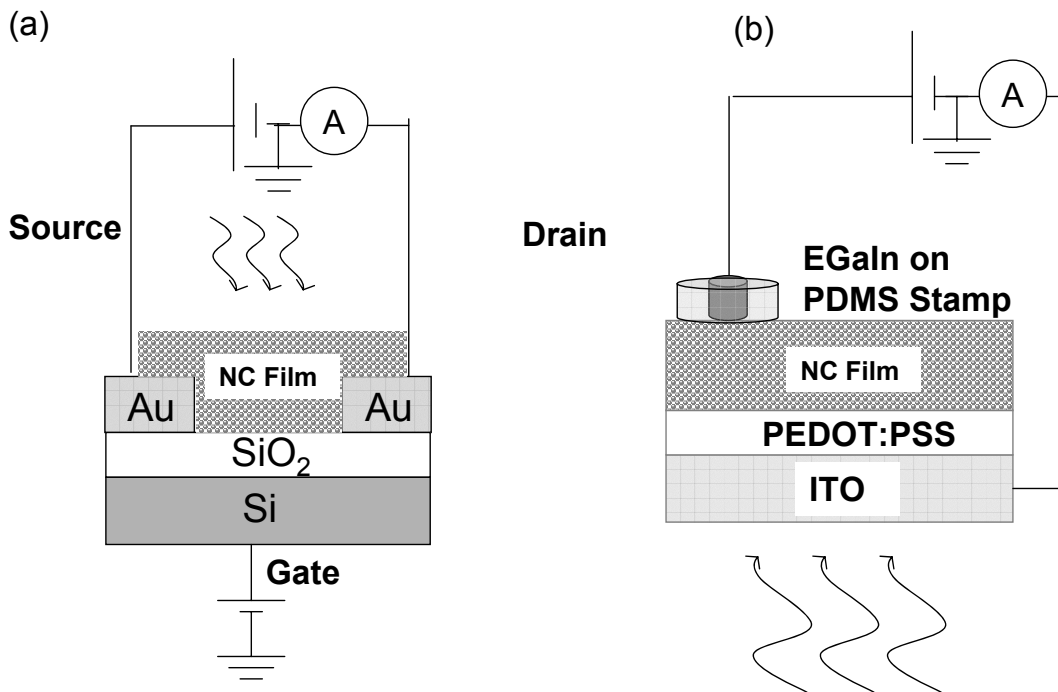


**Figure 5.2:** Schematic of the devices used in the experiments. (a) Planar device structure consisting of gold electrodes 200 X 800 X 0.1  $\mu\text{m}$  patterned on 330 nm of silicon oxide on a silicon back gate or quartz (not shown). The electrodes are spaced by 1 or 2  $\mu\text{m}$ . The NC film, typically 100 – 200 nm, thick is drop cast or spun onto the device and covers the entire surface of the device. (b) Sandwich device structure used in the photovoltaic study. 20 nm of PEDOT:PSS is deposited on ITO covered glass. NC layers, each  $\sim 25$  nm thick, are spun on top of the PEDOT:PSS. The top contact is a eutectic gallium indium solder (EGaIn) which is set in a thin PDMS donut (3.5 mm O.D., 1.5 mm I.D.). The EGaIn settles in the area defined by the PDMS donut and forms a conformal contact with the NC film. The EGaIn is contacted with a Pt wire and the ITO with a metal pin. Photoexcitation occurs through the ITO face of the device.

CdSe/CdTe NBs are not soluble in hexane, and so are dissolved in chloroform after each precipitation. As chloroform does not form smooth films via drop casting, NB films are spun onto both planar and sandwich device structures. To make mixed films of CdSe and CdTe NCs the concentration of each solution is calculated using molar absorptivity values calculated empirically.<sup>34</sup> After taking into account the volume of the CdTe and CdSe NCs, the appropriate amounts of each solution is mixed to give the desired ratio by volume of CdTe to CdSe in the film.

Film treatments employed in this paper are post-deposition cap exchange into butylamine<sup>16</sup> and thermal annealing.<sup>15</sup> For the butylamine cap exchange, the NC film is soaked in a 0.1 M solution of butylamine in acetonitrile for 2 min. The film is then rinsed in acetonitrile and baked in a nitrogen environment for 1 hr to remove excess solvent. For the thermal annealing treatment, films are heated to the desired temperature in a vacuum oven (12 mTorr) for 30 min.

### **5.2.4 R-Cadmium Cap Exchange**

CdTe NCs are precipitated three times following normal procedures for making optically clear close-packed films in an inert atmosphere. Anhydrous solvents are used for the precipitation. To a 1 mL solution of CdTe in hexane ~ 20  $\mu$ L of a 0.4 M cadmium oleate solution is added. After addition of the cadmium oleate, the solution is allowed to sit and brighten for a few hours before use. The solution appears brighter immediately upon cadmium oleate addition and the fluorescence increases over time (Table 1). To prepare the cadmium oleate solution, 1 mmol of cadmium 2,4-pentadionate in 8 mmol of oleic acid is degassed at 100 °C for about an hour. The temperature of the cadmium oleate solution is held above 60 °C to prevent solidification before addition to the CdTe NC solution. The cadmium oleate solution can be stored as a solid in an inert atmosphere and warmed up for use in future experiments.

While addition of the above cadmium oleate solution to the CdTe NC solution resulted in the greatest enhancement of CdTe NC fluorescence, other cadmium ligand complexes improved the fluorescence as well. Table 5.1 lists the composition of the solution and the resulting QY of the CdTe NC solution. All solutions are prepared by degassing 1 mmol cadmium 2,4-pentadionate with the listed chemical reagents at 100 °C. Approximately ~20  $\mu$ L of each

cadmium solution was added to 1 mL of CdTe NCs in hexane. The concentration of the CdTe NC solution is the same for all samples.

A solution consisting of 1 mmol of cadmium 2,4-pentadionate, 2 mmol of oleic acid, and 1 mL (1 M cadmium oleate) does brighten CdTe NCs as well; however, this batch of CdTe cores was processed in air and the cadmium oleate solution added in air. (Anhydrous solvents were still used in the NC precipitation). Results cannot be directly compared to other batches of CdTe cores as when the CdTe NC core emission is <1% QY it is difficult to determine the degree to which the NC surface of the core is degraded before addition of the ligand. Most likely, the NC surface is oxidized to a greater degree when the cores are processed in air. This is consistent with the observation that when bench top, non-anhydrous, solvents were used to precipitate the CdTe NCs the addition of 0.4 M cadmium oleate solution did not enhance the fluorescence. A potential model for this system is that CdTe NCs precipitated in an inert atmosphere have many unpassivated Te atoms on the surface that serve as non-radiative pathways for exciton decay. When the cadmium ligands are added they passivate the Te atoms and the QY increases. However, if the Te atoms have been oxidized, the cadmium ligand cannot bind to the Te and the exciton non-radiatively decays through coupling to a Te-O state. This hypothesis is consistent with the conductivity results discussed in Chapter 4.

NC films deposited from the CdTe NC solution after the addition of the cadmium ligand are cloudy as a result of excess oily ligand. To make optically clear films, the solution must be precipitated an additional time. Only the CdTe NC solutions to which cadmium oleate has been added retain the fluorescent enhancement after precipitation (Cd-TBP and Cd-TOP do not remain bright). In fact, the sample with 50% QY is for a solution to which the cadmium oleate had been added, precipitated, and left to sit in the glovebox for 1 month.



Cd source	Cores, crashed in N <sub>2</sub>	2 ml TBP, 2 mmol DDA	2 mL TOP, 2 mmol DDA	8 mmol oleic acid	8 mmol oleic acid, 1 month	Cores, crashed in air	Oleic acid	0.4 M Cd oleate in TOP
QY (%)	~0.1	31	29	23	50	~0.1	~0.1	5

**Table 5.1:** Quantum yield of CdTe NC solutions after the addition of a cadmium ligand complex. The first five samples (solid line) display the fluorescence quantum yield after the addition of the selected ligand to CdTe NCs which have been processed in an inert atmosphere. The next three samples (triple line) show the results for the addition of the stated reagent to a CdTe NC solution which has been processed in air.

### 5.2.5 Overcoating of CdTe NCs with ZnS

Methods for preparing high QY CdSe/ZnS (core/shell) particles from ZnEt<sub>2</sub> and (TMS)<sub>2</sub>S have been reported previously<sup>28,35,36</sup> and these methods are adapted in an attempt to grow ZnS shells on CdTe cores. In general, the CdTe NC growth solution is precipitated once with methanol and centrifuged. The supernatant is discarded, and the precipitate re-dissolved in 3 ml of hexane and filtered through a 0.2 μm filter. The processing of the CdTe NCs is done in the inert atmosphere of the glovebox. A flask with TOPO and hexaphosphonic acid is heated to 100 °C and degassed for one hour. The solution is cooled to 60 °C and CdTe cores in hexane are added. Hexane is pulled off under vacuum, and the solution is heated to 190 °C. Immediately upon reaching 190 °C, ZnEt<sub>2</sub> and (TMS)<sub>2</sub>S in a 1:1 molar ratio in TOP are added at one drop per minute over about 5 minutes.

### 5.2.6 Electrical Measurements

The planar FETs are attached to a 28-pin chip carrier and electrical contacts are made from the electrodes to the chip carrier by gold wire bonds. Devices are tested for leakage before film deposition by applying high voltage to the source, drain, and gate electrodes. Devices with leakage greater than 0.5 pA are discarded. All conductivity measurements on planar devices are performed in a Janis VPF-100 cryostat under vacuum. Samples are loaded into the cryostat in the glovebox and are never exposed to air. A Keithley 6517 electrometer is used to measure current,  $I$ , and apply voltage across the source and drain electrodes,  $V_{ds}$ . An Agilent 6614C DC power provides the gate voltage,  $V_g$ , is supplied. An Ar<sup>+</sup> laser at 514 nm is used to photoexcite the samples and it has been shown previously that photocurrent is not a result of photoinjection from the electrodes.<sup>17</sup>

The differential conductance measurements are carried out by applying a constant  $V_{ds}$ .  $V_g$  is stepped with a Keithley 2400 sourcemeter. A small AC voltage (13 Hz, 5V) is added to the drain electrode by a function generator. The resulting AC current is sent to a current amplifier (Ithaco 1211), then to a lock-in amplifier (Princeton Applied Research 5301A), and to a digital multimeter (Hewlett Packard 34401A). This technique is the same as used to measure differential conductance of CdTe NC films in Chapter 4.

The activation energy of the dark current in the CdSe/CdTe NB film is measured in the same manner as the activation energy of the dark current in CdTe NC films in Chapter 4. Current as a function of voltage is measured at 87, 110, 140, 170, 200, 230, 260, and 295 K and the temperature is monitored with a Lakeshore 330 temperature controller. The current at each voltage is plotted against temperature and each curve is fit with an Arrhenius equation. The

activation energy at a given voltage is extracted, and that value is plotted versus field to extract the zero field activation energy.

For the sandwich devices, the current is measured in air using the Keithley 6517 electrometer and voltage is supplied by a 7651 Yokogawa DC voltage source. The NCs are photoexcited with an Ar<sup>+</sup> laser at 514 nm for i-V curve measurements. The sample is held perpendicular to the incident light so that the light hits the ITO face and then the NC layer. The EGaIn electrode wets the NC film surface through a 1.5 mm radius hole cut in a thin piece of PDMS. Both the PDMS and EGaIn conformally contact the surface of the NCs and do not slide as the device is held perpendicular to the bench top surface. An image of this sample set up is provided in Appendix A. For photocurrent action spectra (PCA) measurements in which the photocurrent is measured as a function of the wavelength of the excitation light, the samples are photoexcited with a 150 W ozone free xenon arc lamp through a monochromator. To determine the external quantum efficiency a silicon photodiode, Thor Labs DET210, is used as a reference.

### **5.2.7 Optical Measurements**

The absorbance spectrum of the NCs films on glass slides is measured with a Cary 5000 UV-Visible-NIR Spectrometer. Fluorescence measurements are performed using a Horiba Jobin-Yvon Fluoromax-3 spectrometer. The QY of CdTe NCs is calculated using oxazine 720 as the reference dye. The QY of this dye at room temperature in ethanol is 60% and it is 63% in methanol.<sup>37</sup>

### **5.2.8 X-ray Photoelectron Spectroscopy (XPS)**

A Kratos AXIS Ultra Imaging X-ray Photoelectron Spectrometer with Delay Line Detector is employed for XPS measurements. The excitation energy for all spectra is 1487 eV and data is taken in 100 meV steps. CdTe NCs are deposited in the glovebox on a clean piece of polished n-doped silicon. Samples are removed and quickly taken to the XPS for the measurement to limit air exposure. The samples are measured again after storage in air for 3 weeks to observe the effects of oxidation on the composition of the film.

## **5.3 Results and Discussion**

In the following section the conduction mechanism in CdSe/CdTe nanobarbell (NB) films, as well as mixed films of CdTe and CdSe NCs, is compared to that of CdTe NC films. The physics of charge transport through these films is examined using planar devices consisting of NCs drop cast on gold electrodes. In addition, the potential of these materials in photovoltaic devices is studied using the sandwich device structure. Finally, synthetic methods are presented which modify the surface of the CdTe NCs, and the impact of these methods on the photovoltaic properties of the CdSe/CdTe NC films is explored.

### **5.3.1 Study of CdSe/CdTe NB Films and Mixed Films of CdTe and CdSe NCs Between Parallel Electrodes – Photoconductive Mode**

#### *CdTe and CdSe NC mixed films*

Films composed of CdTe and CdSe NCs should theoretically aid exciton separation as these two materials form a Type II junction. If the type II nature of the interface between the two

materials is indeed aiding in charge separation and extraction, films with a 1:1 ratio of CdTe to CdSe should exhibit the lowest resistance. Both secondary photocurrent in which one carrier can be injected from the electrodes and primary photocurrent should saturate when the electron and hole are both extracted from the film at the metal electrodes.<sup>38</sup> Therefore, the photocurrent in the 1:1 CdTe to CdSe film should saturate with electric field at a lower applied field than in pure CdSe NC films.

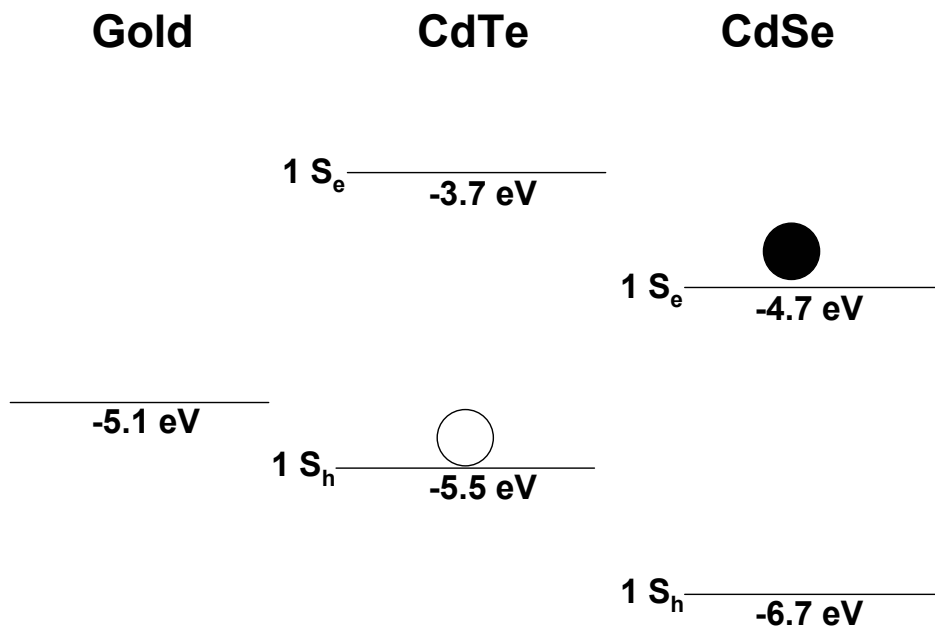


**Figure 5.3:** Energy levels relative to vacuum for the conduction ( $1 S_e$ ) and valence ( $1 S_h$ ) bands of CdTe NCs and CdSe NCs. The work function of gold is provided as a reference. The valence band levels are those for bulk CdTe and CdSe<sup>39</sup> and the conduction band value is determined by adding the band gap energy to the valence band value.

In Figure 5.4 it can be seen that the only film which exhibits saturation of photocurrent with field below  $7 \times 10^5 \text{ V/cm}$  is the film composed entirely of CdSe NCs (line a, Figure 5.4). All films consisting of a mixture of CdTe and CdSe NCs did not display a saturation of current at the fields applied in this experiment. (Film compositions are given in terms of the % by volume of CdTe in a CdSe NC film.) In 14% and 20% CdTe films (lines b and c respectively in Figure 5.4) it appears as though the photocurrent may potentially saturate at high fields, but definitely not at

a field lower than for the pure CdSe NC film. In general, the higher the ratio of CdTe NCs is in the film, the larger the magnitude of the photocurrent (Figure 5.4, inset). These results suggest that the electron trapping site on the surface of the CdTe NCs is affecting the flow of current. When the film is composed entirely of CdSe NCs, both the electron and hole can be extracted from the film; however, as the ratio of CdTe to CdSe increases more electrons become trapped and the photocurrent does not saturate. When the film is about 33% CdTe NCs (line d, Figure 5.4) the photocurrent vs. electric field curve closely resembles that of the 100% CdTe NC film (line i, Figure 5.4) indicating the conduction mechanism in both systems is the same. The larger the percentage of CdTe NCs in the film, the larger the magnitude of the photocurrent as there are fewer CdSe NCs to slow the conduction of holes. CdSe NCs could in principle conduct holes, but the valence band is located  $\sim 1.2$  eV below that of CdTe, and so extra energy must be supplied to conduct through the CdSe NCs. The minimum in conduction at 20% CdTe concentration is most likely a reflection of a percolation threshold in which CdTe NCs are spaced too far apart for hole conduction between CdTe NCs, but present in high enough concentration to lower electron mobility.

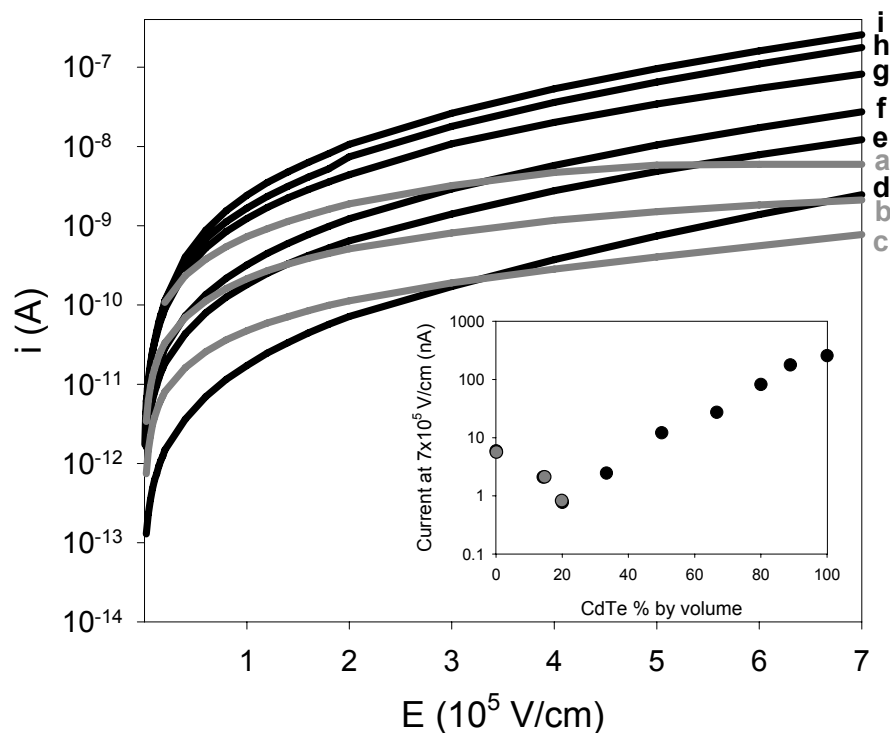


**Figure 5.4:** Photocurrent versus electric field with  $32 \text{ mW/cm}^2$  514 nm excitation for mixed films composed of CdTe and CdSe NCs. Each line represents the photocurrent measured in a film containing a different ratio by volume of CdTe to CdSe: a) 100 % CdSe, b) 14 % CdTe, c) 20 % CdTe, d) 33 % CdTe, e) 50 % CdTe, f) 66 % CdTe, g) 80 % CdTe, h) 88 % CdTe, i) 100 % CdTe. The inset displays the magnitude of the photocurrent at  $7 \times 10^5 \text{ V/cm}$  as a function of volume % of CdTe.

#### *CdSe/CdTe NB films*

In the mixed films of CdTe and CdSe NCs, each NC is separated from its neighbor by an organic tunneling barrier. This potentially reduces the rate of Type II exciton separation in these films and allows the rate of electron trapping on the surface of the CdTe NC to be faster. In CdSe/CdTe NBs the CdTe NC is bonded to the CdSe NRs (Figure 5.1) which should increase the probability of Type II exciton separation. Ideally it will proceed faster than electron trapping. In addition, the ratio of CdTe to CdSe in all areas of the film will be identical with two CdTe NCs

for each CdSe NR, and so potential problems stemming from size segregation of CdTe and CdSe NCs will not be of concern in this film. Unfortunately, the photoconductivity vs. electric field dependence for films of CdSe/CdTe NBs is very similar to those composed entirely of CdTe NCs (Figure 5.5). Differential conductance measurements of the NB films show an increase in dark current with negative gate voltage indicating that holes are the majority carrier (Figure 5.6). The temperature dependence of the dark current in the NB films finds a 0.33 eV activation energy (Figure 5.7), also nearly identical to that of CdTe NC films.

In both mixed films of CdTe and CdSe NCs and CdSe/CdTe NBs the electron trapping on CdTe NC surface appears to dominate charge transport through the films. Even if excitons are separated at the Type-II interface, electron transport does not appear to be segregated to the CdSe NC and NR and electrons still end up deeply trapped at the surface of the CdTe nanoparticle.

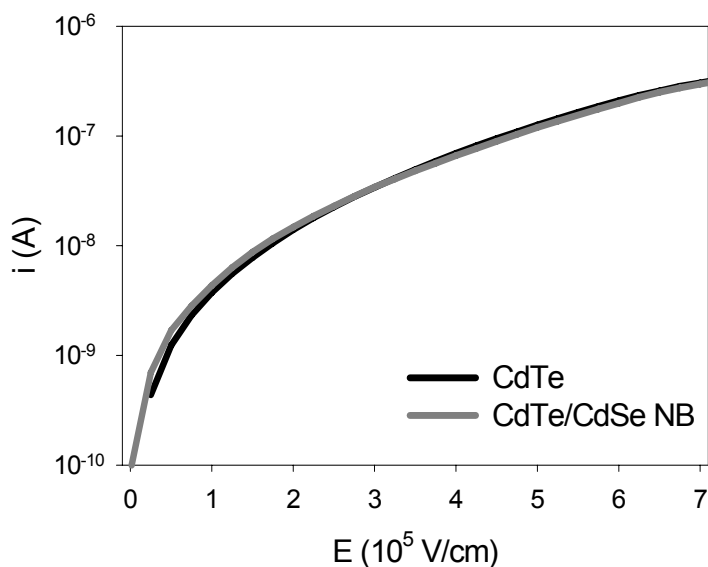


**Figure 5.5:** Photocurrent versus electric field with 32 mW/cm<sup>2</sup> 514 nm excitation for a CdTe NC film (black line) and a CdSe/CdTe NB film (grey line). The magnitude of the photocurrent has not been scaled for either of the films but they were matched to have a similar absorbance value at 514 nm.



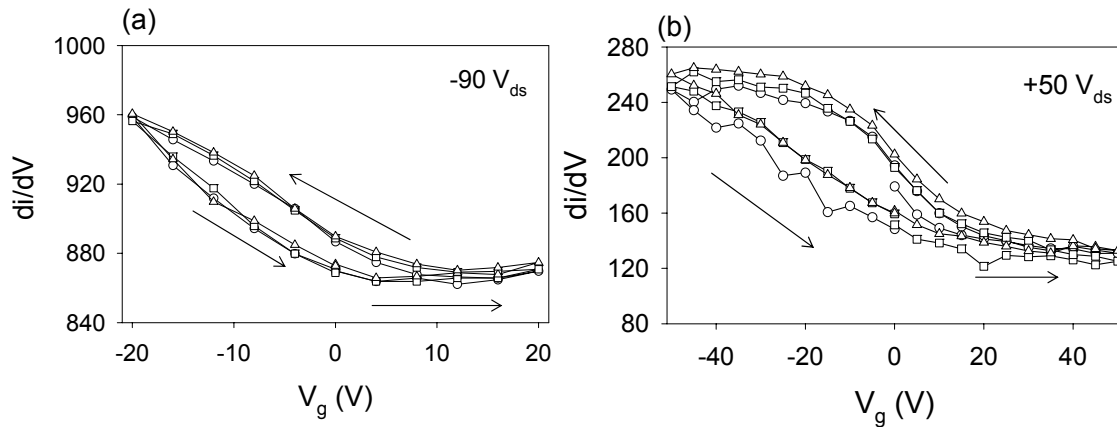


**Figure 5.6:** Room temperature differential conductance  $di/dV$  plotted as a function of gate voltage for a CdSe/CdTe NB film held at (a)  $-90 V_{ds}$  and (b)  $+50 V_{ds}$ .  $V_g$  is applied for 5 s and followed by a recovery of 5 s at 0  $V_g$  before  $V_g$  is stepped to the next value. In (a)  $V_g$  is swept from 0 to +20 V, from +20 V to -20 V, and back to 0 V while in (b)  $V_g$  is swept from 0 to +50 V, from +50 V to -50 V, and back to 0 V. For both (a) and (b) the open circles represent the first sweep, open squares the second sweep, and open triangles the third sweep. The solid line serves as a guide to the eye.

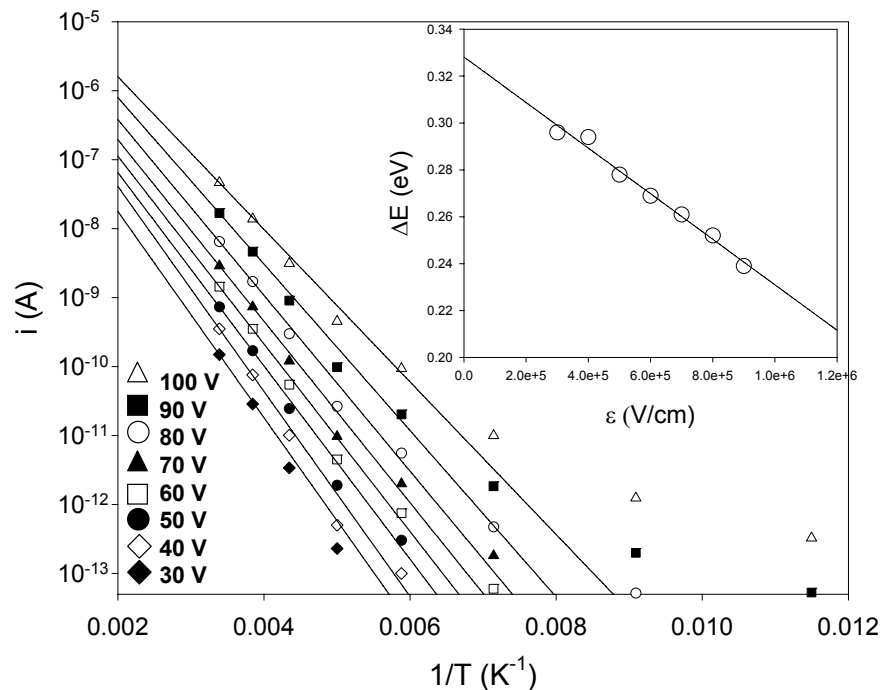


**Figure 5.7:** Temperature dependence of the dark current for a CdSe/CdTe NB film plotted at different values of  $V_{ds}$ . An Arrhenius fit to each data set is given by a solid line. Field dependent activation energies are extracted from the fit and plotted versus electric field in the inset. A solid line gives a linear fit to the data in the inset.

### 5.3.2 Layered CdTe and CdSe Nanocrystal Thin Films Sandwiched between Electrodes – Photovoltaic Mode

While photoconductive devices with gains greater than unity can be used for photodetectors, they do not increase the efficiency of a photovoltaic device. Unlike a photoconductive device, in order for a photovoltaic device to run, both charges must be extracted at the electrodes. This concept can be understood by considering where the energy to drive the photocurrent comes from in each device. In a photoconductor an applied voltage drives the exciton separation and conduction of charges. While initially only one charge is created per absorbed photon, the energy provided by the applied field can amplify the current and generate photoconductive gains greater than one.

However, a photovoltaic device is run with no applied voltage, and the energy to generate photocurrent comes only from absorbed photons. Therefore, the maximum gain is one charge per photon. In a photovoltaic device, there is an internal electric field either from a p-n junction, an electrochemical potential difference between two semiconductors materials, or the work function difference between the electrodes which directs the flow of charge. If the circuit is open, a photovoltage ( $V_{oc}$ ) will be created as photogenerated electrons and holes build up at the two electrodes, and when the circuit is closed a photocurrent ( $I_{sc}$ ) flows as the carriers recombine in the external circuit. To generate power, an external load (a resistor) is placed in the circuit across which a voltage is generated as the photocurrent flows. If the charge carriers cannot reach an electrode, they do not contribute to the photovoltage or current generated by the solar cell. The low efficiencies of many NC/polymer hybrid solar cells is attributed in part to trapping states in the NC/polymer film which cause charge carriers to recombine before they can be extracted at the electrodes.<sup>20</sup>

When run in photoconductive mode, CdTe NC films and CdSe/CdTe NB films between parallel gold electrodes behave as secondary photoconductors with the hole amplifying the current as it cycles through the circuit a number of times before recombining with a trapped electron. If these materials are to work in a photovoltaic device the electron must be able to reach an electrode for extraction. To investigate how CdTe NCs and CdSe/CdTe NBs behave in a thin film photovoltaic device, three different device structures are built. In each device the bottom contact is a transparent electrode, indium tin oxide (ITO), and the top electrode is a gallium indium eutectic solder (EGaIn). When the circuit is connected the ITO and EGaIn electrodes thermalize and EGaIn is positively charged and the ITO negatively charged. Positive current is defined as electrons flowing from ITO to EGaIn and negative current is electron flow in the reverse direction.

Device #1 consists of ITO, PEDOT:PSS, CdTe NC layer (660 nm, band edge abs.), CdSe NC layer (600 nm, band edge abs.), and EGaIn in that order [Figure 5.8(a)]. The PCA and absorbance spectra for this device are given in Figure 5.8(b). At zero bias the photocurrent comes primarily from the CdSe NC layer and there is little contribution from the CdTe NC layer. Excitons created in the CdSe NC layer are separated, most likely at the CdSe/CdTe interface, and holes traverse the CdTe NC layer to the ITO and electrons travel through the CdSe layer from which they are extracted at the EGaIn electrode. The photocurrent is positive [Figure 5.8(c)].

Most likely, electrons created in the CdTe NC layer are trapped in the electron accepting state and do not contribute to the photocurrent. The CdTe and CdSe NC layers are the same thickness and both contribute to the optical absorption spectrum of the film [Figure 5.8(b)]. In addition, photons hit the CdTe layer first, and the layers are only 25 nm thick, so it can be concluded that the limited contribution of CdTe NC layer to the photocurrent is not a

consequence of having fewer excitons generated in that layer. When positive bias (reverse bias) is applied the current in the PCA spectrum still appears to only come from CdSe NCs as 0.6 V is not enough to pull electrons from the CdTe NC trap into the CdSe NC layer. However, when -0.6 V (forward bias) is applied, the photocurrent flows in the opposite direction [Figure 5.8(c)] and the majority of the photocurrent in the PCA spectrum comes from excitons created in the CdTe NC layer. This indicates that electrons from the CdTe NC layer are reaching an electrode; most likely only excitons at the CdTe/PEDOT:PSS interface are separate. Holes must travel through the CdTe NC layer to the CdSe NC layer to the EGaIn. There is little contribution from the CdSe NCs as electrons most likely become trapped in the CdTe NC layer on their way to the PEDOT:PSS and ITO electrode. In conclusion, excitons created in the CdTe NC layer do not significantly contribute to the photocurrent at zero bias and only begins to contribute when the device is run in forward bias.

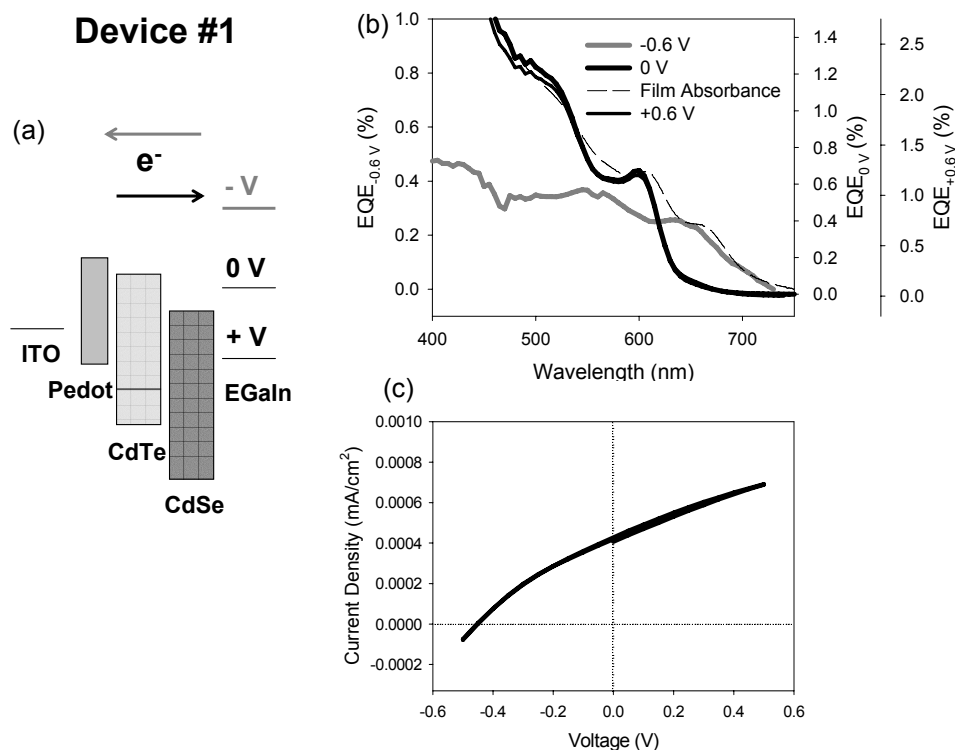


**Figure 5.8:** (a) The structure of device #1 and relative energy levels of each layer are shown in the cartoon. The solid line in the CdTe band represents the proposed location of the electron trap state. The direction of the flow of electrons in the device at each voltage is designated by the arrows and color coded with the label for the bias. The black arrow indicates electrons flow from the ITO to the EGaIn (reverse/positive bias) and the grey arrow indicates electrons flow in the opposite direction (forward/negative bias). (b) The PCA spectra for device structure #1 is displayed at 0 V (black line), + 0.6 V (black line, same as 0 V), and – 0.6 V (grey line). The absorbance of device #1 is given by the dotted line. (c) Current versus voltage plot for the device #1 in which the voltage is swept from 0 to + V, from + V to – V, and back to 0 V. Device #1 is measured at room temperature and photoexcited with 1.6 mW/cm<sup>2</sup> of 514 nm light.

Device #2 [Figure 5.9(a)] is a variation of device #1 and it consists of ITO, PEDOT:PSS, CdSe NC layer, CdTe NC layer, and EGaIn in that order. The structure of device #2 is not optimal as electrons will have to flow through the CdTe NCs to reach the EGaIn and holes through the CdSe NCs to reach the ITO at zero bias. In fact, this process is so unfavorable that at zero bias the photocurrent is negative, flowing in a direction opposite to the field developed by the thermalized electrodes [Figure 5.9(c)]. Like Device #1, only excitons from the CdSe NC

layer contribute to the photocurrent at zero bias [Figure 5.9(b)]. The EQE of this device is also an order of magnitude lower than device #1. Applying a positive bias switches the direction of the photocurrent and electrons from the CdTe NC layer are extracted at the EGaIn. While this device structure is not optimal it demonstrates once again that the CdTe NCs only contributes when the device is run with applied bias.

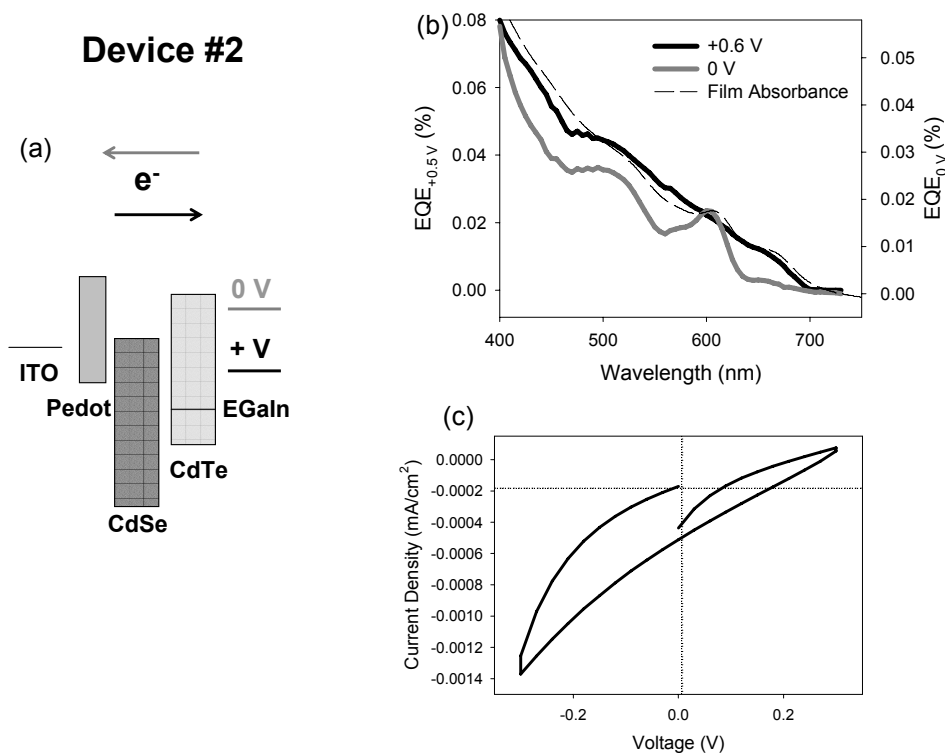


**Figure 5.9:** (a) The structure of device #2 and relative energy levels of each layer are shown in the cartoon. The direction of the flow of electrons in the device at each voltage is designated by the arrows and color coded with the label for the bias. The black arrow indicates electrons flow from the ITO to the EGaIn (reverse/positive bias) and the grey arrow indicates electrons flow in the opposite direction (forward/negative bias). (b) The PCA spectra for device structure #1 is displayed at 0 V (black line) and + 0.6 V (grey line). The absorbance of device #2 is given by the dotted line. (c) Current versus voltage plot for device #2 in which the voltage is swept from 0 to + V, from + V to - V, and back to 0 V. Device #2 is measured at room temperature and photoexcited with  $27 \text{ mW/cm}^2$  of 514 nm light.

CdSe/CdTe NBs are included in device #3 which consists of ITO, CdTe NC layer, CdSe/CdTe NB layer, CdSe NC layer, and EGaIn in that order [Figure 5.10(a)]. This device

resembles device #1 in that current under zero bias comes mainly from the CdSe NC layer and flows in a direction consistent with the thermalized electrodes. Under forward bias the NB and CdTe NC layers contribute to the photocurrent and it flows in the opposite direction [Figure 5.10 (b) and (c)].

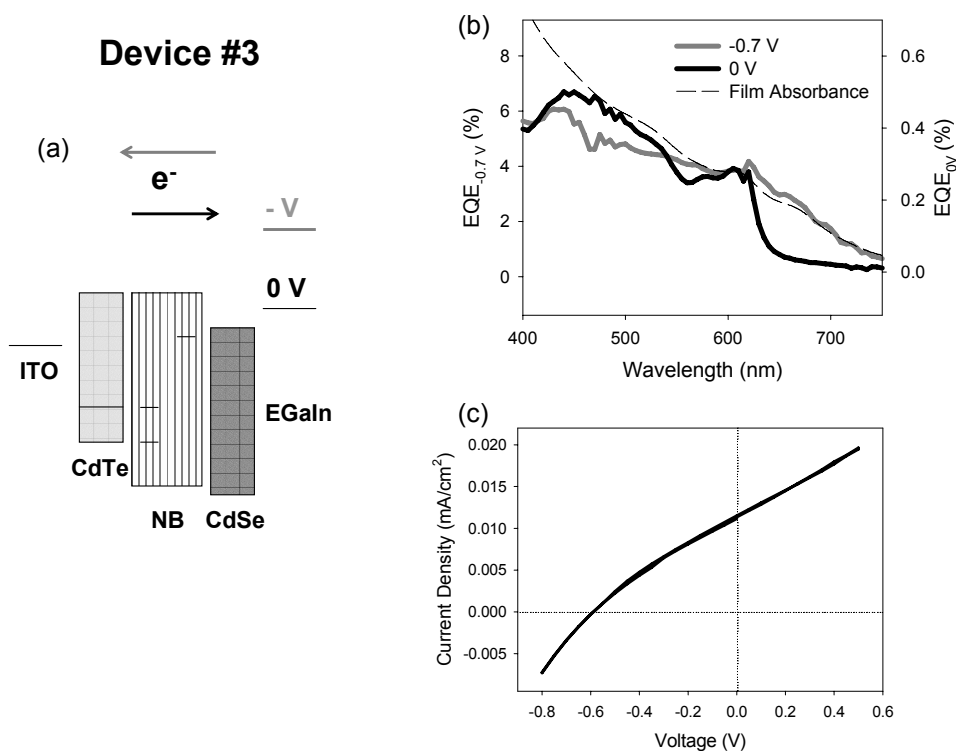


**Figure 5.10:** (a) The structure of device #3 and relative energy levels of each layer are shown in the cartoon. The direction of the flow of electrons in the device at each voltage is designated by the arrows and color coded with the label for the bias. The black arrow indicates electrons flow from the ITO to the EGaIn (reverse/positive bias) and the grey arrow indicates electrons flow in the opposite direction (forward/negative bias). (b) The PCA spectra for device structure #3 is displayed at 0 V (black line) and at -0.7 V (grey line). The absorbance of device #3 is given by the dotted line. (c) Current versus voltage plot for device #3 in which the voltage is swept from 0 to + V, from + V to - V, and back to 0 V. Device #3 is measured at room temperature and photoexcited with 27 mW/cm<sup>2</sup> of 514 nm light.

To summarize, the three photovoltaic devices with different combinations of CdTe NCs, CdSe NCs, and NBs all exhibit contributions to the photocurrent from only the CdSe NC layer when measured at zero applied bias. The CdTe NC and CdSe/CdTe NB layers contribute to the

photocurrent when a bias is applied. These results are consistent with those of photoconductive studies in Chapter 4 in which with the CdTe surface state traps electrons. As electrons are deeply trapped the CdTe NC film, it may actually serve as an excellent hole transport layer and has potential use in this capacity in future devices.

### 5.3.3 Modifying the Surface of CdTe Nanoparticles

#### *Ligand Exchange with Cadmium Oleate*

Evidence points to unpassivated and/or oxidized Te on the surface of the CdTe NC serving as the electron trap state which reduces fluorescence of CdTe NC<sup>40</sup> and it is likely this state dominates the conduction through CdTe NC films as well (Chapter 4). In an attempt to passivate the Te atoms on the surface, eliminate the electron trap state, and allow excitons created in CdTe NCs to contribute to power generation in a photovoltaic device, excess Cd is added to the CdTe NCs. It has been shown that CdTe NCs with a Cd rich surface are brighter than those with a Te rich surface.<sup>41</sup> After three precipitations, the QY of the CdTe NC solution is ~0.1%. However, after addition of cadmium oleate the QY increases as much as 50% and XPS shows a 15 % increase in the ratio of Cd to Te atoms in the CdTe NC film. The Cd atom of the cadmium oleate is believed to bind to the unpassivated Te atoms on the surface. Adding degassed oleic acid does not increase the QY indicating this effect is not a result of ligand passivation alone (Table 5.1). The CdTe NC solution having 50% QY after the addition of cadmium oleate can be precipitated with methanol an additional time so that optically clear films may be deposited. The solution retains its fluorescence after the additional precipitation and remains fluorescent for weeks when stored in air. Figure 5.11(a) is a photo of a dilute solution of CdTe NCs in hexane to which the cadmium oleate has been added (black cap) and a photo of a



dilute solution of untreated CdTe NCs (white cap). These solutions are of the same concentration and have been stored in air for three weeks.

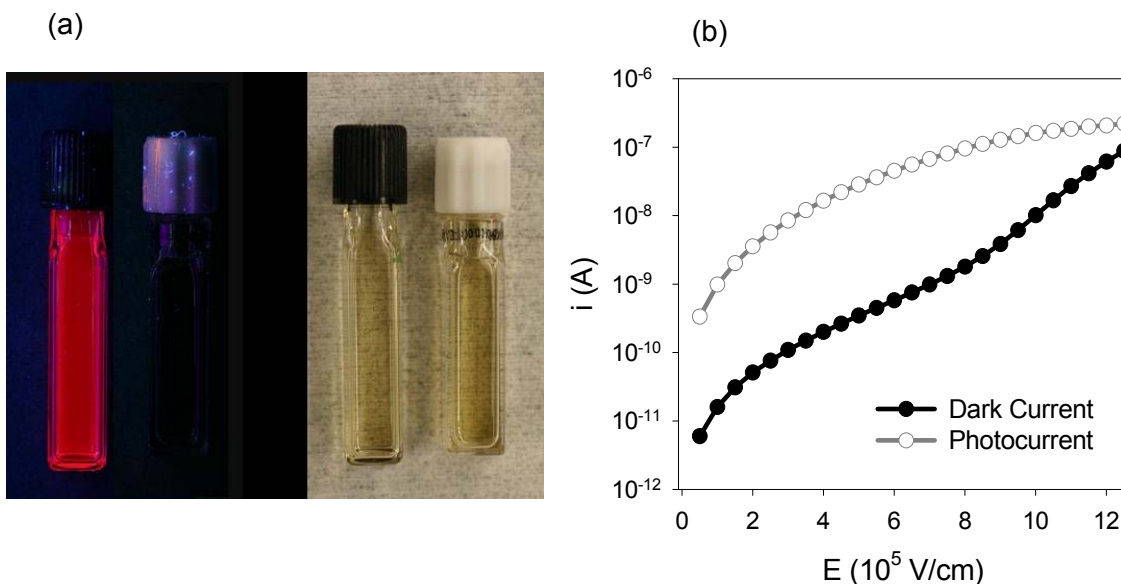


**Figure 5.11:** (a) Image of a dilute solution of CdTe NCs in hexane with (black cap) and without (white cap) the addition of cadmium oleate. The two vials are photographed with (left) and without (right) UV excitation. (b) Dark (closed black circles) and photo (open grey circles) current for a CdTe NC + cadmium oleate film after heating at 150 °C under vacuum for 30 min. This CdTe NC film was deposited from the CdTe NC solution having 50% QY.

Unfortunately, films of CdTe NCs capped with cadmium oleate do not have photocurrent characteristics different from those of CdTe NC films. In the films as deposited, the NCs are too far apart to have significant photo or dark current and so chemical or thermal treatment must be employed to enhance the photocurrent. Figure 5.11(b) shows a  $i$ - $V$  curve for a CdTe + cadmium oleate film (50 % QY in solution) that has been heated at 150 °C for 30 min. The photocurrent does not show saturation of current with voltage even at high fields, and its shape resembles that of CdTe films. The dark current is also high, indicating a large hole density and thus many electron accepting states. It is unlikely that every Te atom on the surface is passivated with the cadmium oleate treatment and so the NC film is still susceptible to oxidation and trapping,

especially after more of the surface exposed following the decomposition or removal of the ligands during heating. This is supported by the observation that the CdTe NCs + cadmium oleate remain fluorescent for weeks in solution, yet in a film the fluorescence of these NCs quenches in a matter of hours. XPS confirms the presence of a Te-O peak in the CdTe + cadmium oleate NCs films. In Figure 5.12 characteristic XPS peaks (Te 4d, Te 3d, and Cd 3d) are shown for CdTe NC and CdTe + cadmium oleate NC films after oxidation. There is a Te-O peak present in Te 4d and Te 3d spectra for both NCs films indicating the presence of cadmium oleate does not prevent oxidation of Te. However, the ratio of the Te-O to Te-Cd peaks is different for the two treatments. The Te-O peak is about twice the value of the Te-Cd peak in CdTe NC film and only slightly larger in the CdTe + cadmium oleate NC film. It is difficult to quantify these numbers as there is another Te species (S-factor in A. Lobo, et al.)<sup>40</sup> which grows in during air exposure located  $\sim 1$  eV to higher binding energy from the Te-Cd peak. It accounts for only  $\sim 10\%$  of the total Te atoms and its origin is undetermined.

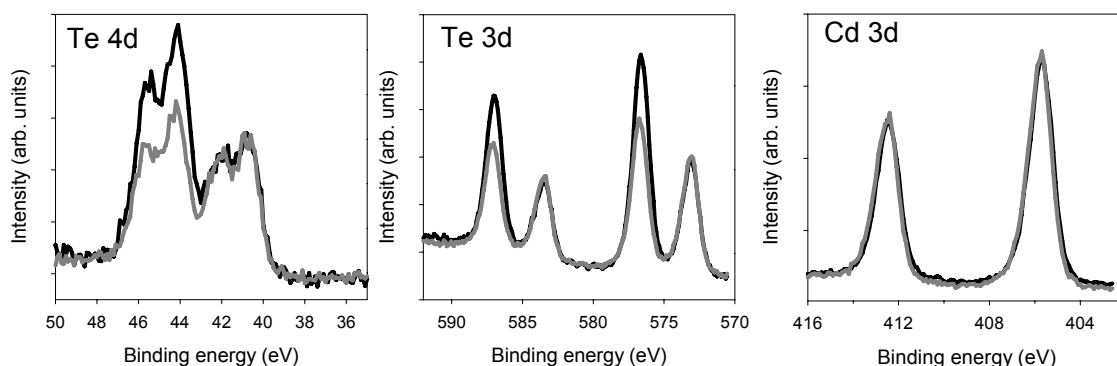


**Figure 5.12:** XPS spectra of a CdTe NC film (black line) and CdTe + cadmium oleate NC film (grey line) after oxidation for three weeks. Spectra are provided for the Te 4d (top left), Te 3d (top right), and Cd 3d (bottom) states.

In conclusion, adding cadmium oleate can improve the fluorescence of CdTe NCs in air by slowing the rate of surface oxidation but it is not possible to passivate every Te atom and so the electron trap state is still present in the CdTe NC film. Other ligands including various thiols<sup>42</sup> and hexa-n-propyl phosphorus triamide<sup>43</sup> have also been shown to increase the fluorescence QY and air stability of CdTe NCs in solution, but these ligands would need to be cap exchanged or decomposed to decrease interparticle spacing and allow for conduction, once again exposing the surface trap site. Ligand exchange does not appear to be the best method for removing the trap states from the CdTe NC surface.

#### *Growing an Inorganic Shell via Overcoating*

One of the most promising methods to remove this trap state involves passivating the CdTe NC with an inorganic shell and then removing all of the organic ligands with heat or chemical treatments as in Chapter 3. The inorganic shell should keep the exciton confined within the NC and prevent the absorption spectrum from shifting to the bulk band edge when ligands are removed. In Chapter 3 it was demonstrated that films of CdSe/ZnS NCs between gold electrodes display 100% extraction of electrons and holes from the device at room temperature after heating to remove all organic ligands and the absorbance spectrum remained quantized. Previously, surface states on CdSe NCs had been responsible for the fast non-radiative decay rate of excitons and 100% extraction of electrons and holes had only been demonstrated at 77 K where the non-radiative decay is slowed. It is possible that this overcoating followed by ligand removal procedure could be transferred to CdTe core/shell NC film system to improve photovoltaic device efficiency.

The greatest challenge in passivating the CdTe NC surface with an inorganic shell is the growth of a thin, high quality shell. A ZnS shell can be grown on the CdTe NCs using methods

similar to those used to overcoat CdSe NCs (Section 5.2.5) and the emission from the CdTe NCs becomes noticeably brighter. Unfortunately, after two precipitations the emission from the CdTe/ZnS NCs is gone. This is true whether the CdTe/ZnS NCs are precipitated in an air or nitrogen environment. Most likely, as a result of the significant lattice mismatch between CdTe and ZnS (16 %) <sup>44</sup> the shell is highly strained or incomplete, and precipitation with polar solvents removes not only excess ligands but the Zn and S atoms on the surface as well. Attempts to grade the ZnS shell with CdS, as is commonly done for CdSe NCs, also do not work. There is still a lot of work to be done before core/shell CdTe/X NC films can be employed for photovoltaic devices.

#### *Sintering of the NC film*

The baking of a CdTe NC film drop cast on gold electrodes at 200 °C in air results in the reduction of the dark current and saturation of the photocurrent with applied field indicating every electron and hole is extracted from the device (Figure 5.13). This is the first time saturation of photocurrent with voltage has been observed in CdTe NC films. (Figure 4.9 is a plot of the typical field dependence of the CdTe NC photocurrent which does not reach saturation.) However, the absorbance spectrum of the CdTe NC film after baking shows over a 30 nm shift in the band edge absorbance peak (Figure 5.13, inset). A red shift of this magnitude represents significant electronic coupling between NCs, most likely a result of the sintering of the NCs.<sup>15</sup> One interpretation of this result is that the surface of the CdTe NC becomes part of a bulk film after sintering, and so the surface electron trap state is no longer present. This significantly reduces the dark current as there is no state into which valence band electrons can be thermally excited and, as there is no state to trap electrons, both of the charge carriers can be extracted from the device. These results are consistent with those of Gur et. al. in which the

CdTe NR film contributes to the PCA spectrum after cap exchange into pyridine and a 200 °C bake and in which devices displayed the highest efficiency after sintering CdSe and CdTe NR films at 400 °C.<sup>22</sup>

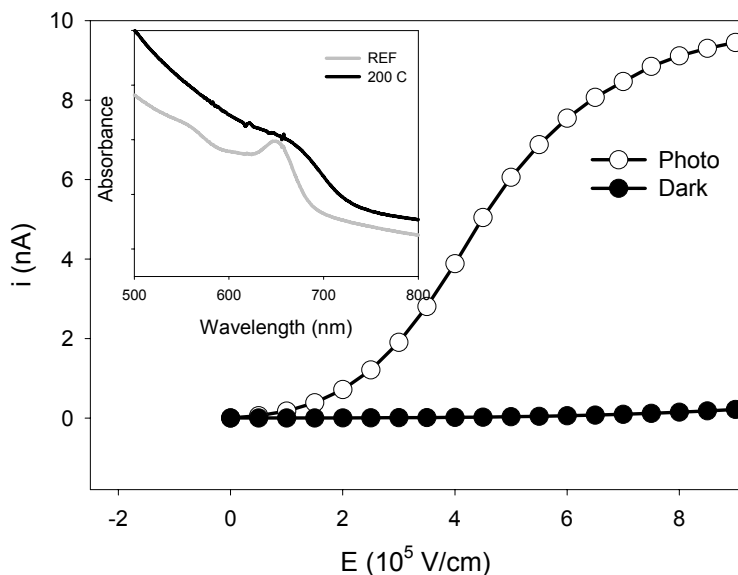


**Figure 5.13:** Dark (closed circles) and photo (open circles) current versus electric field for a CdTe NC film baked at 200 °C for 30 min under vacuum. The sample is photoexcited with 32 mW/cm<sup>2</sup> 514 nm light and measured at room temperature. The inset is the absorbance spectra for the CdTe NC film before (grey line) and after (black line) heating at 200 °C.

## 5.4 Conclusions

Semiconductor NCs have potential for use in photovoltaic devices such as solar cells because they can be processed and deposited from solution, and the band gap can be tuned by changing the size of the NC. In particular, CdTe NCs are of interest as the band gap can be tuned from 1.5 to 2 eV and bulk CdTe forms a type II heterojunction with CdSe and CdS. We find that unpassivated atoms on the surface of CdTe NCs serve to deeply trap electrons, and these trap states prevent excitons created in CdTe NCs from contributing to power generation in a NC solar cell. Different device geometries and combinations of CdTe and CdSe NCs, and NBs, were not able to prevent electrons from becoming trapped on the surface of the CdTe NC. Synthetic methods to modify the surface of the CdTe NC through addition of cadmium containing ligands and passivation with an inorganic shell were unsuccessful as well. Currently, the only effective method for eliminating the trap state is to eliminate the surface of the CdTe NC altogether through sintering the NC film. However, thermal sintering is not the ideal method to eliminate surface traps as the band gap shifts back to the bulk CdTe band gap and the advantages of a tunable band gap are lost. Future work should be directed at modifying the CdTe NC surface, possibly with an inorganic shell having a better lattice match with CdTe than ZnS, so that the surface electron trap state will be removed, but the advantages NCs have to offer solar power generation are preserved.

## 5.5 References

1. C. B. Murray, D. J. Norris and M. G. Bawendi. *Journal of the American Chemical Society* **115**, 8706 (1993).
2. Z. A. Peng and X. Peng. *J. Am. Chem. Soc.* **123**, 183 (2001).
3. R. J. Ellingson, J. L. Blackburn, P. R. Yu, G. Rumbles, O. I. Micic and A. J. Nozik. *Journal of Physical Chemistry B* **106**, 7758 (2002).
4. A. J. Nozik. *Physica E* **14**, 115 (2002).
5. R. D. Schaller, M. Sykora, S. Jeong and V. I. Klimov. *Journal of Physical Chemistry B* **110**, 25332 (2006).
6. V. I. Klimov. *Applied Physics Letters* **89**, (2006).
7. R. D. Schaller, M. Sykora, J. M. Pietryga and V. I. Klimov. *Nano Letters* **6**, 424 (2006).
8. R. D. Schaller, M. A. Petruska and V. I. Klimov. *Applied Physics Letters* **87**, (2005).
9. R. D. Schaller and V. I. Klimov. *Phys. Rev. Lett.* **92**, (2004).
10. V. I. Klimov. *Journal of Physical Chemistry B* **110**, 16827 (2006).
11. J. E. Murphy, M. C. Beard, A. G. Norman, S. P. Ahrenkiel, J. C. Johnson, P. R. Yu, O. I. Micic, R. J. Ellingson and A. J. Nozik. *Journal of the American Chemical Society* **128**, 3241 (2006).
12. R. J. Ellingson, M. C. Beard, J. C. Johnson, P. R. Yu, O. I. Micic, A. J. Nozik, A. Shabaev and A. L. Efros. *Nano Letters* **5**, 865 (2005).
13. M. C. Hanna and A. J. Nozik. *Journal of Applied Physics* **100**, (2006).
14. N. Y. Morgan, C. A. Leatherdale, M. Drndic, M. V. Jarosz, M. A. Kastner and M. Bawendi. *Physical Review B* **66**, (2002).
15. M. Drndic, M. V. Jarosz, N. Y. Morgan, M. A. Kastner and M. G. Bawendi. *Journal of Applied Physics* **92**, 7498 (2002).
16. M. V. Jarosz, V. J. Porter, B. R. Fisher, M. A. Kastner and M. G. Bawendi. *Physical Review B* **70**, (2004).
17. C. A. Leatherdale, C. R. Kagan, N. Y. Morgan, S. A. Empedocles, M. A. Kastner and M. G. Bawendi. *Physical Review B* **62**, 2669 (2000).
18. C. B. Murray, C. R. Kagan and M. G. Bawendi. *Annual Review of Materials Science* **30**, 545 (2000).

19. C. Kagan, Ph.D. thesis, Massachusetts Institute of Technology, Cambridge, 1996.
20. W. U. Huynh, J. J. Dittmer and A. P. Alivisatos. *Science* **295**, 2425 (2002).
21. B. Sun, H. J. Snaith, A. S. Dhoot, S. Westenhoff and N. C. Greenham. *Journal of Applied Physics* **97**, 014914 (2005).
22. I. Gur, N. A. Fromer, M. L. Geier and A. P. Alivisatos. *Science* **310**, 462 (2005).
23. A. Morales-Acevedo. *Solar Energy Materials and Solar Cells* **90**, 2213 (2006).
24. A. Romeo, G. Khrypunov, F. Kurdesau, M. Arnold, D. L. Batzner, H. Zogg and A. N. Tiwari. *Solar Energy Materials and Solar Cells* **90**, 3407 (2006).
25. S. Kim, Y. T. Lim, E. G. Soltesz, A. M. De Grand, J. Lee, A. Nakayama, J. A. Parker, T. Mihaljevic, R. G. Laurence, D. M. Dor, L. H. Cohn, M. G. Bawendi and J. V. Frangioni. *Nature Biotechnology* **22**, 93 (2004).
26. J. Orton, *The Story of Semiconductors*. 2004, New York: Oxford University Press.
27. V. J. Porter, T. Mentzel, S. Charpentier, M.A. Kastner, M.G. Bawendi. *Phys. Rev. B* **73**, 155303 (2006).
28. P. T. Snee, Y. Chan, D. G. Nocera and M. G. Bawendi. *Advanced Materials* **17**, 1131 (2005).
29. J. E. Halpert, V. J. Porter, J. P. Zimmer and M. G. Bawendi. *Journal of the American Chemical Society* **128**, 12590 (2006).
30. C. B. Murray, C. R. Kagan and M. G. Bawendi. *Science* **270**, 1335 (1995).
31. M. V. Jarosz, N. E. Stott, M. Drndic, N. Y. Morgan, M. A. Kastner and M. G. Bawendi. *Journal of Physical Chemistry B* **107**, 12585 (2003).
32. C. R. Kagan, C. B. Murray, M. Nirmal and M. G. Bawendi. *Physical Review Letters* **76**, 1517 (1996).
33. D. C. Oertel, Ph.D. thesis, Massachusetts Institute of Technology, Cambridge, 2007.
34. W. W. Yu, L. H. Qu, W. Z. Guo and X. G. Peng. *Chemistry of Materials* **16**, 560 (2004).
35. M. A. Hines and P. Guyot-Sionnest. *Journal of Physical Chemistry* **100**, 468 (1996).
36. B. O. Dabbousi, J. RodriguezViejo, F. V. Mikulec, J. R. Heine, H. Mattoussi, R. Ober, K. F. Jensen and M. G. Bawendi. *Journal of Physical Chemistry B* **101**, 9463 (1997).
37. R. Sens and K. H. Drexhage. *Journal of Luminescence* **24**, 709 (1981).
38. R. H. Bube, *Photoconductivity of Solids*. 1960, New York: Wiley.



39. H. Landolt and R. Bornestein, *Numerical Data and Functional Relationships in Science and Technology*. 1961, Berlin: Springer-Verlag.
40. A. Lobo, H. Borchert, D. V. Talapin, H. Weller and T. Moller. *Colloids and Surfaces a-Physicochemical and Engineering Aspects* **286**, 1 (2006).
41. H. Borchert, D. V. Talapin, N. Gaponik, C. McGinley, S. Adam, A. Lobo, T. Moller and H. Weller. *Journal of Physical Chemistry B* **107**, 9662 (2003).
42. N. Gaponik, D. V. Talapin, A. L. Rogach, K. Hoppe, E. V. Shevchenko, A. Kornowski, A. Eychmuller and H. Weller. *J. Phys. Chem. B* **106**, 7177 (2002).
43. F. V. Mikulec, Ph.D. thesis, Massachusetts Institute of Technology, Cambridge, 1999.
44. P. Lawaetz. *Physical Review B* **5**, 4039 (1971).

## Chapter 6

### Concluding Remarks

The work in this thesis attempts to bridge the gap between the vision of ‘designer optoelectronic materials’ composed of semiconductor NCs and the inherent insulating nature of the NC solids due to the organic capping ligands. Enhancing conductivity through the NC solid without losing quantum confinement remains the greatest challenge in the realization of NC devices and materials. To improve charge transport through the NC films, this thesis has focused on modifying the surface of the NC in a variety of methods including new organic ligands, inorganic passivation, and even forming heterostructures of different semiconductor materials. Each surface modification alters the mechanism of charge transport through the NC solid, and through the study of the physics of charge transport, we can determine which treatments are optimal for the enhancement of the electrical conduction.

In Chapter 2 it was found that the photocurrent in CdSe NC films can be enhanced by over 1000 times by cap exchanging into smaller ligands which decrease interparticle spacing. As a result of the increase of the photocurrent, the conduction mechanism in the system of CdSe NCs with gold electrodes could be characterized. It was determined that gold forms a ‘blocking contact’ with CdSe NCs in which charges can be extracted, but not injected, from the contacts. The organic ligands on the CdSe NCs were replaced by a ZnS inorganic shell in Chapter 3 which serves to decrease the height of the energetic tunnel barrier between NCs in the film. Through a study of the temperature dependence of the photoconductivity, it was determined that the improved surface passivation provided by the ZnS shell (in comparison to the organic ligands) reduced the rate of non-radiative exciton decay and this aided in the room temperature extraction

of electron and holes from the NC film. Conductivity in CdTe NC films between gold electrodes was studied in Chapter 4. It was found that as a result of the electrical offset between the work function of gold and the valence band of CdTe, as well as surface states on the CdTe NC, the conductivity had a different mechanism than in CdSe NC films. Gold formed a 'non-blocking contact' with CdTe NCs, and so holes could be injected into the film and also the photocurrent could be amplified. The differences in electrical conduction between the CdTe and CdSe NC systems is an example of 'designer NC solids' in which the electrical properties of materials can be varied by changing only the type of semiconductor NC. Finally, in Chapter 5, CdTe and CdSe are combined in an attempt to build a NC photovoltaic material. Though these two semiconductors can be combined to construct efficient thin film bulk heterojunction solar cells, the CdSe/CdTe NC films do not form a good photovoltaic material as trap states on the surface of the CdTe NC hinder charge extraction from the device. The results of Chapter 5 illustrate the important conclusion that though NCs are composed of semiconductors, the electrical conduction through NC solids is different than that in a traditional semiconductor, and so it is necessary to characterize and understand conduction through NC solids before attempting to use them in devices.

## Appendix A

# Size Dependent Charge Transport and Collection in Junctions Containing Multi-Size Arrays of CdSe Nanocrystals\*

### A.1 Introduction

This chapter examines the electrical characteristics of junctions composed of three-dimensional arrays of colloidal CdSe nanocrystals (NCs), and it focuses on a comparison of junctions containing NCs of one size to those of arrays containing NCs of multiple sizes. The incorporation of an array of NCs into an electrical junction in which the two electrodes contact different sizes of NCs results in the possibility of energetic resonance at both contacts. It also results in the presence of a gradient in potential (a set of steps in the energy of the LUMOs) within the array of NCs, along which electrons can, in principle, cascade: from the smallest dots to the largest dots. This cascade suggests strategies for achieving efficient vectoral transport of electrons to an electrode. Additionally, the study of arrays composed of NCs of different sizes allows for the investigation of some of the electronic consequences of quantum confinement that have been largely unexplored and unexploited in devices based on NCs—namely: i) the importance of energetic alignment of the orbitals of the NCs and the electronic states of electrodes;<sup>1,2</sup> ii) the relationship between the size of the NCs and the resistivity of the array; and

---

\* The work in Appendix A was done in collaboration with Dr. Emily Weiss and Dr. Ryan Chiechi from the laboratory of Professor George Whitesides at Harvard University.

iii) the effects of incorporating a gradient of sizes of NCs—and, therefore, a gradient in potential energy—within the junction.

The electronic and optical properties of NCs depend sensitively on their size; therefore, the multi-size architecture also provides a means for spatially-selective photoexcitation within the NC array. This approach enables the determination of: i) the location of the interface at which photoinduced charge separation occurs, ii) the degree to which the energy absorbed by the NCs is redistributed via energy transfer before charge separation, and iii) the dependence of the photovoltage on the locations of various sizes of NCs within the junction. Such a mechanistic understanding of the generation and flow of photocurrent through arrays of NCs, and across NC/electrode interfaces, is critical we if are to exploit a major advantage of NCs as materials to be used in fabricating devices such as solar cells, light-emitting diodes (LEDs), and photodetectors: that is, the ability to tune their absorption and emission spectra by changing their size,<sup>3,4</sup> and thereby to obtain a range of optoelectronic properties. In particular, NCs are of interest as a material for use in tandem solar cells so it is necessary to investigate the issues involved in the transport of charge through an array of multi-sized NCs.

## **A.2 Experimental**

### **A.2.1 Synthesis**

CdSe NCs were synthesized following the general procedure published previously.<sup>5</sup> A solution of cadmium 2, 4-pentanedionate (99%), 1-dodecanol, and tri-*n*-octylphosphine (TOP) was deoxygenated by pulling vacuum on the solution with a roughing pump (pressure = ~150 mTorr) for 1 hour at 100 °C. This solution was cooled under an argon atmosphere, and to it was

added 1.5 M tri-*n*-octylphosphine selenide (TOPSe). The mixture was loaded into a syringe and injected into a 360 °C hot solvent solution consisting of degassed tri-*n*-octylphosphine oxide (TOPO), 90% hexadecylamine (HDA), and TOP. The NCs were grown for approximately 3 min at 260 °C and then cooled to room temperature. Hexane was added to the room temperature growth solution to prevent solidification during storage. The ratio of the precursors used in the synthesis of all sizes of NCs used in this study is 1 mmol cadmium: 2 mmol 1-dodecanol: 3 mmol selenium. To make different sizes of CdSe NCs, the ratio of 90% to 99% TOPO in the solvent solution was varied. 1 g of 90% and 5.25 g of 99% TOPO gave CdSe NCs with a first absorption feature at 650 nm, 4.25 g of 90% and 2 g of 99% resulted in the first absorption feature at 600 nm, and all 90% TOPO resulted in NCs with a band edge at 560 nm.

### **A.2.2 NC Film Preparation**

To make optically clear, close-packed films of CdSe NCs, 5 mL of growth solution was processed via previously reported methods.<sup>6-12</sup> First, methanol was added to the growth solution until the NCs begin to precipitate from solution. The solution was spun in the centrifuge and the supernatant was discarded, leaving behind a powder of NCs. The NCs were then dissolved in hexane and butanol and this solution was filtered through a 0.2 µm syringe filter. The above precipitation process was repeated with a 0.1 µm filter. Finally, the CdSe NCs were precipitated a third time but dissolved in anhydrous chloroform, rather than hexane and butanol, and passed through a 0.02 µm filter.

### **A.2.3 Optical Characterization**

The absorption spectra of CdSe NC films were measured on a Hewlett-Packard 8453 UV-Vis Spectrometer. The films were deposited on glass slides, soaked in the butylamine solution, and baked before the absorbance spectra were measured.

### **A.2.4 Atomic Force Microscopy**

AFM micrographs of the NC and PEDOT:PSS films on ITO were collected in tapping-mode with a Digital Instruments Dimension 3100 Nanoscope, and analyzed using the Nanoscope IV v5.12b18 software package (Digital Instruments, Santa Barbara, CA).

### **A.2.5 Transmission Electron Microscopy and Preparation of NC Cross-sections**

Figure A.1 shows the procedure to prepare a cross-section of the gradient film for imaging by transmission electron microscopy (TEM). We spun three sheets of NCs (S, then M, then L) onto a 5 mm-thick slab of epoxy (Araldite 502) that had been cured in an oven at 60 °C for 6 h. We then applied a drop (~0.25 mL) of the same epoxy to the top of the film to embed the entire sample, baked the sample for at 70 °C for 12 h, and, using an Leica Ultra-cut microtome, cut ~30-nm-thick slices of the embedded film (the thickness necessary to enable high-resolution TEM imaging). Samples were mounted on a lacy carbon TEM grid. TEM images were obtained using a JEOL 2100 TEM operating at 200 keV and imaging was performed using low dose microscopy methods.

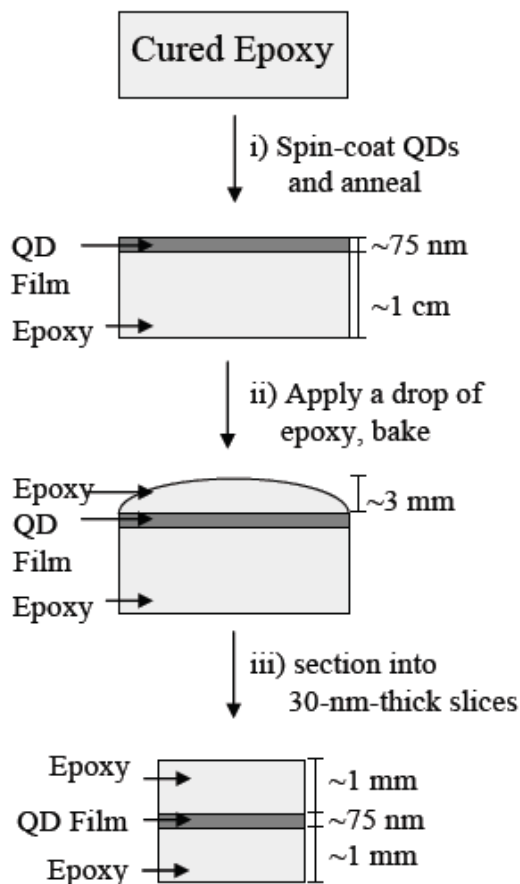


**Figure A.1:** Schematic diagram of the process used to make the TEM samples. i) A film of NCs is spun (using the same conditions as given in the text for the three-layer films on ITO/P) onto a slab of thermally-cured epoxy (annealed at 60° for 6 h). ii) A drop of the same epoxy was applied to the top of the NC film and the sample was heated at 70°C for 12 h. iii) A microtome sliced 30-nm-thick cross-sections of the epoxy-NC composite.

### A.2.6 Device Fabrication

The NC junctions consist of indium-doped tin oxide (ITO) covered with a thin layer of poly(3,4-ethylenedioxythiophene):poly(styrenesulfonate) (PEDOT:PSS). The NCs are deposited on this layer and a eutectic mixture of Ga and In (EGaIn)<sup>13</sup> serves as a conformal top-contact. A schematic of the device is shown in Figure A.2.



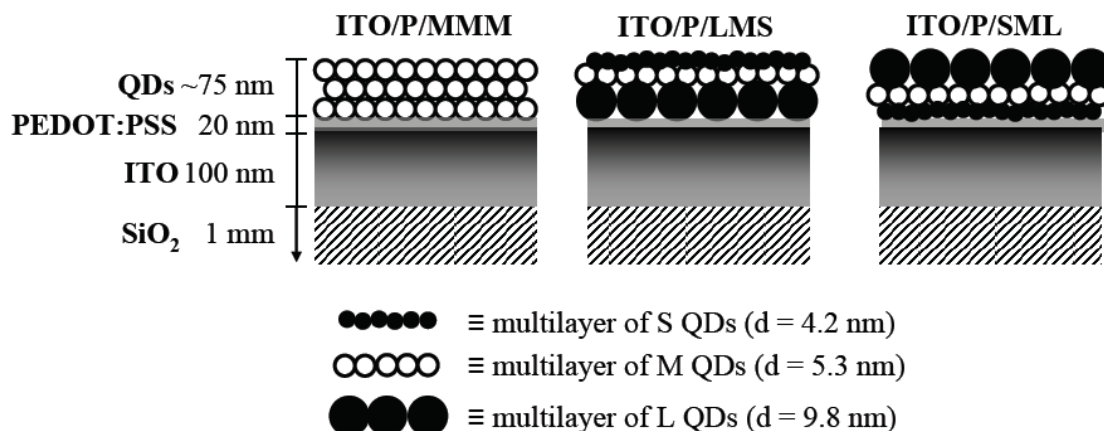


**Figure A.2:** Schematic diagrams of selected films of NCs on ITO/PEDOT:PSS: ITO/P/MMM, ITO/P/LMS, and ITO/P/SML. The symbols “S”, “M”, and “L” indicate small ( $d = 4.2$  nm), medium ( $d = 5.3$  nm), and large ( $d = 9.8$  nm) CdSe nanocrystals respectively, and “P” indicates a  $\sim 20$  nm-thick layer of PEDOT:PSS. The nomenclature is explained in the text. Each row of NCs represents a layer that is 25 - 30 nm thick for the three-layer films, or  $\sim 38$  nm thick for the two-layer films (not shown).

### *Nomenclature*

The symbols “S”, “M”, and “L” are used to designate small ( $d = 4.2$  nm), medium ( $d = 5.3$  nm), and large ( $d = 9.8$  nm) CdSe NCs, respectively, and “P” to indicate a  $\sim 20$  nm-thick layer of PEDOT:PSS (Figure A.2). For example, the film “ITO/P/SML” consists of stacked layers (where each layer was a multilayer, not a monolayer, of NCs) of each of the S, M, and L NCs spun, successively, onto the glass/ITO/PEDOT:PSS substrate, where the multilayer of small dots is adjacent to the PEDOT:PSS. The junction “ITO/P/SML/EGaIn” is an ITO/P/SML film with the layer of large dots contacting the EGaIn electrode. The shorthand “junction SML” means the junction ITO/P/SML/EGaIn, and “ITO/P/LX/EGaIn” is a junction with L NCs adjacent to the PEDOT:PSS layer, and an unspecified combination of NCs (X) in the rest of the array.

### ***ITO and PEDOT:PSS***

Studies of junctions incorporating ITO electrodes are relevant to the development of a wide range of devices: ITO is the most commonly used transparent conducting oxide for photovoltaics, light-emitting diodes, electrochromics, electroluminescent devices, displays, and heat-reflective coatings.<sup>14</sup> ITO is often coupled with the hole-conducting polymer PEDOT:PSS, which, conveniently, may be spin-coated from commercially available aqueous suspensions. This polymer is effectively transparent throughout the long-wavelength UV and visible regions of the spectrum, and provides a smooth, conformal contact between the active material (here, NCs) and the rough, hydrophilic surface of ITO.<sup>15,16</sup> An AFM image showing how the roughness of ITO is smoothed by the PEDOT:PSS is displayed in Figure A.3.

In this study PEDOT:PSS (Baytron®-P) is applied by spin-coating from a 2:1 dilution of the commercially-available aqueous suspension (Bayer, conductive grade) in deionized water at 5000 rpm for 1 min onto ITO (on float glass, Delta Technologies,  $R = 8\text{-}12 \Omega/\square$ ) that had been cleaned with ethanol and dried in a stream of  $N_2$ . The PEDOT:PSS film is annealed at  $100^\circ\text{C}$  for 30 min.

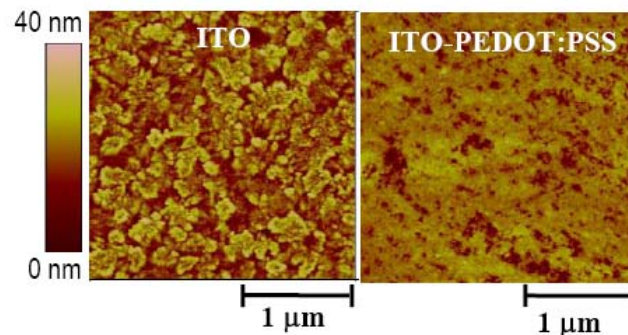


**Figure A.3:** Tapping-mode atomic force micrographs of bare ITO (RMS roughness = 5.6 nm) and ITO covered with a  $\sim 20$ -nm-thick layer of PEDOT:PSS (RMS roughness = 4.1 nm).

### *Layered Films of CdSe NCs*

We have prepared three sizes of NCs, with band-edge absorption maxima at  $\lambda_i = 560$  nm (small dots, S), 604 nm (medium dots, M), and 650 nm (large dots, L). The NCs are spin-coated, one layer at a time, at 5000 rpm for 1 min from solutions in chloroform in the following concentrations:  $1 \times 10^{-5}$  M (L),  $6.5 \times 10^{-5}$  M (M),  $1 \times 10^{-4}$  M (S) for the three-layer films and  $1.5 \times 10^{-5}$  M (L) and  $1.6 \times 10^{-4}$  M (S) for the two-layer film. This combination of concentrations and spinning conditions yielded layers that were  $\sim 26$ - $29$  nm thick each for the three-layer films (as measured by AFM, Figure A.4(a)), and  $\sim 38$  nm thick (as determined by a calibration curve of concentration of spinning solution vs. thickness of the film by AFM, Figure A.4(b)) each for the two-layer films. After the deposition of each layer, we soaked the film in a 0.1 M solution of butylamine in acetonitrile to exchange the TOPO ligands for butylamine ligands,<sup>10</sup> and annealed it at 70 °C for 1 h to drive off any excess (unbonded) organic material, and to reorganize the butylamine ligands into their closest-packed, intercalated configuration (Chapter 2).<sup>10</sup> After butylamine cap exchange and annealing, the NC films are robust and do not dissolve in chloroform, allowing the next NC layer in the gradient to be spun on top without destroying previous layers.

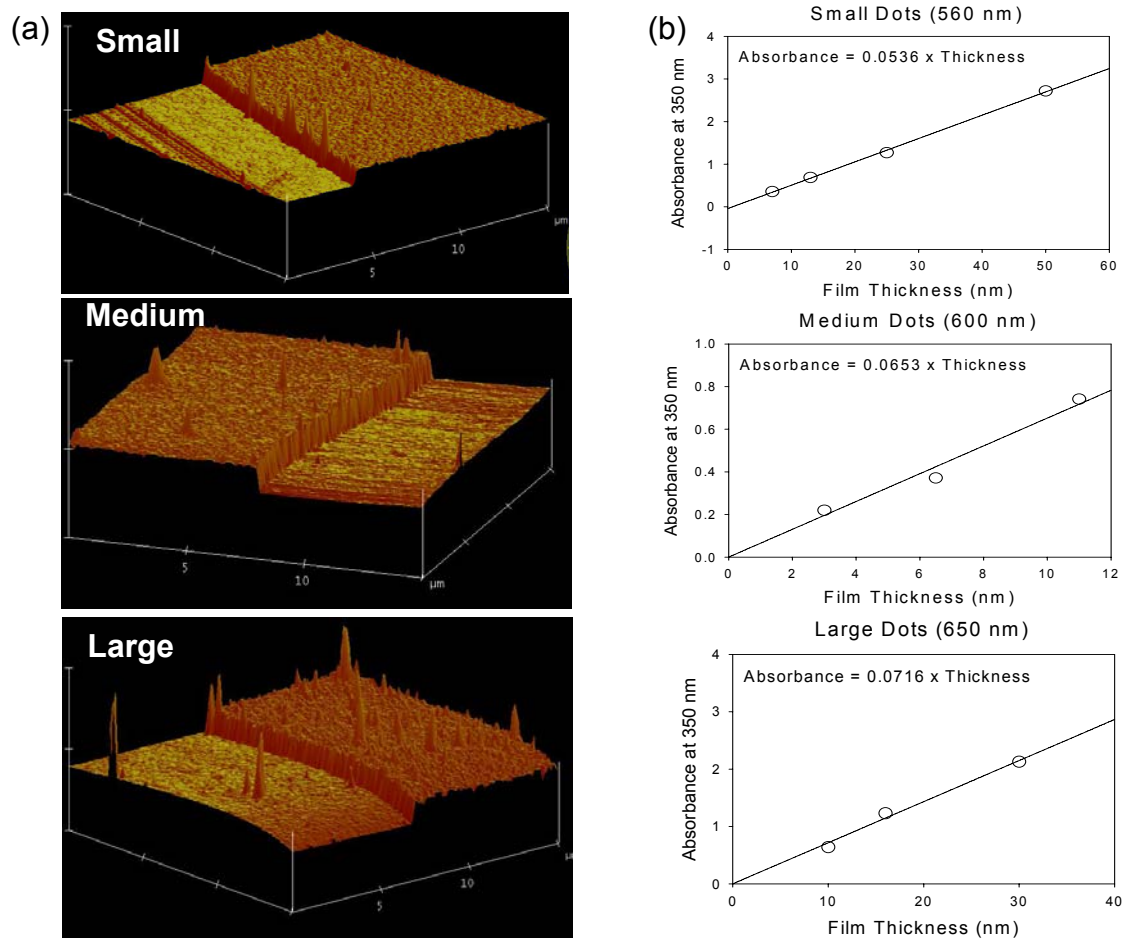


**Figure A.4:** (a) Oblique views of AFM images of the edges of multilayers (sheets) of NCs with diameters of 4.2 nm (S, thickness =  $27.7 \pm 1.5$  nm), 5.3 nm (M, thickness =  $29.0 \pm 1.7$  nm), and 9.8 nm (L, thickness =  $26.4 \pm 4.5$  nm) on glass, made with the same concentrations and spinning conditions used for the films characterized in this study. The uncertainty in the thickness is given by the RMS roughness of the films over an area of  $25 \mu\text{m}^2$ . (b) Calibration curves used to determine the concentration of NC solution from which to spin NC layers of the desired thickness. The calibration curves were made by measuring the height of NC films on glass and plotting it versus the absorbance of the NC solution measured at 350 nm.

### ***Eutectic Gallium Indium Electrode (EGaIn)***

The use of EGaIn as a top-contact allows for easy fabrication of NC junctions in high yield.<sup>13</sup> The eutectic point of Ga/In alloy occurs at approximately 15% indium, at which the melting point depresses to 15.7 °C. Eutectic Ga/In is used commercially as a lubricant in electric

motors, but has yet to be exploited for applications in thin-film devices. It is very well suited for use as an electrode in these devices. The non-Newtonian properties of EGaIn allow it to flow like a liquid, but hold its shape once the shear stress it experiences falls below a characteristic threshold value; EGaIn can therefore form conformal contacts that are smaller than those formed with Hg (the other popular metal for conformal electrodes<sup>17</sup>) when used with apertures of the same diameter. Unlike the evaporation of a top-contact of a solid metal (typically gold), the fabrication of solid-EGaIn junctions does not damage reactive organic materials, form persistent metal filaments that may short the junction, or cause artificially high currents. Eutectic Ga/In junctions are, in general, more stable, and have lower associated cost and toxicity, than Hg-drop junctions, and so have the potential for use in practical devices. EGaIn is particularly suited as an electrode for use with CdSe NCs because its Fermi level ( $E_F \sim -4.2$  eV, an average of that of In and Ga)<sup>18</sup>, is close to the energies of their LUMOs; EGaIn can, therefore, easily exchange electrons with the NCs, unlike Au ( $E_F \sim -5.1$  eV), which forms a so-called “blocking contact”<sup>10,19,20</sup> with many types of semiconductor NCs. Junctions can be created in nearly 100% yield—where yield is the fraction of junctions that did not short from contact between the ITO or PEDOT:PSS and the EGaIn through defects in the film of NCs—using the conformal EGaIn electrode.

Figure A.5 shows the procedure used to prepare EGaIn tips at ambient temperature ( $\sim 298$  K) and under ambient atmosphere. We i) drew EGaIn into a 10  $\mu\text{L}$  gas-tight glass syringe with a permanently affixed metal needle that had been squared off and dulled using a metal file, ii) extruded a small ( $\sim 0.1$   $\mu\text{L}$ ) drop of EGaIn (99.99+%, mp  $\sim 15.7$  °C, used as-received), iii) brought the drop in contact with a bare Ag surface, to which it adhered, iv) slowly ( $\sim 50$   $\mu\text{m/s}$ ) raised it until the tip separated completely from the drop. This process left a tapered drop ( $\sim 0.05$

$\mu\text{L}$ ) of EGaIn on the end of the needle. (The EGaIn remaining on the surface of the Ag was discarded.) This tapered drop is brought into contact with the NC film.

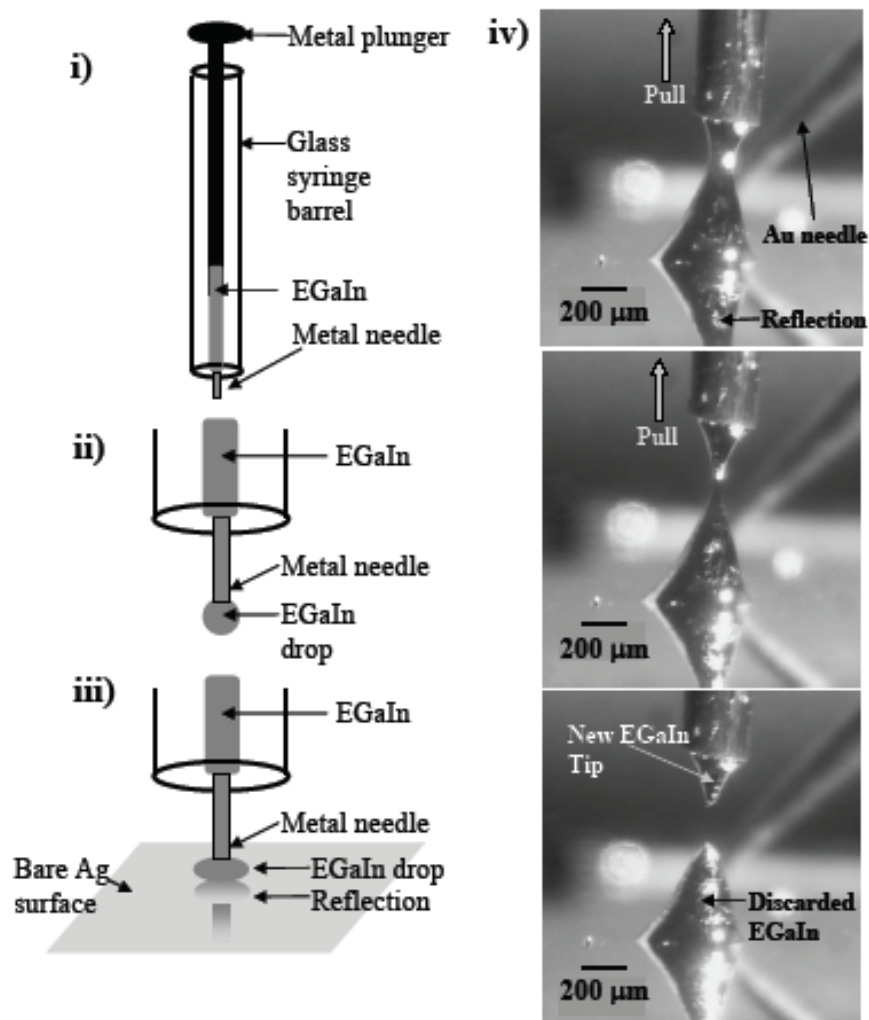


**Figure A.5:** Formation of an EGaIn electrode. We i) drew EGaIn into a glass syringe with a permanently affixed, dulled metal needle, ii) extruded a small drop of EGaIn, iii) brought the drop within a few microns of a bare Ag surface, to which it adhered, iv) slowly raised it until the drop severed. This process left a tapered drop of EGaIn on the end of the needle. The gold counter electrode and reflections of both the counter electrode and the EGaIn appear in the pictures, as labeled.

In order to record current-voltage ( $I$ - $V$ ) traces while illuminating the sample, an electrode is constructed in which EGaIn (99.99+ %, mp 15.7 C°, used as-received) fills the hole in a donut-

shaped disk made of cured poly(dimethylsiloxane). To form the PDMS disk a layer, of PDMS (Silaguard 184) pre-polymer was poured over a silicon wafer to a depth of approximately 1 mm. Immediately after curing for four hours at 60 °C, several circles, 3.5 mm in diameter, were cut out using a biopsy knife. A second circle was cut out in the center of each 3.5 mm circle using a biopsy knife 1 mm in diameter. The resulting PDMS discs were removed from the silicon wafer and transferred to a pre-cleaned glass microscope slide to ensure that no PDMS remained in the smaller-diameter circles in the process. For even contact, EGaIn was injected via a plastic 1 mL syringe fitted with a 20.5 gauge blunt needle directly against the exposed glass in the center of each PDMS disc until enough material was dispensed that it covered slightly more than 1/3 of the PDMS disc. By inspecting the opposite side of the glass slide, a 1 mm mirror, which is formed when the EGaIn wets glass, was clearly visible at the center of each of the discs indicating that the EGaIn had spread evenly against the glass; circles lacking this mirror were discarded. The remaining circles were then peeled off of the glass slide and transferred to each device using a pair of tweezers, taking care that the PDMS circle made conformal contact with the surface of the device as the circle was put into place. The PDMS and EGaIn portions of this electrode adhered conformably to the layer of NCs on the ITO/PEDOT:PSS substrate such that the entire junction could be mounted with the ITO side of the sample facing the excitation source (Figure A.6). Neither the PDMS nor the EGaIn slide or move on the sample even though it is held perpendicular to the bench top.

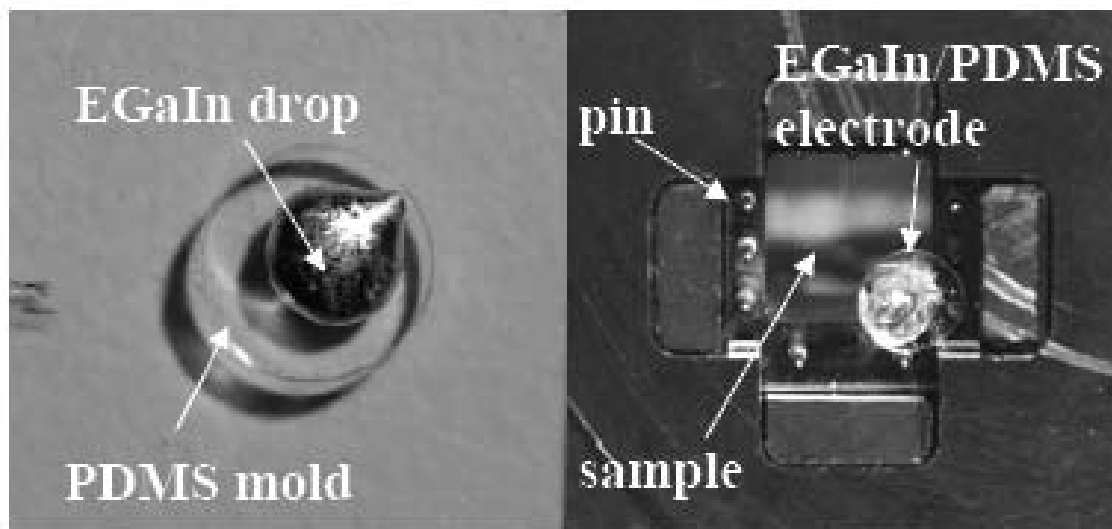


**Figure A.6:** a) Photographs of a PDMS “donut” filled with EGaIn on a glass slide (left), and a sample (in the sample holder) with the EGaIn electrode attached (right).

## A.2.7 Electrical Measurements

### *Forward Bias Measurement Setup*

A schematic of the electrical setup used to measure dark current in the NC junctions is provided in Figure A.7(a). The tapered EGaIn drop contacts the NC film and the junction is imaged with a digital camera at 315 $\times$  magnification to measure the diameter of the NC/EGaIn interface on a size-calibrated computer screen [Figure A.7(b)]. A portion of the surface of the sample where the ITO was exposed is connected to a common electrode (ground) via a gold needle and the circuit is completed by connecting to the EGaIn with a Cu/Sn wire. Current is measured and voltage is sourced with a Keithley Electrometer. The ITO is grounded in all measurements and electrons flowed from ITO to EGaIn when the EGaIn was biased positively with respect to the ITO, and from EGaIn to ITO when the EGaIn was biased negatively with respect to the ITO.<sup>21</sup>



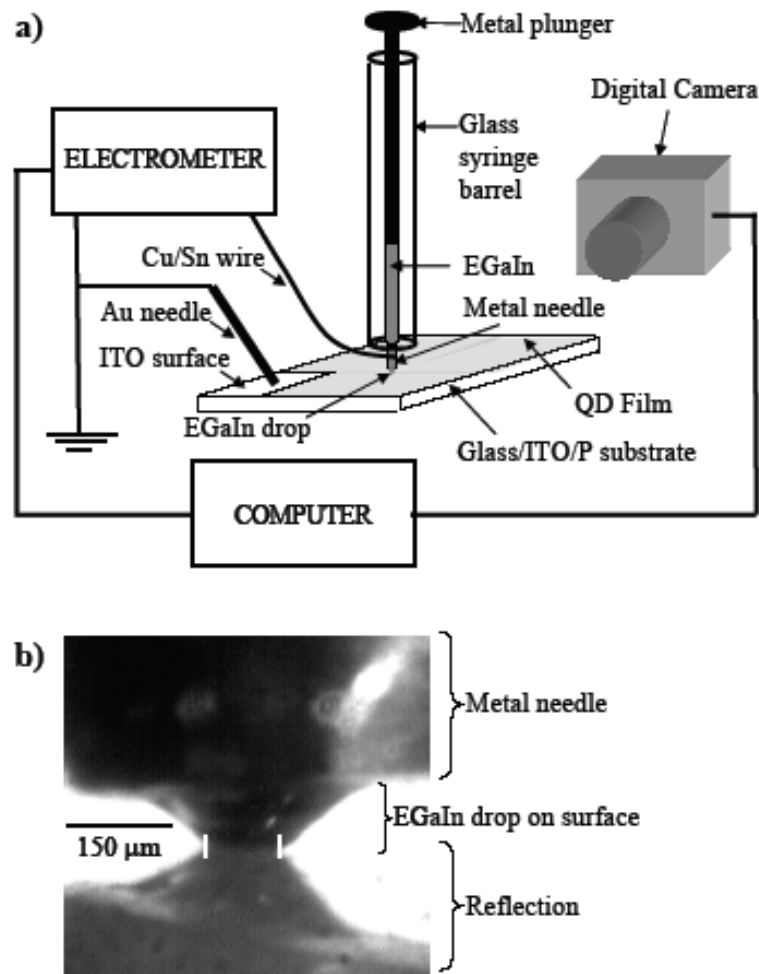


**Figure A.7:** a) Schematic illustration of an ITO/P/NC/EGaIn junction. The electrical circuit is as follows: The EGaIn connects electrically to the metallic needle of the syringe. The electrometer connects to the metallic needle via a metal wire (made of Cu/Sn alloy) wrapped around the needle. A micromanipulator brings the EGaIn into contact with the NC film and the ITO electrode connects to ground via a gold tip in mechanical contact with an exposed area of the ITO surface. We image the junction from the side with a digital camera. b) Digitized, magnified image of the EGaIn drop in contact with a film of NCs. The drop reflects from the surface of the metal stage on which the NC film (on a transparent glass/ITO substrate) sits. We estimated the diameter of the junction for the calculation of  $J$  ( $A/cm^2$ ) by measuring the width of the interface between drop and its reflection (the distance between the two white, vertical lines in this photograph). The diameters (areas) of the junctions ranged from  $\sim 80$  to  $\sim 150$   $\mu m$  ( $5.0 \times 10^{-5}$  to  $5.0 \times 10^{-4}$   $cm^2$ ).

### ***Photocurrent Measurement Setup***

The PDMS and EGaIn portions of this electrode adhered conformably to the layer of NCs on the ITO/PEDOT:PSS substrate such that the entire junction could be mounted with the ITO side of the sample facing the excitation source (Figures A.8). The size of the circular junction (diameter = 1 mm, area = .008 cm<sup>2</sup>) was constant from sample to sample, and equaled the size of the hole cut into the PDMS disk using a biopsy knife. A Pt wire (that was clipped to a cable that went to the electrometer) contacted the EGaIn that protruded from the PDMS, and a pin in the sample holder (connected to ground) contacted a square of exposed ITO on the sample to complete the circuit. Current and voltage were measured and sourced with a Keithley electrometer. For some of the photocurrent measurements the sample was excited with a green (peak excitation at 565 nm, FWHM ~ 10 nm), 5mm LED from Radio Shack (Part # 276-304) or a red (peak excitation at 659 nm, FWHM ~30 nm), 5 mm LED from Radio Shack (Part #276-330). The green LED was operated at the recommended voltage and current (2.1 V, 30 mA) and had a photon density (measured using a Si photodiode) of  $\sim 9.80 \times 10^{13}$  photons/s/cm<sup>2</sup> at a distance of 4 cm. The red LED was operated at the recommended voltage and current (1.8 V, 20 mA) and had a photon density (measured using a Si photodiode) of  $1.30 \times 10^{14}$  photons/s/cm<sup>2</sup>. Other samples were excited with a continuous wave (CW) Ar ion laser, set to 514 or 646 nm which has a higher power (intensity of 10 mW/cm<sup>2</sup> at 646 nm) than the 660-nm LED (intensity of 0.04 mW/cm<sup>2</sup>). These will be distinguished by referring to data as measured with laser or LED excitation. For the photocurrent action spectra (PCA) the tunable excitation source was the SPEX Fluorolog-2 spectrophotometer with a 450 W Hg-Xe arc lamp in combination with a monochromator. The excitation intensity varied as a function of wavelength so data is calibrated

with a silicon photodiode (Thor labs, DET210) to measure the number of photons hitting the sample at each wavelength.

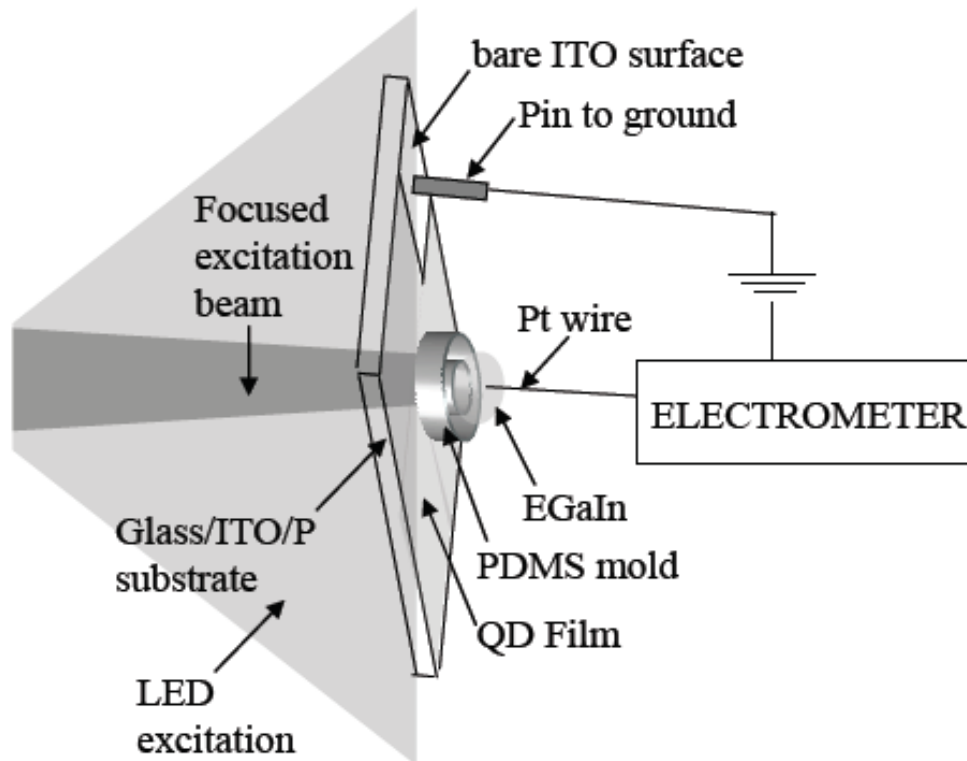


**Figure A.8:** Schematic diagram of the EGaIn junction used for photocurrent experiments: A pin that connects to ground contacts the bare ITO portion of the sample, and a Pt wire that connects to the electrometer is embedded in the drop of EGaIn that protrudes from the PDMS mold. This drop also contacts the NC film. The sample is suspended in the sample holder perpendicular to the excitation source. When the excitation source is the Fluorolog or the Ar laser, the beam is focused down to the area of the sample that contacts the EGaIn ( $.008 \text{ cm}^2$ ). When the excitation source is an LED, the sample is held at a distance of 4 cm from the LED, which emits light with a diffusivity characteristic of the LED.

## **A.3 Results and Discussion**

In this section the results for the conductivity studies of NC arrays composed of multi-sized NCs will be presented. The study will begin with the characterization of the NC arrays and devices used in this study. A discussion of the transport of injected charge over NC/electrode interfaces and through the NC bulk film follows. Finally, the origin of exciton separation is determined, the conduction of photogenerated current is characterized, and the potential use of NC arrays as a photovoltaic material is examined.

### **A.3.1 CdSe NC Film Characterization**

In order to confirm that the NC array consists of stacked layers of different sized NCs and not an inhomogeneous mixture of all sizes, a cross-section of the NC array is imaged with TEM and the results are displayed in Figure A.9. Both images clearly show three distinct layers of NCs of different sizes, and the right image even shows the lattice fringes of the individual NCs. The layer of small dots is thinner than 25 nm, probably because the spinning conditions were not optimized for the epoxy substrate.

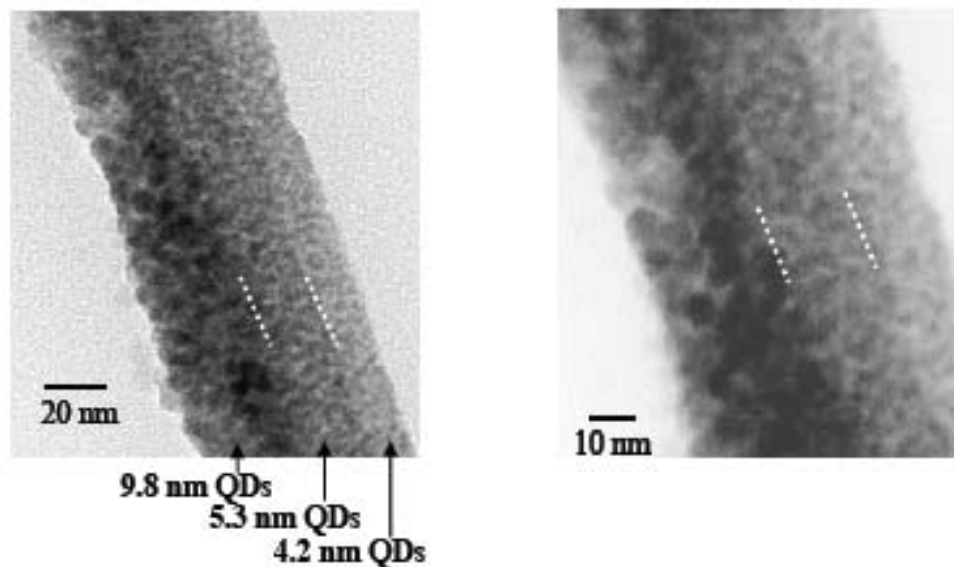


**Figure A.9:** Left - TEM micrograph of a cross-section of the multi-size NC film (on a lacey carbon grid) showing the stratified distribution of sizes of NCs. Right - HRTEM micrograph showing the details of the layer and the lattice fringes in individual NCs. White dashed lines indicate boundaries between the layers of different sizes of NCs.

The NC films have been treated with butylamine and annealed at low temperature; however, to confirm that the NCs have not sintered the absorbance spectrum of a butylamine treated film of each size of NC is provided in Figure A.10. There is a slight 1-5 nm shift in the position of the band edge resulting from increased electronic coupling between NCs in the array, but there are still quantized features in all of the absorbance spectra and the band gap has not shifted to that of bulk CdSe (~710 nm).

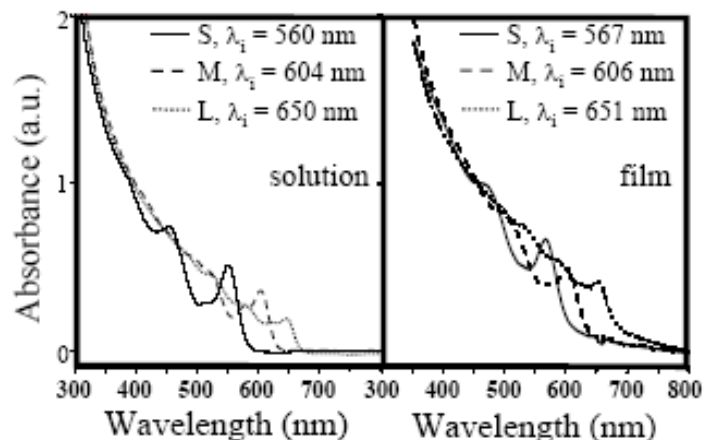


**Figure A.10:** Ground state absorption spectra of the S, M, and L NCs in a hexane solution (left, with concentrations:  $1 \times 10^{-5}$  M (L),  $6.5 \times 10^{-5}$  M (M),  $1 \times 10^{-4}$  M (S)) and in butylamine-treated films (right) spun on glass from  $\text{CHCl}_3$  solutions of the same concentrations. The symbol  $\lambda_1$  indicates the wavelength of the maximum of the band-edge absorption. This maximum is at lower energy in the spectra of the films than in the spectra of the solutions due to electronic interaction between the NCs in the film.

Figure A.11 shows a simplified electronic structure diagram of the ITO/P/NC/EGaIn junction that is used to discuss the observed electrical characteristics: the energy levels of the highest occupied molecular orbital (HOMO) and lowest unoccupied molecular orbital (LUMO) for each size of NC, the Fermi levels of the ITO<sup>22</sup> and EGaIn electrodes,<sup>17</sup> and the conduction band (CB) and valence band (VB) of PEDOT:PSS. The energy levels of the LUMOs of the NCs equal the sum of the optical bandgaps,  $E_g$ , and the energies of the HOMOs (as calculated using the Effective Mass Approximation).<sup>23</sup> The uncertainty in these energies, indicated by the width (along the energy axis) of the levels in the figure, is the full-width-at-half-max of the band-edge absorption peaks that yielded  $E_g$ . In CdSe, the effective mass of the electron is significantly smaller than the effective mass of the hole ( $m_e = 0.13m_0$ ,  $m_h = 1.14m_0$ , where  $m_0$  is the mass of a free electron); therefore, most of the increase in bandgap increase from larger NCs to smaller NCs appears as a shift in their LUMOs.<sup>24</sup>

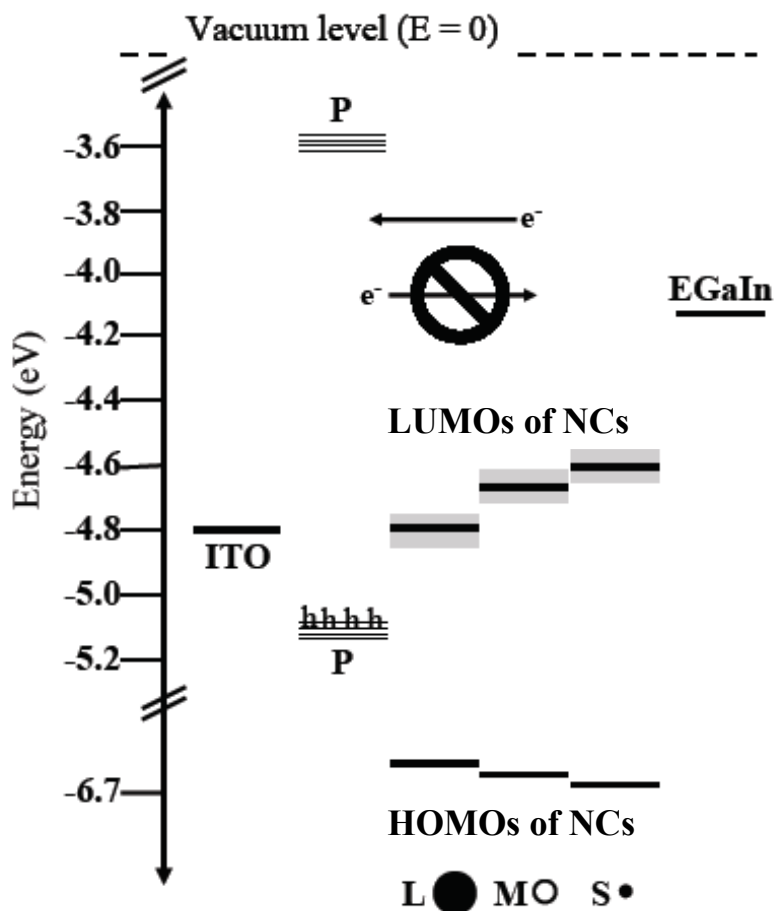


**Figure A.11:** Energy diagram for the ITO/P/NC/EGaIn junctions: the Fermi level of ITO, the valence and conduction bands of PEDOT:PSS (P), the LUMOs of the S, M, and L dots (calculated from the energies of the HOMOs and the measured optical bandgaps), and the Fermi level of EGaIn. The energetic width of the LUMOs of the NCs (gray boxes) is determined by the FWHM of the band-edge absorption peak. Electrons flow from EGaIn to ITO, but not from ITO to EGaIn. The symbol “h” in the VB of PEDOT:PSS indicates the presence of uncharged (counterion-stabilized) holes.

### A.3.2 Forward Bias Measurements – Potential of NC Gradient as a n-type Charge Transport Layer

To determine if electrons, and/or holes, can be injected into, and transport through, the NC array,  $J$ - $V$  data was collected by scanning the voltage either in a range of  $V = -0.5$  to  $+0.5$  V (in steps of 0.05 V) for the junctions LLL, LMS, LLS, and MMM, or a range of  $V = -2.0$  to  $+2.0$

V (in steps of 0.2 V) for the junctions SL, SML, and SSS. (These ranges were chosen after determining the values of  $V_{\text{ON}}$ ). Current is recorded after allowing the junction to equilibrate at the specified voltage for 2 s, and the current is divided by the area of the junction to obtain  $J$ . For the range  $V = -x$  to  $+x$ , one  $J$ - $V$  trace was defined as  $0 \rightarrow +x \rightarrow -x \rightarrow 0$ . Figure A.12(a) shows plots of  $J$  vs.  $V$  for  $\mathbf{X} = \text{LLL}$  and  $\mathbf{X} = \text{SSS}$ . These plots are intended to illustrate the shape of the  $J$ - $V$  curves; Figures A.12(b) and A.12(c) show the error analysis. The asymmetry of the  $J$ - $V$  curves around  $V = 0$  V is representative of that for all of the junctions. They are diodes: electrons flow—at values of  $V$  more negative than  $V_{\text{ON}}$ —from EGaIn to ITO, but not from ITO to EGaIn.<sup>27</sup>

The value for  $J$  for a particular  $V$  in Figure A.12(c) is the log-mean of  $J$  (defined as  $\langle J \rangle_{\log} = 10^{\langle \log J \rangle}$ , where  $\langle \log J \rangle$  is the mean value of  $\log(|J|)$ ) rather than the arithmetic mean ( $\langle J \rangle$ ). We used  $\langle J \rangle_{\log}$  because we observed that, with the exception of  $\mathbf{X} = \text{SL}$ , the values for  $\log(|J|)$  appeared to be distributed normally, while the values for  $J$  did not.<sup>17</sup> Figure A.12(b) gives an example of a histogram for the values of  $\log(|J|)$  for  $\mathbf{X} = \text{LMS}$ . One explanation for the apparent normal distribution of  $\log(|J|)$  is that  $J$  depends exponentially on a physical parameter that is distributed normally, such as the electric field ( $E$ ) across the junction ( $E = V/L$ , where  $L$  is the thickness of the junction). In that case, inhomogeneous disorder in  $L$  could cause  $L$  (and, in turn,  $E$ ) to be distributed normally, and would lead to the observed variation in  $J$ .

Figure A.12(c) shows plots of the absolute value of  $\langle J \rangle_{\log}$  vs.  $V$  for all of the junctions. The standard deviation ( $\sigma$ ) of the Gaussian functions used to fit each of the histograms yielded the error bars in this figure—that is, each point is  $\langle J \rangle_{\log} \pm \sigma$ . We used data from at least four locations on each of two separately-prepared samples (the number of data for each junction is in



the caption to Figure A.12) to compute  $\langle J \rangle_{\log}$  and  $\sigma$ . For  $\mathbf{X} = \text{SL}$ , neither  $J$  nor  $\log(|J|)$  appeared to be distributed normally, possibly because SL was the junction on which we gathered the fewest traces. For  $\mathbf{X} = \text{SL}$ , the average values of  $J$  plotted in Figure A.12(c) are  $\langle J \rangle_{\log}$ , but the error bars equal the total range in  $J$  that we measured, rather than  $\sigma$ .

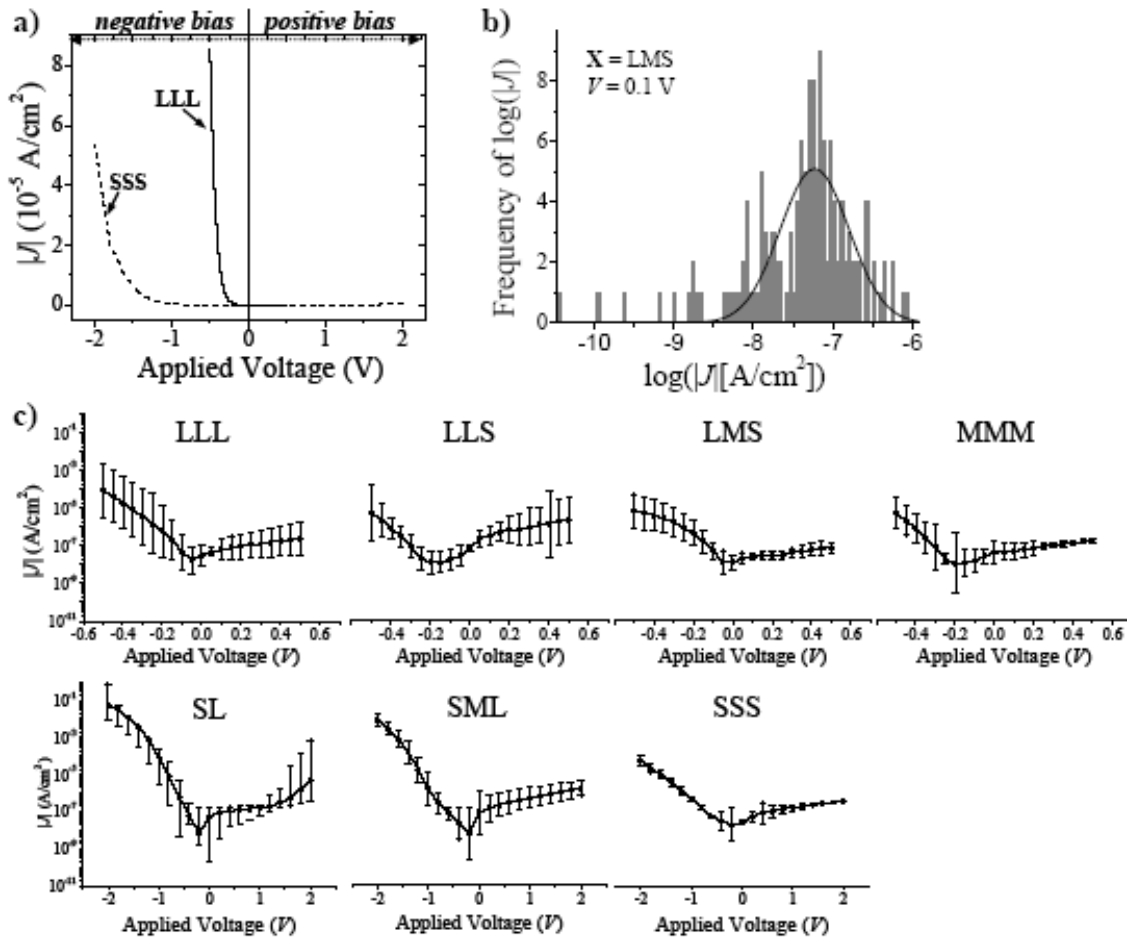


**Figure A.12:** a) Plots of the absolute value of  $\langle J \rangle_{\log}$  (defined in the text) vs.  $V$  (the difference in voltage between the ITO and EGaIn electrodes) for the junctions ITO/P/X/EGaIn,  $\mathbf{X} = \text{LLL}$  ( $V = +0.5 \text{ V} \rightarrow -0.5 \text{ V}$ ) and SSS ( $V = +2.0 \text{ V} \rightarrow -2.0 \text{ V}$ ). The junctions are diodes: they are “on” when the EGaIn is biased negatively with respect to the ITO (labeled “negative bias”), so electrons flow from EGaIn to ITO, but not vice versa. Table A.1 lists the turn-on voltages,  $V_{\text{ON}}$ , for each junction. b) A histogram of all measured values of  $\log |J|$  (with 100 bins) for  $\mathbf{X} = \text{LMS}$  at  $V = 0.1 \text{ V}$ . We fit each histogram with a Gaussian function with standard deviation  $\sigma$ , except for the data for  $\mathbf{X} = \text{SL}$ , which did not appear to be distributed normally. c) Plots of the absolute value of  $\langle J \rangle_{\log} \pm \sigma$  (where  $\langle J \rangle_{\log} = 10^{(\log J)}$ , and  $\langle \log J \rangle$  is the mean value of  $\log(|J|)$ ) vs. voltage

for all of the junctions (except for X = SL, for which the error bars indicate the total range in  $J$  that we measured). Data from at least four locations on each of two separately-prepared samples—for a total of 260 values (LLL), 48 values (LLS), 138 values (LMS), 188 values (MMM), 30 values (SL), 114 values (SML), 88 values (SSS) of  $J$ —were used to compute the average and the uncertainty.

### ***Origin of Rectification***

#### *The “Off” State*

In these devices, there is negligible net flow of electrons from ITO through the NCs to the EGaIn—that is, transport of electrons from ITO to EGaIn, transport of holes EGaIn to ITO, or some combination of the two. There are several aspects of these devices that restrict both of these processes (at least at the values of  $V$  we applied: 0 V  $\rightarrow$  +2.0 V): i) EGaIn could not inject holes into the NCs (that is, oxidize the NCs) because the voltages that we applied were not large enough to bring the energies of the HOMOs of the NCs ( $\sim$ 6.5 – 6.7 eV) above the Fermi level of EGaIn ( $\sim$ 4.15 eV) (Figure A.11). ii) PEDOT:PSS is an electron blocking ( $p$ -type conducting) layer. Its electrical conductivity ( $\sim$ 1 S/cm) comes from the oxidized ( $p$ -doped) PEDOT component, which induces a planar geometry in which the thiophene rings are fully conjugated to one another, and allows for the formation of vacant mid-gap electronic states (charge carriers). The transfer of electrons from ITO to PEDOT:PSS drastically decreases the conductivity of the polymer by annihilating charge carriers (de-doping the PEDOT component) and returning the polymer to the less conjugated benzenoid geometry.<sup>16,26</sup> iii) Electrons that arrived at the PEDOT:PSS/NC interface were trapped (because the VB of PEDOT:PSS ( $\sim$  -5.2 eV) is lower in energy than the LUMOs of the NCs ( $\sim$  -4.8 to -4.6 eV), and because there were no holes in the NC layer with which to combine.

We believe that these three factors combine to prevent flow of electrons—except for a small ( $\sim 10^{-8} - 10^{-7} \text{ A/cm}^2$ ) leakage current—from the ITO to the EGaIn in all of the junctions. We believe that this leakage current originated from thermally excited charge carriers in the NC layers. The mechanism for the leakage current became apparent in our study of photocurrent—discussed in detail in section A.3.3—where the density of charge carriers was amplified by photoexcitation.

The junction ITO/P/EGaIn (with no NCs) showed the same diode-like behavior as the junctions with the NCs (Figure A.13). Electrons injected into PEDOT:PSS were trapped because the voltages that we applied were not large enough to bring the energy of the VB of PEDOT:PSS ( $\sim -5.1 \text{ eV}$ ) into resonance with the Fermi level of EGaIn ( $\sim -4.15 \text{ eV}$ ). This trapping of charge in the polymer film manifested itself as hysteresis in the  $J$ - $V$  curve for the ITO/P/EGaIn junction.

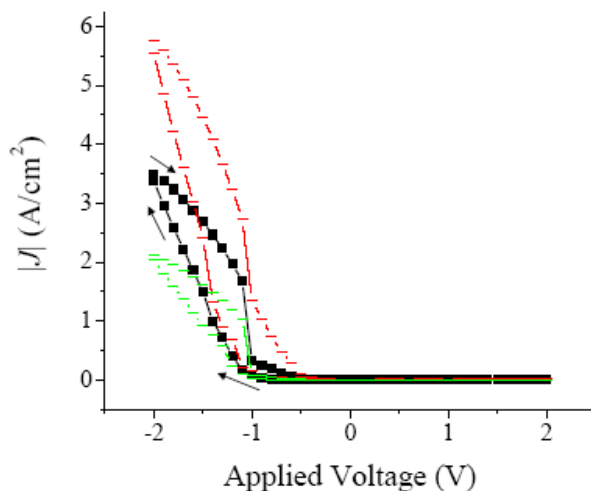


**Figure A.13:** Absolute value  $J$  vs.  $V$  for the junction ITO/P/EGaIn, where  $J = \langle J \rangle_{\log}$ . The error bars (red and green traces) are given by the standard deviation of  $\log J$ . We acquired a total of twelve traces at four different locations on one sample to construct this plot. The junction is “on” when the EGaIn electrode is biased negatively with respect to the ITO electrode. The hysteresis is probably due to discharging of the polymer upon the application of negative potential. The arrows indicate the progression of  $J$  as we scanned from  $V = 0 \rightarrow V = +2.0 \text{ V} \rightarrow V = -2.0 \rightarrow V = 0$  in steps of 0.1 V.

### *The “On” State*

We observed the flow of electrons from EGaIn to ITO when EGaIn was biased negatively with respect to the ITO (for  $|V| > |V_{ON}|$ ), through, we believe, the following set of processes: i) EGaIn injected electrons into the LUMOs of the layers of NCs until the energy required for further injection exceeded the applied voltage. At this “saturation” point, some fraction of the NCs were reduced.<sup>6,27,28</sup> ii) To maintain overall neutrality of charge, positive charges collected in the PEDOT:PSS, and moved to the interface between PEDOT:PSS and the NCs. Positive charge built up at this interface until the holes combined with electrons in the LUMOs of the adjacent partially-reduced NC layers. (The oxidation potential of the NCs is too high for electrons from the HOMOs of the NCs to recombine with holes from the PEDOT:PSS, see Figure A.11) iii) Charge annihilation—combination of electrons from the NCs and holes from the PEDOT:PSS—at the NC/PEDOT:PSS interface resulted in net flow of electrons from the EGaIn to the ITO.

### *What determines $V_{ON}$ ?*

For each junction, we observed a turn-on voltage,  $V_{ON}$ —that is, a voltage at which “significant” current (current beyond that caused by leakage of thermally excited or photoexcited charge carriers into the external circuit) began to flow through the device. We identified  $V_{ON}$  as follows: by inspecting the plots of  $J$  vs.  $V$  (at  $V < 0$ ), we found the value of  $V$  at which  $J$  began to increase with  $|V|$  at a rate faster than it did in its off state (i.e., under positive bias). We then defined  $V_{ON}$  as the midpoint between that voltage and voltage with the next higher measured magnitude. For example, if we identified  $V = -0.8$  V as the voltage at which  $J$  began to increase with  $|V|$  at a rate faster than it did in its off state, and the next higher voltage were  $-1.0$  V, then  $V_{ON}$  would equal  $-0.9$  V.

We also estimated  $V_{\text{ON}}$  from the plots of the lower and upper error bars of  $\langle J \rangle_{\log}$  vs.  $V$

[Figure A.12(c)]; these three values of  $V_{\text{ON}}$  defined the range in Table A.1 and Figure A.14.

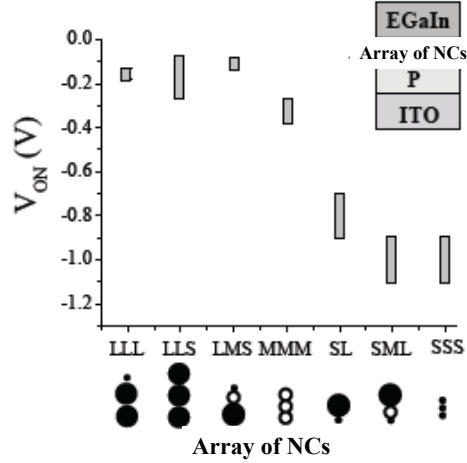


**Figure A.14:** Ranges for the turn-on voltage for all of the junctions studied (Table A.1). The text explains the procedure used to estimate  $V_{\text{ON}}$ . The diagram in the upper right corner of the plot shows the orientation of the arrays of NCs (listed along the x-axis) in the junction.

**Table A.1:** Dark Electrical Characteristics of the Junctions ITO/P/X/EGaIn: Turn-on Voltage ( $V_{\text{ON}}$ ), Resistivity ( $\rho_0$ ), Characteristic Voltage ( $V_0$ ), and Change in Free Energy ( $\Delta G$ ) and Activation Barrier ( $E_A$ ) for the reaction  $\text{NC/PEDOT:PSS}^+ \rightarrow \text{NC/PEDOT:PSS}$

X	$V_{\text{ON}}$ (V) <sup>a</sup>	$\Delta G$ <sup>b</sup>	$E_A$ (eV) <sup>c</sup>	$\rho_0$ ( $\Omega \cdot \text{m}/10^{14}$ ) <sup>d</sup>	$V_0$ (mV) <sup>d</sup>
LLL	-0.13 $\rightarrow$ -0.18	-0.58	0.58	0.70	72
LLS	-0.08 $\rightarrow$ -0.28	-0.58	0.58	0.029	180
LMS	-0.08 $\rightarrow$ -0.13	-0.58	0.58	( $V = -0.15 \rightarrow -0.3$ V): 0.64 ( $V = -0.3 \rightarrow -0.5$ V): 0.085	91 230
MMM	-0.28 $\rightarrow$ -0.38	-0.69	0.87	100	55
SL	-0.70 $\rightarrow$ -0.90	-0.78	1.2	( $V = -0.8 \rightarrow -1.4$ V): 37 ( $V = -1.4 \rightarrow -2.0$ V): 0.014	100 240
SML	-0.90 $\rightarrow$ -1.1	-0.78	1.2	( $V = -1.0 \rightarrow -1.5$ V): 300 ( $V = -1.5 \rightarrow -2.0$ V): 0.26	110 210
SSS	-0.90 $\rightarrow$ -1.1	-0.78	1.2	16	250

<sup>a</sup>The turn-on voltage ( $V_{\text{ON}}$ ) is given as a range ( $V_1 \rightarrow V_2$ ); see the text for the procedure for estimating the range.

<sup>b</sup>See equation 4b. <sup>c</sup>See equation 5; for this calculation,  $\lambda = 0.1$  eV. <sup>d</sup>From a fit of the data in Figure 10 to the equation  $J = V/(\rho_0 L) \exp(-|V|/V_0)$  for  $|V| > |V_{\text{ON}}|$ .

## ***Electron Injection and Extraction***

### *Identification of the Current-Limiting Step in the Flow of Electrons from EGaIn to ITO.*

In order to determine which step (of steps (i), (ii), and (iii) listed in the previous section) limited the current at  $|V| < V_{\text{ON}}$ , trends in the values of  $V_{\text{ON}}$  are examined in the various arrays. It is clear that  $|V_{\text{ON}}|$  was lowest for the junctions where the large NCs were adjacent to the PEDOT:PSS, and highest for the junctions where the small NCs were adjacent to the PEDOT:PSS. This trend suggests that the step that determines the magnitude of the current through the device is step (iii), the electron transfer from the NC having an extra electron to the electron-deficient PEDOT:PSS—that is, the annihilation reaction  $\text{PEDOT:PSS}^+/\text{NC}^- \rightarrow \text{PEDOT:PSS}/\text{NC}$ . It appears that the larger the gap between the energy of the LUMOs of the NCs at the interface and the energy of the VB of PEDOT:PSS (Figure A.11), the larger the electric field needed to induce this reaction.

*What dictates the rate of the charge annihilation reaction at the NC/PEDOT:PSS interface?*

The importance of alignment of electron donor and acceptor levels—here, the electron donor is the reduced NC ( $\text{NC}^-$ ) and the electron acceptor is the oxidized polymer ( $\text{PEDOT:PSS}^+$ )—for conduction of electrons across an interface between an active material, such as an array of NCs or a film of polymer or molecules, and its electrode is well-recognized.<sup>29,30</sup> However, it is not immediately obvious why the annihilation reaction  $\text{PEDOT:PSS}^+/\text{NC}^- \rightarrow \text{PEDOT:PSS}/\text{NC}$ , which is exothermic ( $\Delta G < 0$ ) for all of the sizes of NCs studied required an electric field to occur, or why the rate of this reaction depended inversely on the size of the gap between the LUMOs of the NCs and the valence band of PEDOT:PSS.

These two questions can be answered by writing down an expression for the rate constant,  $k_{eT}$ , for an electron transfer reaction between two components that are not intimately electronically coupled (through a covalent bond or a highly conjugated series of covalent bonds) (Equations A.1a and A.1b). These equations, which are derived from Fermi's Golden Rule,<sup>31</sup> give the rate

$$k_{eT} = \frac{2\pi}{\hbar} V_{el}^2 FC \quad (\text{A.1a})$$

$$FC = \sum_i \sum_j \rho_i \langle \chi_{Pj} | \chi_{Ri} \rangle^2 \delta(\varepsilon_{Pj} - \varepsilon_{Ri}), \quad (\text{A.1b})$$

of a transition from a vibronic manifold of reactant states  $\{i\}$  to a vibronic manifold of product states<sup>33</sup>, with two assumptions: i) that the Born-Oppenheimer approximation is valid, and ii) that the system is in thermal equilibrium—that is, the population of the states in the reactant manifold follows a Boltzmann distribution ( $\rho_i$ ).<sup>31,33</sup> In Equations A.1a and A.1b,  $\chi_{Ri}$  and  $\chi_{Pj}$  are the equilibrium nuclear wavefunctions for the reactant (PEDOT:PSS<sup>+</sup>/ NC<sup>-</sup>) at level  $i$  (with energy  $\varepsilon_{Ri}$ ) and product (PEDOT:PSS/NC) at level  $j$  (with energy  $\varepsilon_{Pj}$ ), respectively,  $V_{el}$  is the overlap of the electronic wavefunctions of the reactant and product, and  $\delta(\varepsilon_{Pj} - \varepsilon_{Ri})$  ( $= 1$  for  $\varepsilon_{Pj} = \varepsilon_{Ri}$  or  $0$  for  $\varepsilon_{Pj} \neq \varepsilon_{Ri}$ ) is a delta function that expresses the important requirement that the transition can only occur at a nuclear configuration where the reactant and product states are degenerate in energy (i.e., the point at which their potential energy surfaces cross). The thermally averaged vibronic overlap between the potentials of the reactant and product states (the set of probabilities that the reactant and product species will simultaneously be in nuclear configurations such that they are energetically degenerate) is the Franck-Condon weighted density of states ( $FC$ ).<sup>34,35</sup>

Equations A.1a and A.1b imply that the greater the overlap (energetically) of the densities of states of the reactant and product—i.e., the bigger the value of  $FC$ —the faster the

reaction. Calculation of Franck-Condon factors is difficult. Marcus developed a method by which  $FC$  is expressed as a function of  $\Delta G$ , and a parameter called the reorganization energy ( $\lambda$ ).<sup>36-38</sup> The reorganization energy is that needed to reorganize the geometries of the reactant and product (and the solvent molecules, if present) such that the electron transfer can take place. In addition to its traditional role in predicting rate constants in solution-phase molecular systems and proteins,<sup>39,40</sup> Marcus theory has proven a valuable tool to describe resonant electron transfer within arrays of NCs,<sup>41</sup> and heterogeneous electron transfer within dye-sensitized nanocrystalline solar cells,<sup>42</sup> across metal-organic interfaces,<sup>35,43</sup> and between CdSe NCs and TiO<sub>2</sub> NCs.<sup>44</sup>

In Marcus theory, the electron transfer is coupled to a single averaged nuclear mode of energy  $\hbar\omega$  (such that  $\lambda = S\hbar\omega$ , where  $S$  is the Huang-Rhys factor, the strength of the coupling between the electronic transition and the relevant vibration) and the potential surfaces of the reactant and product are reduced to two parabolas, Equations A.2a and A.2b. The two parabolas are

$$U_R(Q) = \frac{\hbar\omega}{2} Q^2 \quad (\text{A.2a})$$

$$U_P(Q) = \frac{\hbar\omega}{2} (Q - \Delta)^2 + \Delta G \quad (\text{A.2b})$$

separated by  $\Delta G$  along the potential energy ( $U$ ) axis, and by  $\Delta$  along the nuclear coordinate ( $Q$ ) axis. In the classical limit (where  $kT > \hbar\omega/4$ ),  $FC$  converges to the form in Equation A.3.<sup>36</sup> The definition for  $\lambda$ , and Equations 2a and 2b, yield an expression for the activation energy (eq.A. 4).

$$FC = \frac{1}{\sqrt{4\pi\lambda kT}} \exp(-E_A / kT) \quad (\text{A.3})$$

$$E_A = \frac{(\Delta G + \lambda)^2}{4\lambda} \quad (\text{A.4})$$



It is assumed that the charge annihilation reaction  $\text{PEDOT:PSS}^+/\text{NC}^- \rightarrow \text{PEDOT:PSS}/\text{NC}$  is coupled only to the C=C stretching mode within the PEDOT chains ( $\hbar\omega \sim 1500 \text{ cm}^{-1}$ );<sup>39,46</sup> since  $kT > \hbar\omega/4$ , the classical Marcus equations (A.3 and A.4) can be used to calculate the barriers for this reaction. Estimating  $\lambda$  in doped conducting polymers is complicated, due to the effects of counterion stabilization and “pre-reorganization” of nuclei upon doping. A reasonable estimate for  $\lambda$  is 0.1 eV ( $S = 0.54$ ), which is approximately the internal reorganization energy for the process of positively charging and discharging pentacene, which, like oxidatively doped PEDOT, is a flat, highly conjugated organic system.<sup>38,46</sup>

Table A.1 contains the values of  $\Delta G$  (in Equation 4) for the reaction  $\text{PEDOT:PSS}^+/\text{NC}^- \rightarrow \text{PEDOT:PSS}/\text{NC}$  for each of the junctions.  $\Delta G$  is approximated to be the difference in energy between the VB of PEDOT:PSS and the LUMO of the NCs in the adjacent layer (the additional contribution of Coulomb forces to the free energy difference between these two states is discussed in the next section). For all of the junctions,  $\Delta G > \lambda$ , which puts this reaction in the so-called Marcus inverted region.<sup>35</sup> The parabolas for the reactant and product states (which are defined by equations that have the form of Equations A.2a and A.2b) look like those in Figure A.15.

From Figure A.15, it is clear that, as  $\Delta G$  increases, the difference in energy between the minimum of the potential well of the reactant state and the point at which the reactant and product surfaces cross also increases. Since the reaction can only occur at this crossing point (as dictated by Equation A.1), this difference in energy is the activation energy for the reaction,  $E_A$ . Qualitatively, the activation barrier  $E_A$  is caused by a decrease in the vibronic overlap (or Franck-Condon factor,  $FC$ ) between reactant and product surfaces as their minima are moved further apart energetically. Table A.1 contains the values of  $E_A$  for this reaction for each of the

junctions, calculated using the Marcus equations (Equations A.3 and A.4). As the NCs at the interface with PEDOT:PSS get smaller in size, the energetic barrier for charge transfer increases ( $E_A = 0.58$  eV (LX), 0.87 eV (MX), 1.2 eV(SX)), and the annihilation reaction slows. The values for  $E_A$  depend, of course, on the choice of  $\lambda$ , but since  $\lambda$  is the same for all of the junctions, this choice does not affect our qualitative prediction for the trend in the height of the tunneling barrier as a function of the size of the NCs at the interface.

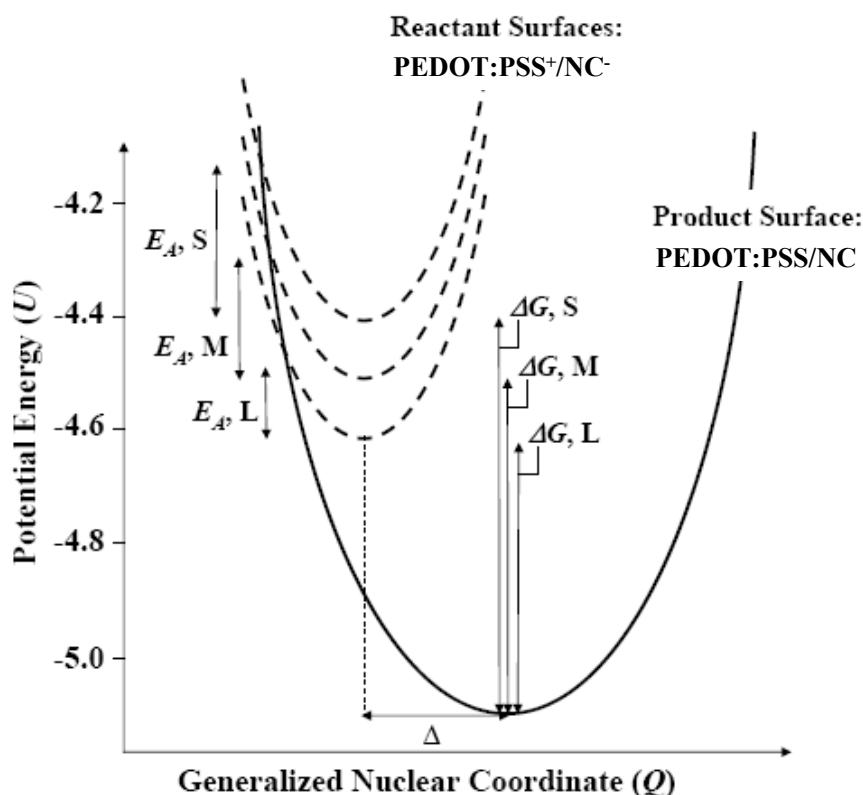


**Figure A.15:** Hypothetical parabolic potential energy surfaces (potential energy was not calculated) for the reactant ( $\text{NC}^-/\text{PEDOT:PSS}^+$ ) and product ( $\text{NC}/\text{PEDOT:PSS}$ ) states for the charge annihilation reaction at the NC/PEDOT:PSS interface when the reaction is in the Marcus inverted region ( $-\Delta G > \lambda$ ). We assume that  $\Delta G$  for the reaction is the difference in energy between the LUMO of the NCs (minima of the reactant parabolas) and the top of the VB of PEDOT:PSS (minimum of the product parabola). As  $\Delta G$  increases, the activation barrier for the reaction,  $E_A$ , increases, and the rate slows (Equations A.1a, A.3, A.4). In general, these parabolas have a form dictated by Equations A.2a and A.2b; in our case  $\hbar\omega$  from these equations is the energy of the C-C stretching mode in PEDOT ( $1500\text{ cm}^{-1}$ ).

*Mechanism of Turn-On: A Coulomb Force Overcomes the Barrier at the NC/PEDOT:PSS Interface.*

Before the predicted trend in activation barriers ( $E_A(\text{LX}) < E_A(\text{MX}) < E_A(\text{SX})$ ) can be connected to the observed trend in  $V_{\text{ON}}$  ( $|V_{\text{ON}}|(\text{LX}) < |V_{\text{ON}}|(\text{MX}) < |V_{\text{ON}}|(\text{SX})$ ), we must discuss how applied voltage allows the electrons in the NCs to overcome the barrier at the NC/PEDOT:PSS interface. Figure A.16 shows two representations of the problem, the “Energy Gap” (left) and “Tunneling Barrier” (right) representations. Two states must be in resonance in order for an electron to tunnel from one to the other (Equation A.1). The two non-resonant states—shown in the Energy Gap representation—must be perturbed such that they are brought into resonance; the degree of perturbation that is necessary may be represented by a tunneling barrier between two resonant states. (Marcus theory (Equation A.4) is one method—and the method we have chosen here—for relating the energy gap ( $\Delta G$ ) to the height of the barrier ( $E_A$ )).

At  $|V| < |V_{\text{ON}}|$ , electrons accumulate in the NCs, and holes accumulate in the PEDOT:PSS at the interface between the two materials. There are two major effects of this charge accumulation: i) [Figure A.16(a)] As  $|V|$  increases, electrons are added to the LUMOs of the NCs (probably just a single electron per NC<sup>6</sup>), and the energies of the LUMOs increase.<sup>47</sup> ii) [Figure A.16(b)] The potential energy of electrons in the NCs near the interface decreases because they are coulombically stabilized by the presence of positive charges in the adjacent PEDOT:PSS layer. These two effects compete to determine the fate of the charges at the interface. As is shown in Figure A.16(a), effect i) brings the electron-donating and electron-accepting states in the two materials further out of resonance, and therefore *does not* promote charge annihilation.<sup>48-50</sup> Effect ii) [Figure A.16(b)] imposes a Coulomb force on the electrons and holes; this force *does* promote charge annihilation.

Clearly, since charge annihilation is observed—in the form of the device turning on—effect ii) must ultimately dominate, probably because the magnitude of the energetic perturbation of energy levels at the interface (effect i)) is small relative to the attractive force between two charges separated by only nanometers: The increase in the energy of a LUMO of a NC due to its population with an electron is, approximately, the difference between the second reduction potential,  $E_{red}^2$ , and the first reduction potential,  $E_{red}$ , of the NC ( $\sim 0.25 \text{ V}^{51}$ ). The potential energy of an electron a distance  $d$  from a positively-charged hole (assuming no dielectric screening) is lowered by  $\Delta U = q_1 q_2 / 4\pi\epsilon_0 d$ . We do not know the average distance between electrons and holes at the interface, but, even if  $d = 10 \text{ nm}$ , and each negative charge “sees” only one positive charge,  $\Delta U = 0.14 \text{ eV}$ . In reality, each negative charge sees many positive charges over a distribution of  $d$ 's (where  $10 \text{ nm}$  is probably at the high end of this distribution). It is thus probable that effect ii) (the Coulomb force, Figure A.16b) dominates effect i) (the increase in  $\Delta G$ , Figure A.16a).

If, in fact, the mechanism of turn-on is that a Coulomb force at the interface overcomes the barrier for charge annihilation caused by the offset in energy levels, then the height of the barrier would determine the magnitude of the force and, in turn the voltage, that is necessary to precipitate annihilation. Based on the calculations of  $E_A$  using Marcus theory, we would then predict that  $|V_{ON}|(\text{LX}) < |V_{ON}|(\text{MX}) < |V_{ON}|(\text{SX})$ , which is the trend we observed (Figure A.14 and Table A.1). Figure A.14 also shows that  $|V_{ON}|(\text{SL}) < |V_{ON}|(\text{SML}) \sim |V_{ON}|(\text{SSS})$ . This trend is believed to result from a dependence of the number of charges at the interface (for a given  $V$ ) on the sizes of the dots in the array. This trend is addressed in the next section.

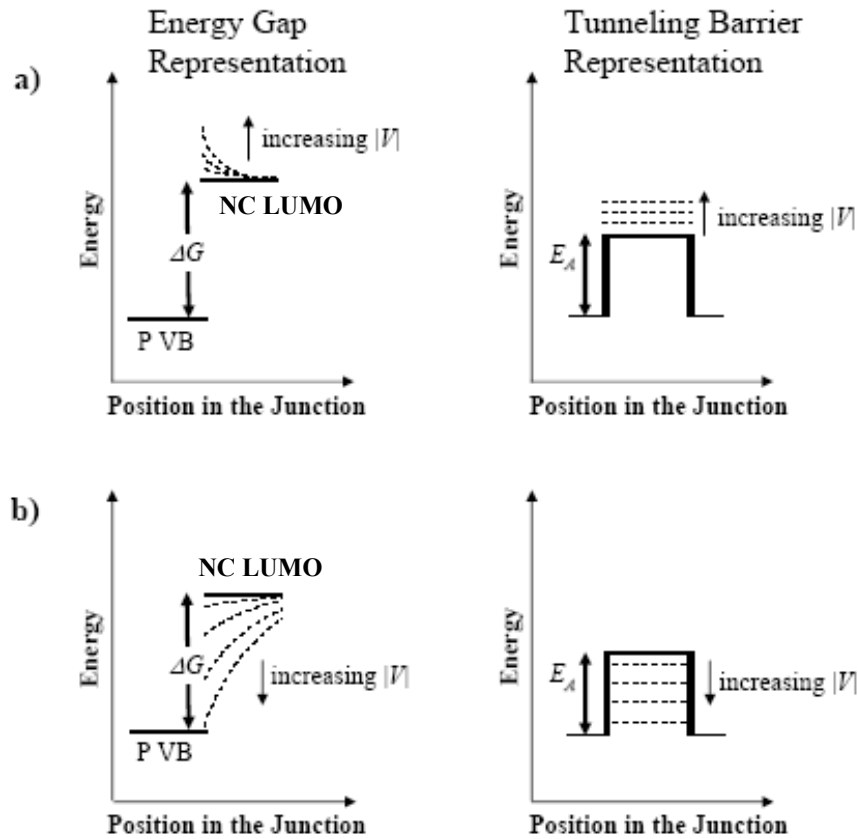


**Figure A.16:** Energy Gap (left) and Tunneling Barrier (right) representations of the effect of the accumulation of charge at the NC/PEDOT:PSS interface. The energy gap between the LUMOs of the NCs and the VB of PEDOT:PSS,  $\Delta G$ , corresponds to a rectangular tunneling barrier of height  $E_A$  (according to Equation A.4); these quantities are indicated on the plot for the system with no charge accumulated. a) As  $|V|$  increases, electrons are added to the LUMOs of the NCs, the energies of the LUMOs (and, therefore, the height of the tunneling barrier) increase, as indicated by the dotted lines. b) As  $|V|$  increases, the potential energies of electrons in the NCs near the interface (and, therefore, the height of the tunneling barrier) decrease due to Coulombic stabilization by positive charges in the adjacent PEDOT:PSS layer, as indicated by the dotted lines.

### ***Field Dependence of the Current***

#### *A Model for Current Limited by Interdot Transport.*

We observed that the dependence of  $J$  on  $V$  at  $|V| > |V_{ON}|$  fit well to the phenomenological expression given in Equation A.5 (Figure A.17). This expression is that expected for transport

$$J = \frac{V}{\rho_0 L} \exp\left(\frac{|V|}{V_0}\right) \quad (\text{A.5})$$

mediated by dot-to-dot tunneling (for a rectangular tunneling barrier).<sup>19,52</sup> This model makes sense because, at  $|V| > |V_{ON}|$ , charge annihilation occurs at the interface between the NCs and the PEDOT:PSS, so the observed current should be limited by transport of electrons through interfaces between the NCs. In Equation A.5,  $\rho_0$  and  $V_0$  are fitting parameters—that is, if we assume that the observed current is limited by transport through the array of NCs,  $\rho_0$  and  $V_0$  are a resistivity ( $\Omega\cdot\text{m}$ ), and voltage (V) characteristic of this array—and  $L$  is the thickness of the array (here,  $\sim 75$  nm). Figure A.17 shows plots of  $\ln(J/V)$  vs.  $|V|$  (these quantities should be linearly proportional to one another according to Equation A.5), and Table A.1 lists the values of the parameters extracted from linear fits to each plot. Equation A.5 implies that the effective resistivity,  $\rho$ , of the junction has the form in Equation A.6. As  $V$  increases, the NC film becomes doped with injected electrons,<sup>53</sup> and its

$$\rho = \rho_0 \exp\left(-\frac{|V|}{V_0}\right) \quad (\text{A.6})$$

resistivity decreases from its “sheet” or undoped value,  $\rho_0$ .<sup>54,55</sup> The undoped resistivity of the arrays depends, in principle, on multiple factors that depend on the preparation of the film, such as: i) the average distance between NCs in the film, ii) the presence of cracks in the film formed while the samples were heated to expel solvent, iii) the number of unpassivated  $\text{Cd}^{2+}$  and  $\text{Se}^{2-}$  ions on the surface of the NCs that can trap and repel electrons, respectively, and iv) the number of dot-to-dot tunneling events that must occur for the electron to hop across the film. It is, difficult to predict or rationalize the observed values in  $\rho_0$ .

There is not yet a generally accepted physical interpretation for  $V_0$ ,<sup>52</sup> but, according to Equation A.6,  $\rho \rightarrow \rho_0$  as  $V_0 \rightarrow \infty$ , where  $\rho_0$  is the resistivity of the array before any electrons

have been injected from the EGaIn. As  $V_0$  increases, it becomes more difficult to dope the array with electrons. It is proposed that  $V_0$  is a measure of the energy needed to inject a charge into the array, and corresponds to (or is somehow proportional to) the charging energy of the NCs that are accepting the electrons. The energy needed to put a charge onto the surface of a nanocrystal,  $E_c$ , is inversely proportional to its radius,  $r$  ( $E_c = e^2/8\pi\epsilon_0\epsilon r$ , where  $\epsilon$  is the dielectric constant of the nanocrystal, and  $e$  is the charge on an electron).<sup>3</sup> Using this equation,  $E_c$  for an S NCD ( $r = 2.1$  nm) is a factor of 2.3 higher than  $E_c$  for a L NC ( $r = 4.9$  nm). The ratio between the average of all of the values of  $V_0$  that are presumed to correspond to S NCs and the average of all of the values of  $V_0$  that are presumed to correspond to L NCs is 2.5. These two ratios are similar, so it is possible that  $V_0$  is the minimal difference in voltage between the two electrodes necessary to inject an electron into the array, and that this threshold voltage depends on the charging energy of the NCs in the array.

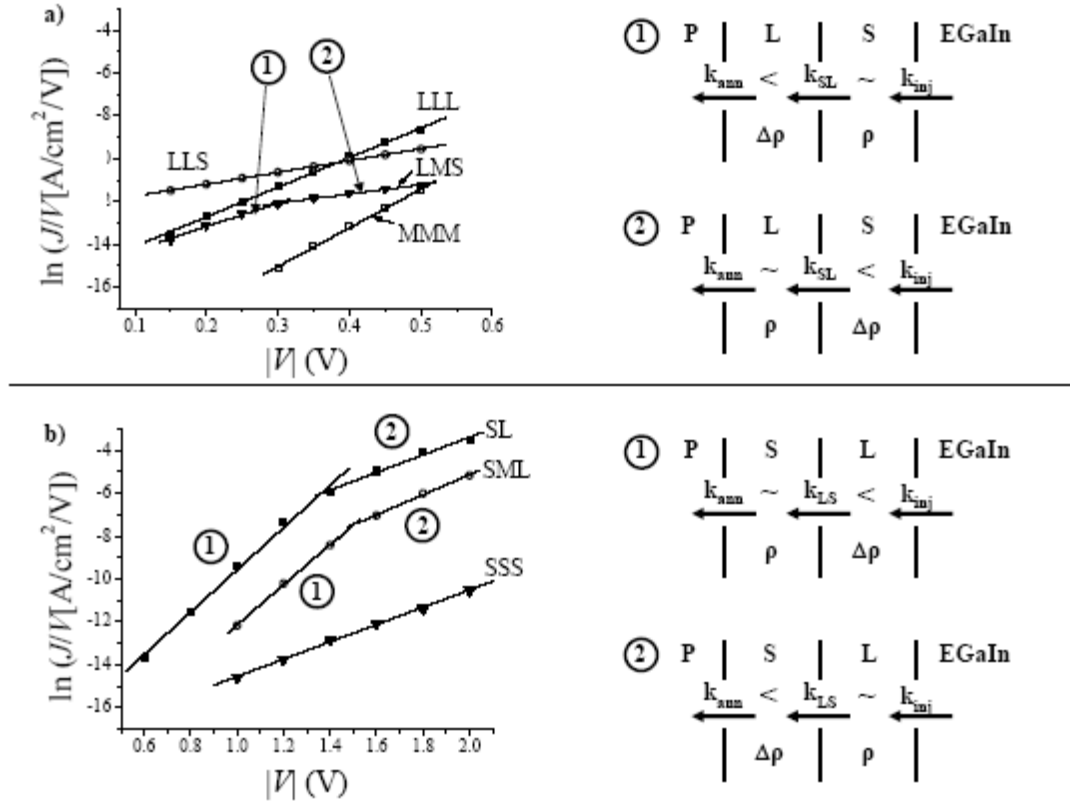


**Figure A.17:** Plots of  $\ln(J/V)$  vs.  $|V|$  (where  $J = \langle J \rangle_{\log}$ ) at  $V > V_{ON}$  for the junctions ITO/P/X/EGaIn. a) X = LLL, LMS, LLS, MMM, and b) X = SL, SML, SSS (grouped according to the range in  $V$  over which we measured  $J$ ; the scales of the y-axes are the same on both plots). From these plots, we obtained the undoped resistivities,  $\rho_0$ , and voltages,  $V_0$ , of the arrays of NCs according to the equation  $J = (V/\rho_0 L)\exp(-|V|/V_0)$  (Equation A.6), where  $L$  is the thickness of the layer of NC layer (here, 75 nm). The fitting parameters are listed in Table A.1. The arrays LMS, SL, and SML are best fit by two lines. Right: Diagrams that show the relative rates of electrons moving from EGaIn into the NCs ( $I_{inj}$ ), between the layers of NCs, ( $I_{SL}$  and  $I_{LS}$ ), and from the NCs into the PEDOT:PSS ( $I_{ann}$ ) in response to a step in  $V$  for the two regimes (labeled “1” and “2” in the plots of  $\ln(J/V)$  vs.  $|V|$ ). The symbols “ $\Delta\rho$ ” (“ $\rho$ ”) indicate that the effective resistivity of that portion of the junction is changing (remains constant) in response to the step in  $V$ .

### *Mechanism for a Sequential Doping Process in the Multi-Size Films.*

Interestingly, the plots of  $\ln(J/V)$  vs.  $|V|$  for the multi-size junctions SML, SL, and LMS each had two distinct regimes (labeled “1” and “2” in the plots in Figure A.17). The value of  $V_0$  for regime 1 (the lower end of range of applied voltage) matched closely with that of LLL, and the value of  $V_0$  for regime 2 (the higher end of the range of applied voltage) matched closely with



that of SSS (Table A.1). This result implies that, for the junctions LMS, SML, and SL, the doping process took place in stages. To illustrate the mechanism of doping in the multi-size films, diagrams in Figures A.17(a) and A.17(b) are used. These diagrams show the EGaIn electrode, the layer of PEDOT:PSS (“P”) and the layers of NCs (“S” and “L”). (The layer of M NCs is omitted in the diagrams because the shape of the  $J$ - $V$  response is not influenced by doping of these NCs. This is discussed below.) The notation is as follows:  $I_{inj}$  is the rate of electron transport from EGaIn into the adjacent layer of NCs (L or S depending on the junction),  $I_{LS}$  is the *effective* rate of electron transport from the L layer to the S layer (i.e., for  $\mathbf{X} = \text{SML}$ ,  $I_{LS}$  is some convolution of  $I_{LM}$  and  $I_{MS}$ ),  $I_{SL}$  is the effective rate of transport from the S layer to the L layer (in the junction LMS), and  $I_{ann}$  is the rate of charge annihilation at the NC/PEDOT:PSS interface. The symbol  $\Delta\rho$  indicates that the resistivity of that region of the junction changes in response to a step in  $V$  (because the NCs in that region are being doped with electrons) in the specified regime; the symbol  $\rho$  indicates that the resistivity of that region of the junction remains constant in response to a step in  $V$ .

Before the junction reaches the steady state (at which, by definition,  $I_{inj} = I_{ann} = I_{SL}$  or  $I_{LS}$ ), these rates have some relationship to one another that leads to the observed dependence of  $\ln(J/V)$  vs.  $|V|$ . As shown in Figure A.17, for  $\mathbf{X} = \text{LMS}$ , in regime **1**,  $V_0(\text{observed}) \sim V_0(\text{LLL})$ ; so, in response to a step (to higher magnitude) in  $V$ , the overall resistivity of the junction decreases due to the decrease in the resistivity (by doping) of the layer of L NCs, while the resistivity of the layer of S NCs remains constant. To achieve this state, we must have  $I_{inj} \sim I_{SL} > I_{ann}$  in regime **1**. As  $V$  increases, the layer of L NCs fills with electrons, and  $I_{SL}$  slows until the system reaches the state  $I_{inj} > I_{SL} \sim I_{ann}$  (regime **2**). In regime **2**, the population of electrons in the layer of L

NCs remains constant, but the layer of S NCs becomes doped with electrons such that  $V_0(\text{observed}) \sim V_0(\text{SSS})$ .

The mechanism for the flow of current through the junctions SML and SL is very similar. In regime **1**, again  $V_0(\text{observed}) \sim V_0(\text{LLL})$ , such that it is the decrease in the resistivity of the layer of L NCs that is responsible for the decrease the overall resistivity of the junction. The system must therefore be in a state where  $I_{\text{inj}} > I_{\text{LS}} \sim I_{\text{ann}}$  in regime **1**. It is suspected that  $I_{\text{LS}}$  is slower than  $I_{\text{inj}}$  because the transfer of electrons from L NCs to S NCs is endothermic, and the applied voltage in regime **1** does not supply enough energy to overcome the barrier. This energy, however, eventually comes from the electric field that forms as electrons fill the layer of L NCs, and the system achieves a state where  $I_{\text{inj}} \sim I_{\text{LS}} > I_{\text{ann}}$  (regime **2**). In this state, the overall resistivity of the junction is gated by that of the layer of small NCs, and  $V_0(\text{observed}) \sim V_0(\text{SSS})$ .

In summary, the doping of the multi-size can be partitioned into several stages corresponding to the charging of different sizes of NCs. The order of the NC layers relative to the direction of flow of the electrons determines whether the rate of electron transfer between layers of NCs is faster or slower than the rate of injection or absorption of electrons; therefore, the distribution of sizes of NCs in the junction determines, in part, the order in which these layers are doped, and, in turn, the shape of the  $J$ - $V$  response of the junction.

For  $\mathbf{X} = \text{LLS}$ , the contributions of the S NCs and the L NCs are not resolved— $V_0(\text{observed}) \sim \text{average}(V_0(\text{SSS}), V_0(\text{LLL}))$ —and it appears that resistivity of both the L and S layers is decreasing throughout the range of  $V$  studied. This result implies that  $I_{\text{inj}} > I_{\text{SL}} > I_{\text{ann}}$ . The array LLS is identical to LMS at the interfaces with both electrodes, so, in principle,  $I_{\text{inj}}$  and  $I_{\text{ann}}$  should be the same for both arrays. The potential difference between them is  $I_{\text{SL}}$ , which, as mentioned previously, is a convolution of  $I_{\text{SM}}$  and  $I_{\text{ML}}$  in the case of LMS and is actually  $I_{\text{SL}}$  in

the case of LLS. We suspect that the direct transfer of electrons from the layer of S NCs to the layer of L NCs ( $\Delta G = \sim -0.2$  eV) is slower than the indirect transfer through the M NCs (two processes, each with  $\Delta G = \sim -0.1$  eV) because the total reorganization energy for the NC to NC electron transfer is probably less than 0.05 eV. These reactions are, therefore, in the Marcus inverted region, and  $I$  decreases as  $|\Delta G|$  increases. If  $V_0$  is a measure of the energy needed to charge the NCs in the array, then the fact that the M NCs had an unexpectedly low value for  $V_0$ , but an unexpectedly high value for  $\rho_0$ , might indicate that, due to some aspect of their preparation, they have a higher density of charge traps per unit surface area than do the L or S NCs. Defects in the surface trap electrons that charge the array of NCs; electrostatically, the higher the density of trap sites, the more difficult it is for current to flow through an array of NCs. Cationic surface traps also accept, but do not donate, electrons easily, so it is possible that the M NCs are charged before the device turns on, and remain charged such that the current density at  $|V| > V_{ON}$  is never gated by the doping of this layer.

*The Connection between the Resistivity of the Array and  $V_{ON}$ .*

Table A.1 and Figure A.14 show that  $|V_{ON}|(\text{SSS}) \sim |V_{ON}|(\text{SML}) > |V_{ON}|(\text{SL})$ . This result is explained by considering that, for a given voltage  $V < V_{ON}$ , the applied electric field allows electrons to overcome the barrier imposed by the organic capping layers, and to move through the array of NCs to the interface with PEDOT:PSS. The greater the resistivity of the array, the fewer electrons present at this interface for a given  $V < V_{ON}$ , and the smaller the Coulomb force that precipitates charge annihilation. Figure A.17 shows that the junction SL is less resistive than SML and SSS. It is proposed, but not proven, that at low voltages ( $|V| < |V_{ON}|$ ), the number

of electrons at the interface—and consequently, the magnitude of the Coulomb force—is limited by transport through the array; thus the trend  $|V_{\text{ON}}|(\text{SSS}) \sim |V_{\text{ON}}|(\text{SML}) > |V_{\text{ON}}|(\text{SL})$ .

### ***Summary***

In Section A.3.2, the dependence of dark electrical characteristics of junctions containing an array of a single size of colloidal CdSe NCs is compared with those containing an array of multiple sizes of NCs. The overall characteristics of the junctions depend on the size of the NCs, specifically the size-dependent effects at the NC/electrode interfaces and size-dependent effects within the NC array. The following conclusions were reached regarding the transport of injected charge in the NC arrays.

i) The devices are diodes: electrons do not flow from ITO to EGaIn, primarily because, at the voltages applied, not enough energy is supplied for electrons in the PEDOT:PSS to enter the LUMOs of the NCs, or for electrons in the HOMOs of the NCs to enter the EGaIn. Electrons do flow from EGaIn to ITO, after application of a threshold voltage,  $V_{\text{ON}}$ . The value of  $V_{\text{ON}}$  depended primarily on the size of the NCs next to the PEDOT:PSS. This observation led to the conclusion that the current-limiting step in transport of electrons from EGaIn to ITO is the charge annihilation reaction  $\text{NC}^-/\text{PEDOT:PSS}^+ \rightarrow \text{NC}/\text{PEDOT:PSS}$ .

ii) At  $|V| < |V_{\text{ON}}|$ , this reaction is slow due to a tunneling barrier caused by a gap between the energies of the electron donor (the LUMO of the NC anion) and the electron acceptor (the valence band of PEDOT:PSS). The size of this barrier is estimated from the size of the energy gap and the parameter  $\lambda$  (the reorganization energy), using Marcus formalism; that the height of this barrier would increase as the size of the NCs at the NC/PEDOT:PSS interface decreased, qualitatively explained the trend observed:  $|V_{\text{ON}}|(\text{LX}) < |V_{\text{ON}}|(\text{MX}) < |V_{\text{ON}}|(\text{SX})$ . It is

hypothesizes that, at  $V_{ON}$ , the Coulomb force between accumulated positive charges in the PEDOT:PSS and negative charges in the NCs at the interface overcomes the barrier, and induced the annihilation reaction. The “Coulomb force” mechanism that is proposed for precipitation of the annihilation reaction is analogous to image-potential lowering of tunneling barriers at metal-semiconductor contacts.<sup>18</sup>

iii) At  $|V| > |V_{ON}|$ , the dependence of  $J$  on  $V$  fits well to a model that assumes that the current through the junctions is limited by sequential tunneling from dot to dot within the array. The data suggest that, as the arrays were doped with electrons injected from the EGaIn, the sequential tunneling process became more facile, probably because the electrons occupied trap sites on the surface of the NCs that would have otherwise trapped electrons.<sup>9,10,56</sup> The degree to which the resistivity of the arrays changed as a function of  $V$  depended on the size of the NCs; this dependence was reflected in  $V_0$ , a parameter extracted from fitting the data with this model. It is proposed that  $V_0$  is a measure of the energy needed to put an electron onto the NCs. Data for most multi-size arrays fit into two regimes, each with its own value for  $V_0$ . The hypothesis is that, when more than one size of NCs were present in one junction, the doping of these NCs took place in stages (one size at a time), the order of which depends on the relative rates of electron injection, electron absorption, and transport across boundaries between layers of different sizes of NCs. These rates, in turn, depend on the ordering of the different sizes of NCs in the junction.

### **A.3.3 Photoexcitation – Origin of Exciton Separation and Photovoltaic Effect in the NC Gradient**

In this section, a study is presented of photoinduced charge transport through a series of junctions containing single-size and multi-size arrays of NCs. The study of the single-size array will reveal, in principle, the dependence of the electrical characteristics of the junctions on the size of the NCs, while the analysis of photoconduction in multi-size arrays of NCs will allow the contributions from transport across the NC/electrode interfaces to be distinguished from contribution from transport through the bulk of the array. Multiple sizes of NCs with distinct band-edge absorptions in a single junction allow spatial selectivity of photoexcitation. This can uncover the relationship between the location of a NC within the junction and its contribution to the observed photocurrent. Furthermore, once the charge separation interface is identified, the multi-size architecture potentially allows funneling of absorbed light to that location through a downhill energy transfer process; this type of “cascaded energy transfer structure” was realized in arrays of CdTe nanocrystals.<sup>57</sup>

#### ***Photocurrent Mechanism***

It was shown in section A.3.2 that, in the dark, the ITO/PEDOT:PSS/NC/EGaIn junctions are diodes: they turn “on” when the EGaIn is biased negatively with respect to the ITO (negative bias), and pass only a small, positive leakage current for all of the junctions when the EGaIn electrode is biased positively with respect to the ITO (positive bias). In this section, it is observed that photoexcitation with light that has a frequency resonant with, or of higher energy

than, the absorption of the NCs in the junction produced photocurrent ( $I_{\text{light}} - I_{\text{dark}}$ ) under zero and positive bias.<sup>58</sup>

Figure A.18(a) shows the values of the current ( $I$ ) measured when the voltage is scanned from  $V = 0 \rightarrow +1.0 \text{ V} \rightarrow 0$  (in steps of 0.1 V) for the junction SSS in the dark, and when the sample was illuminated with 565 nm and 660 nm light. The junction is allowed to equilibrate at the specified voltage for 1 s before recording the current. Each point in the plot in Figure A.18(a) is the log-mean of 14 values  $I$  (defined as  $\langle I \rangle_{\log} = 10^{\langle \log I \rangle}$ , where  $\langle \log I \rangle$  is the mean value of  $\log(|I|)$ ) measured over five separate junctions.<sup>59</sup> This plot is meant to demonstrate the presence of a photo-effect; the error analysis on the magnitude of this effect in all of the junctions is in Figure A.18(b), which is discussed in the next paragraph. The sources of excitation used to gather the data in Figure A.18(a) were light-emitting diodes (LEDs) that were positioned 4 cm from the glass substrate, and that illuminated the sample as shown in Figure A.8. The trace measured with 660 nm excitation (which the S NCs did not absorb, see Figure A.10b) is almost identical to the trace measured in the dark, while the current increased by  $\sim 10^3$  with 565 nm excitation (which the S NCs did absorb). This result indicates that, as observed previously,<sup>6</sup> current created upon illumination (photocurrent) was not simply a local heating effect, nor was it a result of thermal or photoexcitation of other materials (besides the NCs) within the device.

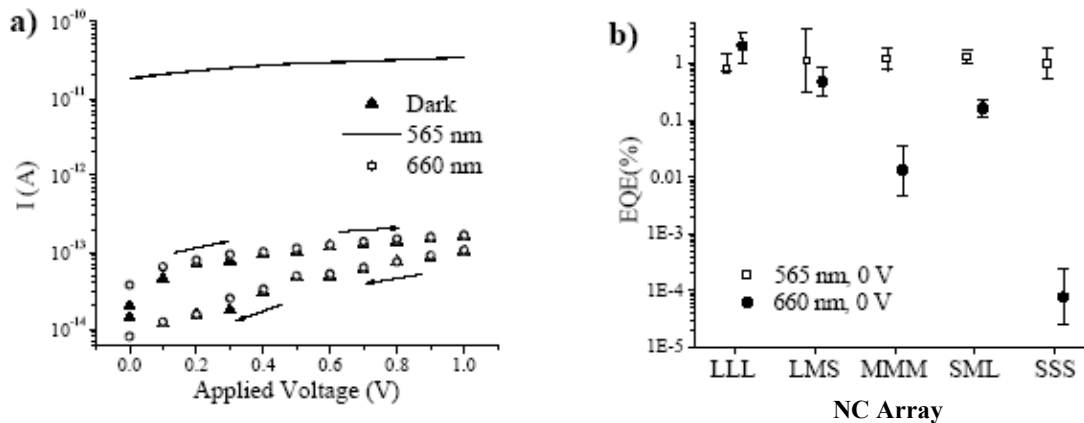


**Figure A.18:** a) Current-voltage ( $I$ - $V$ ) plots for the junction ITO/P/SSS/EGaIn: i) in the dark, and with ii) 565 nm and iii) 660 nm (LED) excitation. b) Plots of external quantum efficiency (EQE: electrons that enter the external circuit per incident photon; see a list of these values and the equation for EQE in Table A.2) at  $V = 0$  V for ITO/P/X/EGaIn, X = LLL, LMS, MMM, SML, and SSS with 565 nm and 660 nm (LED) excitation.

Table A.2 and Figure A.18(b) give the external quantum efficiencies (EQEs) for the junctions ITO/P/X/EgGaIn, X = LLL, MMM, SSS, LMS, and SML when excited by LEDs at 565 nm and 660 nm. External quantum efficiency is defined as the number of electrons that enter the external circuit per photon incident upon the junction (*not* per photon absorbed by the junction); the formula for EQE is in the footnote to Table A.2. In general, the EQE is determined by the amount of light the array of NCs absorbs at the excitation wavelength, the number of resulting excitons that separate into charge carriers (electrons and holes), and the efficiency of the charge collection process. The density of incident photons is determined by shining the LED light on a silicon detector of known photo-responsivity and area (the LED was positioned 4 cm from the detector, as with the NC samples). In order to calculate the number of incident photons, this density is integrated over the area of the EGaIn junction defined by the PDMS mold (.008 cm<sup>2</sup>).



The ranges for each EQE in Table A.2 and the error bars in Figure A.18b reflect the error in the EQE propagated from the uncertainty in the photocurrent (using between 14 and 21 measurements for each array at each voltage). Even with this large error, Table A.2 and Figure A.18(b) show that, as expected from inspection of Figure A.18(a) and the absorption spectrum of the S NCs (Figure A.10), EQE(SSS)<sub>660</sub> is effectively zero. Furthermore, EQE(MMM)<sub>660</sub> is approximately a factor of 10<sup>2</sup> smaller than EQE(MMM)<sub>565</sub> at  $V = 0$ , and approximately a factor 10 smaller than EQE(MMM)<sub>565</sub> at  $V = 0.5$  V. It is not expected that EQE(MMM)<sub>660</sub> would be as small as EQE(SSS)<sub>660</sub>, because the “660-nm” LED still emits at half its maximum intensity at 640 nm, so the emission spectrum of the LED and the absorption spectrum of the M NCs in the film (Figure A.10) do overlap. These results re-emphasize that the photocurrent originates from excitations of the NCs, since electrons are not produced from photons that have energies below that of the optical bandgap ( $E_g$ ) of the NCs.

**Table A.2.** External Quantum Efficiency (EQE) of the Junctions ITO/P/X/EGaIn under Illumination (with excitation from LEDs at 565 nm and 660 nm) at Selected Voltages

X	EQE(%) <sup>a,b</sup>		0 V		+0.5 V	
	565 nm	660 nm	565 nm	660 nm	565 nm	660 nm
LLL	<b>(0.80)</b> 0.71 – 1.5	<b>(3.8)</b> 1.9 – 6.7	<b>(2.1)</b> 1.4 – 3.2	<b>(7.9)</b> 3.9 – 14.0		
LMS	<b>(1.1)</b> 0.31 – 3.9	<b>(0.84)</b> 0.46 – 1.5	<b>(2.3)</b> 0.87 – 6.1	<b>(1.8)</b> 0.59 – 5.5		
MMM	<b>(1.2)</b> 0.77 – 1.9	<b>(0.019)</b> 0.0064 – 0.056	<b>(1.5)</b> 0.99 – 2.3	<b>(0.21)</b> 0.081 – 0.54		
SML	<b>(1.3)</b> 1.0 – 1.7	<b>(0.27)</b> 0.19 – 0.39	<b>(1.7)</b> 1.3 – 2.2	<b>(0.49)</b> 0.39 – 0.61		
SSS	<b>(1.0)</b> 0.52 – 1.9	<b>(8.5×10<sup>-5</sup>)</b> 2.6×10 <sup>-5</sup> –2.8×10 <sup>-4</sup>	<b>(1.6)</b> 0.70 – 3.6	<b>(5.8×10<sup>-5</sup>)</b> 2.5×10 <sup>-5</sup> –1.4×10 <sup>-4</sup>		

<sup>a</sup>EQE(%) = electrons/photon × 100 =  $(J_{\text{light}} - J_{\text{dark}})/[(1.6 \times 10^{-19} \text{ C})(x)] \times 100$ ,  $x = 9.80 \times 10^{13}$  photons/s/cm<sup>2</sup> for 565 nm or  $1.30 \times 10^{14}$  photons/s/cm<sup>2</sup> for 660nm. <sup>b</sup>The EQE(%) is presented as an average (**in bold**), and a range.

*Spatially-Selective Photoexcitation of the NCs Shows that Photocurrent Originates from Charge Separation at the NC/PEDOT:PSS Interface.*

A second observation about the data in Table A.2 and Figure A.18(b) is that  $\text{EQE}(\text{SML})_{565}$  is approximately a factor of five larger than  $\text{EQE}(\text{SML})_{660}$  at  $V = 0$ , and more than a factor of three larger than  $\text{EQE}(\text{SML})_{660}$  at  $V = 0.5$  V, while  $\text{EQE}(\text{LMS})_{565}$  is within experimental error of  $\text{EQE}(\text{LMS})_{660}$  at  $V = 0$  and  $V = 0.5$  V. The arrays SML and LMS have identical absorption coefficients at these two wavelengths (Figure A.19). It is also assumed that the mobility of charges through these two arrays is similar, as they have the same proportion of each size of NC; therefore, the difference in their EQEs probably comes from differences in the yields of charge carriers from excitons (their charge separation efficiency). The junctions LMS and SML absorb approximately the same number of 660 nm photons, but the excitation is spatially-selective—that is, in SML, the excitons are created in the L NCs (and somewhat in the M NCs), and are localized (or trapped) away from the interface with PEDOT:PSS because they have an energy less than  $E_g$  of the S NCs.<sup>3</sup> In LMS, the excitons created by 660-nm photons in the L NCs are also trapped, but they are trapped at or near the interface with PEDOT:PSS. This result implies that it is only the excitons created at the interface with PEDOT:PSS (or that travel to this interface via energy transfer<sup>12</sup>)—and not those trapped at the interface with EGaIn or in the bulk of the NC array—that contribute to the photocurrent. Therefore, the charge separation event that creates electrons and holes from the excitons occurs at the NC/PEDOT:PSS interface.

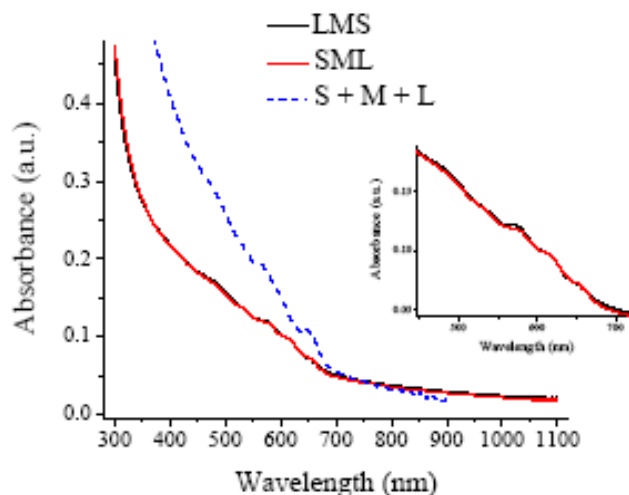


**Figure A.19:** Ground state absorbance spectra of the films LMS (black solid line) and SML (red solid line) spun on glass; these spectra are approximately identical. Also shown is the sum of the spectra of the films L, M, and S on glass (blue dotted line). Inset: Spectra for the films LMS and SML zoomed into the region containing the band-edge absorptions for each of the sizes of NCs.

To confirm this observation,  $I$ - $V$  curves were recorded for the junctions LMS and SML in the dark and when photoexcited at 646 nm a continuous wave (CW) Ar ion laser, which has a higher power (intensity of 10 mW/cm<sup>2</sup>) than the 660-nm LED (intensity of 0.04 mW/cm<sup>2</sup>). The ratio of current under illumination to dark current ( $I_{\text{light}}/I_{\text{dark}}$ ) is plotted in Figure A.20. It is clear that the enhancement of current upon illumination is far greater for LMS ( $I_{\text{light}}/I_{\text{dark}} = \sim 2300$  at  $V = 0$ ), where the excitons are trapped at the interface with PEDOT:PSS, than for SML ( $I_{\text{light}}/I_{\text{dark}} = \sim 73$  at  $V = 0$ ), where the excitons are trapped away from the interface. As expected, the ratio  $I_{\text{light}}/I_{\text{dark}}$  for LMS drops off precipitously at voltages more negative than  $V_{\text{OC}}$  (at which point, the current begins to flow in the opposite direction: from EGaIn to ITO). This ratio also decays as the voltage is increased from 0 in the positive direction, probably because  $I_{\text{dark}}$  increases faster than  $I_{\text{light}}$ .

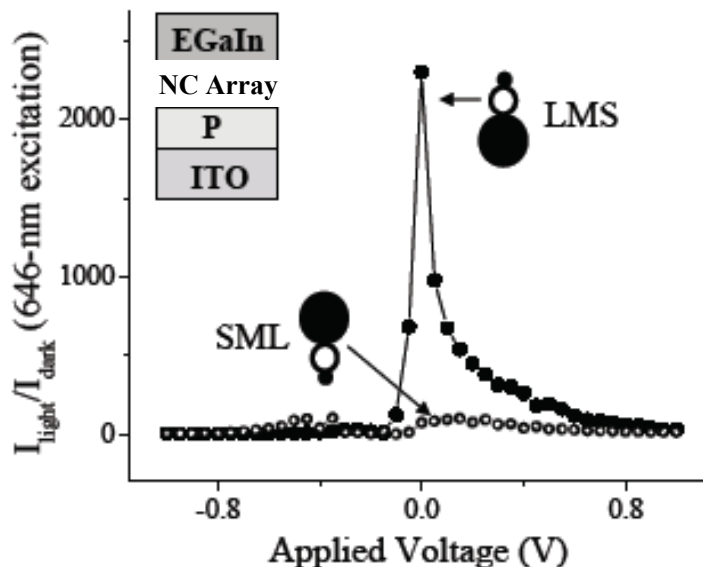


**Figure A.20:** Ratio of current under illumination ( $I_{\text{light}}$ ) to dark current ( $I_{\text{dark}}$ ) as a function of voltage for the junctions ITO/PEDOT:PSS/X/EGaIn, X = SML and LMS. The excitation source was the 646 nm line of an Ar ion laser (intensity = 10 mW/cm<sup>2</sup>).

A final experiment supporting the hypothesis that it is only excitons that can reach the NC/PEDOT:PSS interface that contribute to the photocurrent is the measurement of the photocurrent action (PCA) spectra of the junctions. The PCA spectrum reveals which excited states produce charge carriers in junctions that contain multiple chromophores with different absorption spectra. The peaks in the PCA spectrum should match the absorbance features of those NCs whose excitons either separated into charge carriers that contributed to the observed photocurrent, or traveled (via energy transfer) to other NCs, where they separated into charge carriers. The PCA spectra of the junctions LLL, LMS, and SML are displayed in Figure A.21 (right y-axis) along with the absorption spectra of the S, M, and L NCs (left y-axis). The PCA spectra show the normalized photocurrent ( $I_{\text{light}} - I_{\text{dark}}$ ) at  $V = 0$  as a function of excitation wavelength.

As expected, the PCA spectrum for LLL closely matched the absorbance spectrum of the L NCs. The PCA spectrum for LMS matched the combined absorbance spectra of its component NCs. (This will be discussed in the context of energy transfer below.) The key piece of evidence is the PCA spectrum of SML. This PCA spectrum only mirrors the absorbance features of the S NCs, which are the NCs at the interface with PEDOT:PSS. In this junction, excited states in the L and M NCs (created at excitation energies lower than  $E_g$  for the S NCs), cannot migrate to the S NCs at the interface. This spectrum shows that it is *only* excited states at the NC/PEDOT:PSS interface that contribute to the photocurrent.

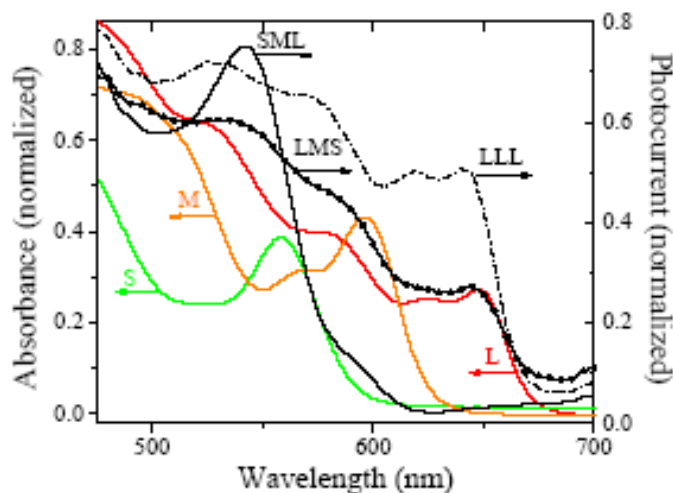


**Figure A.21:** Ground state absorbance spectra for films of the S, M, and L NCs on glass (left axis), and photocurrent action spectra (normalized photocurrent as a function of excitation wavelength) for the junctions ITO/PEDOT:PSS/X/EGaIn, X = LLL, LMS and SML.

In light of the evidence presented in the preceding section, a mechanism for the generation of photocurrent (and also for the small, positive dark current, where the carriers are thermally generated) can be proposed. In this mechanism (Figure A.22)—which is referred to as “electron conduction”—PEDOT:PSS donates electrons to the half-filled HOMOs of thermally or photoexcited NCs in the layer adjacent to the PEDOT:PSS. The electron-accepting NCs near the

PEDOT:PSS are now negatively charged, and an electric field forms in the NC array that pushes electrons toward the EGaIn electrode via the LUMOs of the NCs, and eventually across the NC/EGaIn interface. This process results in net *electron transport* from ITO to EGaIn, and yields a positive leakage or photocurrent. In this mechanism, the current originates from thermally or photoexcited carriers in the NC layers near the PEDOT:PSS/NC interface.

Electron transfer from the LUMOs of the NCs (with energies of  $\sim -4.5$  to  $-4.7$  eV) to the EGaIn (with a work function of  $\sim -4.2$  eV) is facilitated by thermal equilibration of the population of electrons in the NCs, the ITO, and the EGaIn upon formation of the junction—that is, at zero bias, electrons move from the EGaIn to ITO via the external circuit. This equilibration lowers (makes more positive) the effective work function of EGaIn, as indicated in Figure A.22, and makes the transfer of electrons from the NCs to EGaIn more energetically favorable.

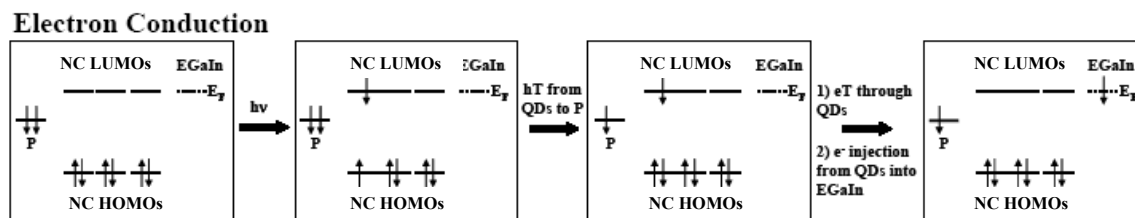


**Figure A.22:** The proposed “electron conduction” mechanism for the generation of photocurrent in the ITO/P /NC/EGaIn junctions (where the energies of the frontier orbitals of the NCs are drawn as constant throughout the array, for simplicity): i) PEDOT:PSS donates electrons to half-filled HOMOs of adjacent NCs created by photoexcitation. ii) The resulting electric field at this interface pushes electrons through the LUMOs of the NCs toward the EGaIn, and through the NC/EGaIn interface. (The dotted lines indicate an approximate value of the Fermi energy of EGaIn,  $E_F$ , once it thermally equilibrates by donating electrons to the adjacent NCs and to ITO through the external circuit). In this diagram, P  $\equiv$  PEDOT:PSS,  $h\nu$   $\equiv$  photoexcitation of the NCs,  $eT$   $\equiv$  electron transfer, and  $hT$   $\equiv$  hole transfer.

*Alternative Mechanisms for Photocurrent: Hole Conduction and Exciton Ionization.*

There are two other possible sources for photocurrent in these junctions, the difference between the three mechanisms being the location within the junction that the charge carriers are created. These mechanisms are not believed to be responsible for the photocurrent in the NC junctions and the reasons are presented in this section. One mechanism—referred to as “hole conduction” is as follows: i) Thermal equilibration at the NC/EGaIn interface induces the formation of an electric field at this interface. ii) The electric field, which is amplified by the application of a positive bias to the junction, sweeps photoexcited electrons from the NCs to the EGaIn, and leaves the NCs at the interface with a positive charge. iii) The holes in the NCs propagate through the HOMOs and recombine with electrons in the PEDOT:PSS layer to result in net positive current. In this mechanism, the *hole transport*-mediated current originates from thermally or photoexcited carriers in the NC layers near the NC/EGaIn interface, a process that does not appear to take place from the data in Table A.2 and Figures A.20 and A.21.

A second possible mechanism is exciton ionization, in which i) the excitons in the bulk of the array separate due to the applied or internal electric field, ii) the holes travel through the NC HOMOs and recombine with electrons in the PEDOT:PSS, and iii) the electrons travel through the NC LUMOs and are absorbed by the EGaIn.<sup>6</sup> The data in Figure A.20 and A.21 were measured at  $V = 0$ , so there was probably very little, if any, exciton ionization occurring to produce the photocurrent in those cases; however, it is possible that this mechanism could contribute increasingly as the applied field increased. Experiments using the multi-size NC array allowed it to be concluded that the photocurrent at zero (and very low) bias was due to charge transfer at the NC/PEDOT:PSS interface, but it has not been definitively determined the field at

which exciton ionization or hole conduction begins to participate in the generation of photocurrent in these junctions.

### ***Energy Transfer***

Fluorescence quenching experiments have shown that the rate of resonant energy transfer in CdSe NC arrays is, at least,  $10^8 \text{ s}^{-1}$ , and that NCs will transfer energy to other NCs with larger diameters.<sup>3</sup> Inspection of the PCA spectrum is a straightforward way to determine whether excitons created away from the NC/PEDOT:PSS interface migrate to the interface and charge-separate to contribute to the photocurrent. Assuming charge separation occurs at this interface at 0 V, then the fact that the PCA spectrum (recorded at 0 V) for LMS matched the combined absorbance spectra of its component NCs (Figure A.21) means that excitons in all three layers of NCs migrated to the NCs with the lowest-energy excited state (the L NCs), and separated into charge carriers that contributed to the photocurrent.

The values for EQE present conflicting evidence as to whether only excitons created at or near the NC/PEDOT:PSS interface contribute to photocurrent or whether excitons created away from the interface migrate (via energy transfer) to the interface and also contribute to the photocurrent. The fact that  $\text{EQE}(\text{LLL})_{660}$  was approximately a factor of four greater than  $\text{EQE}(\text{LMS})_{660}$  (at both  $V = 0$  and  $V = 0.5$  V) implies that excitons created in the entire LLL array contributed to the photocurrent since the entire LLL array—but only  $\sim 1/3$  of the LMS array—absorbed 660-nm light. This result is misleading because  $\text{EQE}(\text{LLL})_{660}$  is also about a factor of four greater than  $\text{EQE}(\text{LLL})_{565}$ ; in this case, since both wavelengths excite the entire array, it would be expected that the EQEs should be approximately equal at both wavelengths. It is possible, therefore, that the values of EQE for LLL at 660 nm are anomalously high. Using the EQEs—which depend on the rates of numerous processes whose description is beyond the scope



of this work—to address the question of energy transfer is an over-interpretation (especially considering that the uncertainties of the EQEs make them indistinguishable from one another in many cases).

### ***Open Circuit Voltage***

**Table A.3.** Open Circuit Voltage ( $V_{OC}$ ) of the Junctions ITO/P/**X**/EGaIn in the Dark and under Illumination (with excitation from LEDs at 565 nm and 660 nm)

<b>X</b>	$V_{OC}$ (V) <sup>a</sup>		
	<b>Dark</b>	<b>565 nm</b>	<b>660 nm</b>
LLL	-0.06±0.02 <sup>b</sup>	-0.12±0.03	-0.09±0.02
LMS	-0.06±0.03 <sup>b</sup>	-0.17±0.01	-0.07±0.04
MMM	-0.51±0.14 <sup>b</sup>	-0.52±0.04	-0.57±0.15 <sup>b</sup>
SML	-0.64±0.14 <sup>b</sup>	-0.56±0.03	-0.48±0.10 <sup>b</sup>
SSS	-0.66±0.14 <sup>b</sup>	-0.69±0.14	-0.61±0.13 <sup>b</sup>

<sup>a</sup> $V_{OC}$  is presented as a mean  $\pm$  standard deviation of between 14 and 21 values (depending on **X**).

<sup>b</sup>These traces were hysteretic;  $V_{OC}$  was taken from the segment  $-V \rightarrow 0$ , after the junction discharged under negative bias (see the text for further explanation).

Table A.3 shows that for all junctions and wavelengths,  $V_{OC}$  is similar in the dark and under illumination. Under all conditions,  $V_{OC}(LX) < V_{OC}(MX) < V_{OC}(SX)$ , so it appears that  $V_{OC}$  is dictated by the size of the NCs at the NC/PEDOT:PSS interface. This result is reasonable considering that  $V_{OC}$  can be given by the smallest energy gap in the junction (i.e.,  $V_{OC}$  is the net energy gained by an electron upon being excited from its ground state and traveling from its point of origin into the EGaIn electrode). The energy gained by the electron via photoexcitation is  $E_g$  ( $\sim E_{LUMO} - E_{HOMO}$ ) of the NC. According to the proposed mechanism for photocurrent, the excited state of the NC at the NC/PEDOT:PSS interface is quenched by donation of an electron from the valence band of PEDOT:PSS to the half-filled HOMO of the NCs. The PEDOT:PSS has accepted an electron from ITO, so this charge transfer process subtracts an energy  $E_F(\text{ITO}) - E_{HOMO}(\text{NC})$  from  $E_g$ , where  $E_F(\text{ITO})$  is the Fermi level of ITO; the *net* energy gained by the

electron is, therefore,  $E_{\text{LUMO}}(\text{NC}) - E_{\text{F}}(\text{ITO})$ . This difference is dictated by  $E_{\text{LUMO}}(\text{NC})$ , which increases as the diameter of the NC decreases;<sup>60</sup> therefore, one would predict  $V_{\text{OC}}(\text{LX}) < V_{\text{OC}}(\text{MX}) < V_{\text{OC}}(\text{SX})$ , which is, approximately, what is observed. This is just one proposed mechanism for the origin of  $V_{\text{OC}}$  in the NC junctions and a study of the potential of these devices in, or as, a photovoltaic device is still underway.

### *Summary*

In this section the magnitude of the photocurrent produced when single-size and multi-size arrays of colloidal CdSe NCs within ITO/PEDOT:PSS/NC/EGaIn junctions were excited with various wavelengths of light was measured. In the multi-size junctions, the excitations could be localized in different parts of the junction (i.e., near the NC/PEDOT:PSS interface or near the NC/EGaIn interface) by using light that was absorbed primarily by only one of the three sizes of NCs. This spatially-selective excitation allowed the investigation of the mechanism by which photocurrent was produced in these junctions. Through this study the following three conclusions were reached about photoinduced charge transport in the NC arrays.

i) At the voltages applied in this study ( $0 \rightarrow 1.0$  V) charge separation at the NC/PEDOT:PSS interface dominates the production of photocurrent, but we did not determine the voltage at which other mechanisms (hole conduction and exciton ionization) begin to contribute.

ii) The PCA spectrum of the multi-size NC junctions indicated that, when energetically favorable, excitons created away from the NC/PEDOT:PSS interface traveled this interface and split to create charge carriers.

iii) The magnitude of the photovoltage correlated with the size of the NCs at the NC/PEDOT:PSS interface. This result supports our proposed mechanism for generation of photocurrent because it implies that the photovoltage comes from the promotion of the electron from the HOMO to the LUMO of the NC, followed by donation of an electron from the PEDOT:PSS to the half-filled HOMO of the NC.

## A.4 Conclusions

Through the study of the electrical characteristics of junctions composed of three-dimensional arrays of both single and multi-sized colloidal CdSe nanocrystals (NCs), we are better able to understand the impact of energetic resonance between electrodes and the NCs on the transport of injected and photogenerated charge through the device. We learned that the HOMO of the polymer and the conduction band of the NC must be brought into resonance before charge can be transported through this NC array, and the smaller the energy difference between these two levels, the smaller the voltage that needs to be applied to turn on the device. In addition, the open circuit voltage of these NC junctions also appears to be sensitive to the energy offset between the NC and electrode. Finally, the effects of incorporating a gradient of sizes of NCs—and, therefore, a gradient in potential energy—within the junction were explored. We found that the energy gradient did not aid in the transport of injected charge and that transport appears to be dominated by the number of tunnel junctions, i.e. the number of NCs in the array. An array of all L NCs displayed the lowest resistivity. However, the energy gradient did affect the transport of photoexcited charge carriers as it funneled excitons, via energy transfer, to the largest NC. If the largest NC is located at the exciton separation interface all sizes of NCs in the array contribute to the photocurrent. While we have a better understanding of how the NC/electrode interface and the gradient in NC size effects both the photo and injected current, more work needs to be done before the NC array can become part of an efficient photovoltaic device.

## A.5 References

1. D. Selmarten, M. Jones, G. Rumbles, P. Yu, J. Nedeljkovic and S. Shaheen, *J. Phys. Chem. B* 109, 15927 (2005).
2. D. S. Ginger and N. C. Greenham, *Phys. Rev. B* 59, 10622 (1999).
3. C. B. Murray, C. R. Kagan and M. G. Bawendi, *Ann. Rev. Mat. Sci.* 30, 545 (2000).
4. M. Grundmann, J. Christen, N. N. Ledentsov, J. Bohrer and D. Bimberg, *Phys. Rev. Lett.* 74, 4043 (1995).
5. P. T. Snee, Y. Chan, D. G. Nocera and M. G. Bawendi, *Adv. Mater.* 14, 739 (2002).
6. C. A. Leatherdale, C. R. Kagan, N. Y. Morgan, S. A. Empedocles, M. A. Kastner and M. G. Bawendi, *Physical Review B* 62, 2669 (2000).
7. C. B. Murray, D. J. Norris and M. G. Bawendi, *Journal of the American Chemical Society* 115, 8706 (1993).
8. C. B. Murray, C. R. Kagan and M. G. Bawendi, *Science* 270, 1335 (1995).
9. M. V. Jarosz, N. E. Stott, M. Drndic, N. Y. Morgan, M. A. Kastner and M. G. Bawendi, *Journal of Physical Chemistry B* 107, 12585 (2003).
10. M. V. Jarosz, V. J. Porter, B. R. Fisher, M. A. Kastner and M. G. Bawendi, *Physical Review B* 70, 195327 (2004).
11. C. Kagan, Ph.D. thesis, Massachusetts Institute of Technology, 1996
12. C. R. Kagan, C. B. Murray, M. Nirmal and M. G. Bawendi, *Physical Review Letters* 76, 1517 (1996).
13. R. C. Chiechi, E. A. Weiss and G. M. Whitesides, Eutectic Gallium-Indium: A Versatile, Electrically-Conductive, Non-Newtonian Liquid Metal, submitted to \_\_\_\_.
14. J. Cui, A. Wang, N. L. Edleman, J. Ni, P. Lee, N. R. Armstrong and T. J. Marks, *Adv. Mater.* 13, 1476 (2001).
15. G. P. Kushto, W. Kim and Z. H. Kafafi, *Applied Physics Letters* 86, 093502 (2005).
16. J. Ouyang, C.-W. Chu, F.-C. Chen, Q. Xu and Y. Yang, *Adv. Func. Mater.* 15, 203 (2005).

17. E. A. Weiss, R. C. Chiechi, G. K. Kaufman, J. K. Kriebel, Z. Li, M. Duati, M.-A. Rampi and G. M. Whitesides, *J. Am. Chem. Soc.* 129, 4336 (2007).
18. S. M. Sze, *Physics of Semiconductor Devices*. 2nd ed. 1981, New York: John Wiley and Sons.
19. V. J. Porter, T. Mentzel, S. Charpentier, M. A. Kastner and M. G. Bawendi, *Phys. Rev. B* 73, 155303/1 (2006).
20. D. S. Ginger and N. C. Greenham, *J. Appl. Phys.* 87, 1361 (2000).
21. The direction of flow of electrons is formally opposite that of current, so, under positive bias, the current flows from EGaIn through the NCs to ITO, and under negative bias, the current flows from ITO through the NCs to EGaIn.
22. H. Ishii, K. Sugiyama, E. Ito and K. Seki, *Adv. Mater.* 11, 605 (1999).
23. A. L. Efros and M. Rosen, *Ann. Rev. Mat. Sci.* 30, 475 (2000).
24. D. J. Norris and M. G. Bawendi, *Phys. Rev. B* 53, 16338 (1996).
25. Occasionally, when a voltage between +1.0 and +2.0 V was applied, the NC junctions failed: the current density increased suddenly by one or more orders of magnitude. Failure of the devices was probably caused by a build-up of negative charge in the PEDOT:PSS layer; accumulation of negative charge leads to over-reduction, and ultimately dielectric break-down.
26. J. Ouyang, Q. Xu, C.-W. Chu, Y. Yang, G. Li and J. Shinar, *Polymer* 45, 8443 (2004).
27. Each NC will never be more than singly charged until the entire array has been filled b/c the charging energy--greater than 150 meV for a 4-5 nm NC--is much larger than thermal energy available at RT
28. B. Alpers, S. Cohen, I. Rubinstein and G. Hodes, *Phys. Rev. B* 52, R17017 (1995).
29. Y.-C. Tseng, K. Phoa, D. Carlton and J. Bokor, *Nano Lett.* 6, 1364 (2006).
30. A. J. Mäkinen, I. G. Hill, M. Kinoshita, T. Noda, Y. Shirota and Z. H. Kafafi, *J. Appl. Phys.* 91, 5456 (2002).
31. Basic Electron Transfer Theory
32. V. Albe, C. Jouanin and D. Bertho, *Phys. Rev. B* 58, 4713 (1998).
33. C. Cohen-Tannoudji, B. Diu and F. Laloe, *Quantum Mechanics*. 1977, New York: John Wiley and Sons. 295.

34. R. Marcus, *Rev. Mod. Phys.* 65, 599 (1993).
35. S. Gosavi and R. A. Marcus, *J. Phys. Chem. B* 104, 2067 (2000).
36. R. A. Marcus, *J. Chem. Phys.* 43, 679 (1965).
37. R. A. Marcus, *J. Chem. Phys.* 81, 4494 (1984).
38. Y. Olivier, V. Lemaire, J. L. Bredas and J. Cornil, *J. Phys. Chem. A* 110, 6356 (2006).
39. J. R. Bolton and M. D. Archer, *Adv. Chem. Ser.* 228, 7 (1991).
40. P. L. Dutton and C. C. Mosser, *Proc. Natl. Acad. Sci. U. S. A.* 91, 10247 (1994).
41. C. R. Kagan, C. B. Murray and M. G. Bawendi, *Phys. Rev. B* 54, 8633 (1996).
42. J. N. Clifford, E. Palomares, M. K. Nazeeruddin, M. Graetzel, J. Nelson, X. Li, N. J. Long and J. R. Durrant, *J. Am. Chem. Soc.* 126, 5225 (2004).
43. R. J. Miller, G. L. McLendon, A. J. Nozik, W. Schmickler and F. Willig, *Surface Electron-Transfer Processes*. 1995, New York: VCH.
44. I. Robel, M. Kuno and P. Kamat, *J. Am. Chem. Soc. ASAP*, (2007).
45. It is possible that there is some coupling of the charge annihilation reaction to vibrational modes in the NCs-probably the long optical (LO) phonon ( $\omega = 210 \text{ cm}^{-1}$ ), the out-of-phase vibration of Cd and Se atoms-but, even if  $S = 1$  for this coupling,  $\lambda$  (0.026 eV) is much smaller than that estimated for coupling to vibrations in the polymer.
46. N. E. Gruhn, D. A. da Silva Filho, T. G. Bill, M. Malagoli, V. Coropceanu, A. Kahn and J. L. Bredas, *J. Am. Chem. Soc.* 124, 7918 (2002).
47. We will assume that, because the density of states at the top of the VB of PEDOT:PSS is so high, injection of holes at the relatively low voltages we applied will not significantly alter the position of the top of this band.
48. This scenario is in contrast to the traditional "band-bending" picture in which an endothermic charge transfer is aided by increased resonance of donor and acceptor states due to an applied interfacial electric field.
49. Marcus theory also fails to predict that the junction will turn on as charges build up at the interface: If only the magnitude of FC at the interface determined the height of the barrier, the reaction would become less probable the higher the magnitude of the applied voltage, because charging at the interface would become increasingly difficult due to Coulombic repulsion and the charge-separated state would be destabilized relative to the

neutral product state (a phenomenon seen frequently in inverted region rate processes under applied electric fields).

50. S. Franzen, R. F. Goldstein and S. G. Boxer, *J. Phys. Chem.* 94, 5135 (1990).
51. A study that monitored the quenching of electronic transitions as a function of applied potential<sup>88</sup> showed that, for NC solids (solid-state arrays) containing CdSe NCs from 5.3 nm to 8.4 nm in diameter, this difference was consistently  $\sim 0.25$  V. We will, therefore, assume that the energies of the LUMO levels of the NCs at the interface are pushed up by 0.25 eV from their neutral levels due to energetic perturbation of energy levels at the interface (effect i).
52. M. Drndic, M. V. Jarosz, N. Y. Morgan, M. A. Kastner and M. G. Bawendi, *J. Appl. Phys.* 92, 7498 (2002).
53. To "dope" in this context is to add electrons (reduce) or to add holes (oxidize) to a material, either chemically or electrochemically, not to dope in the chemical sense (i.e., to introduce impurities into a crystalline semiconductor.)
54. Typically, insulators have resistivities of  $\sim 10^{16}$   $\Omega\cdot\text{m}$
55. D. Yu, C. J. Wang and P. Guyot-Sionnest, *Science* 300, 1277 (2003).
56. C. Wang, M. Shim and P. Guyot-Sionnest, *Appl. Phys. Lett.* 80, 4 (2002).
57. T. Franzl, T. A. Klar, S. Schietinger, A. L. Rogach and J. Feldmann, *Nano Lett.* 4, 1599 (2004).
58. We also saw up to a 100-fold (but usually less than 10-fold) increase in current upon photoexcitation when the EGaIn was biased negatively with respect to the ITO (i.e., under forward bias), but this enhancement is probably due to secondary photocurrent; i.e., by exposing the devices to light, we created charge carriers from quantum-confined photoexcited states in the NC layers, and filled cationic surface traps on the NCs.
59. As previously<sup>[refdarkpaper,defects]</sup>, we have used the log-mean, rather than the arithmetic mean ( $\langle I \rangle$ ), because the values for  $\log(I)$  fit a normal distribution better than did the values for  $I$ .
60. E. A. Weiss, R. C. Chiechi, V. J. Porter, S. Geyer, M. G. Bawendi and G. M. Whitesides, *NC paper--Dark* (2007).



# Curriculum Vitae

## Venda Porter

### Education

#### **Massachusetts Institute of Technology**

Ph.D. Candidate. Department of Chemistry, expected degree date June 2007.

Thesis work: Exploring and Enhancing Conductivity in Semiconductor Nanoparticle Films.

**GPA 5.0/5.0**

#### **Hamline University**

B. A. Chemistry and B. A. Physics, Summa Cum Laude, May 2002.

**GPA 3.95/4.0**

### Honors and Awards

Excellence in Teaching Award – Massachusetts Institute of Technology, 2003

Pat Paterson Award (senior female athlete for leadership) – Hamline University, 2002

Phi Beta Kappa — Hamline University, 2001

Carter Scholarship Fund (junior chemistry major for achievement) – Hamline University, 2001

Scott Filstrup Endowed Scholarship Fund (junior physics major) – Hamline University, 2001

Batchelder Memorial Scholarship in Chemistry – Hamline University, 2000

Robert M. Page Scholarship (academic achievement in physics) – Hamline University, 2000

Outstanding Sophomore Student Athlete Award – Hamline University, 2000

First-year Physics Award – Hamline University, 1999

### Research Experience

#### **MIT, Department of Chemistry**

Cambridge, MA

Advisor: Professor Mounqi G. Bawendi

November 2002- June 2007

*“Exploring and Enhancing Conductivity in Semiconductor Nanoparticle Films”*

#### **Hamline University, Department of Chemistry**

St. Paul, MN

Advisor: Professor Joann Pfeiffer

June 2001 – April 2002

*“Study of the photoacoustic spectrum in molecules”*

Advisor: Professor Eugene T. Smith

September 2000 – May 2001

*“Elemental analysis of wisdom teeth”*

#### **3M. Technical Assistant**

St. Paul, MN

Supervisor: Steve Znameroski

May 2000 – August 2002

*“Attachment of metal to fiber optic cables”*

## Teaching and Service

- MIT, Chemistry R.E.F.S.** Cambridge, MA  
**(Resource for Easing Friction & Stress)** 2004 -2007  
Serve as a resource for fellow graduate students to help manage conflict and stress  
Massachusetts State Certified in mediation
- MIT, Women in Chemistry** Cambridge, MA  
Serve on organizing board and plan events 2005 - 2007
- MIT, Chemistry Outreach Volunteer** Cambridge, MA  
Conduct exciting chemistry demonstrations for local high school students 2003 - 2006
- MIT, Teaching Assistant** Cambridge, MA  
5.112, General Chemistry (fall) and 5.61, Thermodynamics (spring) 2002 - 2003

## Publications

- Porter, V. J.**; Geyer, S.; Halpert, J.; Kastner, M. A.; Bawendi, M. G. "Room Temperature Photocurrent Displaying 100 % Internal Quantum Efficiency in CdSe/ZnS Nanocrystal Films," (submitted 2007).
- Porter, V. J.**; Geyer, S.; Halpert, J.; Mentzel, T.; Kastner, M. A.; Bawendi, M. G. "A Study of Photoconductivity in CdSe/CdTe Nanocrystal Solids for Photovoltaic Devices," (submitted 2007).
- Weiss, E. A.; **Porter, V. J.**; Chiechi, R. C.; Geyer, S.; Bell, D. C.; Bawendi, M. G.; Whitesides, G. M. "Size-Dependent Charge Transport and Collection in Junctions Containing Single-Size and Multi-Size Arrays of Colloidal CdSe Quantum Dots," (submitted 2007).
- Weiss, E. A.; **Porter, V. J.**; Chiechi, R. C.; Geyer, S.; Bell, D. C.; Bawendi, M. G.; Whitesides, G. M. "The Use of Spatially-Selective Photoexcitation to Study the Mechanism of Photocurrent Generation in Junctions containing Multi-Size Arrays of Colloidal CdSe Quantum Dots," (submitted 2007).
- Mentzel, T.; **Porter, V. J.**; Geyer, S.; MacLean, K.; Bawendi, M. G.; Kastner, M. A. "Charge Transport in Arrays of PbSe Nanocrystals," (submitted 2007).
- Porter, V. J.**; Mentzel, T.; Charpentier, S.; Kastner, M. A.; Bawendi, M.G. "Temperature-, gate-, and photoinduced conductance of close-packed CdTe nanocrystal films." *Phys. Rev. B.*, **2006**, 73, 155303
- Halpert, J. H.; **Porter, V. J.**; Zimmer, J.; Bawendi, M. G. "Synthesis of CdSe/CdTe Nanobells." *J. Am. Chem. Soc.*, **2006**, 128, 12590

Jarosz, M. V.; **Porter, V. J.**; Fisher, B. R.; Kastner, M. A.; Bawendi, M. G. "Photoconductivity studies of treated CdSe quantum dot films exhibiting increased exciton ionization efficiency." *Phys. Rev. B.*, **2004**, 70, 195327

**Porter, V. J.**; Sanft, P. M.; Dempich, J. C.; Dettmer, D. D.; Erickson, A. E.; Dubauskie, N. A.; Myster, S. T.; Matts, E. H.; Smith, E. T. "Elemental Analysis of Wisdom Teeth by Atomic Spectroscopy Using Standard Additions." *J. Chem. Ed.*, **2002**, 79, 1114-1116

### Presentations

**Porter, V. J.**; Geyer, S.; Halpert, J. H.; Mentzel, T.; Kastner, M. A.; Bawendi, M. G. "Tuning the Height of the Tunnel Barrier in Colloidal Semiconductor Nanoparticle Films" *National Meeting of the American Physical Society*, Denver, CO, March 2007 (oral)

**Porter, V. J.**; Halpert, J. H.; Nair, G. P.; Mentzel, T.; Kastner, M. A.; Bawendi, M. G. "Efficient exciton separation in mixed films of CdSe and CdTe nanoparticles." *231<sup>st</sup> American Chemical Society Meeting*, Atlanta, GA, March 2006 (oral)

**Porter, V. J.**; Kastner, M. A.; Bawendi, M. G. "Effect of an Injecting Contact on the Conductivity of Close Packed CdTe Quantum Dots Films." *Materials Research Society*, Boston, MA, December 2005 (oral)

**Porter, V. J.**; Kastner, M. A.; Bawendi, M. G. "Influence of a Non-Blocking Contact on the Conductivity in CdTe Quantum Dot Films" *Cluster, Nanocrystals, and Nanostructures Gordon Conference*, August 2005 (poster)

**Porter, V. J.**; Jarosz, M. V.; Fisher, B. R.; Kastner, M. A.; Bawendi, M. G. "Photoconductivity Studies of Treated CdSe Quantum Dot Films Exhibiting Increased Exciton Ionization Efficiency" *National Meeting of the American Physical Society*, Los Angeles, CA, March 2005 (oral)

## Acknowledgements

Graduate school was challenging and exhausting at times; however, as I look back on the past five years I can say with confidence that I enjoyed my time spent in the basement of building 18. This is easy to say now that all of the stressful events (cumes, oral exams, etc...) of graduate school are over, but truthfully I can't think of a single day that I woke up and did not want to come into lab. This is a true reflection on the great people, both friend and labmates, who shared some part of my time spent at MIT and I would like to thank everyone for their support.

I'd first like to thank Mounqi for letting me join his research group even after I got a big old 'F' on his cume, my first at MIT. Mounqi has been an ideal advisor for me in that he was always available for guidance and scientific advice, yet he gave me the freedom to pursue experiments at my own pace and even design some of my own. Unlike other advisors at MIT, Mounqi does not run a lab fueled by stress and fear. Instead, I found the Bawendi lab to be an environment in which people enjoyed doing experiments, and individuals pushed themselves because they wanted to. In the Bawendi lab, I learned that research was fun in and of itself, and did not have to be coupled to getting the best grade or highest score and I am grateful to Mounqi for that.

Of course, all of my labmates (a.k.a. Nanoballers) also contributed to the atmosphere of the lab. Mirna welcomed me to the conductivity project and never faltered in her patience as she imparted her knowledge of synthesis, films, and measurements to me. Besides being an excellent mentor, Mirna has also been a great friend as we shared a love of puppies, pop music, Starbucks, and those silly lawn geese you can dress up in seasonal clothing. Scott, you had the guts to join the conductivity project despite not being a tall, brown haired girl from the Pacific Northwest, and I am glad that you did. It has been a lot of fun working with you this past year and a half and I want to thank you for being so easy going and always bringing a sense of humor to work with you. I leave confident the project is in good hands. Also, coining the phrase 'Nanoballers' for the volleyball team is a significant achievement for which you deserve a lot of credit. The next shout out goes to Jon Halpert for all of the fun he brought to the lab. Despite the occasional, how shall I put it, 'clutter' in our hood you were a good hoodmate and friend and I always enjoyed our discussion about science or other random topics. Four o'clock coffee, lunch, softball, poker night, and volleyball would not have been the same without you. Good luck with the Rubik's cube next year. I'd next like to thank Preston for always sharing an office with me. You made lab entertaining from our first day in the 'first-year' office when you tried to convince me that you didn't know what an electron was. I'd also like to thank you for being a great teacher and always taking time from your own research to help me with a calculation or synthesis. Yinthai was also a mentor to me, both in the ways of synthesis and in the ways of group lunch.

Next, I would like to thank some of the laser lab and electronics people who all aided in my attempts at spectroscopy and electrical measurements over the years: Gautham for being one the smartest people I know, both in terms of science and in celebrity gossip (perhaps the more important field?); Lisa for being the only other girl to attend Hao's bachelor party with me; Hao for his endless energy and happiness; Dave for being meticulous and always designing and maintaining nice equipment I could 'borrow'; August for his helpful advice; Dirk for helping

welcome me to the group; Jean-Michel for his patient assistance; Inhee for caring about everyone; and Brent for his humor. I would also like to thank Jane and Wenchao who joined the Bawendi lab at the same time as me. To everyone else – Nathan, Sungjee, Joe, John Z., Jonny, Brian Y., Numpon, Wen, Cliff, Xavier, Binil, Jongnam, Sonwook, Sonja, Juwell, Becky, Andrew, Hideyuki, Juan, Brian W., Peter, and Hee-Sun -- I have enjoyed working with all of you and wish you the best in the future.

I have been very lucky in that I have had the fortune to work with excellent collaborators outside of the Bawendi group. Emily Weiss and Ryan Chiechi have been a pleasure to work with this past year and a half, and have brought a lot to my research and the Bawendi lab; both in new scientific methods and in stories and chemistry gossip from the University down the river (a.k.a Harvard). From the Kastner lab, I got to work with another great person in Tamar Mentzel. I am so glad that you decided join the QD project, not only because I had someone to work on experiments with, but because I got a running partner and friend as well. I enjoyed our discussions as we ran around the Charles both about research and life in general. I would also like to thank the other Kastner group members who worked with me over the years – both Maria's, Fumi, Laurie, and Sophie – and I would like to thank Marc Kastner for his interest in NC conductivity and for being an endless source of knowledge and advice.

Finally, I would like to thank the people outside of my research who made my time in Boston special. Lauren thanks for suffering through quantum I and II with me and for your friendship. Andrea, we have shared a lot of fun times together and I always looked forward to Wednesday TV night (be it Top Model or Project Runway) to add some sanity to my week. To my roommates at 42 Fulkerson (Kyle and Chris), thanks for letting a girl move in into your bachelor pad and for the fun times over the years. I also want to thank my furrier roommates (the puppies, Coors and Coconut) for always being happy to see me when I came home from work. I want to thank my parents and family for their love and support of my goals. Finally, I want to thank Kevin for being my best friend and always pushing me to succeed whether it was on the softball field or by encouraging me to come into lab every Saturday because you did. I would not be where I am without you.